Quantum Theory for the Computer Age
Unit 5

$E = 8^2 = 64$ *(Bohr units)*

$E = 6^2 = 36$ *(Bohr units)*

$E = 4^2 = 16$ *(Bohr units)*

1st B_1B_2 re-crossing

$E = 2^2 = 4$ *(Bohr units)*
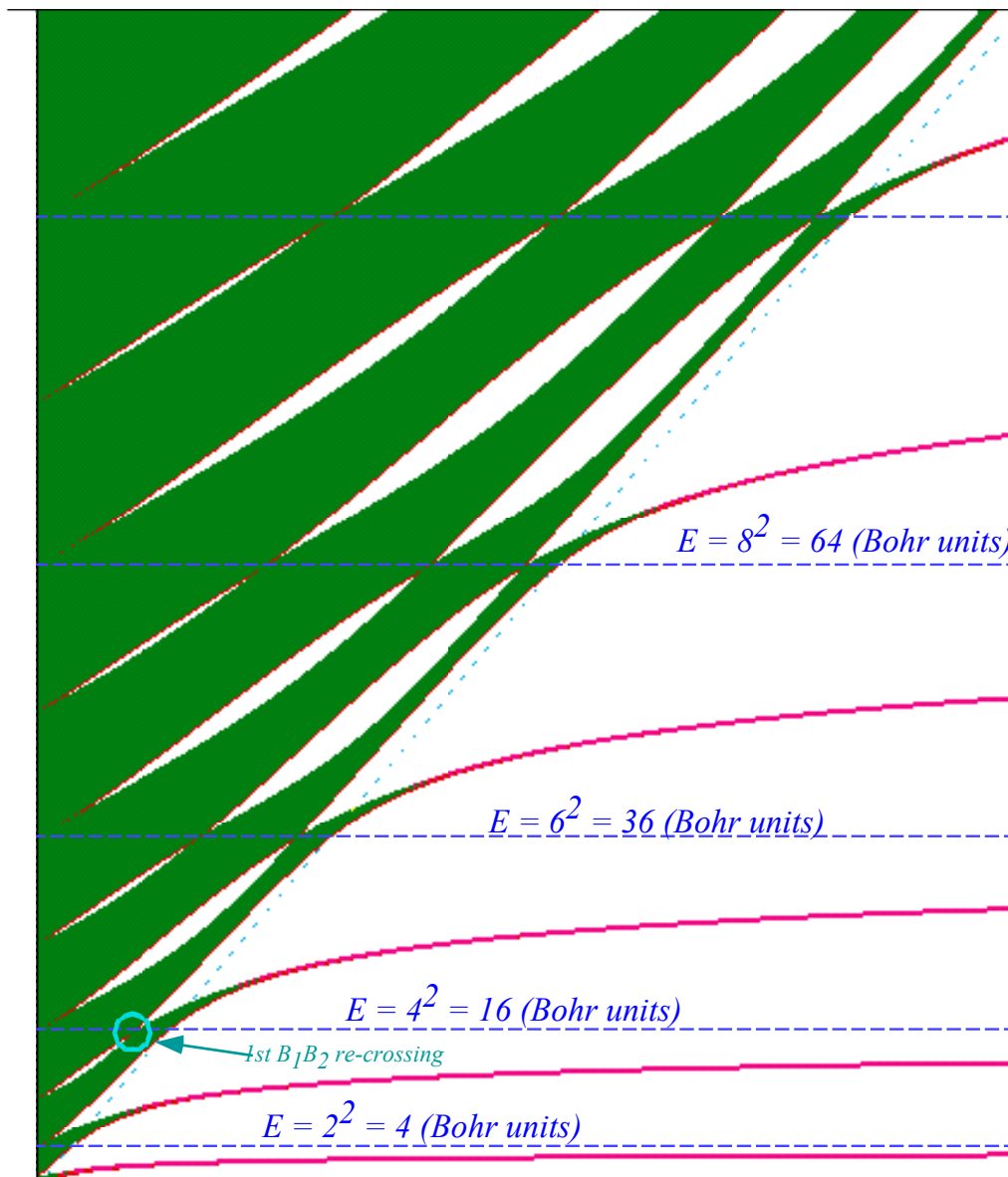
Multiple Barriers and Resonance Bands

Unit 5 Periodic Potentials

Unit 4 introduced the Schrodinger time equation with piecewise constant potential barriers and wells with their strong distinction between resonance in a continuum and discrete bound states. This Unit 5 introduces periodic potential barriers for which these distinctions begin to disappear. In the real world every state is a resonance; some are more so but nothing lives forever. Symmetry is a key property that encourages high quality resonance because it means having two or more parts that are similar or identical and this implies frequencies that are similar or identical, the *sin qua non* for resonance. Examples are given of potential well systems with symmetry equal to or greater than that of the C_n sytems of Unit 3 Chapter 9. Energy bands and states of periodic potentials are introduced using the ideas of resonant and nonresonant eigenchannels introduced in the preceding Chapter 13. Kronig –Penney solutions are related to resonance band structure in Chapter 14, to non-commutative symmetry group algebra in Chapter 15, and to different flavors of Fourier symmetry analysis in Chapter 16.
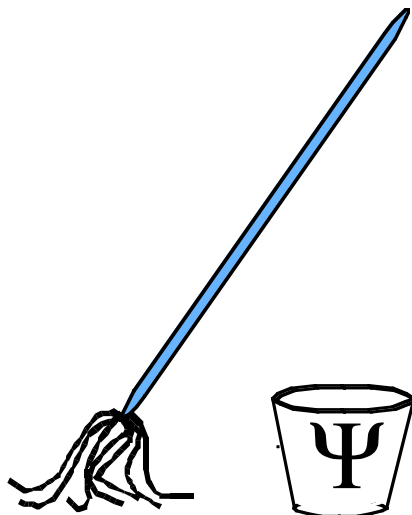
W. G. Harter

Department of Physics

University of Arkansas

Fayetteville

QM
for
AMOP

Chapter 14

Multiple Barriers

and Resonance Bands

W. G. Harter

The preceding Chapter 13 dealt with simple potential well and barrier states in what amounted to minimum-security prisons. This Chapter 14 deals with more clever forms of wave incarceration involving repeated sets of barriers and quantum wells that resemble the discrete C_N-symmetric quantum dot structures of Chapters 8 and 9. While the latter had discrete spectra, the quantum wells described in this Chapter have a continuous spectrum, but it is peppered with resonance bands and wave states quite like the discrete C_N-bands. Now the distinction becomes blurred between the free and the imprisoned or continuous and discrete; they're two sides of the same coin!

Chapter 14. Multiple Barriers and Resonance Bands

14.1 Waves and Potential Barriers: Crossing Matrices

A revealing approach to the band theory of solids involves stringing together multiple copies of barriers and wells in various symmetric arrays or sequences. In Sec. 13.1 (b) we noted that the crossing matrix for a sequence of potential structures is the matrix product of the *C*-matrices of the component sub-structures. If each sub-structure is the same except for its location, then the component *C*-matrices all have the same form and nearly the same numerical values differing only in phase factors here and there.

(a) Well-well

Consider stringing two identical wells together as in Fig. 14.1.1.
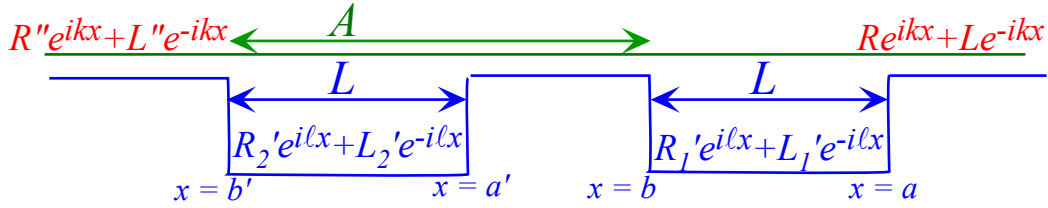
Fig. 14.1.1 *C₂-symmetric double square well* .

Using the preceding *C*-matrix (13.3.33) in a product yields the desired well-well or (well)² *C*-matrix.

$$\begin{pmatrix} R'' \\ L'' \end{pmatrix} = C' \cdot C \begin{pmatrix} R \\ L \end{pmatrix} = \begin{pmatrix} e^{ikL}\chi^* & -ie^{-ik(a'+b')}\xi \\ ie^{ik(a'+b')}\xi & e^{-ikL}\chi \end{pmatrix} \cdot \begin{pmatrix} e^{ikL}\chi^* & -ie^{-ik(a+b)}\xi \\ ie^{ik(a+b)}\xi & e^{-ikL}\chi \end{pmatrix} \begin{pmatrix} R \\ L \end{pmatrix}$$

$$= \begin{pmatrix} e^{i2kL}\chi^{*2} + e^{-i2kA}\xi^2 & -i\xi\left(e^{-i2kb}\chi^* + e^{-i2ka'}\chi\right) \\ i\xi\left(e^{i2kb}\chi + e^{i2ka'}\chi^*\right) & e^{-i2kL}\chi^2 + e^{i2kA}\xi^2 \end{pmatrix} \begin{pmatrix} R \\ L \end{pmatrix} \qquad (14.1.1a)$$

where the following matrix components are defined:

$$\chi = cos\ \ell L + i\ cosh\ 2\alpha\ sin\ \ell L \quad \text{and:} \quad \xi = sinh\ 2\alpha\ sin\ \ell L \qquad (14.1.1b)$$

The well-length *L* and distance or *lattice constant A* between wells are, respectively, the following.

$$L = a - b = a' - b' \quad \text{and,} \quad A = a - a' = b - b' \qquad (14.1.1c)$$

The kinetic factors are a repeat of those in (13.3.33c).

$$cosh\ 2\alpha = \frac{1}{2}\left(\frac{\ell}{k} + \frac{k}{\ell}\right) = \frac{\ell^2 + k^2}{2k\ell}, \qquad sinh\ 2\alpha = \frac{1}{2}\left(\frac{\ell}{k} - \frac{k}{\ell}\right) = \frac{\ell^2 - k^2}{2k\ell}, \qquad (14.1.1d)$$

As shown just before equation (13.1.25), a resonance has zero reflection, that is, *L″= 0* or

$$0 = L'' = C_{21}R = i\xi\left(e^{i2kb}\chi + e^{i2ka'}\chi^*\right)R . \qquad (14.1.2)$$

This also implies perfect transmission *(|T|=1)* with the following inverse transmission ratio.

$$1/\sqrt{|T|} = |R''|/|R| = 1 = |C_{11}| = \left|e^{i2kL}\chi^{*2} + e^{-i2kA}\xi^2\right|. \qquad (14.1.3)$$

For energy below barrier *V*, this ratio, with *ik=−κ*, goes to zero for bound states. (Recall Fig. 13.2.2.)

$$|R''|/|R| = |C_{11}| = \left|e^{-2\kappa L}\chi^{*2} + e^{2\kappa A}\xi^2\right| \to 0 \qquad (14.1.4)$$

        For the double well, resonant and bound states come in nearly degenerate pairs. In Fig. 14.1.2 a and b are two orthogonal bound state waves for a potential $V=-25$ of width $L=1.5$ and separation $A=2.0$. The ground state (a) has energy $E(0^+) = -23.468$ and while the first excited state has energy $E(0^-) = -23.437$ is barely *0.03* above the ground state. The probability envelopes for the two states are practically indistinguishable except at the mid-point between the two wells where the excited state has a node but the ground state does not. This pair is analogous to the NH_3 inversion doublet discussed in Chapter 10.

(b) *Antisymmetric E(0⁻)*
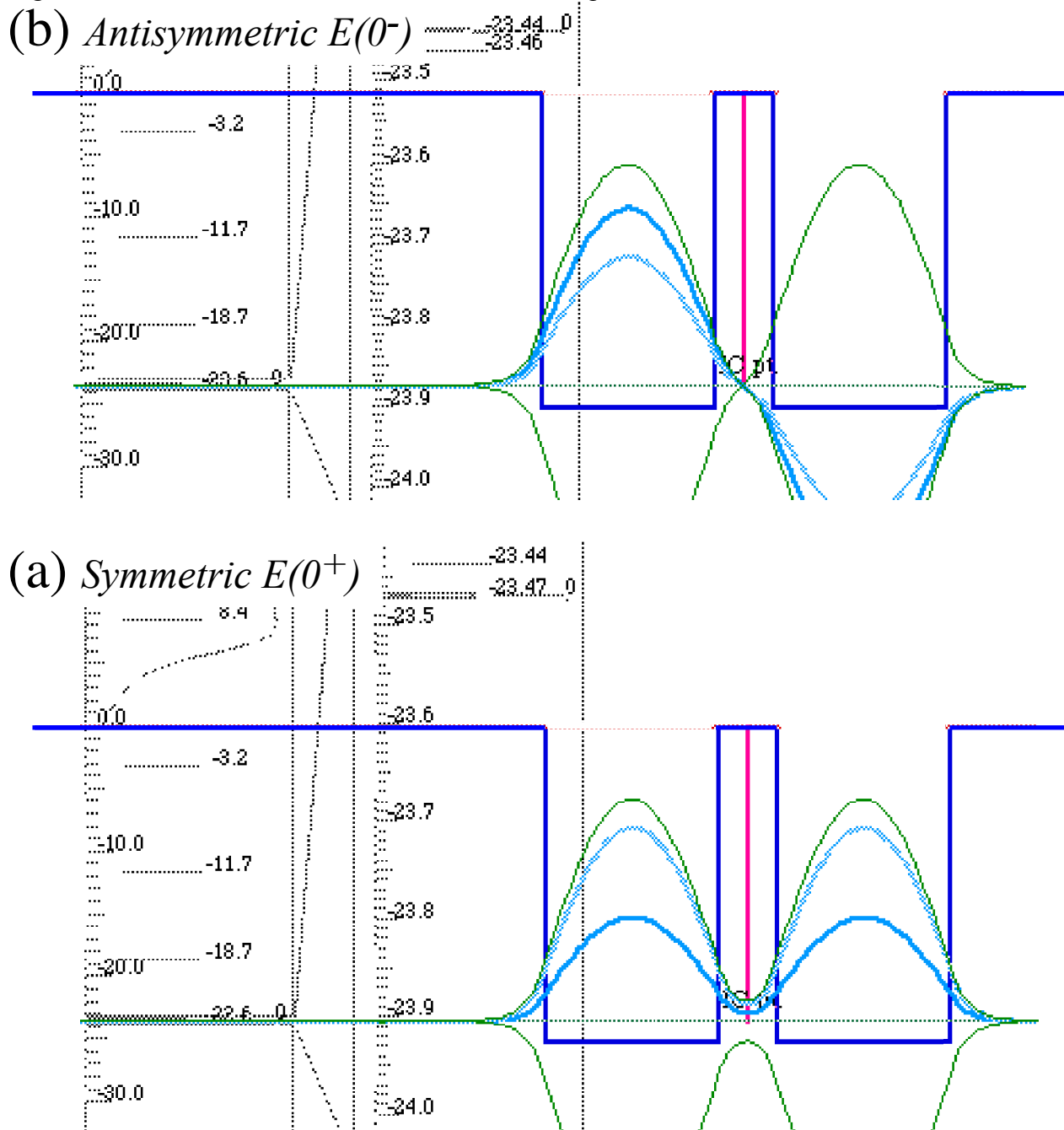
(a) *Symmetric E(0⁺)*

Fig. 14.1.2 Lowest inversion-doublet pair in double well . (a) Symmetric, (b) Anti-symmetric

Energy eigenlevels $E(1^+) = -18.96$ and $E(1^-) = -18.81$ are paired, too, into an antisymmetric and symmetric set of waves shown in Fig. 14.1.3 a and b. However, now energy difference $\Delta E=0.15$ is not quite so small.

(b) *Antisymmetric E(1⁻)*
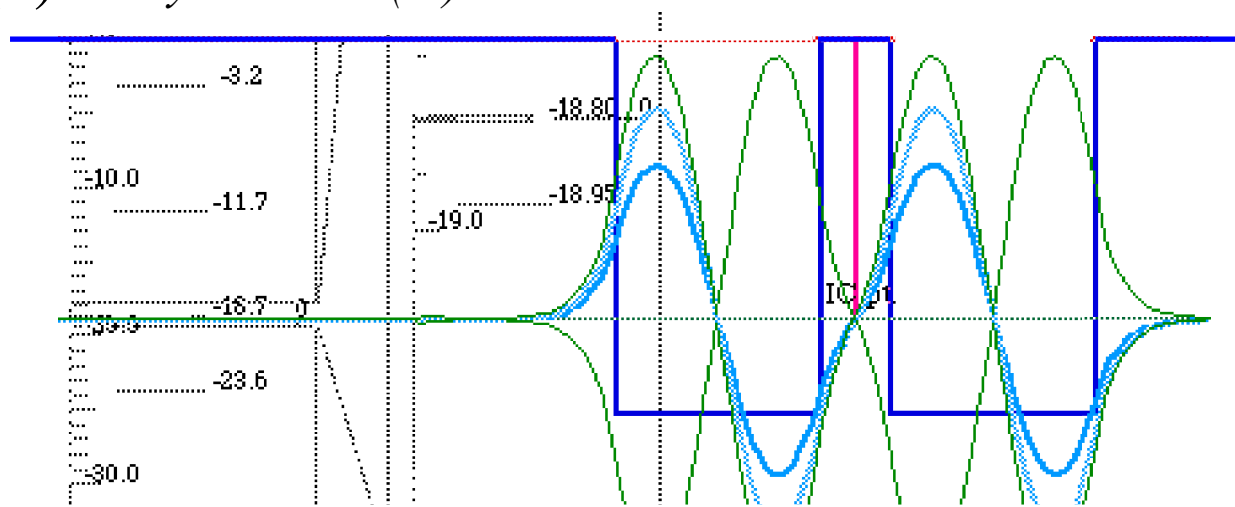
(a) *Symmetric E(1⁺)*
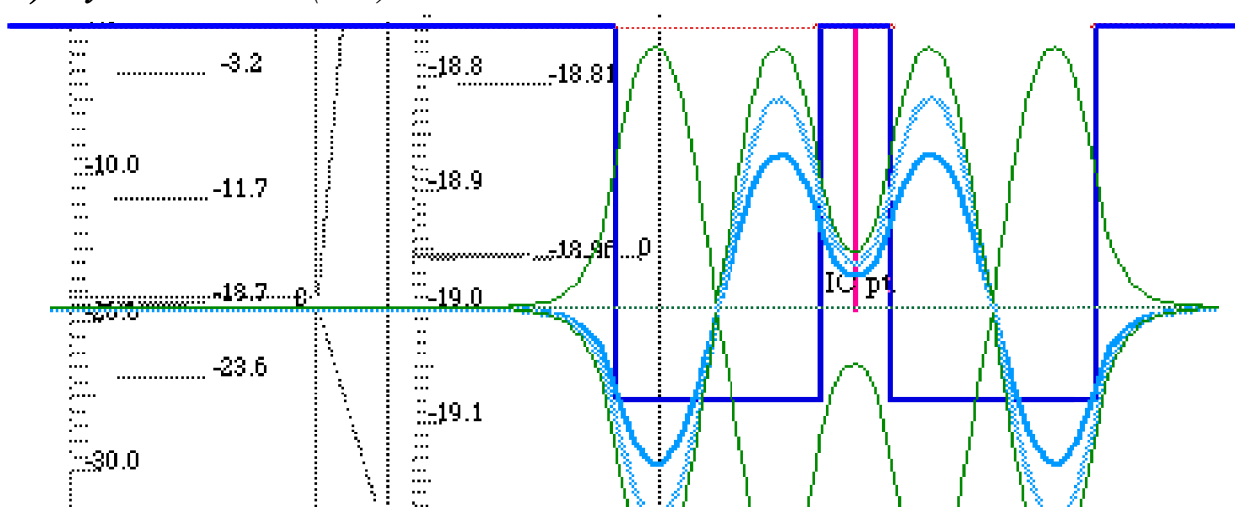
Fig. 14.1.3 Next lowest inversion-doublet pair in double well . (a) Symmetric, (b) Anti-symmetric

Each eigenlevel of the single well namely, $E(0)= -23.453$, $E(1)= -18.88$, and so forth, is found to lie nearly midway between an inversion doublet pair of the double-well potential. In other words, each pair is described by the familiar 2-state bilaterally symmetric *B*-type Hamiltonian matrix from (10.2.4c).

$$\begin{pmatrix} \langle 1|\mathbf{H}|1\rangle & \langle 1|\mathbf{H}|2\rangle \\ \langle 2|\mathbf{H}|1\rangle & \langle 2|\mathbf{H}|2\rangle \end{pmatrix} = \begin{pmatrix} A & B \\ B & A \end{pmatrix} = \begin{pmatrix} H & -S \\ -S & H \end{pmatrix} \qquad (14.1.5)$$

Here $\Delta E=2S$ is the splitting between each pair of double well states having energy $E^+=H-S$ or $E^-=H+S$. This notation was adapted in the *NH₃* discussion beginning with (10.3.3).

The beat dynamics of the waves in Figs. 14.1.2-3 are the same as that which was discussed in Chapter 10.2b. A mixture of an n^+ and n^- state (particularly a 50-50 mixture) results in a beat oscillation back and forth at the difference or tunneling frequency $\Delta E/\hbar =2S/\hbar$. The only difference is that these frequencies can be exponentially small for pairs that lie deep down in their respective wells. Then tunneling looks more like a diffusive "oozing" process than a resonant process that it must be.

Resonance states also come in pairs. The transmission spectrum for a pair of nearest grazing resonances in Fig. 14.1.4 shows a barely resolved doublet corresponding to resonances $E(4^+) = +8.4$ and $E(4^-) = +10.0$. The waves shown belong to carefully prepared *S*-matrix eigenchannel states using the center of symmetry as the origin. Note how the symmetric wave piles up more charge on the central barrier than the antisymmetric wave which has a node at origin. For a more nearly grazing resonance this charge localization effect is even more pronounced, particularly with a narrow central barrier like this potential.

At higher energy or for thicker separation barriers, the barrier-top resonances such as pictured in Fig. 13.1.6, will contribute to transmission variation along with the intra-well resonances shown here in Fig. 14.1.4. Later on in Sec. 14.2 (c-3), we shall encounter situations where the two occur together. As pointed out in previous discussions (For example, recall Fig. 13.1.7.), much of this sharp resonance phenomena owe their existence to sharp-walled potentials with flat tops!

(b) *Antisymmetric Resonance E(4⁻)*
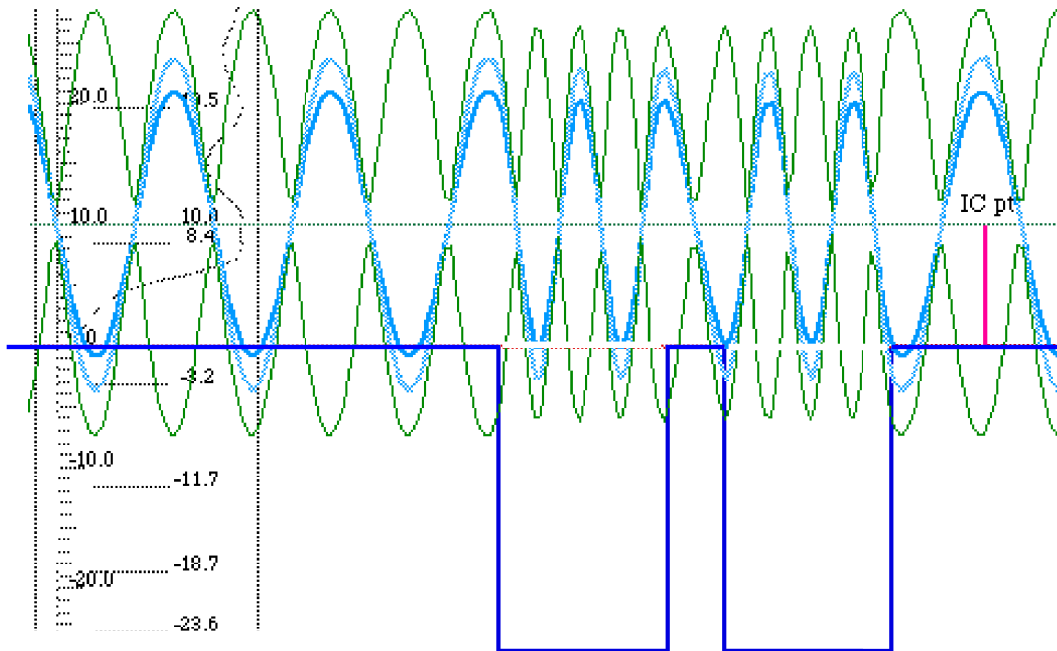
(a) *Symmetric Resonance E(4⁺)*
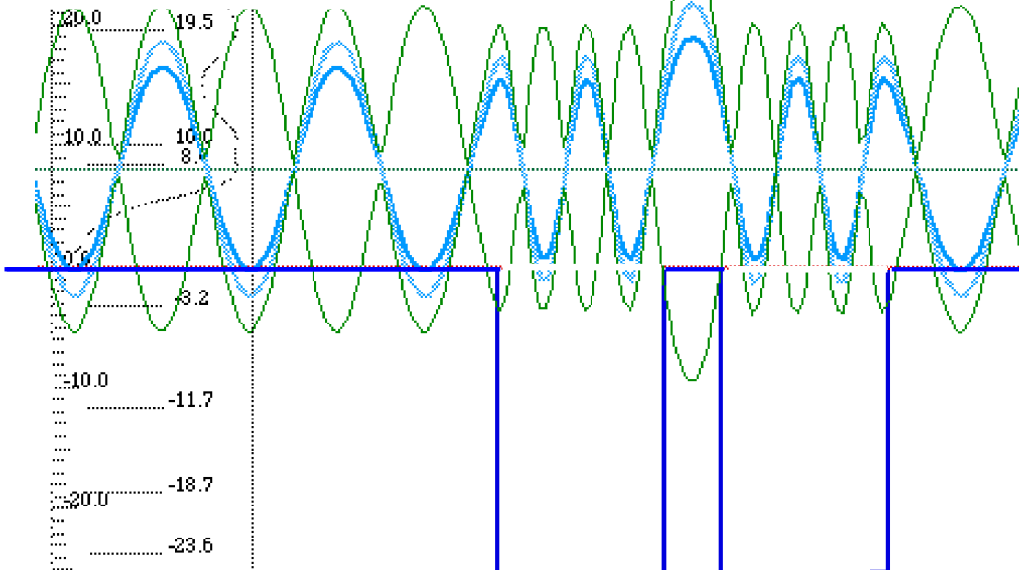
Fig. 14.1.4 Resonance-doublet pair above double well . (a) Symmetric, (b) Anti-symmetric

(b) Hump-hump

The same equations (14.1.1) with minor changes apply to a pair of humps shown in Fig. 14.1.5.

$R''e^{ikx}+L''e^{-ikx}$ $R_2'e^{i\ell x}+L_2'e^{-i\ell x}$ $R_1'e^{i\ell x}+L_1'e^{-i\ell x}$ $Re^{ikx}+Le^{-ikx}$

A

L L

$x = b'$ $x = a'$ $x = b$ $x = a$
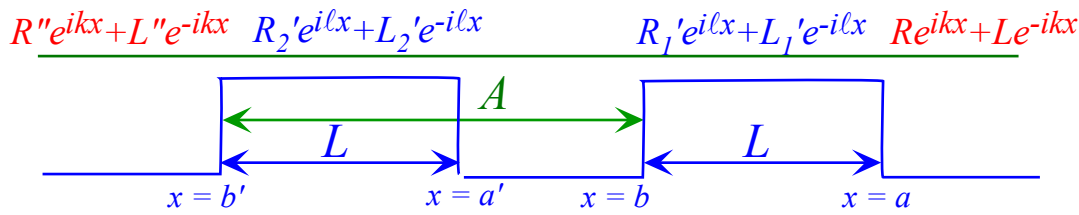
Fig. 14.1.5 C_2-symmetric double barrier .

No modification of (14.1.1) is needed as long as the energy E is above the barrier top V.

$$\begin{pmatrix} R'' \\ L'' \end{pmatrix} = \begin{pmatrix} e^{i2kL}\chi^2 + e^{-i2kA}\xi^2 & -i\xi\left(e^{-i2kb}\chi^* + e^{-i2ka'}\chi\right) \\ i\xi\left(e^{i2kb}\chi + e^{i2ka'}\chi^*\right) & e^{-i2kL}\chi^2 + e^{i2kA}\xi^2 \end{pmatrix}\begin{pmatrix} R \\ L \end{pmatrix} \tag{14.1.6}$$

However, if $E<V$, the wavevector ℓ is replaced by $i\kappa$, i times an evanescent parameter, and the following matrix components are redefined accordingly from those of (14.1.1b),

$$\chi = cosh\ \kappa L - i\ sinh\ 2\beta\ \ sinh\ \kappa L, \quad and: \quad \xi = cosh\ 2\beta\ \ sinh\ \kappa L, \tag{14.1.7}$$

using barrier parameters in (13.3.34).

$$cosh\ 2\beta = \frac{1}{2}\left(\frac{\kappa}{k}+\frac{k}{\kappa}\right) = \frac{\kappa^2+k^2}{2k\kappa}, \quad sinh\ 2\beta = \frac{1}{2}\left(\frac{\kappa}{k}-\frac{k}{\kappa}\right) = \frac{\kappa^2-k^2}{2k\kappa} \tag{14.1.8}$$

The main difference between the analysis of two wells and two humps is that the latter has no bound states; only resonances. However, the resonances are true *trapping resonances* in the sense that enormous amplification is easy to achieve, so they should be distinguished from the less spectacular Ramsauer-Townsend non-trapping resonances described so far.

For example, let us use the same depth $V=25$ and the same dimension $b-a' = 1.5$ for the interior well of Fig. 14.1.5 as was used for the width $L=1.5$ in the preceding example involving Fig. 14.1.1. The result is an enormous resonance shown in Fig. 14.1.6 when the energy is tuned to the lowest peak at $E = 1.546$. (Note that the top-relative energy is $-25+1.546 =-23.454$; very close to the lowest E value of the single-well bound state or the H-value of the double well in the preceding section.)

The resonance amplitude in the well is amplified by approximately the sum of the magnitudes of the C_{11} or C_{12} components of barrier matrix (13.3.34a) each of which contributes about *32*.

$$C_{12} = -i\ cosh\ 2\beta\ sinh\ \kappa L = -31.8i \quad (for\ k = 6.8,\ \kappa = 1.76,\ L = 0.5\ )$$

So this resonance ends up with about *64* times the amplitude of the incoming wave or $64^2=4096$ times the intensity! By making the barriers thicker or higher we increase this amplification exponentially. (Recall single barrier tunneling problem 2.3.)

With amplitudes amplified so much you can expect that the sensitivity of the eigenchannel combinations will be extreme, too. Such strongly resonant systems are very sensitive to input amplitudes and phases as well as to changes in energy.
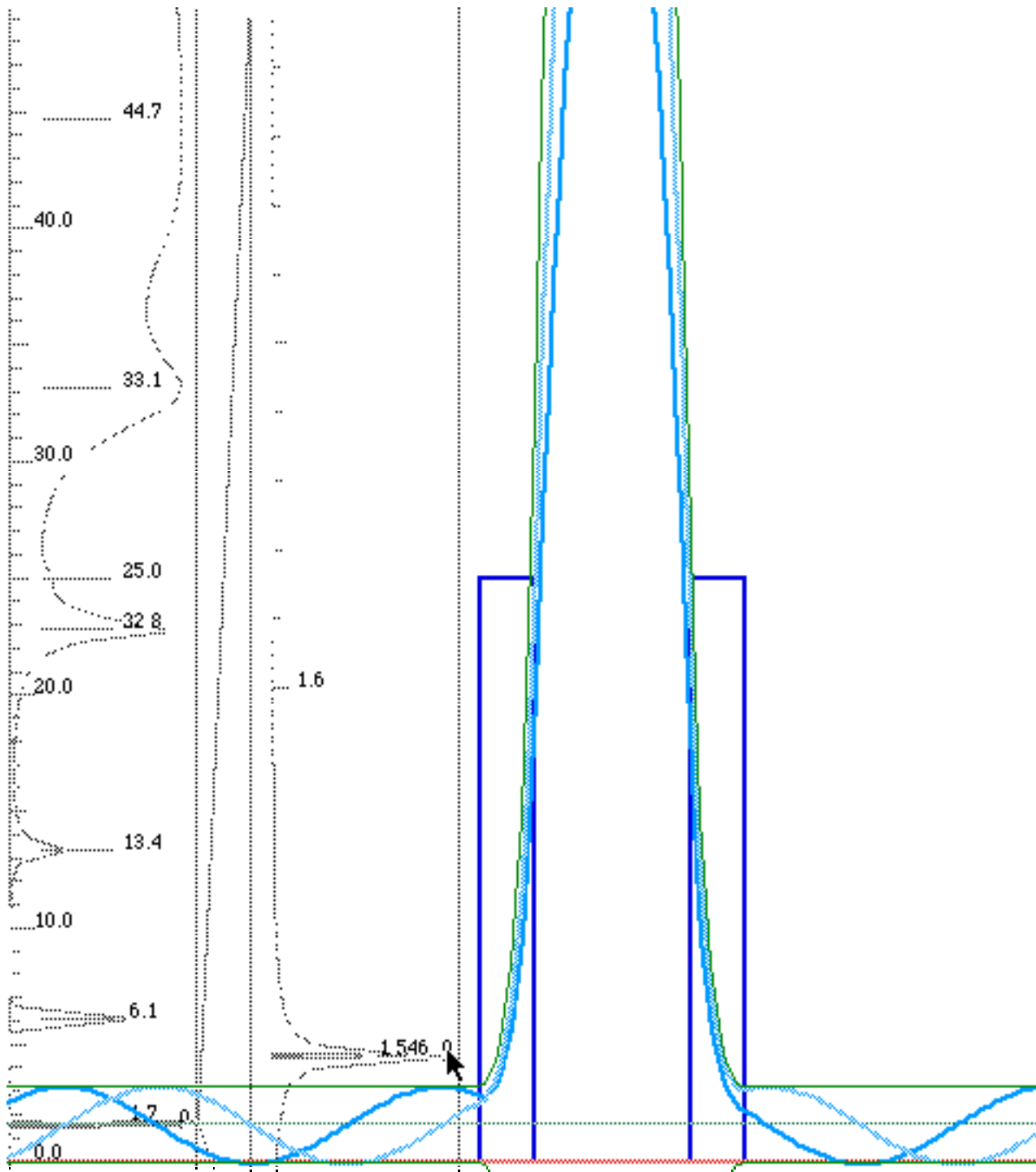
Fig. 14.1.6 Lowest (E= 1.546) resonance in L=0.5 well between two width=0.5 barriers(V=25) .

The next lowest resonance at (*E= 6.117 or -25+6.117 =-18.883*) is shown in Fig. 14.1.7. It is an antisymmetric wave with one node in the well. It has less amplification than the monster in Fig. 14.1.6, but still amounts to a gain of about 100 in intensity.

Fig. 14.1.7 Second (E= 6.117) resonance in L=0.5 well between two width=0.5 barriers(V=25) .

(1) C-and-S-Matrix Analytic properties: Resonance Widths and Lifetimes

Resonances in the preceding Fig. 14.1.6-7 can be made to exponentially approach bound states by raising or thickening the barriers. Even the flimsy walls used in the examples are sufficient to give resonance energies that approximate with 4-figure accuracy the bound-state energy eigenvalues for the same *(height = V =25, width = W =1.5)* well with infinitely thick walls. (See also Section 14.1(f).)
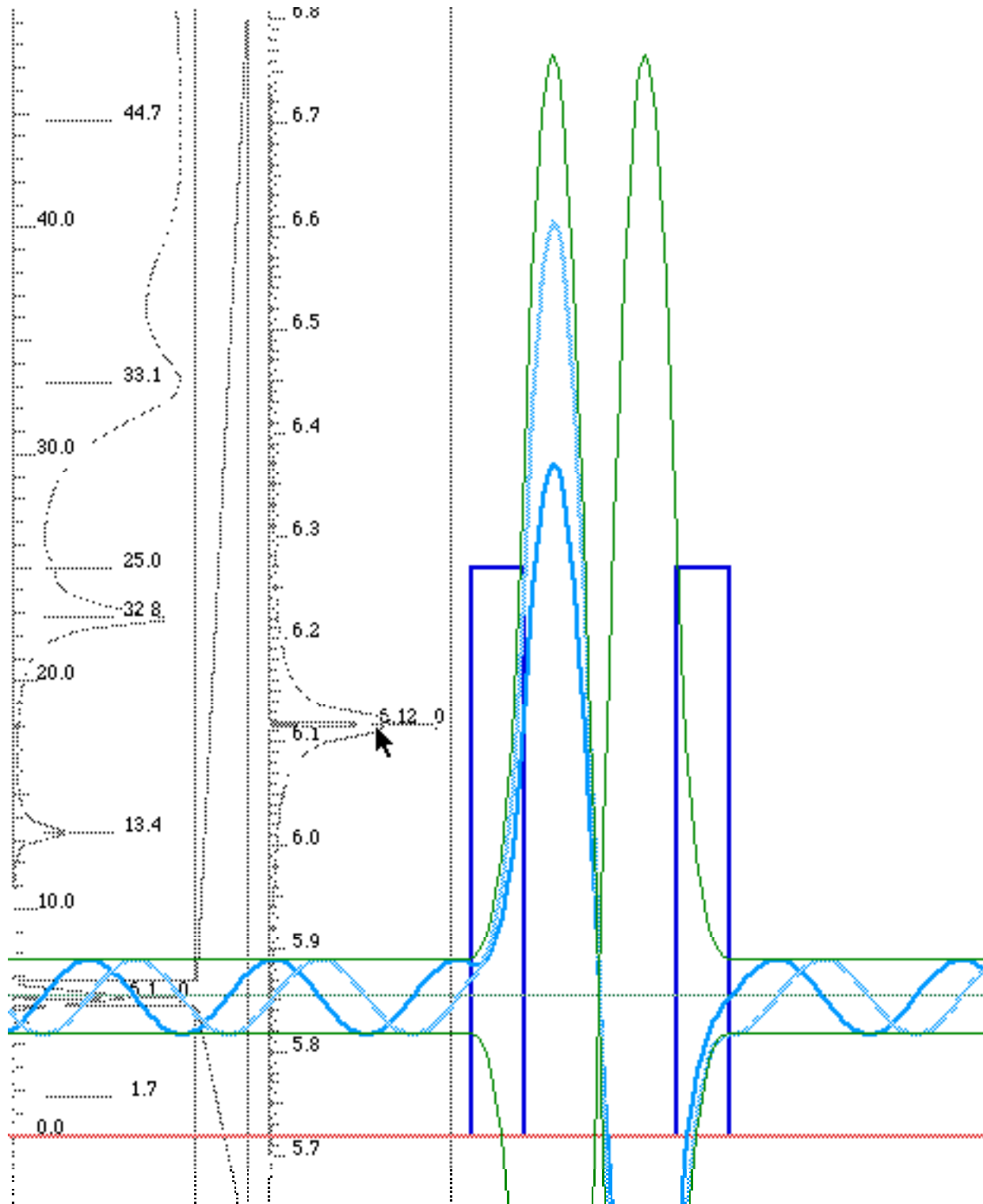
We have previously (in (14.1.4) and (13.2.2)) associated bound states with zeros of the ratio R''/R or, equivalently, poles of the ratio R/R''. Bound states require the amplitude R'' of the right moving wave $e^{i(kx - \omega t)}$ to vanish when the wavevector factor ik becomes a real evanescent parameter $-\kappa$ to avoid an exponential blow-up of $e^{-\kappa x}$ on the left side as x approaches $-\infty$. On the other side, amplitude R of the same wave can be non-zero since $e^{-\kappa x}$ vanishes automatically on the right hand side as x approaches $+\infty$.

So zeros of *C*-matrix component C_{11}, or equivalently, poles of *S*-matrix component $S_{12} = 1/C_{11}$, correspond to bound states if the wavevector becomes imaginary. Now we try a very strange but famous trick. We suppose that resonances for *real k* correspond to zeros of C_{11}, or equivalently, poles of S_{12} somewhere out in the *complex energy plane* but near the real *E*-axis.

The reasoning behind what seems, at first, to be crazy, is based on Fourier analysis. So far we haven't mixed states belonging to resonances and most of the pictures have been of states with a single energy carefully placed smack on top of a resonance peak. But, suppose for a minute that the peak is only the beginning of a huge (infinite) *S*-pole-mountain just below the real *E*-axis. More to the point, suppose C_{11} has a zero at complex energy $\hbar \Omega_n$ or complex frequency value $\Omega_n = \omega_n - i \Gamma_n$ just below the real resonance frequency ω_n. In other words, let the first Taylor-Laurent series expansion term of C_{11} be, for some coefficient c_n, as follows

$$C_{11}(\omega) = (\omega - \Omega_n)/c_n = (\omega - \omega_n + i\Gamma_n)/c_n \qquad (14.1.9)$$

in the neighborhood of Ω_n. Then the transmitted output amplitude R of the barrier system has the form

$$R_{k(\omega)} = \frac{1}{C_{11}(\omega)} R''_{k(\omega)} = \frac{c_n}{\omega - \Omega_n} R''_{k(\omega)} = \frac{c_n}{\omega - \omega_n + i\Gamma_n} R''_{k(\omega)} \qquad (14.1.10)$$

where we approximate coefficient c_n to be a constant in the neighborhood of the *n*-th resonance root Ω_n.

Suppose now that a continuous combination of near-resonant wave states are mixed together to make a non-stationary state whose wavefunction is approximately given by a frequency integral.

$$\Psi(x,t) = \int d\omega \, R_{k(\omega)} e^{i(kx-\omega t)} = \int d\omega \, \frac{c_n e^{i(kx-\omega t)}}{\omega - \omega_n + i\Gamma_n} R''_{k(\omega)}$$

$$\cong R''_{k(\omega_n)} c_n e^{ik(\omega_n)x} \int d\omega \, \frac{e^{-i\omega t}}{\omega - \omega_n + i\Gamma_n} \qquad (14.1.11)$$

Here we make approximations that you will see often in resonance theory. First, we suppose that the frequency distribution of the input amplitude $R''_{k(\omega)}$ is constant in the neighborhood of the resonance so it can go outside the integral. That is a good approximation since it could, in fact, be arranged. Next we move c_n outside, too, since it was previously assumed constant. This approximation depends on the approximate form of the *C*-matrix being what we said it was. (Not always so!) Finally, the wavevector $k(\omega)$ is assumed frozen at the resonance value $k(\omega_n)$. This is the most questionable of our approximations, and it will prevent us from seeing the group wave

interference outside of the barrier. However, since we are here interested only in rough overall time behavior this will be OK for now. Besides, it's the only way we can get a really simple analytic integral.

The integral itself is now approximated by appealing to *Cauchy's integral theorem* of complex *f(z)*.

$$\oint_C dz\, \frac{f(z)}{z-a} = \begin{cases} 0 & \text{if } a \text{ outside of contour } C, \\ 2\pi i\, f(a) & \text{if } a \text{ inside of contour } C. \end{cases} \qquad (14.1.12)$$

This is sometimes called *the residue theorem* and gives the value of an integral around a complex counter-clockwise contour *C* of a function *f(z)* (that has no poles inside *C*) divided by *(z-a)*. The value is *2πif(a)* or else zero depending on whether *a* is enclosed by contour *C* or not, respectively.

The integral (14.1.11) is a real integral but it can be made into a contour integral just like (14.1.12) by attaching a non-contributing "return loop" path that goes in ω-regions where the integrand, particularly the numerator $e^{-i\omega t}$, is practically zero. Such contours are sketched in Fig. 14.1.8. The upper contour is used for past time (*t*<0) because then ω=*i(large)* gives $e^{-i\omega t} = e^{(large)t}$ which is negligibly small for negative *t*. But, for the future times (*t* >0) we have to take the lower contour along which ω = *-i(large)* so, once again, the phasor values $e^{-i\omega t} = e^{-(large)t}$ are negligible for positive *t*. Either contour has to be big enough or far enough away from the pole to make $e^{-i\omega t}/(\omega - \Omega_n)$ have negligible magnitude on its return loop.
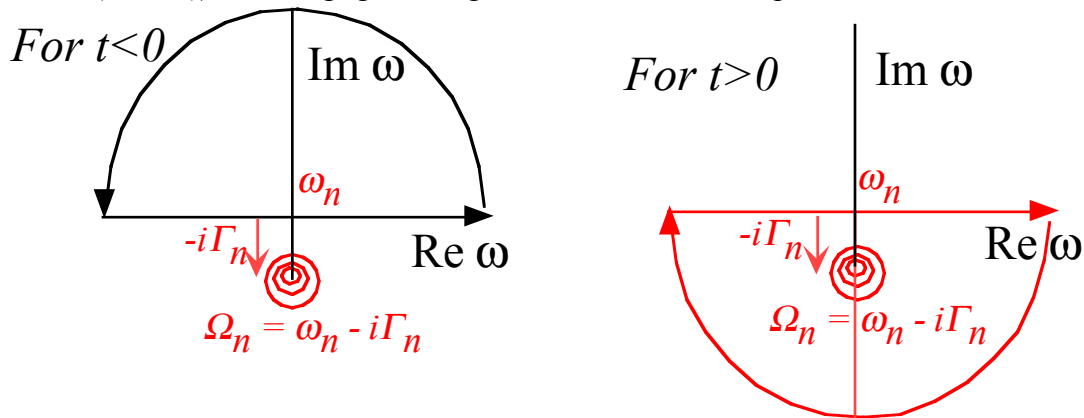
Fig. 14.1.8 Possible contours for resonance wave calculation.

The result of combining (14.1.11) and (14.1.12) is the following decaying ($e^{-\Gamma t}\, e^{-i\omega t}$)oscillation for *t* > 0.

$$\Psi(t) \cong \int d\omega\, \frac{e^{-i\omega t}}{\omega - \omega_n + i\Gamma_n} = \begin{cases} 0 & \text{for: } t<0 \\ -2\pi i\, e^{-i(\omega_n - i\Gamma_n)t} & \text{for: } t>0 \end{cases} \qquad (14.1.13)$$

The *resonance decay rate* Γ_n is just the distance the root of C_{11} or pole of S_{12} lies below the real-ω axis. The minus sign (on *-2πi*) is needed since the (*t*>0) contour goes clockwise or negatively.

It should be pointed out that roots of rational functions come in conjugate pairs. So the upper contour will also enclose a conjugate pole of the *S*-matrix component and the integral for past time will not be zero for the rational function as it is for our simple model approximation in (14.1.10).

How do we find the actual root displacement Γ_n or, for that matter, the real value ω_n of resonance frequency? Finding complex roots of functions like (14.1.7) is not trivial. An easy solution is to simply plot the

magnitude $|S_{12}(\omega)| = |1/C_{11}(\omega)|$ for real ω in the vicinity of each resonance and see how closely it fits the *model Lorentz resonance function* arising from the assumed form (14.1.10).

$$\left|\frac{1}{C_{11}(\omega)}\right|^2 = \left|\frac{c_n}{\omega - \omega_n + i\Gamma_n}\right|^2 = \frac{|c_n|^2}{(\omega - \omega_n)^2 + \Gamma_n^2} \qquad (14.1.10)$$

If the fit is close, then accurate values for *resonance frequency* ω_n, *resonance decay rate* Γ_n, as well as *resonance peak strength* $|c_n/\Gamma_n|^2$ may be obtained fairly quickly. There is a little trick to this that comes from noting that the Lorenztian has half its peak value when $\omega - \omega_n = \pm \Gamma_n$. In other words, the decay rate Γ_n is the *Lorenztian Half-Width at Half-Maximum (HWHM)*.

Fig. 14.1.9(a) below shows a pretty close fit of a Lorentzian to a numerical plot (b) of the *13.45* resonance which is just above the *6.12* resonance in Fig. 14.1.7. This is a "textbook" resonance except for a slight "background" which "lifts" the numerical resonance peak and is due to the potential having thin walls and being slightly "transparent" at all frequencies.
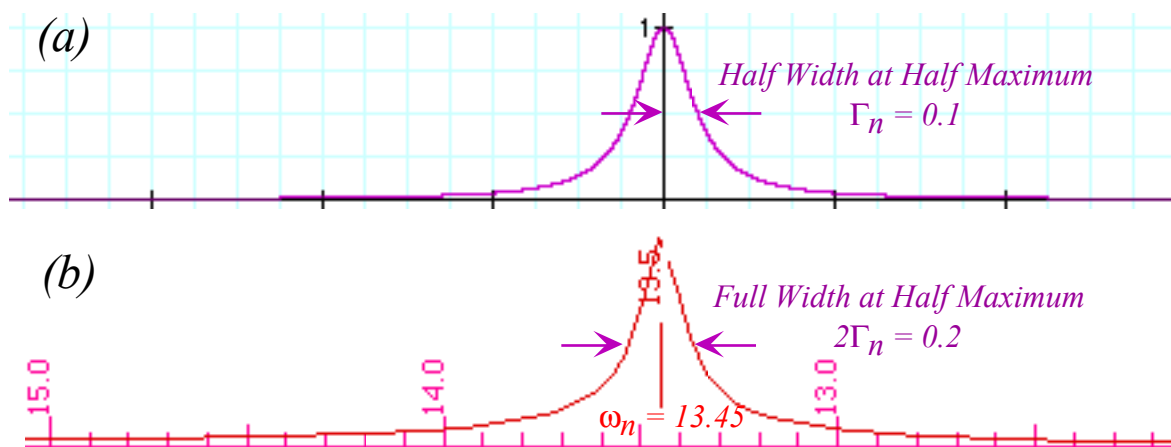
Fig. 14.1.9 Will the true Lorenztian please stand up!

We mentioned previously, that e^{-3} is nearly 5% so the *resonance 95% lifetime is $3/\Gamma_n$*. That's the time it would take for a "monster" like Fig. 14.1.6 to drain 95% of its amplitude if it was uniformly excited over its spectral band. Half that time, or *$3/2\Gamma_n$* is what would be needed to drain 95% of its intensity or probability. The *probability decay rate $2\Gamma_n$* is the *Lorenztian Full-Width at Half-Maximum (FWHM)*.

If the Lorentzian fit is not very close, then that says that this simple theory is wrong and some hidden mechanisms are present that need further study. The sub-grazing *22.8* resonance just below the *V=25* barrier top is an example. It appears to be "tipped" like a "hill-billy" living on mountain slope. The slope represents the growing transparency as energy approaches the barrier top. Shortly, we will see other examples of failure for simple Lorenztian fits such as happens with "clumps" of resonances. The first example in the following section deals with a pair of neighboring resonances.

(d) Hump-hump-hump

Let a third thin *(L=0.5)* wall be placed so that two wider *(W=1.5)* wells lie between three walls of height *(V=25)* as shown in Fig. 14.1.10 below.
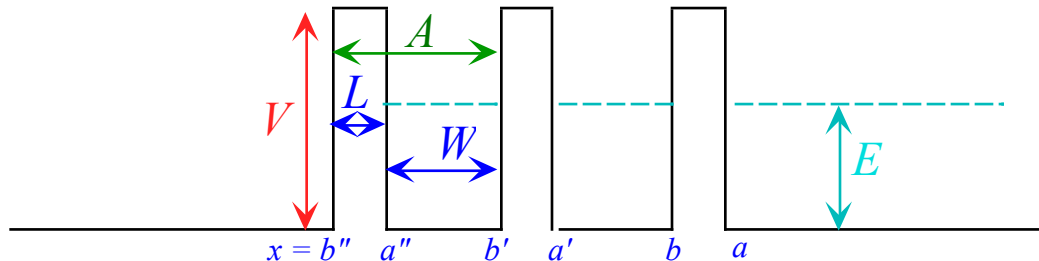
Fig. 14.1.10 Triple-barrier double-well potential

Each of the three barriers each has a *C*-matrix which enters a product to make the overall *C*-matrix.

$$C^{3-barrier} = C'' \cdot C' \cdot C$$

$$= \begin{pmatrix} e^{ikL}\chi^* & -ie^{-ik(a''+b'')}\xi \\ ie^{ik(a''+b'')}\xi & e^{-ikL}\chi \end{pmatrix} \cdot \begin{pmatrix} e^{ikL}\chi^* & -ie^{-ik(a'+b')}\xi \\ ie^{ik(a'+b')}\xi & e^{-ikL}\chi \end{pmatrix} \cdot \begin{pmatrix} e^{ikL}\chi^* & -ie^{-ik(a+b)}\xi \\ ie^{ik(a+b)}\xi & e^{-ikL}\chi \end{pmatrix} \quad (14.1.11a)$$

Except for the phases $k(a''+b'') = 2k\bar{x}''$, $k(a'+b') = 2k\bar{x}'$, and $k(a+b) = 2k\bar{x}$ at barrier centers, the parameters in the three matrices are identical. For energy below barrier top *(E<V)* the parameters are

$$\chi = \cosh \kappa L - i \sinh 2\beta \, \sinh \kappa L, \text{ and: } \xi = \cosh 2\beta \, \sinh \kappa L, \quad (14.1.11b)$$

using barrier coefficients from (14.1.7).

$$\cosh 2\beta = \frac{1}{2}\left(\frac{\kappa}{k} + \frac{k}{\kappa}\right) = \frac{\kappa^2 + k^2}{2k\kappa}, \quad \sinh 2\beta = \frac{1}{2}\left(\frac{\kappa}{k} - \frac{k}{\kappa}\right) = \frac{\kappa^2 - k^2}{2k\kappa} \quad (14.1.11c)$$

Well wavevector *k* and barrier evanescence κ are given using rationalized (theorist units) energy ε and potential υ.

$$k = \sqrt{\frac{2mE}{\hbar^2}} = \sqrt{2\varepsilon}, \quad \kappa = \sqrt{\frac{2m(V-E)}{\hbar^2}} = \sqrt{2(\upsilon - \varepsilon)}. \quad (14.1.11c)$$

The resonance transmission spectrum for the triple-barrier double-well is composed of pairs of peaks with each peak resembling a Lorentzian. The first three of these are plotted using scales of decreasing (with energy) magnification in Fig. 14.1.11. It is evident that a simple phenomenological modeling of each resonance cannot be done with a single Lorentzian but requires at least a *double Lorentzian*, something like that of a coupled damped two-dimensional pendulum system.

$$S_{12}(\omega) = \frac{1}{C_{11}(\omega)} = \frac{c(n^+)}{\omega - \omega(n^+) + i\Gamma(n^+)} + \frac{c(n^-)}{\omega - \omega(n^-) + i\Gamma(n^-)} \quad (14.1.12)$$

This model would require six parameters $c(n^\pm)$, $\omega(n^\pm)$, and $\Gamma(n^\pm)$ for each resonance *n=0, 1, 2,...*, and that's too many. (It would be more like quantum chemistry than physics!)
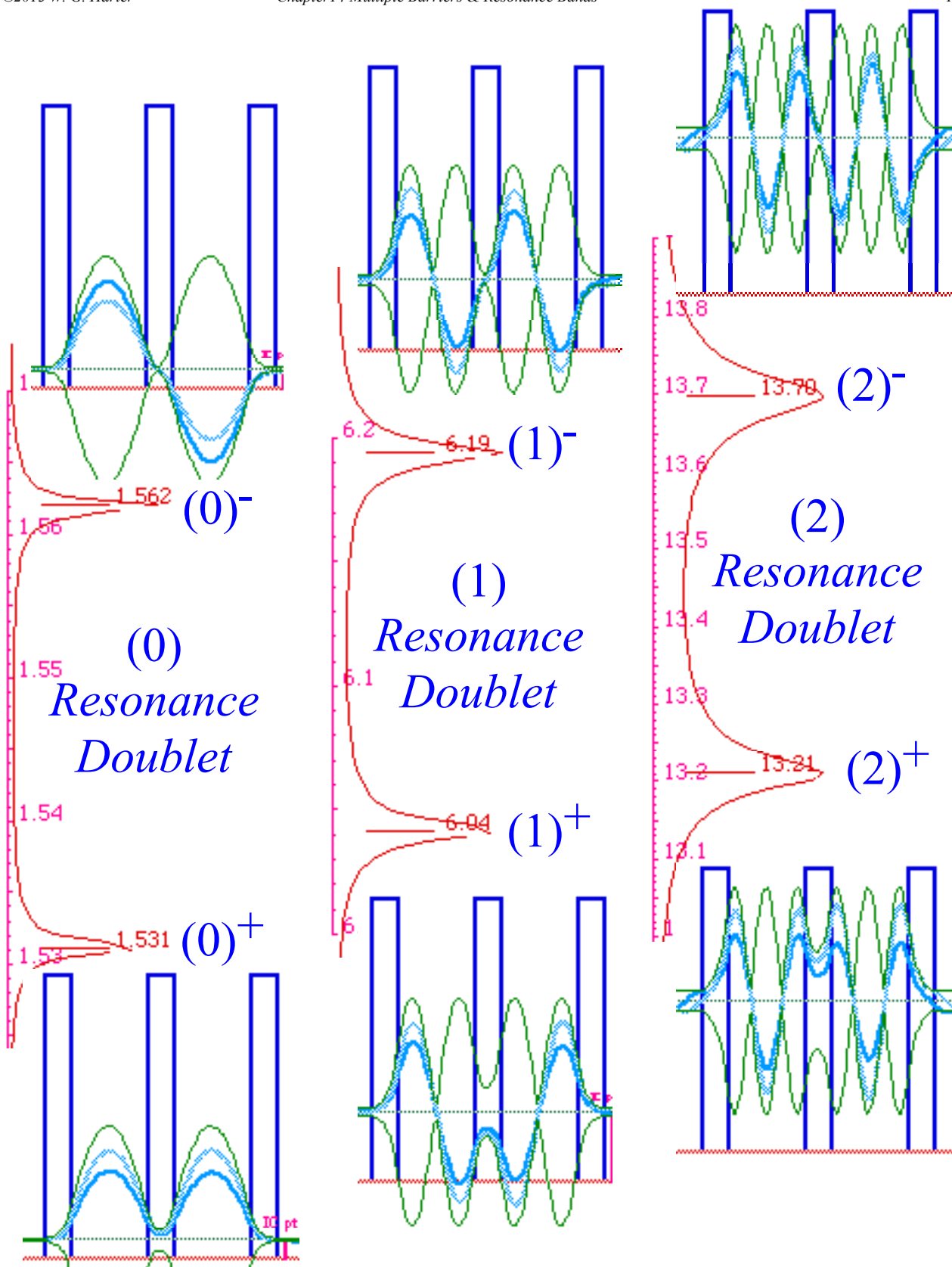
Fig. 14.1.11 Lowest three triple-barrier double-well resonance parity doublets

Instead, C_2 symmetry lets us whittle that number down to three: the even and odd doublet frequencies $\omega(n^+)$ and $\omega(n^-)$, which are eigenvalues of a bilateral symmetry (*B*-type) Hamiltonian (14.1.5).

$$\omega(n^+) = H(n) - S(n) , \qquad\qquad \omega(n^-) = H(n) + S(n) ,$$

and a single decay rate $\Gamma(n^+) = \Gamma(n) = \Gamma(n^-)$. The latter gives the *Half-Width-at-Half-Maximum (HWHM=$\Gamma(n)$)* of either doublet peak. Fig. 14.1.11 shows that peaks within each pair have nearly the same width but that this width grows quasi-exponentially for increasing quantum number *n* of higher energy doublets. The parameter $S(n)$ is the *half-splitting (HS = S(n))* of the *n-th* doublet. It also grows quasi-exponentially with *n*.

Finally, $H(n)$ is the *center of gravity (CG = H(n))* of the *n-th* doublet and evidently it is, once again, remarkably close to the bound-state eigenvalue of a well of the same width *(W=1.5)* and height *(V=25)* but with walls of infinite thickness *(L=∞* for the "high-security prison.") even though the walls used here are relatively flimsy *(L=0.5)*. The *CG* of resonance *(0)* in Fig. 14.1.11 is

$$H(0) = (1.562 + 1.531)/2 = 1.5465$$

This is close to the bound state eigenvalue $E(0) = 1.547$ derived earlier.

Note that maximum amplitudes of transmission peaks are all 100% *($|C_{11}(\omega(n^\pm))|=1$)* for resonances in C_2 symmetric potentials (Prove this!). So amplitude coefficients $c(n)$ are all equal to the decay rate $\Gamma(n)$ and the $c(n^\pm)$ parameters are not needed here.

Fig. 14.1.11 shows that doublet peak half-width $\Gamma(n)=HWHM$ grows more rapidly with increasing quantum number *n* than doublet half-splitting $S(n)=HS$, so that when *n=2* or *3* the two peaks are practically rubbing shoulders. In other words, the decay or "probability leakage" rate $2\Gamma(n)$ increases relative to the transition or "quantum beat" frequency $2S(n)$. Each successively higher doublet resonance, if excited uniformly, will behave more and more like a rusty old damped pendulum. Finally, it becomes "over damped" when $\Gamma(n)>S(n)$, and the beat oscillation dies before it can complete a single cycle.

The beat frequency $2S(n)$ is determined mainly by the central barrier which, as it becomes thicker, reduces coupling between the two wells. If, instead, the central barrier is made thinner and finally removed altogether, the doublet splitting $2S(n)$ increases until it is comparable to the spacing between the neighboring $CG=H(n)$ values. Finally, the double-well spectrum becomes that of a single well.

Plots of *(2$^\pm$)* doublet resonance wavefunctions in Fig. 14.1.12 show that the two waves differ appreciably only in the middle barrier. The lower energy *(2$^+$)* channel wave is, at the moment shown,

$$\Psi^{2+}(x,0) = C \cosh \kappa_+ x + i\, S \sinh \kappa_+ x. \quad (\,-L/2 < x < L/2) \qquad\qquad (14.1.13a)$$

Its hyperbolic cosine part is much larger than the imaginary hyperbolic sine part.*(C>>S)* At an equivalent moment of time, the (slightly) higher energy *(2$^-$)* channel wave inside the barrier is,

$$\Psi^{2-}(x,0) = S \sinh \kappa_- x - i\, C \cosh \kappa_- x, \quad (\,-L/2 < x < L/2) \qquad\qquad (14.1.13b)$$

with the hyperbolic sine much larger than the imaginary cosine. *(S>>C)* Ψ^{2-} has a slightly larger κ-value, too, ($\kappa_- > \kappa_+$), but that difference is relatively small. To understand (14.1.13) we view each *channel* wave as combinations of their respective *eigenchannel* waves which were introduced in Sect. 13.3(c).

(2^+) *Left-source channel*

(2^-) *Left-source channel*

$E = 13.2112$

$E = 13.6985$

~sinh κx

~cosh κx

~sinh κx

~cosh κx

2S(2) =
$(2^+)(2^-)$
*Doublet
Splitting*

(2^+) *Resonant eigenchannel*

(2^-) *Resonant eigenchannel*

$E = 13.2112$

$E = 13.6985$
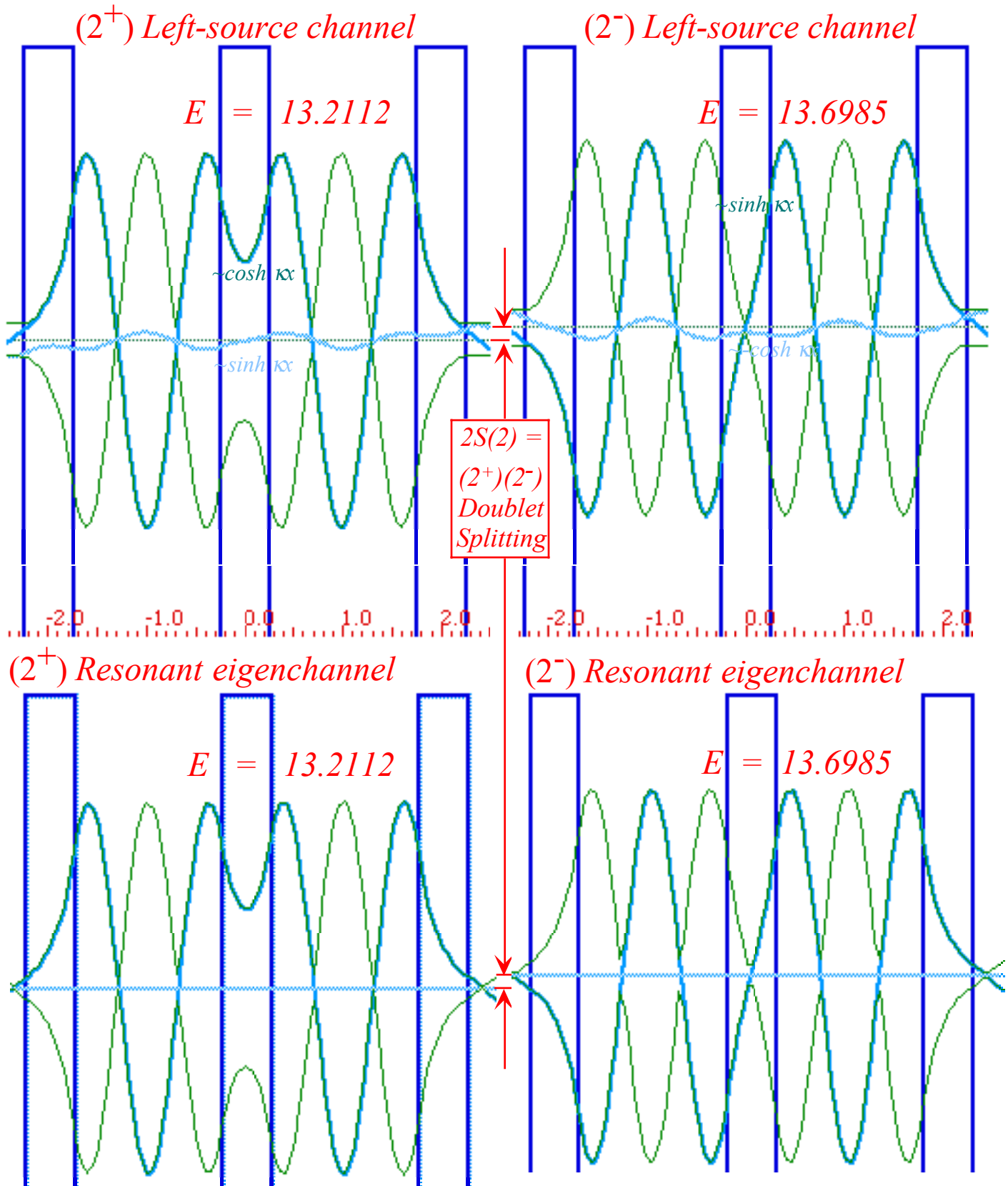
Fig. 14.1.12 (n=2) resonant parity doublet. Channel states have100% transmission. Eigenchannels, none.

      Recall that eigenchannels must be standing waves as shown by (13.3.15a-b). A left-source channel wave must be have pure moving wave (*coskx+isinkx*) in the output (right) channel and therefore be a complex *50-50*

combination of eigenchannels. However, the interior parts the channel states, *(2⁺)* or *(2⁻)*, are combinations, (14.1.13a) or (14.1.13b), respectively, of interior eigenchannel waves which appear to be anything but *50-50*, in fact one dominates the other as we see now.

      In the preceding resonance example there is a pure moving wave in the input (left) channel since transmission happens to be *100%*. To have moving waves (*coskx+isinkx*) on both sides requires equal amounts of both symmetric ("cosine-like") and antisymmetric ("sine-like") eigenchannel wave components in the exterior region. One of the eigenchannel components will be a *resonant eigenchannel* with large amplitude in the interior (well) region while the other component will be a *non-resonant eigenchannel* with a small interior amplitude, just like equations (14.1.13).

      The resonant *(2⁺)* and *(2⁻)* eigenchannels are plotted in the lower portion of Fig. 14.1.12, and clearly these account for most of the interior part of *(2⁺)* or *(2⁻)* channel waves. However, each channel wave has a *non-resonant component that has the *opposite* symmetry with a small interior contribution as plotted in Fig. 14.1.13. The non-resonant plot amplitudes are exaggerated over the resonant ones so the symmetry of small interior standing waves are clearly visible. The non-resonant *(2⁺)* wave is anti-symmetric and the non-resonant *(2⁻)* wave is symmetric; opposite to the resonant waves in Fig. 14.1.12.

      This explains why channel waves are slightly lopsided; the asymmetry of *(2⁺)* in Fig. 14.1.11 is not due to numerical error. Current flow requires a non-zero phase lag downstream and all the more so if the current is large compared to interior amplitudes. The required asymmetry is supplied by a nonresonant part, which, for *100%* transmission at a resonant energy, has an exterior amplitude equal but *90°* out of phase with the resonant part of the same energy, but it comes with a small interior wave, too.
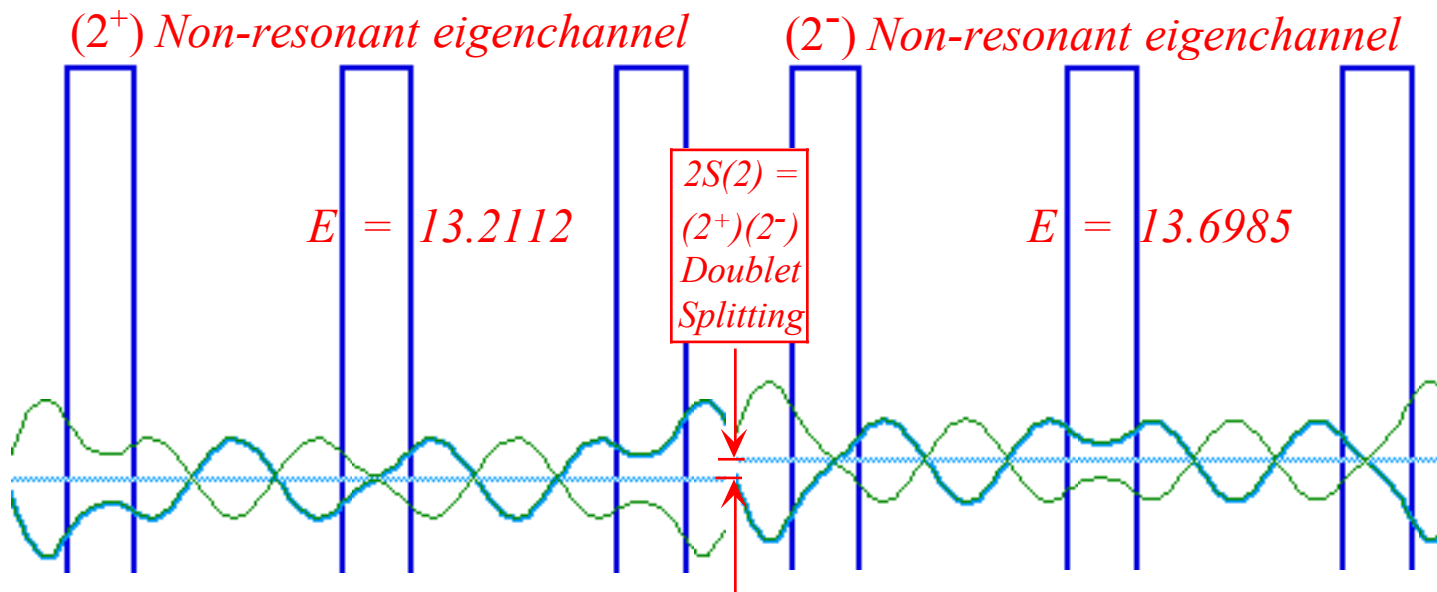
Fig. 14.1.13 (n=2) non-resonant eigenchannel parity doublet. Amplitude is exaggerated over Fig. 14.1.12.

      Recall that eigenchannels have a full *SU(2)* freedom. The preceding figures display only the eigenchannels referred to origin at the center of C_2 symmetry as, for example, in (13.3.39). However, any combination of the resonant and non-resonant eigenchannels is an eigenchannel, too, having the same energy but

a different reference origin. Experimentally, a range of eigenchannels is obtained by dragging the source or initial condition (*IC*) point along the *x*-axis for half a wavelength or by scanning the initial *R* or *L* phase component through π or varying the *a*-parameter, as in Fig. 13.3.3. Only the waves shown in Fig. 14.1.12 and 13 have a pure C_2 odd or even (±) parity. Others are "non-descript" symmetry like some examples of (2^+) waves shown below.
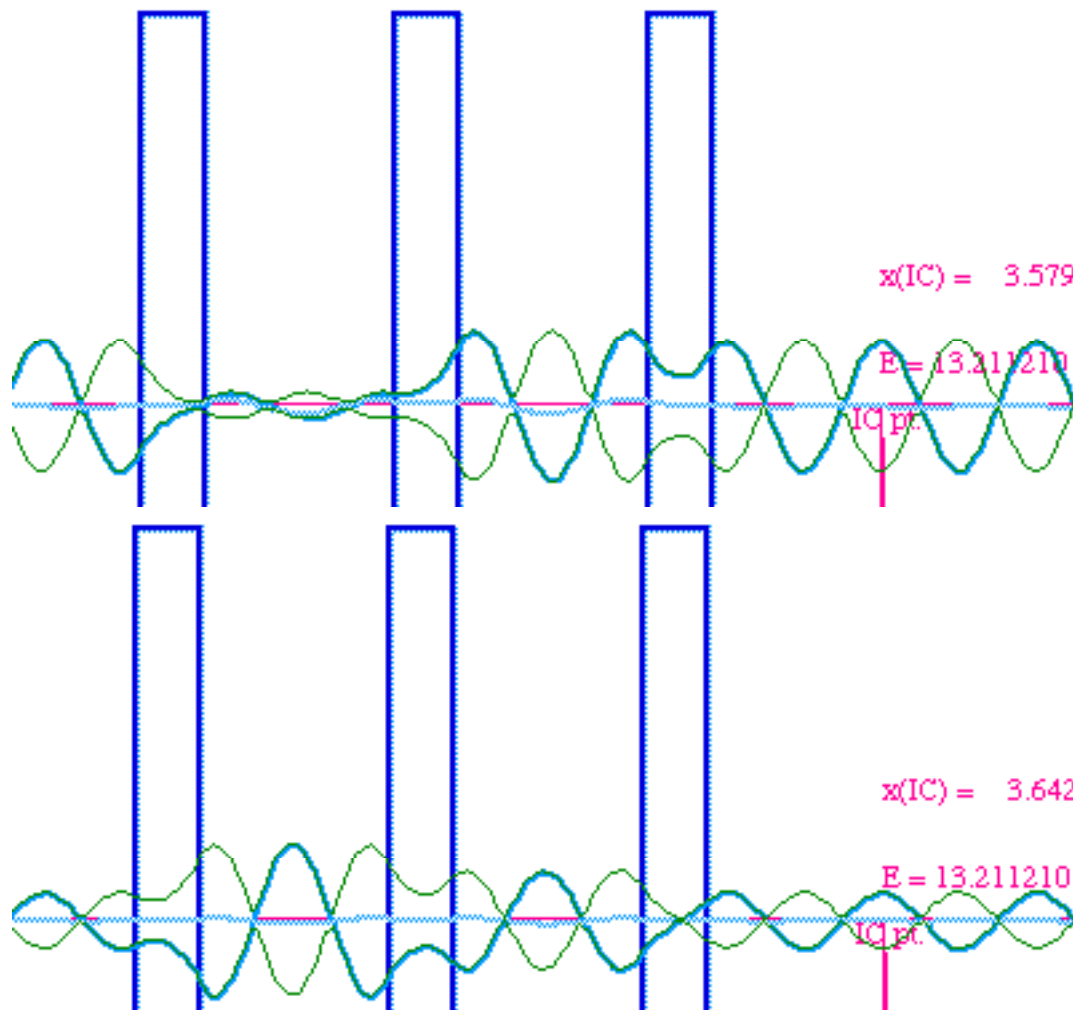
Fig. 14.1.14 Generic (2^+) eigenchannel wave combinations of indefinite parity.

The doublet coupling and splitting parameter *S(n)* is determined by the middle barrier, but the decay rate Γ*(n)* is determined mostly by the outer walls. Making them thicker on the outside (increasing *L* without changing the middle barrier L_M or the well width *W*) makes the resonance peaks thinner and the resonances stronger without appreciably altering either the *CG* or *HS* values. Infinitely thick exterior walls give singlet-level bound states shown in Fig. 14.1.2 and 3. Each one is a resonant eigenchannel wave, the winning partner of a doublet level. The losing and forgotten partner is the non-resonant eigenchannel wave which is squeezed out to the infinite *L*. Old states don't die, they just fade away!

(1) Breaking C_2 symmetry

It is important to see how the resonances described so far are sensitive to the presence or lack thereof of the bilateral *B*-type of C_2 symmetry. As was pointed out in Sec. 10.3, the reduction of *B*-type to *AB*-type and finally to asymmetric-diagonal *A*-type symmetry begins when the diagonal **H**-matrix components $H_{11}=A$ and

$H_{22}=D$ differ by more that the off-diagonal $H_{12}=HS=S$ components. For the lower resonances of the triple-barrier double-well the $S(n)=HS$ parameter is tiny so it doesn't take much diagonal asymmetry to wholly upset this system and thereby spoil its strong resonances and perfect transmission properties.

This is what is seen in Fig. 14.1.15. A tiny perturbation or "bump" at the bottom of the left hand well is enough to almost completely destroy the giant *(n=0)* resonances shown on the left side of Fig. 14.1.11 and reduces its 100% transmission to less than 1%. However, the higher *(n=2)* resonance fares better since its 2*S(2)* =*0.49* parameter is much larger than 2*S(0)=0.031*, and so it is perturbed into only slightly asymmetric combinations. The transmission is still not exactly *100%* but still close to it.

There are many ways to make or break the C_2 symmetry. Adjusting the depth or width of one of the wells or the thickness or height of one of the outer barriers will have the same effects. So will adding a uniform electric field which puts a slope on the entire potential system as shown in Fig. 14.1.16. The latter is an example of the electric Stark splitting. Generally this quickly spoils 100% transmission, too.
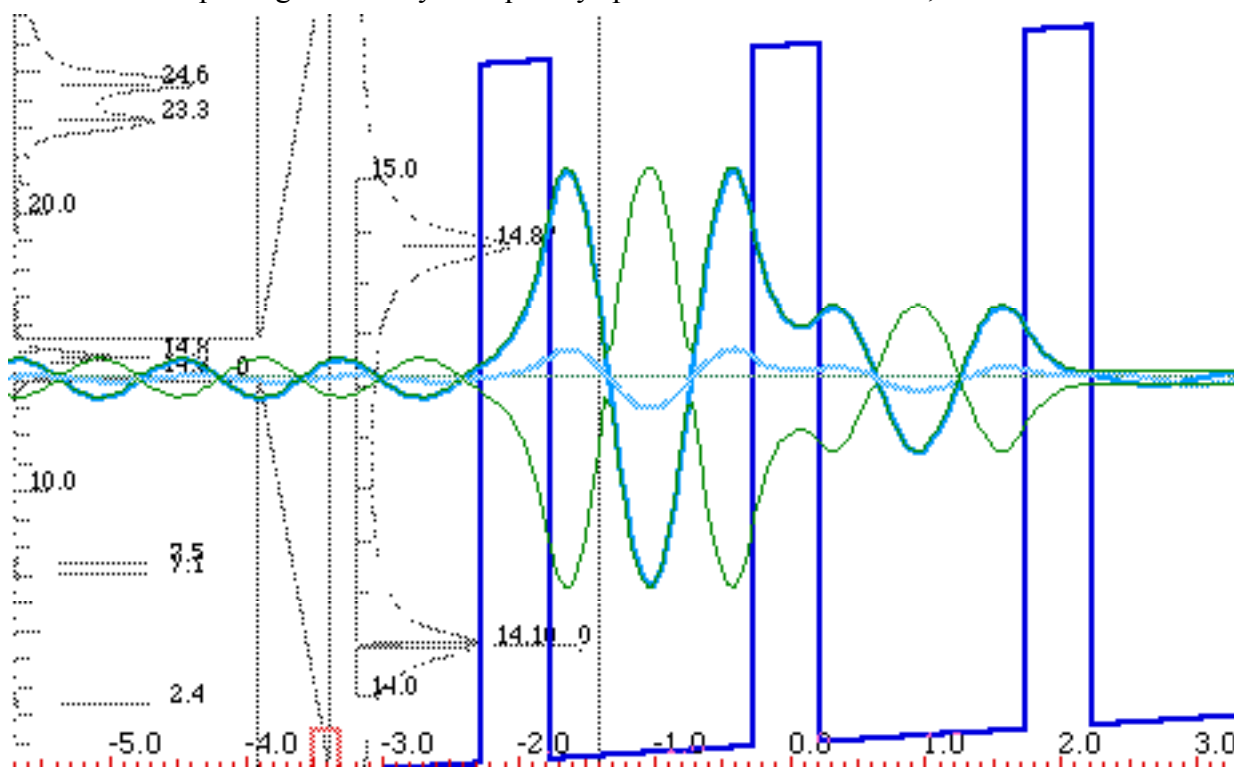
Fig. 14.1.16 Lower state of Stark split (2$^+$) resonance doublet.
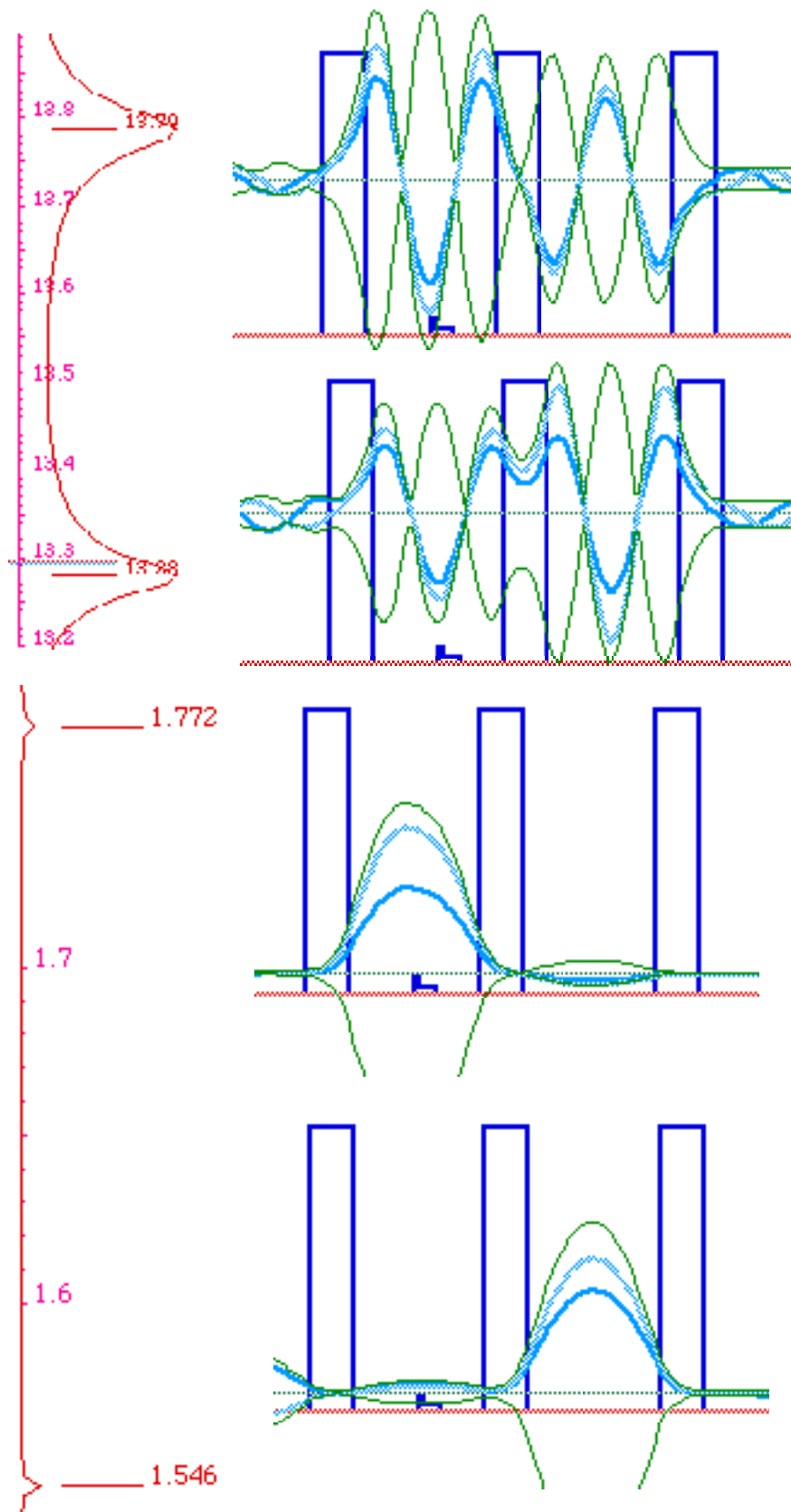
Fig. 14.1.15 Small symmetry breaking ruins (n=0) resonance doublet and slightly perturbs (n=2).

(2) Accidental degeneracy

If one well is detuned sufficiently it may come back into resonance, but with the next higher level of the neighboring well. In the Fig. 14.1.17 the *(n=0)* state of the left well has been pushed up so it is in resonance with the *(n=1)* wave of the right hand well. This is called an *accidental degeneracy* even if it is no accident. (It takes some effort to pull this off!) The difficulty with this kind of "accident" is that none of the other levels are likely to also have degenerate mates since no over-riding symmetry is present.
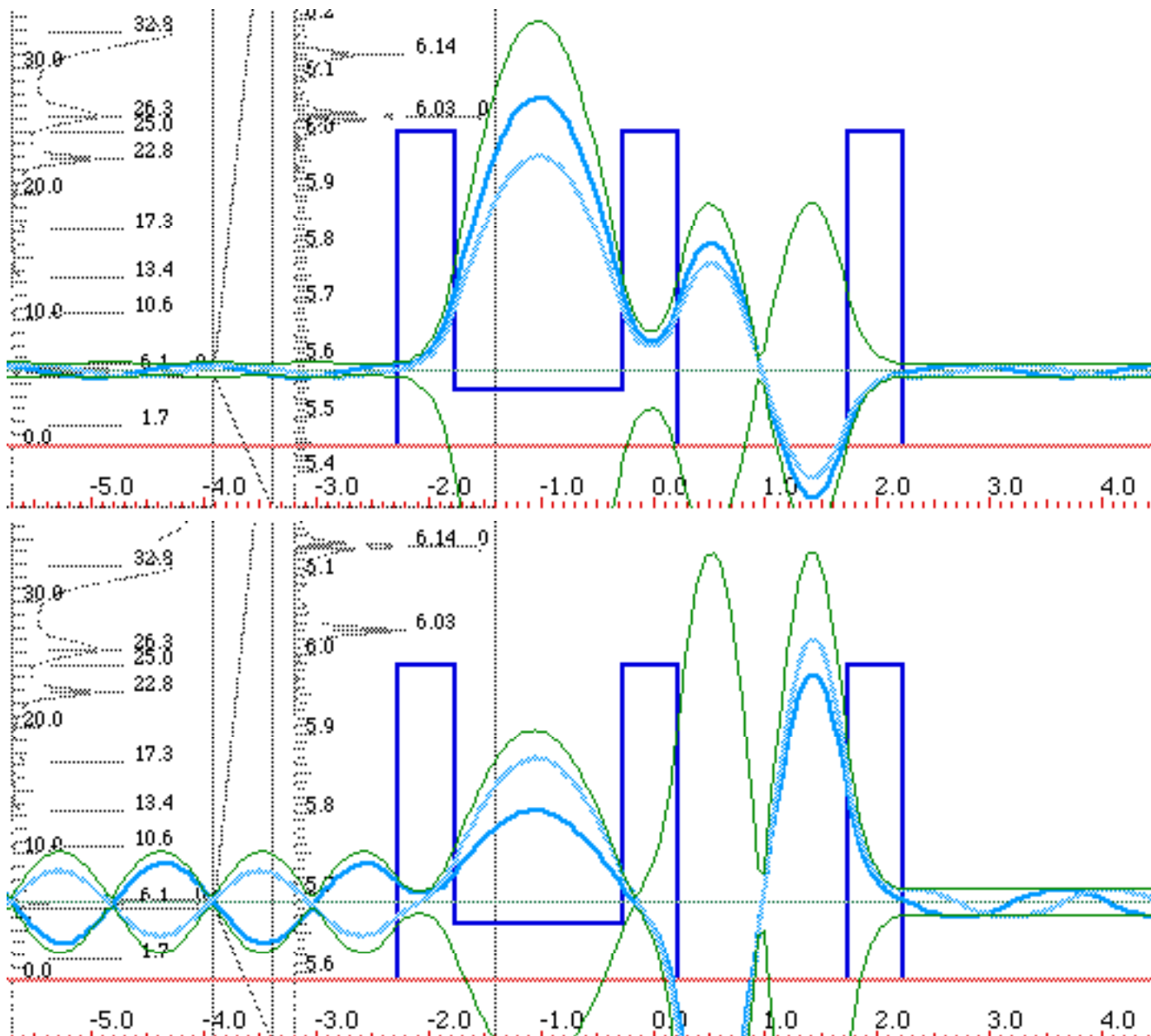
Fig. 14.1.17 Extreme symmetry breaking brings (n=0) resonance up to (n=1).

(e) Multiple humps or wells

By increasing the number N of identical potential wells strung together between $N+1$ barriers, as in Fig. 14.1.18, we find transmission spectra that begin to resemble band spectra of crystalline solids.
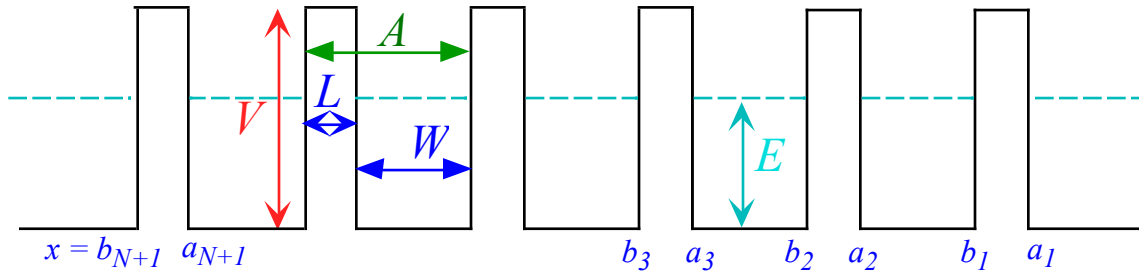
Fig. 14.1.18 (N+1)-barrier (N)-well potential

Each of the $N+1$ barriers has a C-matrix which enters a product to make the overall C-matrix.

$$C^{N+1\,barrier} = C^{[N+1]}\cdots C'\cdot C =$$

$$\begin{pmatrix} e^{ikL}\chi^* & -ie^{-ik(a_{N+1}+b_{N+1})}\xi \\ ie^{ik(a_{N+1}+b_{N+1})}\xi & e^{-ikL}\chi \end{pmatrix}\cdots\begin{pmatrix} e^{ikL}\chi^* & -ie^{-ik(a_2+b_2)}\xi \\ ie^{ik(a_2+b_2)}\xi & e^{-ikL}\chi \end{pmatrix}\cdot\begin{pmatrix} e^{ikL}\chi^* & -ie^{-ik(a_1+b_1)}\xi \\ ie^{ik(a_1+b_1)}\xi & e^{-ikL}\chi \end{pmatrix} \quad (14.1.17a)$$

As in (14.1.11) the parameters for $(E<V)$ are $k = \sqrt{(2E)}$, $\kappa = \sqrt{(2V-2E)}$, and $sinh\ 2\beta = (\kappa^2-k^2)/(2k\kappa)$,

$$\chi = cosh\ \kappa L - i\ sinh\ 2\beta\ sinh\ \kappa L, \quad \text{and:}\quad \xi = cosh\ 2\beta\ sinh\ \kappa L, \quad\quad (14.1.17a)$$

and for $(E>V)$ they are $\ell = \sqrt{(2E-2V)}$, and $cosh\ 2\alpha = (\ell^2+k^2)/(2k\ell)$ from (13.3.33).

$$\chi = cos\ \ell L + i\ cosh\ 2\alpha\ sin\ \ell L, \quad \text{and:}\quad \xi = sinh\ 2\alpha\ sin\ \ell L. \quad\quad (14.1.17b)$$

(1) N=3: Coupled pendulum model

With three barriers the transmission peaks derived from (14.1.17 a and b) for $(E<V)$ come in triplets. The lowest triplet and associated channel wavefunctions are shown in Fig. 14.1.19. The triplet eigensolutions can be approximated by treating each the three wells as one of three base states $\{|1\rangle,|2\rangle,|3\rangle\}$ in a three-by-three tunneling Hamiltonian eigenvalue equation. It is analogous to three pendulums in a line.

$$\mathbf{H}|\varepsilon_k\rangle = \begin{pmatrix} H & -S & 0 \\ -S & H & -S \\ 0 & -S & H \end{pmatrix}\begin{pmatrix} \langle 1|\Psi\rangle \\ \langle 2|\Psi\rangle \\ \langle 3|\Psi\rangle \end{pmatrix} = \varepsilon_k\begin{pmatrix} \langle 1|\Psi\rangle \\ \langle 2|\Psi\rangle \\ \langle 3|\Psi\rangle \end{pmatrix} = \varepsilon_k|\Psi\rangle \quad\quad (14.1.18)$$

We solve this by a trick where (14.1.18) is embedded (twice) in a C_8 matrix equation. (Recall Fig. 12.2.6.)

$$\mathbf{K}|\Psi\rangle = \begin{pmatrix} H & -S & & & & & & -S \\ -S & H & -S & 0 & & & & \\ & -S & H & -S & & & & \\ & 0 & -S & H & -S & & & \\ & & & -S & H & -S & & \\ & & & & -S & H & -S & 0 \\ & & & & & -S & H & -S \\ -S & & & & & 0 & -S & H \end{pmatrix}\begin{pmatrix} \langle 0|\Psi\rangle \\ \langle 1|\Psi\rangle \\ \langle 2|\Psi\rangle \\ \langle 3|\Psi\rangle \\ \langle 4|\Psi\rangle \\ \langle 5|\Psi\rangle \\ \langle 6|\Psi\rangle \\ \langle 7|\Psi\rangle \end{pmatrix} = \varepsilon\begin{pmatrix} \langle 0|\Psi\rangle \\ \langle 1|\Psi\rangle \\ \langle 2|\Psi\rangle \\ \langle 3|\Psi\rangle \\ \langle 4|\Psi\rangle \\ \langle 5|\Psi\rangle \\ \langle 6|\Psi\rangle \\ \langle 7|\Psi\rangle \end{pmatrix} = \varepsilon|\Psi\rangle \quad\quad (14.1.19)$$

(0)
Resonance
Triplet
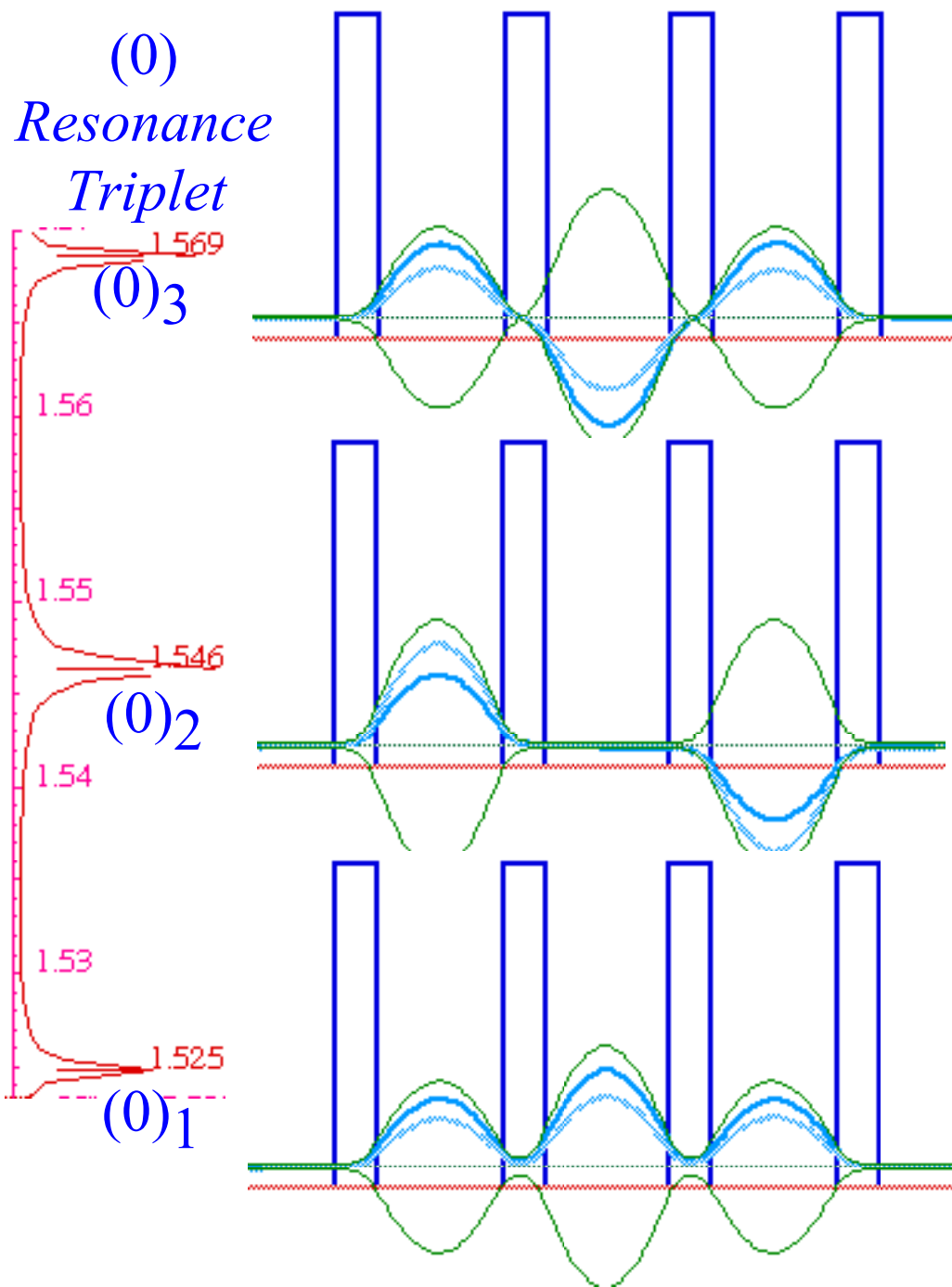
Fig. 14.1.19 Lowest triple-well resonance triplet.

The trick works because the C_8 superset problem has three solutions which make the components $\langle 0|\Psi\rangle$ and $\langle 4|\Psi\rangle$ equal to zero. Then (14.1.18) is solved by the 3-by-3 part of (14.1.19) using the general C_N solutions for $N=8$ from (9.3.5a-e) and discarding five symmetric (cosine-like) eigensolutions. Three sine-like eigensolutions from (9.3.5g) for *(m=1, 2, 3)* remain for which $\langle 0|\Psi\rangle=0=\langle 4|\Psi\rangle$.

$$\varepsilon_m = H - 2\,S\cos k_m\, a = H - 2\,S\cos(2\pi\, m/8) \qquad\qquad (14.1.20a)$$

The k_m–eigenvectors, listed in (9.3.5b) as ±moving waves, need to be combined into sine waves.

$$\langle +k_m | = \left(\begin{array}{c|ccc|ccc} 1 & e^{ik_m a} & e^{2ik_m a} & e^{3ik_m a} & e^{4ik_m a} & e^{-3ik_m a} & e^{-2ik_m a} & e^{-ik_m a} \end{array} \right)/\sqrt{8} \qquad (14.1.20b)$$

$$\langle -k_m | = \left(\begin{array}{c|ccc|ccc} 1 & e^{-ik_m a} & e^{-2ik_m a} & e^{-3ik_m a} & e^{4ik_m a} & e^{3ik_m a} & e^{2ik_m a} & e^{ik_m a} \end{array} \right)/\sqrt{8} \qquad (14.1.20c)$$

$$k_m a = 2\pi m / 8 = 0, \ \pi/4, \ \pi/2, \ 3\pi/4, \ and \ \pi \qquad (14.1.20d)$$

The desired standing sine wave eigenvectors are the difference between the two moving wave states.

$$\langle s_m | = \left(\langle +k_m | - \langle -k_m | \right)/ i\sqrt{2}$$

$$= \left(\begin{array}{c|ccc|ccc} 0 & \sin k_m a & \sin 2k_m a & \sin 3k_m a & 0 & -\sin 3k_m a & -\sin 2k_m a & -\sin k_m a \end{array} \right)/2$$

The 3-well resonances use only the components $m=1, 2,$ and 3 of the (renormalized) sine eigenvectors

$$\langle \varepsilon_m | = \left(\begin{array}{ccc} \sin k_m a & \sin 2k_m a & \sin 3k_m a \end{array} \right)/\sqrt{2} = \left(\begin{array}{ccc} \sin \dfrac{\pi m}{4} & \sin \dfrac{2\pi m}{4} & \sin \dfrac{3\pi m}{4} \end{array} \right)/\sqrt{2}, \quad (14.1.21a)$$

for $m = 1, 2,$ and 3, which give the three eigensolutions using (14.1.20a).(See also Fig. 14.1.20 below.)

$$\varepsilon_m = H - 2 S \cos (\pi \, m/4) . \qquad (14.1.21b)$$

$$\langle \varepsilon_1 | = \left(\begin{array}{ccc} 1 & \sqrt{2} & 1 \end{array} \right)/2 \qquad \varepsilon_1 = H - \sqrt{2}S$$

$$\langle \varepsilon_2 | = \left(\begin{array}{ccc} 1 & 0 & -1 \end{array} \right)/\sqrt{2} \qquad \varepsilon_2 = H \qquad (14.1.21c)$$

$$\langle \varepsilon_3 | = \left(\begin{array}{ccc} 1 & -\sqrt{2} & 1 \end{array} \right)/2 \qquad \varepsilon_3 = H + \sqrt{2}S$$

Using the value of the tunneling or splitting parameter $S(0) = 0.031/2 = 0.0155$ from the splitting of the double well in Fig. 14.1.11 we can estimate the splitting of the triple-well to be $S(0)\sqrt{2} = 0.0219$ for the $(0)_m$ triplet. This is close to the 0.022 splitting found in the exact calculation plotted in Fig. 14.1.19. A minor swindle of a missing factor-of-two is due to our cutting open a C_N-loop as discussed later.

The trick here is to embed a linear N-fold symmetric system (Here $N=3$.) into a circular $2N+2$-fold or C_{2N+2} system (Here, an octagonal C_8 ring.) and then discard all but the N solutions that are sine-like. This approximation depends on the linear N-fold system having exterior amplitudes which are small enough that they can be modeled by zeros of the $2N+2$-fold sine-wave nodes.($\langle 0 | \Psi \rangle = 0 = \langle N+1 | \Psi \rangle$)

$$\varepsilon_3 = H + \sqrt{2} \, S$$
$$\varepsilon_2 = H$$
$$\varepsilon_1 = H - \sqrt{2} \, S$$
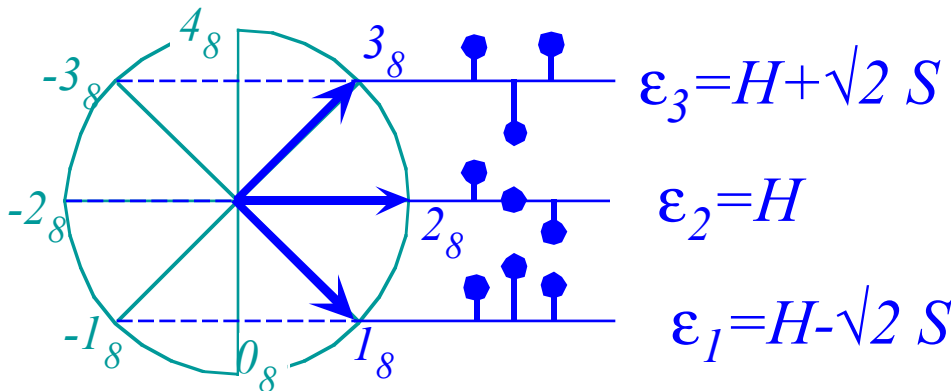
Fig. 14.1.20 Approximate "coupled pendula" C_8 tunneling model for triple-well resonance triplets.

So, it shouldn't be surprising that the approximation is best in strong resonance where huge interior resonance waves dwarf the exterior (input-output) wavefunctions, but it deteriorates for higher resonances which "escape" easily. High-security prisons make this model look better!

Compare the *(1)* doublet parameter $S(1) = 0.15/2 = 0.075$ in Fig. 14.1.11 to the *(1)* triplet splitting of $6.23-6.12=0.11$ in Fig. 14.1.21. This is close to the approximate prediction of $\sqrt{2}\,(0.75) = 0.106$ but, perhaps, not quite as close as the comparison between the lower energy *(0)* resonances made previously.

However, For the *(1)*-triplet the most symmetric $(1, \sqrt{2}, 1)/2 = |(1)_1\rangle$ state comes out on top instead of being the lowest as in the *(0)*-triplet while the $(1, -\sqrt{2}, 1)/2 = |(1)_3\rangle$ is lowest. This is as it should be since waves with more nodes are always higher energy, so tunneling parameter $S(1)$ the opposite sign of $S(0)$.
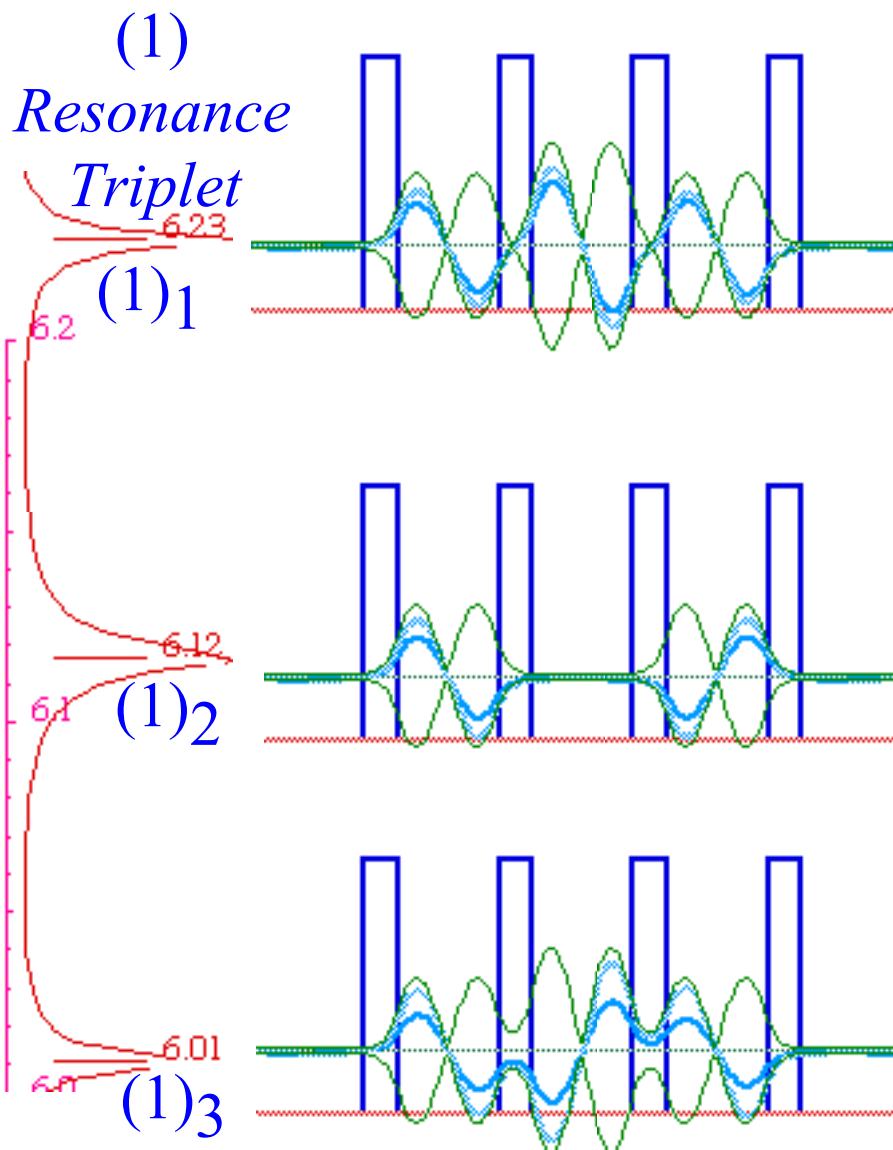
Fig. 14.1.21 Next lowest triple-well resonance triplet.

Another problem with the simple model (14.1.21) is it does not predict *splitting asymmetry*, that is, that ε_1-ε_2 isn't quite equal to ε_2-ε_3 . We could say that the evanescence or tunneling parameter $S(n)$ varies with energy within each triplet (while changing sign between them), but this sort of "hand-waving" defeats the elegance of the model. Sec. 14.2 has some ways to improve multplet or band modeling and explain quantitatively how the tunneling and phase vary.

(2) Forbidden gaps

With $N= 4, 5,...$ wells or more, the resonances begin to resemble bands of N peaks spaced out more or less according to the C_{2N+2} eigenvalues from (14.1.20a) with allowed $m = 1, 2, ...N$, only.

$$\varepsilon_m = H - 2 S \cos k_m a = H - 2 S \cos (2\pi m/(2N+2)) \qquad (14.1.20a)_{repeated}$$

In between each of these bands of peaks lies a "no-man's-land" of energy values that give a disappointing transmission probability which falls off exponentially with the length NA of the potential region. The technical name for a "no-man's-land" is *a forbidden energy gap*.

An example of some pitiful waves trying to penetrate through the first forbidden gap in an $N=4$ system is shown in Fig. 14.1.22. The top wave (Fig. 14.1.22(a)) is only detuned by $\Delta E=0.1$ from the powerful *(0)* resonance band around $E=1.547$. (Recall Fig. 14.1.11 and 19.) Transmission is essentially zero, but it's enormous compared to that of the plot below in which the detuning is doubled to $\Delta E=0.2$. Further detuning attenuates the wave so badly that even the first well has no visible life. Dead on arrival!
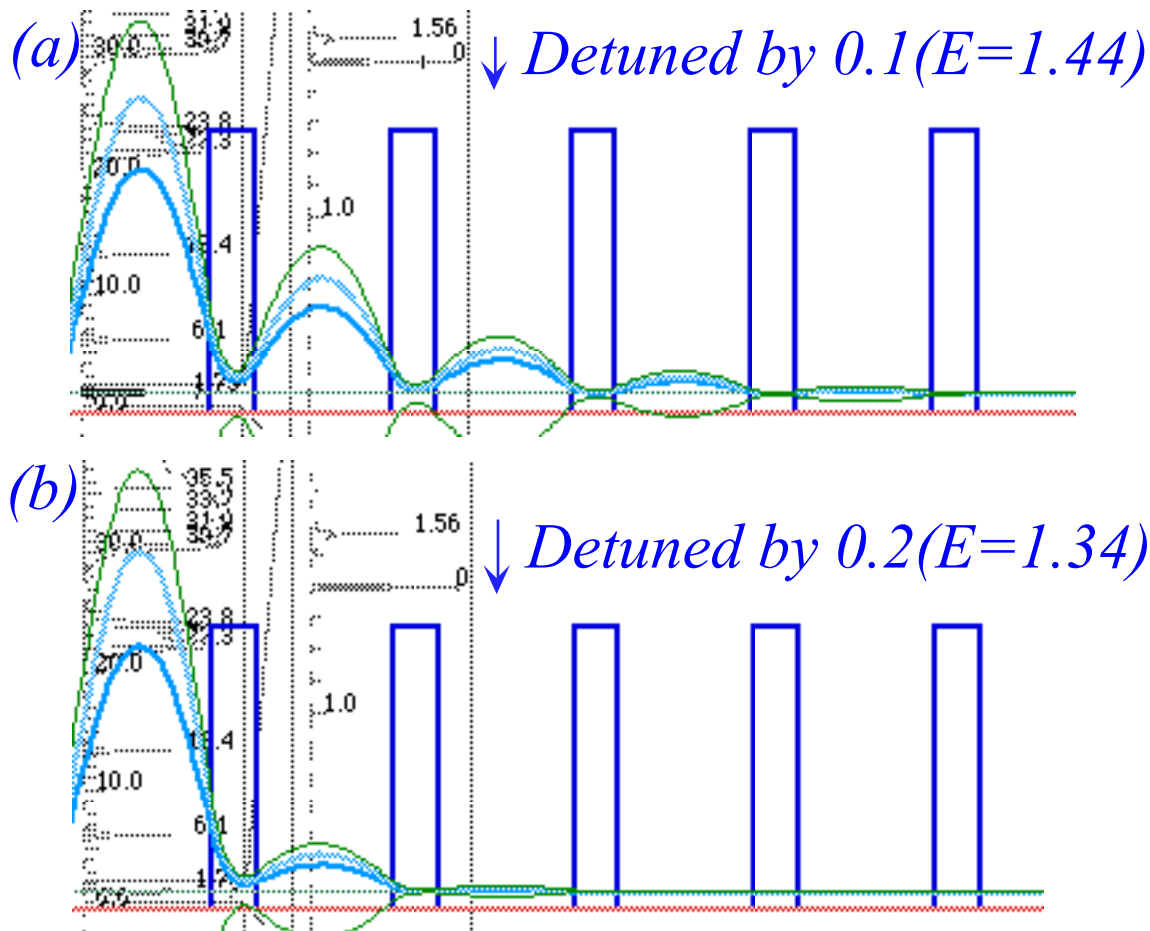
Fig. 14.1.22 Examples of waves dying from detuning into a "forbidden gap" below a resonance band.

(f) Comparing bound *versus* resonant energies

Before beginning energy band theory, let us do a precise comparison of bound-state well energy values with those of resonance peaks. Consider first the well bound-state eigenvalues in Fig. 14.1.23. The energies are listed both from top and bottom while their units are related to standard *mks* units, or, the more appropriate nano-technology *Å(eV)s* units
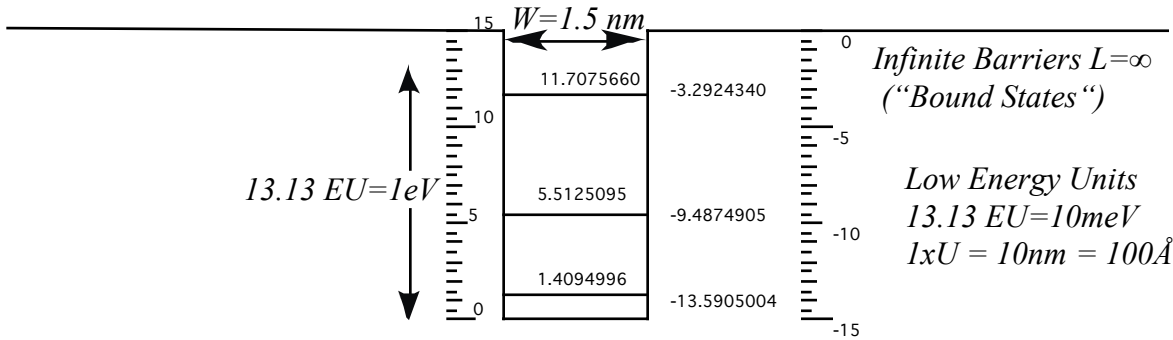
Fig. 14.1.23 Width W=1.5 Square well with Potential Depth V=15.0EU.

It is interesting to compare the bound energies to resonance values for wells of the same potential depth *V=15EU* and width *W=1.5 nm*, but varying outer wall thickness . Three examples, varying from thin wall *(L=0.5)* to thick wall *(L=2.0)*, are shown in Fig. 14.1.24.
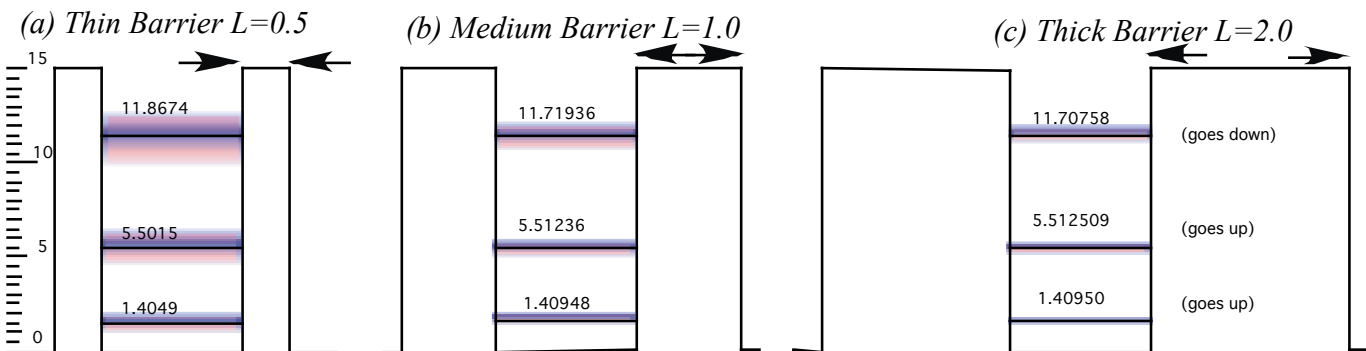
Fig. 14.1.24 Width W=1.5 Resonance wells with Potential Depth V=15.0EU and varying wall thickness.

The resonance values in Fig. 14.1.24 are quite close approximations to the "exact" bound-state energies in Fig. 14.1.23 in each case, and they become closer as the outer walls become thicker. The lower resonance values rise slightly as the wall becomes less penetrable, but surprisingly, perhaps, the highest one drops. The variation of energy is complicated by the mixing of resonant and non-resonant eigenchannels. For thick wall and low energy, the bound state wave will approach that of the resonant eigenchannel wave while the non-resonant eigenchannel wave becomes more and more excluded. However, for thin walls, the overlap between the two increases as shown in the discussion of Fig. 14.1.12 and Fig. 14.1.13. Then, their mixing becomes an important part of the energy equation.

Next we compare the case of double-wells. The bound state double-well eigenvalues for this example are dispalayed in Fig. 14.2.25. Note that the doublet centers are quite close to the corresponding singlet values in Fig. 14.1.23. The separating barrier length is *L=0.5 nm*.
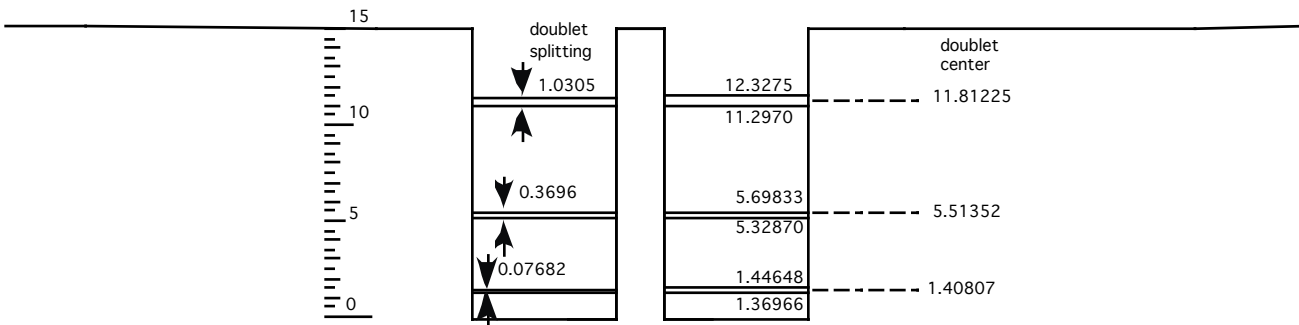
Fig. 14.1.25 Double-well bound state doublets.

In Fig. 14.1.26 below, the doublet bound-state energies above may be compared to resonance values arising from identical double wells surrounded by more or less penetrable walls of thickness length *L=0.5 nm* for Fig. 14.1.26a and *L=1.0 nm* for Fig. 14.1.2b.
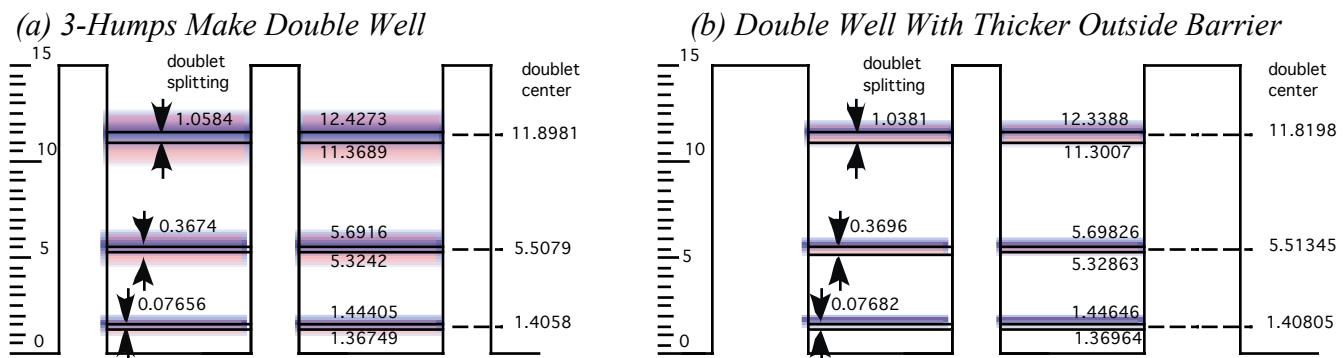
Fig. 14.1.26 Double-well resonance doublets. (a) Thin outer walls (L=0.5 nm), (b) Thick outer walls (L=1.0 nm),

Again, there is a slight downshift of the lower resonances while the highest pair rise slightly. Also, the doublet splitting rises more for the highest doublet particularly in the case of thinner walls. Interaction between resonant and non-resonant eigenchannels is enhanced by having closely spaced doublet energy values.

14.2 Allowed bands: Kronig-Penney Conditions

Forbidden waves like the ones shown in Fig. 14.1.22 get killed because each application of a barrier C-matrix gives right and left wave amplitudes (R', L') with magnitudes that are products by some factor F with the amplitudes (R, L) going into that C-matrix. The result is an unstable geometric or exponential ($\sim e^{Fx}$) growth or decay and that kills transmission or propagation. If a wave in a forbidden energy gap fails to pass a few barriers, what chance has it in a real crystal with trillions of such barriers? When a crystal says a wave energy is "forbidden" it means it! Fuggedaboutit! Get out'a here!

To see what allows wave propagation we focus on one C-matrix factor from the chain (14.1.17).

$$\begin{pmatrix} R' \\ L' \end{pmatrix} = \begin{pmatrix} e^{ikL}\chi^* & -ie^{-ik(a_1+b_1)}\xi \\ ie^{ik(a_1+b_1)}\xi & e^{-ikL}\chi \end{pmatrix} \cdot \begin{pmatrix} R \\ L \end{pmatrix} \tag{14.2.1}$$

The output wave $\psi'(x)$ and input wave $\psi(x)$ are the following by definition. (Recall Fig. 14.1.5.)

$$\psi'(x) = R'\,e^{ikx} + L'\,e^{-ikx}\,, \qquad \psi(x) = R\,e^{ikx} + L\,e^{-ikx}. \tag{14.2.2}$$

Now let's force propagation by demanding that the output wave and its derivative be the same at point $x=A = L + W$ after each barrier-well as it was at the starting point $x=0$. This is a little <u>too</u> strict, but surely if each unit of a lattice puts out the same initial conditions for its wave, then the wave can exist everywhere in the whole system with the same amplitude. That would be perfectly periodic propagation.

So our "strictly periodic" demands take the following forms.

$$\psi'(0) = \psi(A) \qquad \text{implies} \quad R' + L' = R\,e^{ikA} + L\,e^{-ikA}\,,$$

$$\frac{d}{dx}\psi'(0) = \frac{d}{dx}\psi(A) \quad \text{implies} \quad R' - L' = R\,e^{ikA} - L\,e^{-ikA}\,. \tag{14.2.3a}$$

Solving gives $R'=Re^{ikA}$ and $L'= L\,e^{-ikA}$. Putting this into C-relation (14.2.1) gives

$$\begin{pmatrix} R' \\ L' \end{pmatrix} = \begin{pmatrix} e^{ikL}\chi^* & -ie^{-ik(a_1+b_1)}\xi \\ ie^{ik(a_1+b_1)}\xi & e^{-ikL}\chi \end{pmatrix} \cdot \begin{pmatrix} R \\ L \end{pmatrix} = \begin{pmatrix} R\,e^{ikA} \\ L\,e^{-ikA} \end{pmatrix} = \begin{pmatrix} e^{ikA} & 0 \\ 0 & e^{-ikA} \end{pmatrix}\begin{pmatrix} R \\ L \end{pmatrix} \tag{14.2.3b}$$

So the following matrix M has only zero eigenvalues.

$$M \cdot \begin{pmatrix} R \\ L \end{pmatrix} = \begin{pmatrix} e^{ikL}\chi^* - e^{i2kA} & -ie^{-ik(a_1+b_1)}\xi \\ ie^{ik(a_1+b_1)}\xi & e^{-ikL}\chi - e^{-i2kA} \end{pmatrix} \cdot \begin{pmatrix} R \\ L \end{pmatrix} = \begin{pmatrix} 0 \\ 0 \end{pmatrix} \tag{14.2.4a}$$

Setting its determinant to zero and using unimodularity ($|\chi|^2-\xi^2=1$) yields the following conditions.

$$\det M = \left(e^{ikL}\chi^* - e^{ikA}\right)\left(e^{-ikL}\chi - e^{-ikA}\right) - \xi^2 \quad = 0$$

$$= |\chi|^2 - e^{ikL}\chi^* e^{-ikA} - e^{-ikL}\chi e^{ikA} + 1 - \xi^2 = 0 \tag{14.2.4b}$$

$$\mathrm{Re}\left(e^{ik(L-A)}\chi^*\right) = 1 = \mathrm{Re}\left(e^{ikW}\chi\right)$$

where $W=A-L$ is the width of the well and $L=A-W$ is the barrier length. Using (14.1.17a-b) this becomes

$$\left.\begin{array}{l} (for\ E>V):\quad \cos kW\ \cos \ell L - \cosh 2\alpha \sin kW\ \sin \ell L \\ (for\ E<V):\quad \cos kW \cosh \kappa L + \sinh 2\beta \sin kW \sinh \kappa L \end{array}\right\} = 1 \qquad \text{(14.2.5a)}$$

The last equations are called the *Kronig-Penney band conditions*. These are plotted in Fig. 14.2.1 for the potential with $L=0.5$, $W=1.5$. Observed bands are located inside the regions between $\mathrm{Re}(e^{ikW\chi})=\pm1$. Indeed, the *1* in (14.2.5a) needs to be relaxed to ±1, or, better, to $cos(2\pi m/N)$ for C_N bands.
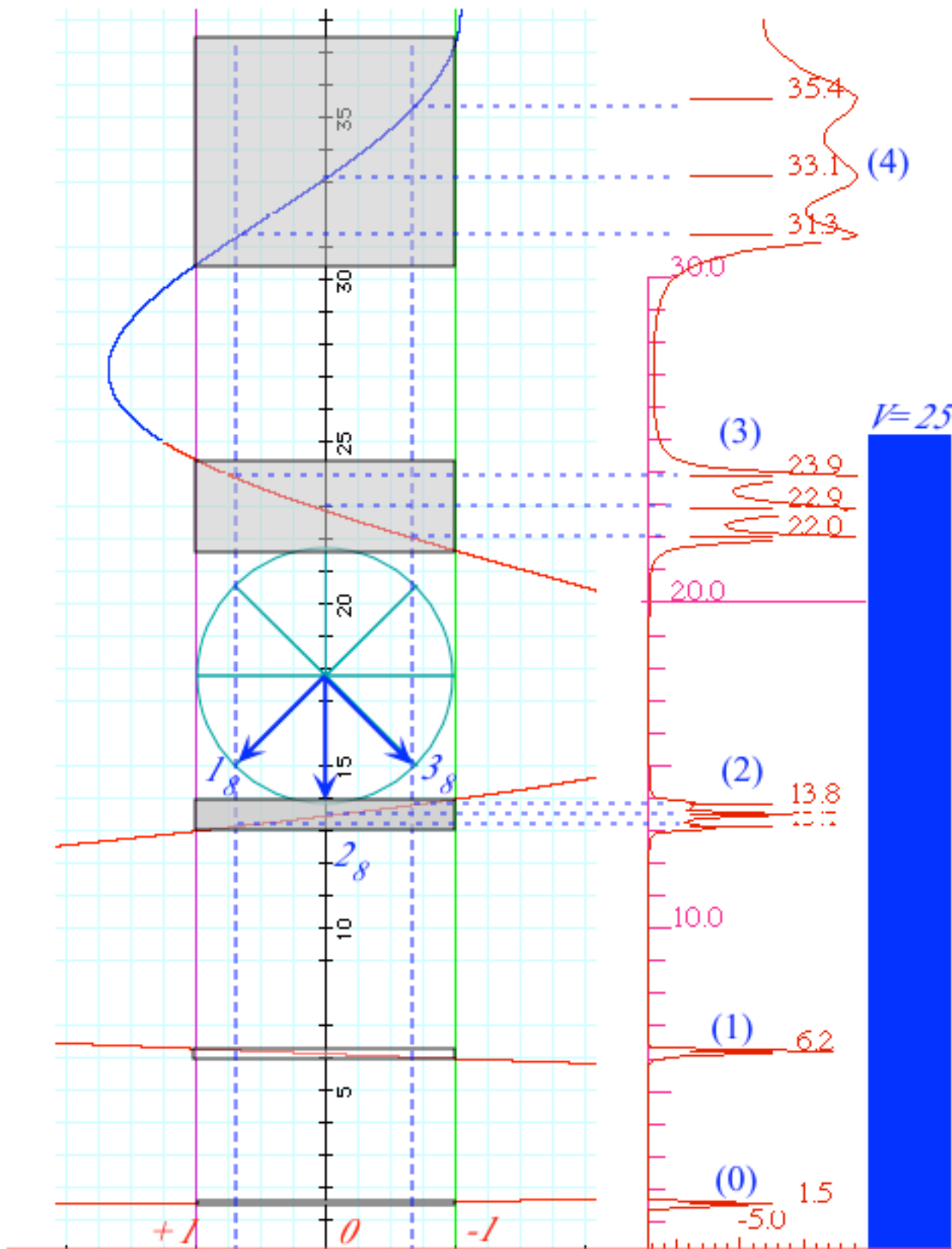
Fig. 14.2.1 Kronig-Penney functions and related 3-well-4-barrier triplet resonance bands.

It is too strict to demand that the wave recover its original form after *each* well-barrier. If instead we demand ψ recover only after passing *N* well-barriers for some integer *N*, then ψ needs to pick up an equal phase $\phi = 2\pi\, m/N$ from each barrier so it recovers after *N*. This gives the following.

$$\left.\begin{array}{l} (for\ E > V):\quad \cos kW\ \cos \ell L - \dfrac{2E - V}{2\sqrt{E\left(E - V\right)}}\sin kW\ \sin \ell L \\[1.5em] (for\ E < V):\quad \cos kW \cosh \kappa L + \dfrac{V - 2E}{2\sqrt{E\left(V - E\right)}}\sin kW \sinh \kappa L \end{array}\right\} = \cos\phi \qquad (14.2.5b)$$

where rational units are used for energy.

$$\phi = m\frac{2\pi}{N}\ , \qquad k = \sqrt{2E}\ , \qquad \ell = \sqrt{2\left(E - V\right)}\ , \qquad \kappa = \sqrt{2\left(V - E\right)}\ . \qquad (14.2.5c)$$

The values of the phase shift $\phi = 2\pi\, m/N$ are indicated as angles from the horizontal in Fig. 14.2.1. The middle member of the triplet experiences a phase shift of $\phi = \pi/2$.

An exactly zero phase shift is not possible with a line of wells because the wavefunction needs to taper off as it approaches the right or left hand walls of a linear *N*-well system. Only a circular or periodic (Bohr-like) C_N ring (discussed next) can afford to have a zero or π phase shift. The tapering can be visualized by imagining an enveloping sine wave for each of the *N*-well multiplets. The longest allowed sine wave has one wave length enveloping the entire *2N+2*-well double-ring C_{2N+2} system. That amounts to a half wave over the space occupied by *N+1* wells, or the smallest possible phase shift of

$$\phi_{min} = \pi\,/(N+1) \qquad\qquad\qquad (14.2.6)$$

That is an angle $\phi_{min} = \pi\,/4$ or *45°* for the *N=3*-well system in Fig. 14.2.1.

The enveloping sine shapes are seen more clearly as *N* increases as shown in Fig. 14.2.2 below.
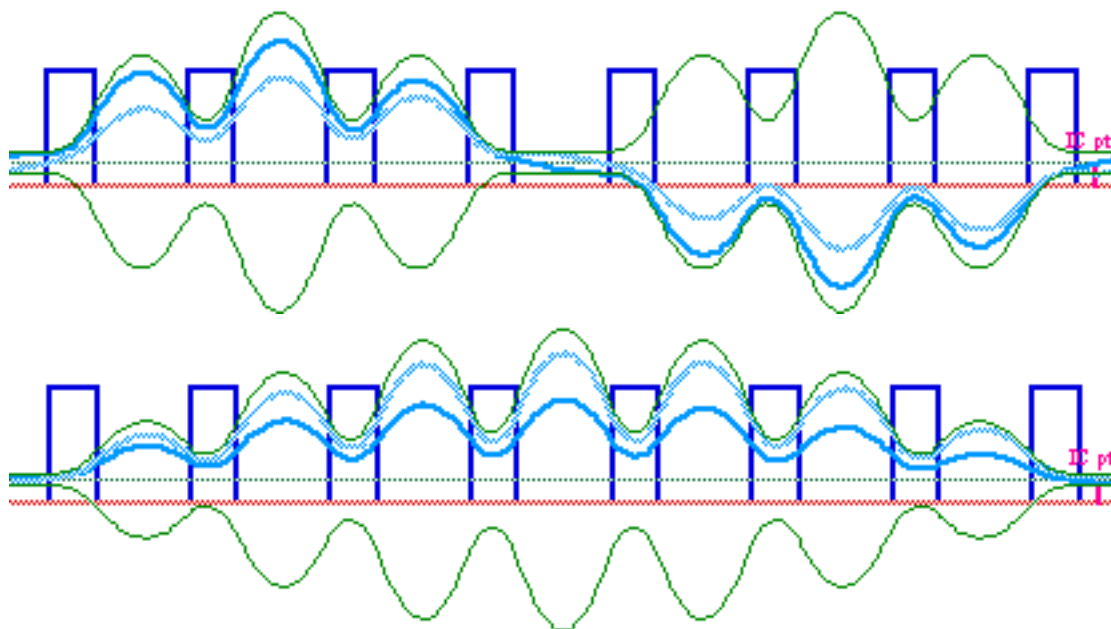
Fig. 14.2.2 Lowest two members of the (0)-septet resonance band in a linear 7-well system..

The highest allowed phase shift is just ϕ_{min} short of π. An example of such a wave is shown if Fig. 14.2.3 is the highest energy member of the *(0)*-octet whose lowest waves are shown above Fig. 14.2.2.
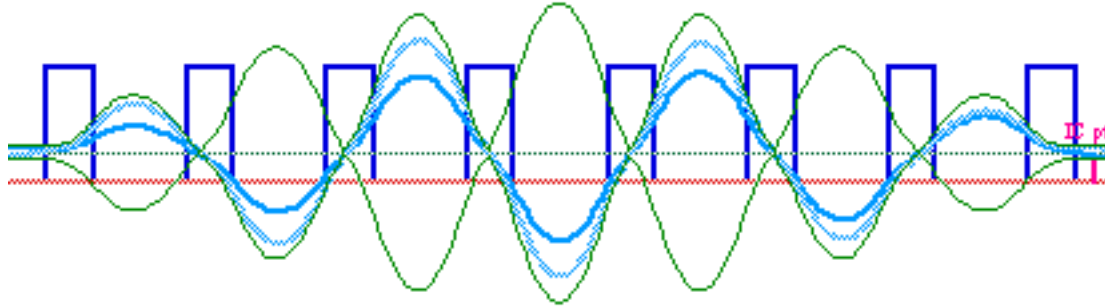
Fig. 14.2.3 Highest member of the (0)-septet resonance band in a linear 7-well system..

The slope and curvature of the Kronig-Penney (KP) functions inside the limits ±1 determine the band or multiplet structure. Only when the KP functions approach straight lines do the simple coupled pendulum model formulas (14.1.20) become precise. This happens for the lower resonances of deep wells. But for the upper resonances, and certainly for the *E*-above-*V* waves, the KP functions undergo ever longer oscillations barely exceeding the ±1 limits. At higher *E* the bands begin to dominate the spectrum while the gaps become narrow, quite the opposite of the lower spectral regions where the reverse is true.

Even in the lower *E* regions there are observable effects of the curved KP functions some of which were mentioned before. One of these is the asymmetry of the multiplet splitting. For the even multplets (0), (2), (4),... the KP function curves upward going left to right in Fig. 14.2.1. This will generally make the upper members of each multiplet have slightly greater splitting than the lower ones. The odd (1), (3),..multiplets have their order reversed since the KP function curves upward right to left so again it is the higher energy multiplet members that experience phase and energy enhancement.

(a) Band structure for large-N periodic lattices

As more and more identical well-barriers are strung together, the resonance multiplets in the transmission spectrum acquire more and more peaks. In the limit of an infinite number of barriers (Perhaps, it is wiser to just say *many* barriers.) a sharp band structure emerges that is characteristic of the shape of the individual well-barrier. Fig. 14.2.4 shows a summary of the transmission spectra for the *W=1.5* well and *L=0.5* barrier of height *V=25* for *N=1, 2, 3, 4,* and *5* wells such as have been studied in the preceding sections. As *N* increases the band structure begins to emerge from the individual well structure. The forbidden gaps become more forbidden and the allowed bands become more allowed. This is particularly noticeable in the energy regions above the barrier where the multiplet splitting is large and can be seen filling up the allowed bands as *N* increases. Recall that the minimum phase ϕ_{min} of (14.2.6) decreases with *N* so that the outer multiplets can more closely approach the Kronig-Penney band edges.
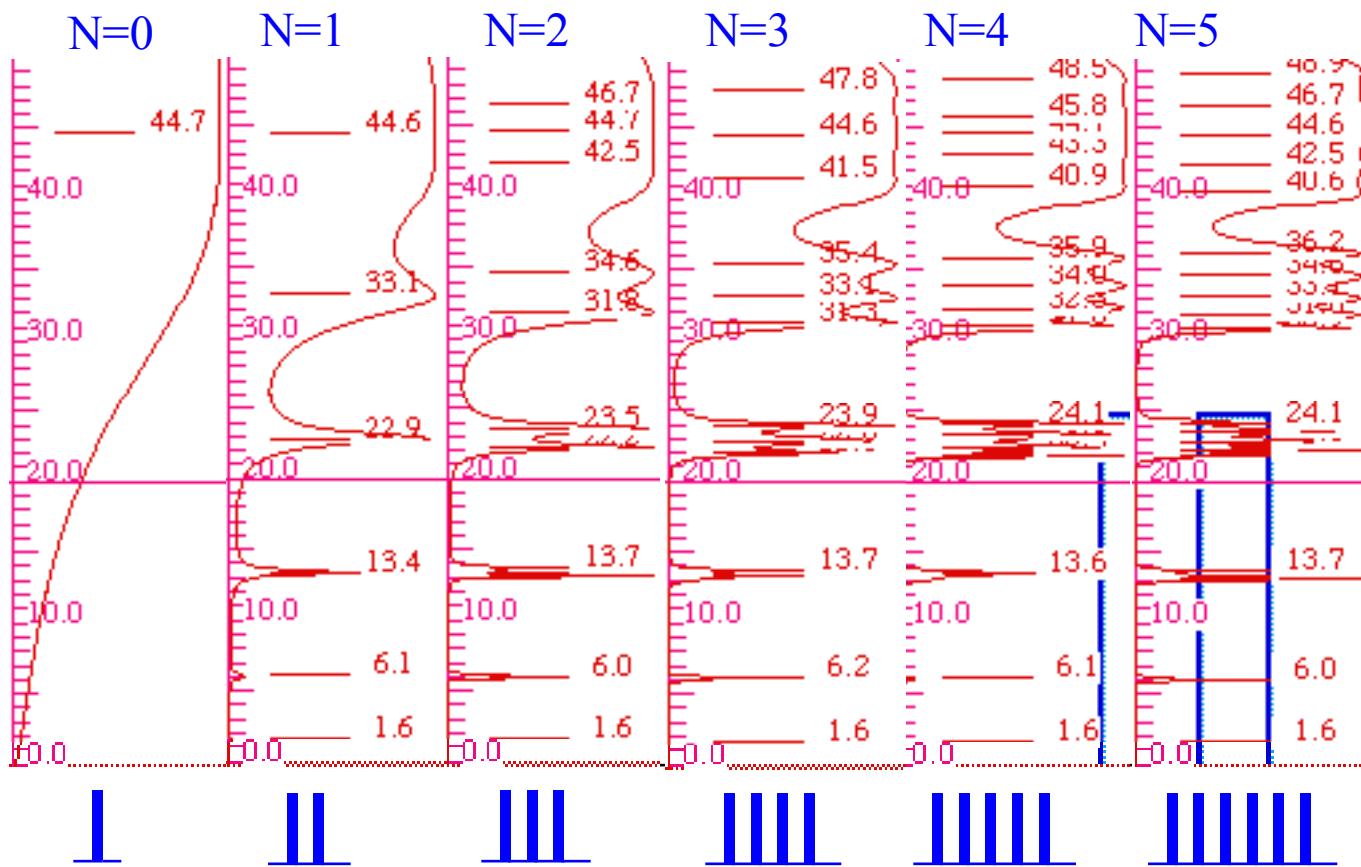
Fig. 14.2.4 Transmission resonance spectrum becoming more like band structure as N increases.

The variation of KP band edges with barrier height *V* is plotted in Fig. 14.2.5 for the *W=1.5* well and *L=0.5* barrier ending with barrier height *V=25*. This is a plot for the limit of large *N* and the allowed regions are shaded while the forbidden gaps are blank. The KP bands for *V=25* from Fig. 14.2.1 are related to the *V*-plot in Fig. 14.2.5.

Note that KP band edges pass over the barrier top without any disruption. Without the diagonal line representing *E = V*, it would be practically impossible to tell where the barrier top was located. This is in contrast to the disruption we noted in going above the barrier top for a square well as in Fig. 13.2.2. The difference is that the latter disruption resulted from going from a discrete bound state system to a wholly different continuum topology. Here, the energy is always in a continuum though that continuum is divided into allowed and forbidden band regions by the presence of a periodic lattice potential.

The lower allowed bands *(0), (1), (2)*,...become extremely narrow as *V* increases. Deeper wells make the tunneling splitting parameters *S(0), S(1), S(2)*,...exponentially small. For large *V* the lower curves in Fig. 14.2.5 become lines that approximate the discrete square well eigenvalues of Fig. 13.2.5-6 and approach the infinite-well energies discussed in Section 12.1a. This is shown more clearly a few pages ahead in Fig. 14.2.7 and Fig. 14.2.11.

(next page)   *Fig. 14.2.5 Band structure as V increases for 0<V<25. (W=1.5 well ,L=0.5 barrier)*

E

$E = V_-$
(top of barrier)

(4)

(3)

(2)

(1)

(0)

$V = 25$
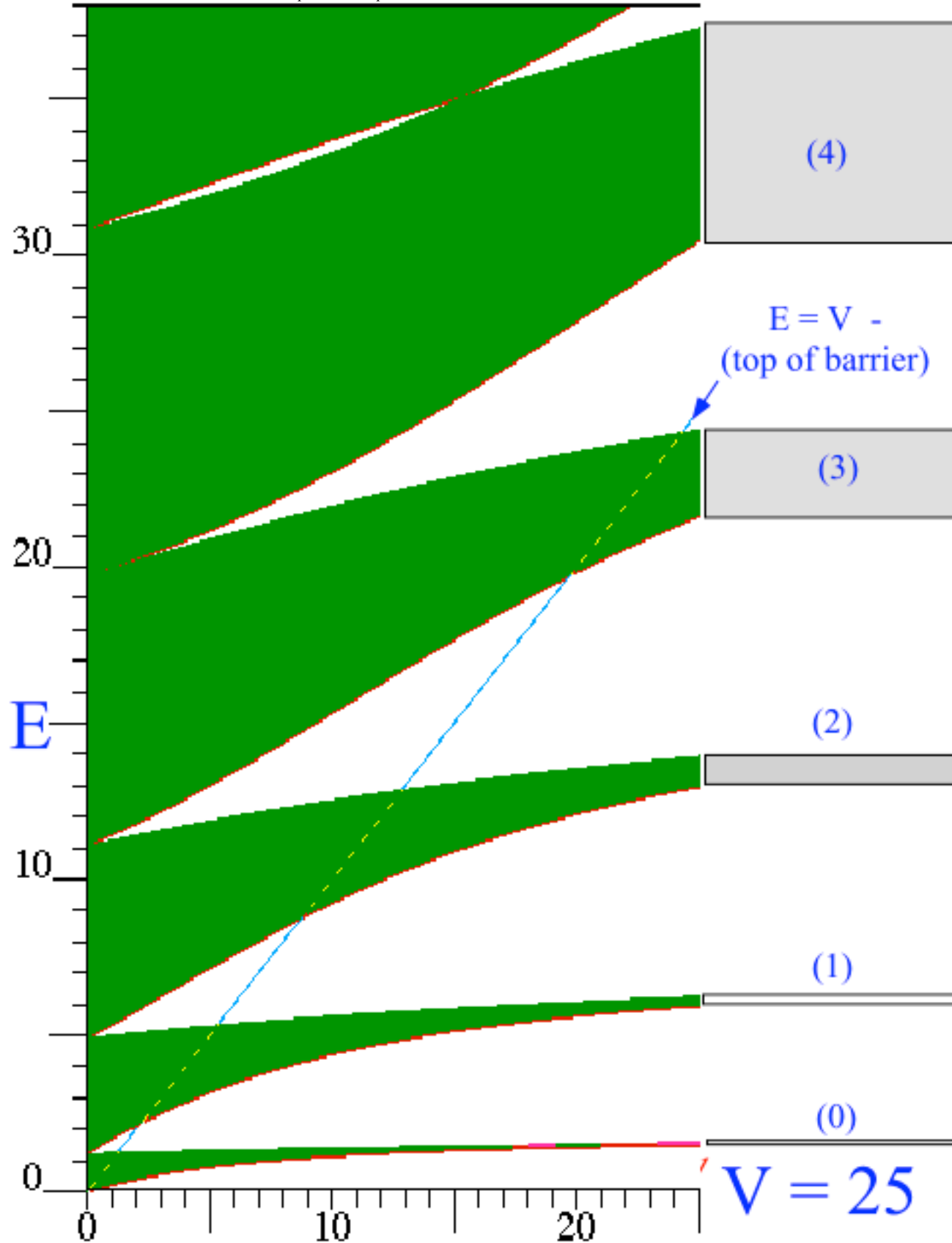
(b) Bohr and Bloch lattices and band structure

The splitting and crossing of the Kronig-Penney bands can be understood by imagining the *N*-well lattices to be wrapped around a cylinder so that the left hand barrier is identical to the right hand one. Some examples are shown in Fig. 14.2.6. If we close a loop with *periodic boundary conditions* we get a discrete Bohr-like or Bloch-like spectrum as described in Sec. 9.3. (Recall Fig. 9.3.3.) As *N* increases the cylinder gets larger so as to maintain the dimensions *W* and *L* of each well and the barrier, respectively. Also, as *N* increases, the discrete energy level density increases as discrete bands become continuous.
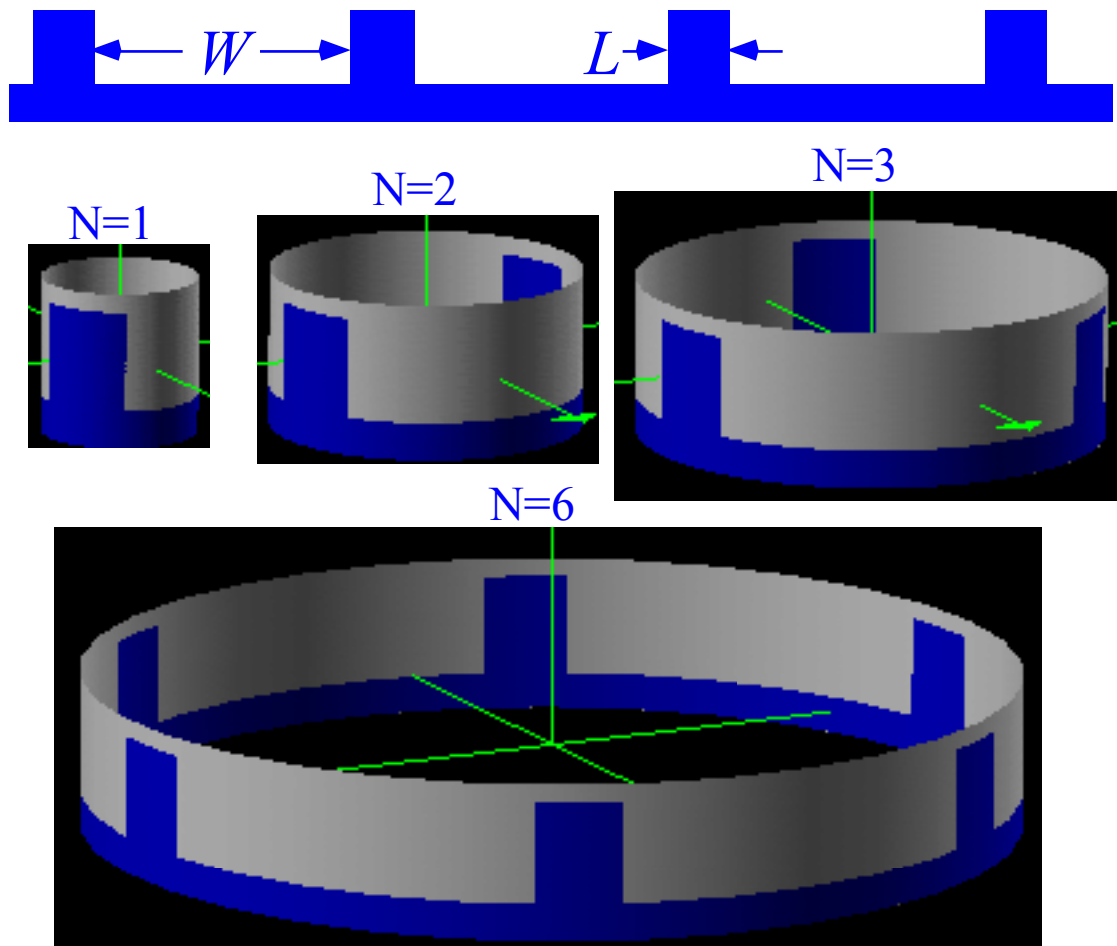
Fig. 14.2.6 Periodic lattices for Bohr-Bloch orbital problem. (W=1.5 well ,L=0.5 barrier)

A key unit of distance is the lattice length constant $A = L + W$. For reasons that will soon be seen, we take twice this distance to be a fundamental *(υ=1)* Bohr wavelength of the *N=2* ring.

$$\lambda_{Bohr} = 2A = 2W + 2L \qquad\qquad (14.2.7)$$

(This would be exactly one <u>half</u> wavelength per well lattice spacing *A*.) The resulting Bohr wavevector is

$$k_{Bohr} = \frac{2\pi}{\lambda_{Bohr}} = \frac{\pi}{A} = \frac{\pi}{W + L} \qquad\qquad (14.2.8)$$

The energy of such a unit quantum *(υ=1)* Bohr orbital in the absence of a potential *V* is (Recall 12.2.11.)

$$\varepsilon_1^{Bohr}(A) = \frac{\hbar^2}{2M}k_{Bohr}^2 = \frac{\hbar^2}{2M}\frac{\pi^2}{A^2} = \frac{\hbar^2}{2M}\frac{\pi^2}{(W+L)^2} \qquad (14.2.9)$$

Now we will use 10^{-8}m=10nm = 100 Å units of distance since it is one used in some studies of super-lattices, that is $L = 0.5$ will be 50.0 Å and $W=1.5$ will be 150 Å. The resulting lattice spacing constant of A, that is $200A$ Å or 20nm, would give an energy in the milli-electron Volt (meV) range.

$$\varepsilon_1^{Bohr}(A) = \frac{\hbar^2}{2M}\frac{\pi^2}{A^2} = \frac{\left(1.05\cdot10^{-34}\pi\text{J}\cdot\text{s}\right)^2}{\left(2\cdot9.109\cdot10^{-31}\text{kg}\right)}\frac{10^3\text{meV}}{1.602\cdot10^{-19}\text{J}}\frac{1}{\left(A\cdot10^{-8}\text{m}\right)^2} \qquad (14.2.10a)$$

$$= \frac{3.76\text{meV}}{A^2} \quad (A \text{ in units of } 100\text{Å})$$

Our favorite lattice constant of $A = L + W = 0.5+1.5 = 2.0$ or 200 Å gives

$$\varepsilon_1^{Bohr}(2) = 0.94 \text{ meV}. \qquad (14.2.10b)$$

Our rational units, for which $\hbar^2/M = 1$, relate to units of meV by a factor $3.76(2/\pi^2) = 0.762$ from (14.2.10), that is, *10* rational *E*-units is *7.6*meV. In rational *E*-units the Bohr unit energy for our lattice is

$$\varepsilon_1^{Bohr}(A) = \frac{\pi^2/2}{A^2} = \frac{4.93}{A^2} = 1.23 \quad \text{(for: } A=2 \text{ in } 100\text{Å units)} \qquad (14.2.11)$$

These unit relations are displayed prominently in Fig. 14.2.7 which shows more detail of the KP band picture first plotted in Fig. 14.2.5. Of particular note is the band splitting which occurs at the following quantum Bohr energies (in rational units).

$$\varepsilon_\upsilon^{Bohr} = \left(\upsilon_2\right)^2 E_{Bohr}(A) = 1.23\left(\upsilon_2\right)^2 \quad \text{(for: } A=2 \text{ in } 100\text{Å units)}, \qquad (14.2.12)$$

Here each <u>non</u>-zero Bohr quantum number $\upsilon_2 = 1, 2, 3,....$, has two curves splitting out from the extreme left hand side of the plot. These curves are the *Brillouin band boundaries* for bands, each of which contains N energy states, one state for each well in the ring. The very lowest *($\upsilon_2=0$)* curve is the only singlet. The rest are doublet pairs which start out as a basic Bohr $\pm\upsilon_2$-doublets (14.2.12) for zero potential barrier height *(V=0)*.

The *V*-barriers split the Bohr doublets, and for two barriers *(N=2)* the band boundaries account for the entire spectrum of two *(N=2)* levels in each "band." The shaded bands of Fig. 14.2.7 disappear since a Bohr ring cannot have a continuum, and for *(N=2)* there are no additional discrete levels inside. (Nothing is left of Alice's Cheshire cat but its smiles! Two "smiles" are seen in the upper portion of Fig. 14.2.7 which we discuss later.) The *(N=2)* spectrum is entirely composed of single levels which start out on the left hand *(V=0)* side as degenerate Bohr pairs (except for the lone Bohr singlet *($\upsilon=0$)*), and only achieve a sort of "re-pairing" for large potential barrier height *V*, on the right hand side of the figure.

However, lower "re-paired" levels on the right hand side of Fig. 14.2.7 are nearly degenerate. The "re-pairs" are a lot like the "inversion doublets" in a linear double-well. Folding linear *(N=2)* wells into the *(N=2)* circular ring potential shown in Fig. 14.2.6 erases the band between the "re-pairs." Circular Bohr-like *N*-well rings regain linear-well band continua within boundary level pairs as N approaches infinity.
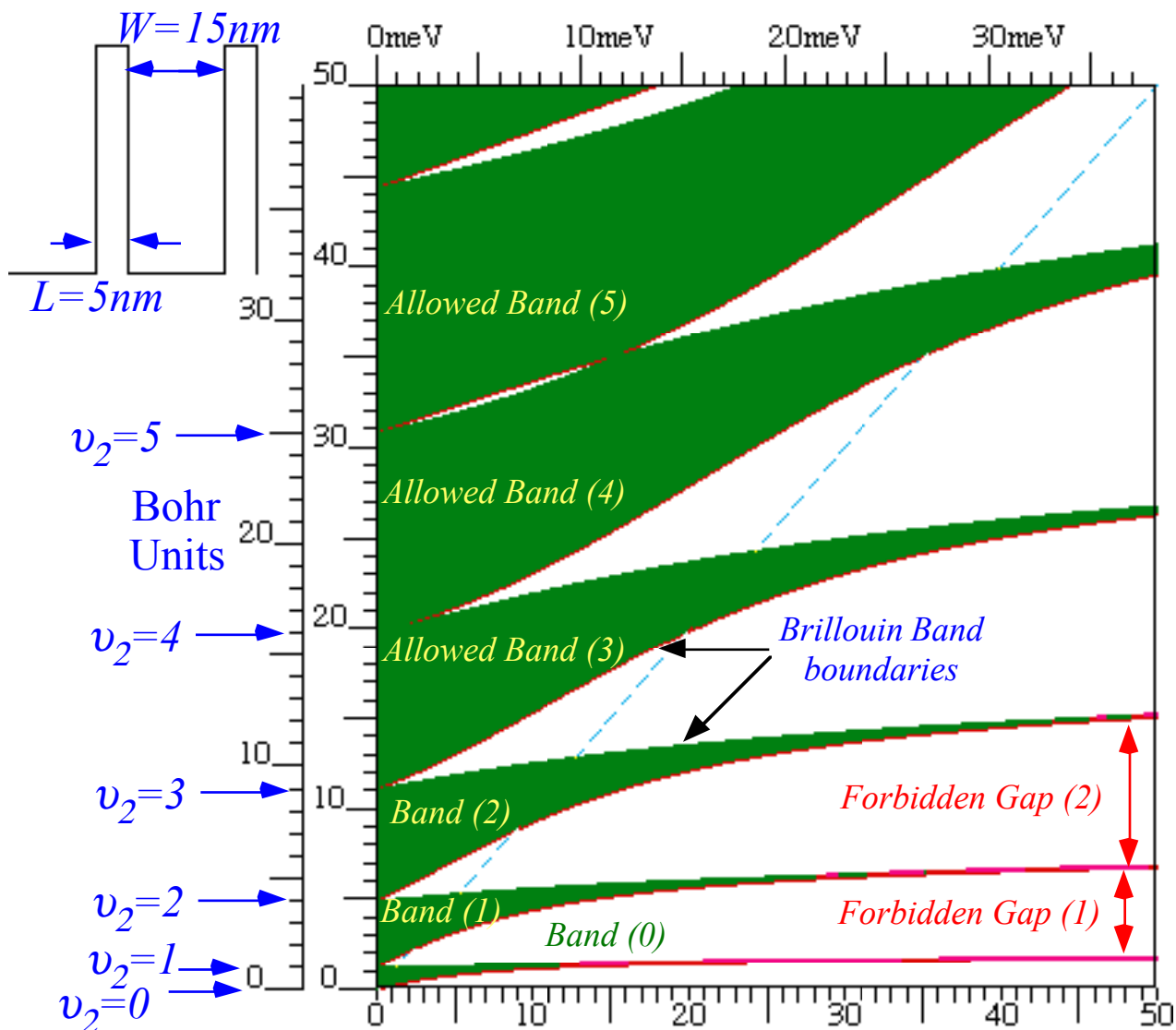
Fig. 14.2.7 Bands vs. V.(W=15nm well ,L=5nm barrier) showing Bohr splitting for (N=2)-ring.

    Waves in a circular double wells can couple to each other through either barrier. This should make doublet splitting of linear double wells (which couple only through their middle barrier) about <u>half</u> that of circular wells. The pendulum model (14.1.21) treats a linear double *(N=2)* well *(±)*-wave-doublet as the "sine" parts of circular *(2N+2=6)*-well ring waves 1_6 and 2_6 , and the splitting is, indeed, <u>half</u> the tunneling parameter $S=S(\upsilon)$.

$$\varepsilon(m_6) = H - S \cos 2\pi m/6 = H + (-1)^m(^1/_2)S \quad \text{for: } m_6 = 1_6 \text{ or: } 2_6 \quad (14.2.13)$$

    This is part of the "minor swindle" alluded to after equation (14.1.21) which can be finally put to rest if we consider the circular *N=6* potential in Fig. 14.2.6. It is a prototype for the linear *N=2* potential and is three times as big as the circular *N=2* ring potential in Fig. 14.2.6. Hence, the *N=6* ring has room for three times as many Bohr quantum waves as the *N=2* ring, and we need to triple the Bohr quantum numbers listed in Fig. 14.2.7. Now splittings occur at $\upsilon_6= 3, 6, 9, 12, 15,..$ and correspond to C_6 *Brillouin Zone band boundaries*. Each band contains six levels labeled by C_6 quantum numbers $0_6, 1_6, 2_6, 3_6, -2_6,$ and -1_6, deployed according to a

hexagonal projection shown in Fig. 9.3.1 of Chapter 9. Levels $\pm 1_6$ are degenerate as are $\pm 2_6$. In the prototype linear $N=2$ potential we would only keep the sine parts of $\pm 1_6$ and $\pm 2_6$ doublets while discarding the other four. So the linear $N=2$ problem ends up with split doublets like the circular $N=2$ one, but its doublet splitting is only half the Kronig-Penney (KP) band width.

A main difference between the resonance peak spectra of linear N-well systems and the discrete E-levels of prototype circular $(2N+2)$-well systems is that the latter can use the KP band edges while the former never can,... quite. The minimum lattice phase shift of linear wells was $\phi_{min} = \pi /(N+1)$ according to (14.2.6) but a circular wave system can have perfectly periodic waves with exactly zero or exactly π phase shift from well to well. In fact an even-N circular C_N-well system uses <u>all</u> the KP band edges while an odd-N C_N-well system uses <u>half</u> the KP band edges, skipping every other one. This is shown in Fig. 14.2.8 by comparing $N=3$ and $N=6$ ring spectra.

The potentials in Fig. 14.2.8 have V reduced from $V=25$ to $V=5$ so it is easy to see the splitting of even the first *(0)* band of multiplets. As before in Fig. 14.2.1, the KP function snakes back and forth across the vertical "tracks" left by the phase projections *cos* ϕ = *cos m(2π/N)*. Intersections of "tracks" with the KP function determine the energy eigenvalues of the multiplets in each band *(0), (1), (2), ...,* and there will be exactly N energy states per band.

One feature present here that was absent from the linear N-well resonances is the double degeneracy of every energy level that lies inside the ± 1-tracks that define the band edges. This is because right moving waves with positive wavevector $+k_N = +m(2\pi/N)$ are assumed to have the same frequency and phase speed as left-moving waves with reversed wave vector $-k_N = -m(2\pi/N)$. Each such m-pair leads to a *symmetry doublet E_m state* that is labeled E_m on the right hand side of the diagrams in Fig. 14.2.8. Pure moving-wave eigenstates are impossible for a linear N-well structure; indeed, we tossed out all the "cosine parts" of the circular prototypes in the linear-coupled-pendulum model. So, there went the "cosine-half" of each doublet. Circular C_N-rings, on the other hand, need both sine and cosine parts to make a complete set of $U(2)$ wave states.

The other "cosine parts" that were discarded from the linear N-well problem are the ones with phase $\phi = 0$ and $\phi = \pm\pi$ which lie right on the *cos* ϕ = ± 1 tracks that define the band boundaries. These are all singlet (non-degenerate) standing-wave states labeled as *symmetry singlet A_1, B_1, A_2, or B_2, states*, depending on where they fall on the KP diagram, which fixes their wave symmetry as is sketched below.   The letter "A" means "<u>A</u>lways-the-same" from well to well, that is the wave is translationally invariant and looks the same in every well. The letter "B" means "<u>B</u>ack-and-forth" from well to well, that is, the wave flips phase by π but otherwise looks the same in every well. "B" also can mean "<u>B</u>rillouin <u>B</u>and <u>B</u>oundary" since that π-flip is the earmark of the first Brillouin boundary state. (Recall (2.8.18).) However, "A" states also serve as band boundaries, for even numbered gaps. The subscripts "$_1$" and "$_2$" mean C_2 *-symmetric* and *anti-symmetric*, respectively, to reflections through the center of each well, that is, *anti-node* and *node*, respectively. Better subscripts might be the binary "0" and "1" of C_2 ("odd" and "even") but *"1-2"* notation has a long group-theoretical history.
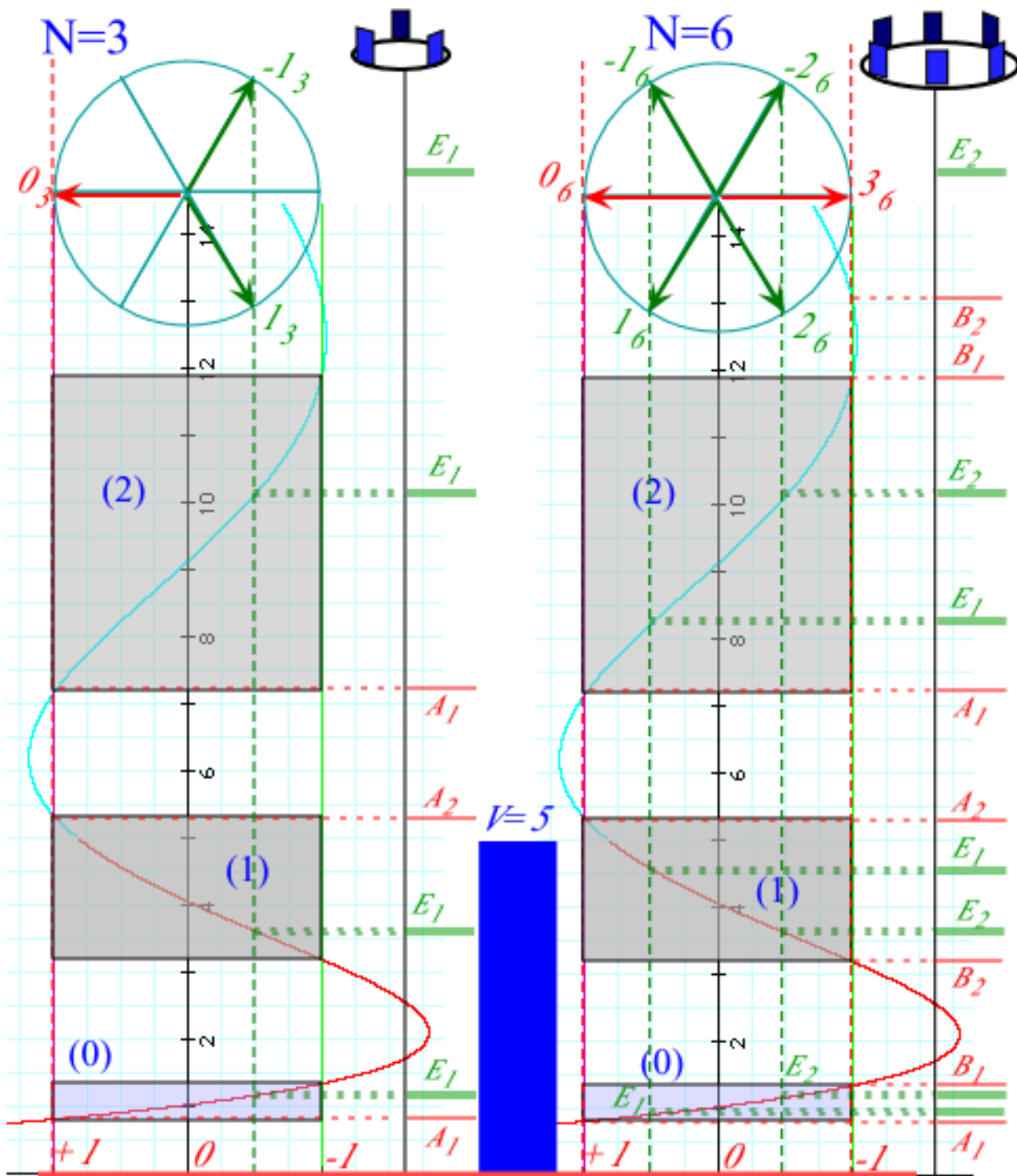
Fig. 14.2.8 Multiplets for V=5.(W=15nm well ,L=5nm barrier) for (N=3)-ring and (N=6)-ring.

The *(N=6)-ring* levels are a repeat-after-12 sequence (A_1, E_1, E_2, B_1)-*(gap)*-(B_2, E_2, E_1, A_2)-*(gap)* while the *(N=3)-ring* levels repeat-after-6 sequence (A_1, E_1,)-*(gap)*-(E_1, A_2)-*(gap)* , a subset of *(N=6)*.

(c) N=6 ring versus N=3, 2, 1 structures

Indeed, the *(N=6)*-well ring energy eigenvalues are exact copies of eigenvalues for *N*-well rings for all the integers *N* that are factors of the integer *N=6*, namely, *N=3*, *N=2*, and *N=1*. Add to this the excellent approximate spectrum of the <u>linear</u> *(N=2)*-well system resonance peaks shown in Fig. 14.2.9, and it appears that *five* different eigenvalue problems are treated in a single stroke!

As we said before, the circular *(N=2)*-well spectrum consists of the KP band boundaries alone, but it has a particular symmetry sequence (A_1, B_1)-*(gap)*-(B_2, A_2)-*(gap)*. Its bands are as empty as its gaps since the (E_1, E_2) pairs of doublets are gone. The circular *(N=2)*-well waves are virtually identical to the to the linear *(N=2)*-well waves shown in Fig. 14.1.11. The difference is due to coupling being cut in half in the linear case. This is reflected in the half-as-big splitting of the $(0^+, 0^-)$-*(gap)*-$(1^+, 1^-)$-*(gap)*- etc. sequence in Fig. 14.1.11 and Fig. 14.2.9 which is well approximated by the *(N=6)*-ring levels (E_1, E_2)-*(gap)*-(E_2, E_1)-*(gap)* except that the levels are all singlets as shown in Fig. 14.2.9. ("Sines" only, "cosines" are deleted.) So, finally, the circular *(N=2)*-spectrum (A_1, B_1)-*(gap)*-(B_2, A_2)-*(gap)* is about twice the splitting and encloses linear *(N=2)*-spectrum consisting of inversion doublets $(0^+, 0^-)$-*(gap)*-$(1^+, 1^-)$-*(gap)*- etc. in Fig. 14.1.11 and Fig. 14.2.9.

There is an apparent symmetry labeling inconsistency between the three types of doublets.

$$\text{Circular } (N=2)\text{-well spectrum: } \quad (A_1, B_1)\text{-}(gap)\text{-}(B_2, A_2)\text{-}(gap) \qquad (14.2.14a)$$

$$\text{Circular } (N=6)\text{-well doublets: } \quad (E_1, E_2)\text{-}(gap)\text{-}(E_2, E_1)\text{-}(gap) \qquad (14.2.14b)$$

$$\text{Linear } (N=2)\text{-well doublets: } \quad (0^+, 0^-)\text{-}(gap)\text{-}(1^+, 1^-)\text{-}(gap)... \qquad (14.2.14c)$$

The third sequence goes (+,-)-(+,-)-... while the first goes (A,B)-(B,A)-...that is, one "zigs" while the other "zags." How can this be, if the waves are, in fact, virtually the same shape and symmetry?

To answer this, note that the first labels *A* and *B* tell if the wave is even or odd, respectively, to lattice translation or a *2π/N*-rotation around the *z*-axis of the *N*-ring. (*N=6* here.) On the other hand, the (+) or (-) labels tell if a wave is odd or even, respectively, to reflection through the barrier between the wells or inversion of the wells. For even *(0), (2), (4),...*bands there is no difference between these two definitions of even and odd, but for odd *(1), (3), (5),...*bands, the two are reversed, hence the "zag" in (14.2.14c).Closer examination of the (E_1, E_2) sine-waves reveals that they, too, are symmetric and anti-symmetric to lattice translation like *A* and *B* , so (14.2.14b) is consistent with the rest of (14.2.14).

(1) Chiral symmetry breaking

Cyclic or circular C_N ring symmetry is called D_N or C_{Nv} symmetry if it also has transverse *180°* rotational symmetry or reflection plane symmetry, in other words, if right and left moving waves have the same speeds. The *A, B,* and *E* symmetry labels belong to these higher symmetries. However, they are useless if there is any chiral or *C*-type (Zeeman-like) symmetry breaking that distinguishes right from left. Then the E_m-doublets will be Zeeman or Coriolis-split, and the old $(0)_N, (1)_N, (2)_N, ..$ labels of C_N must be used. The effect of this type of symmetry breaking on C_6 spectra was diagrammed in Fig. 9.3.2 in which the energy hexagon is rotated by an amount determined by the relative left-right coupling phase. That same angle of rotation would apply to the phase hexagon in Fig. 14.2.8. From this one can calculate the Zeeman splitting of an *N*-well KP system.
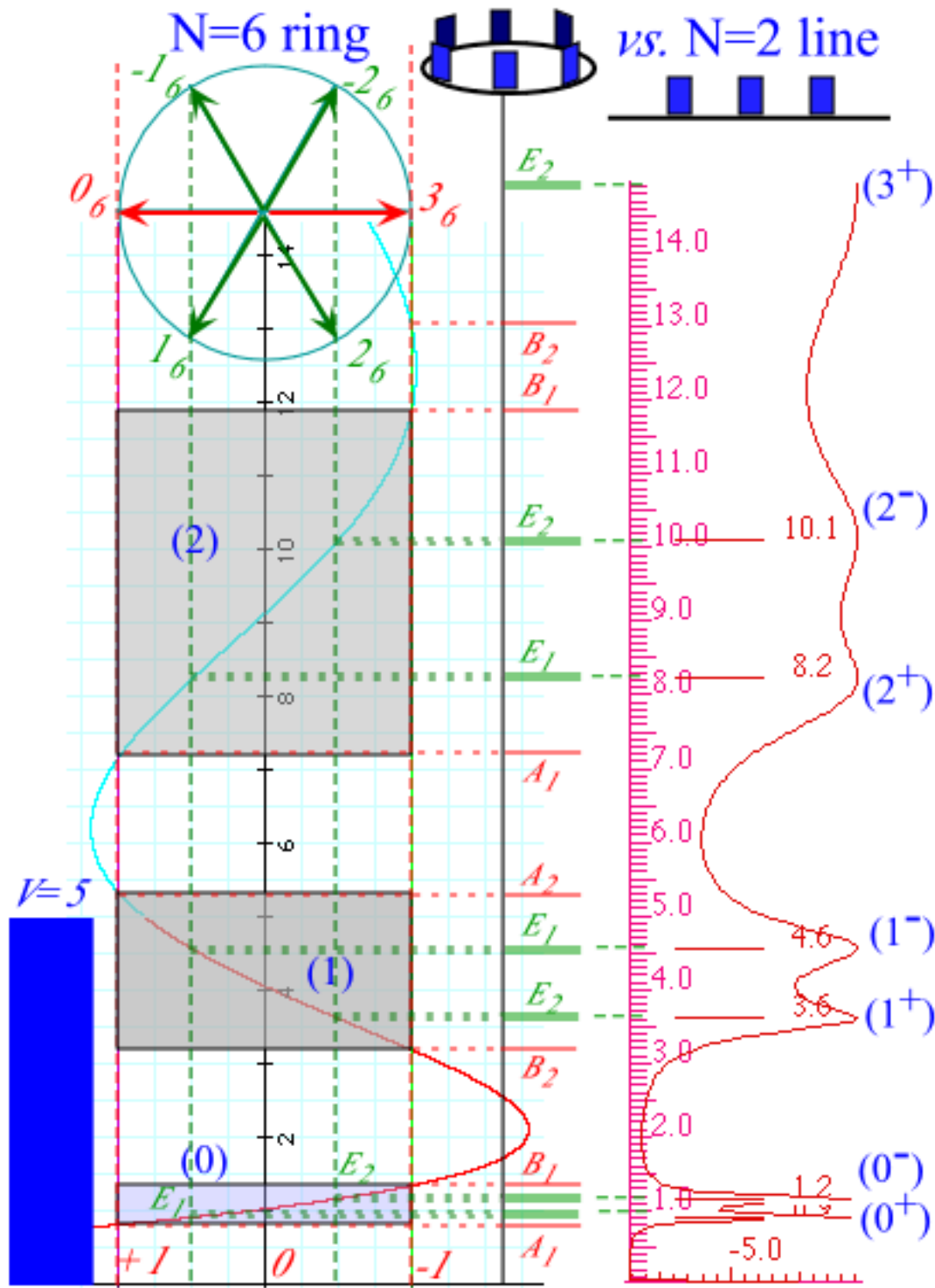
Fig. 14.2.9 Multiplets for (N=6)-ring and (N=2)-line potential. (V=5, W=15nm well ,L=5nm barrier)

(2) Reflection symmetry breaking

In Fig. 14.1.15, we showed that tiny amounts of "dirt" or "micro-symmetry breaking" could totally ruin any multiplet spectral structure and associated perfect 100% transmission properties. On the other hand, it is

possible to obtain quite perfect multiplet structure using "ruined" potentials of the type shown in Fig. 14.2.10 below. It is only necessary that they be identically "ruined" and spaced.

      Such a potential, if wrapped onto a ring will also show band multiplet structure quite similar to that which is exhibited in Figs. 14.2.8-9. Furthermore, the moving wave degeneracy would not be lifted unless there was also a chiral or Zeeman-like perturbation as well. This will be discussed further in later chapters.
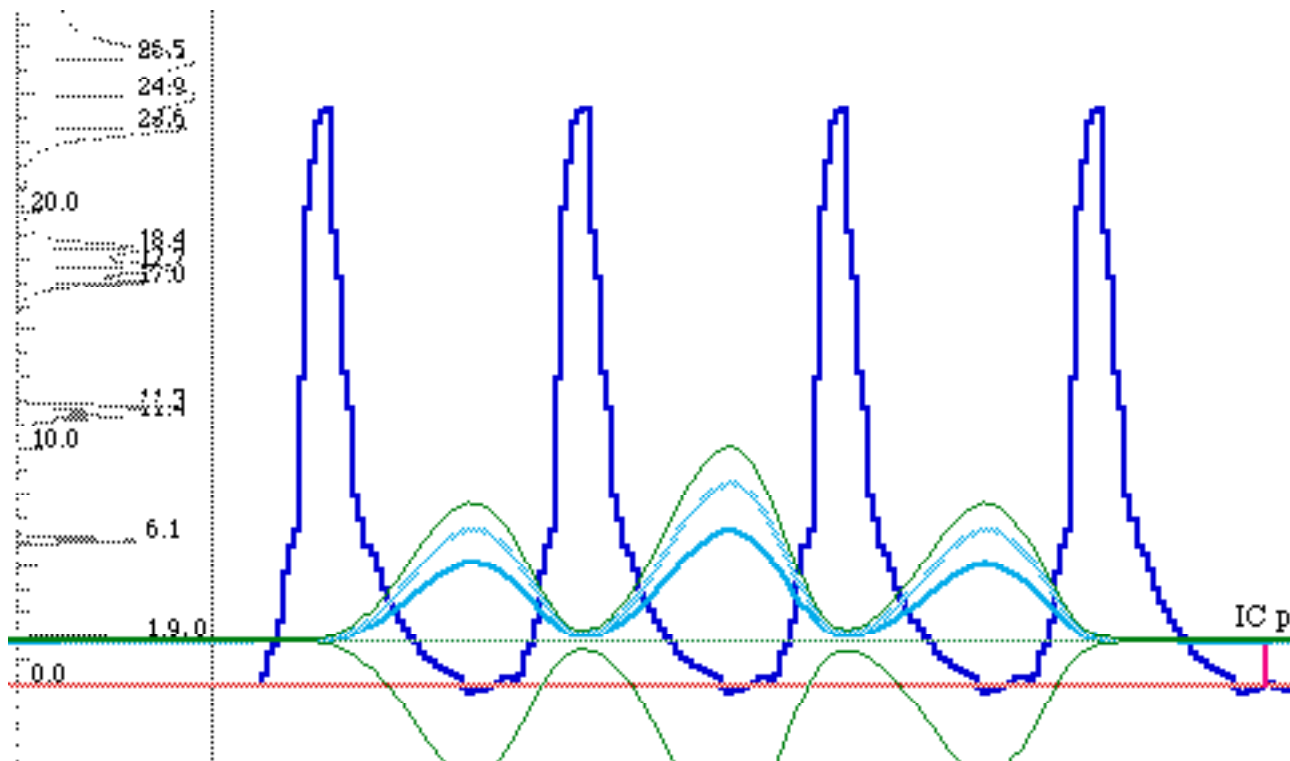
Fig. 14.2.10 Asymmetric wells of (N=4)-line potential still give 100% transmission if repeated perfectly.

(3) Band "smiles": Where BZ waves can still move

      The crossing and recrossing of KP band boundaries yields a phenomenon that is peculiar to flat-topped or flat-bottomed potentials such as we have been treating. Parts of what look like "smiles" are seen in the upper left-hand side of Fig. 14.2.7. They are more obvious in a more extensive KP band plot in which the well and barrier have the same value (*L=W=1.0*) while *V* varies, as shown in Fig. 14.2.11 below.

      The crossing points for the "smiles" all fall on energy lines that are perfect squares of even integers in Bohr units. These happen to be the energies for an infinite square well whose width *W* takes up exactly one quarter of the Bohr ring circumference. The nearly degenerate multiplet bands are seen to be very slowly approaching these asymptotic values.
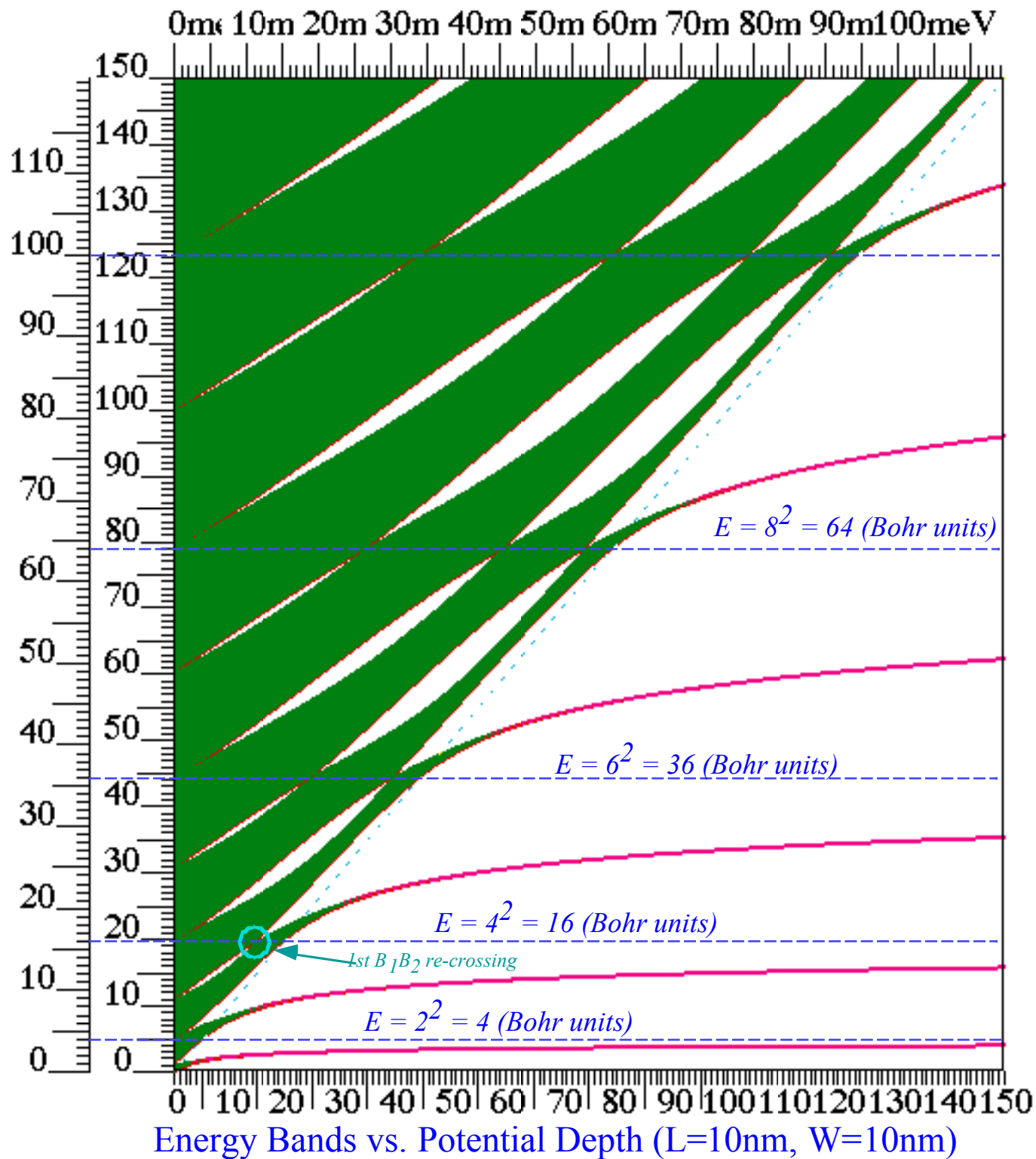
Fig. 14.2.11 *Energy E-bands versus barrier height for equal width wells and barriers.*

The resonances above the barrier also correspond to these energies but at finite V as shown in Fig. 13.2.6.

The two sides of Fig. 14.2.11 define the energy units for the Bohr problem with no potential ($V=0$) on the left hand side, and the infinite square well ($V=\infty$) to the extreme right hand side. Either extreme displays a quadratic dependence on a quantum number υ which gives the fraction of the maximum wavelength allowed by the boundary conditions for either situation.

For the Bohr limit ($V=0$) the maximal wavelength takes up N lattice spacings of $A = W + L$ or

$$\lambda_0(\upsilon, N) = \frac{N(W+L)}{\upsilon}, \quad \text{or:} \quad k_0(\upsilon, N) = \frac{2\pi}{\lambda} = \frac{2\pi}{N(W+L)}\upsilon \qquad (14.2.15a)$$

Here: $\upsilon = 1, 2, 3,..., \infty$. For the box limit ($V=\infty$) the maximal wavelength is twice a well length W or

$$\lambda_\infty(\upsilon) = \frac{2W}{\upsilon}, \quad \text{or:} \quad k_\infty(\upsilon) = \frac{2\pi}{\lambda} = \frac{\pi}{W}\upsilon \qquad (14.2.15b)$$

The latter is independent of N and barrier length L since the N wells are no longer speaking to each other. Their waves are totally confined to their respective maximum-security prison wells W. The resulting energy level doublets at $V=0$ and $V=\infty$ are, respectively, the following

$$E_0(\upsilon, N) = \frac{k_0^2}{2} = \frac{2\pi^2}{N^2(W+L)^2}\upsilon^2, \quad (14.2.15c) \qquad E_\infty(\upsilon) = \frac{k_\infty^2}{2} = \frac{\pi^2}{2W^2}\upsilon^2 \quad (14.2.15d)$$

(Natural energy units are used.) For $W = L$, as in Fig. 14.2.11, the values are

$$E_0(\upsilon, N) = \frac{k_0^2}{2} = \frac{\pi^2}{2N^2W^2}\upsilon^2, \qquad (14.2.15e) \qquad E_\infty(\upsilon) = \frac{k_\infty^2}{2} = \frac{\pi^2}{2W^2}\upsilon^2 \quad (14.2.15f)$$

If $N=2$ (two wells on the ring) and $L=1$ (100A=1nm) then E_0 gives the same Bohr unit $(\pi^2/2)/4 = 1.23$ (natural units) as (14.2.11). So, the lowest doublets at $V=0$ and $V=\infty$ are the following with $\upsilon = 1$.

$$E_0(\upsilon, 2) = \frac{\pi^2}{8}\upsilon^2, \quad (V=0) \qquad (14.2.15g) \qquad E_\infty(\upsilon) = \frac{\pi^2}{2}\upsilon^2 \; (V=\infty) \quad (14.2.15h)$$

That is one Bohr-unit (1 $Bu = \pi^2/8$ *nat.u.*) on the left of Fig. 14.2.11 and four Bohr-units on the right.

The infinite-V limit is approached slowly by the energy values. The sine-line solution shows how slowly the asymptotic energies are reached as a function of V and υ. Evanescent waves are gradually squeezed out and the bound state kW approaches multiples of π. (See exercises.) However, we noted that square well resonance kW values occur <u>exactly</u> at multiples of π, since they are not encumbered by evanescence. So, there can be E and V values for which barrier-top wavelengths fit L and inside-the-well wavelengths match W.

$$k_{TOP} = \sqrt{2(E-V)} = \frac{\pi}{L}\upsilon_{TOP}, \quad \text{and} \quad \ell_{WELL} = \sqrt{2E} = \frac{\pi}{W}\upsilon_{WELL}. \qquad (14.2.16)$$

The first non-zero-V solution to the equations (14.2.16) for $W = L$ (in Bohr-units of $Bu = \pi^2/8$) is $E = 16\ Bu$ and $V = 12\ Bu$ located at the corner of the first closed "smile" at $(V,E) = (12,16)\ Bu$ in Fig. 14.2.11. Two wavefunctions corresponding to this "accidentally degenerate" solution are shown in Fig. 14.2.12. Their symmetries are clearly B_1 and B_2 as marked. This is a singular case of exactly degenerate Brillouin zone boundary states. All the $N=2$ eigenstates except these are required to be standing waves. But, the B_1 and B_2 (at the degenerate point only) can make $U(2)$ current carrying eigenstates. It is a case where two eigenchannels resonate simultaneously. It is quite unusual!
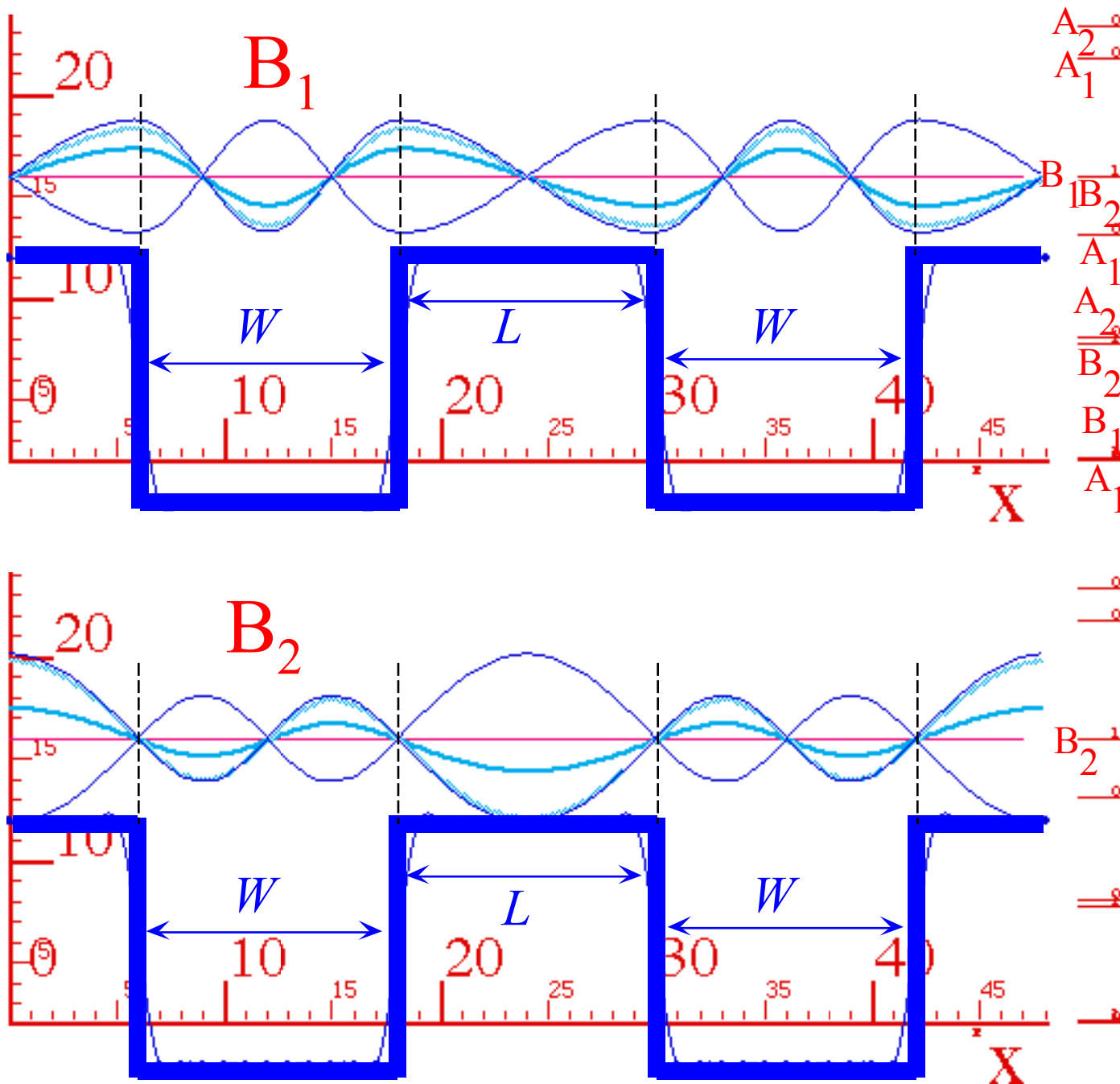
Fig. 14.2.12 Accidentally degenerate (B₁, B₂) doublet at V=12 and E=16.

An expanded view of the E vs.V plot for $N=2$ is shown in Fig. 14.2.13. It shows where the B_1 and B_2 levels cross in order to recover the "normal" (A_1, B_1)-*(gap)*-(B_2, A_2)-*(gap)* symmetry ordering mentioned previously in the discussion of below-barrier levels. Above the barrier, the levels can go wild! (And, they do it with a "smile!") In the higher resonance regions they can get "bent" many times. However, as the barrier value V grows they all untwist back to "normal" before descending into the wells. Their prison has strict rules of order!
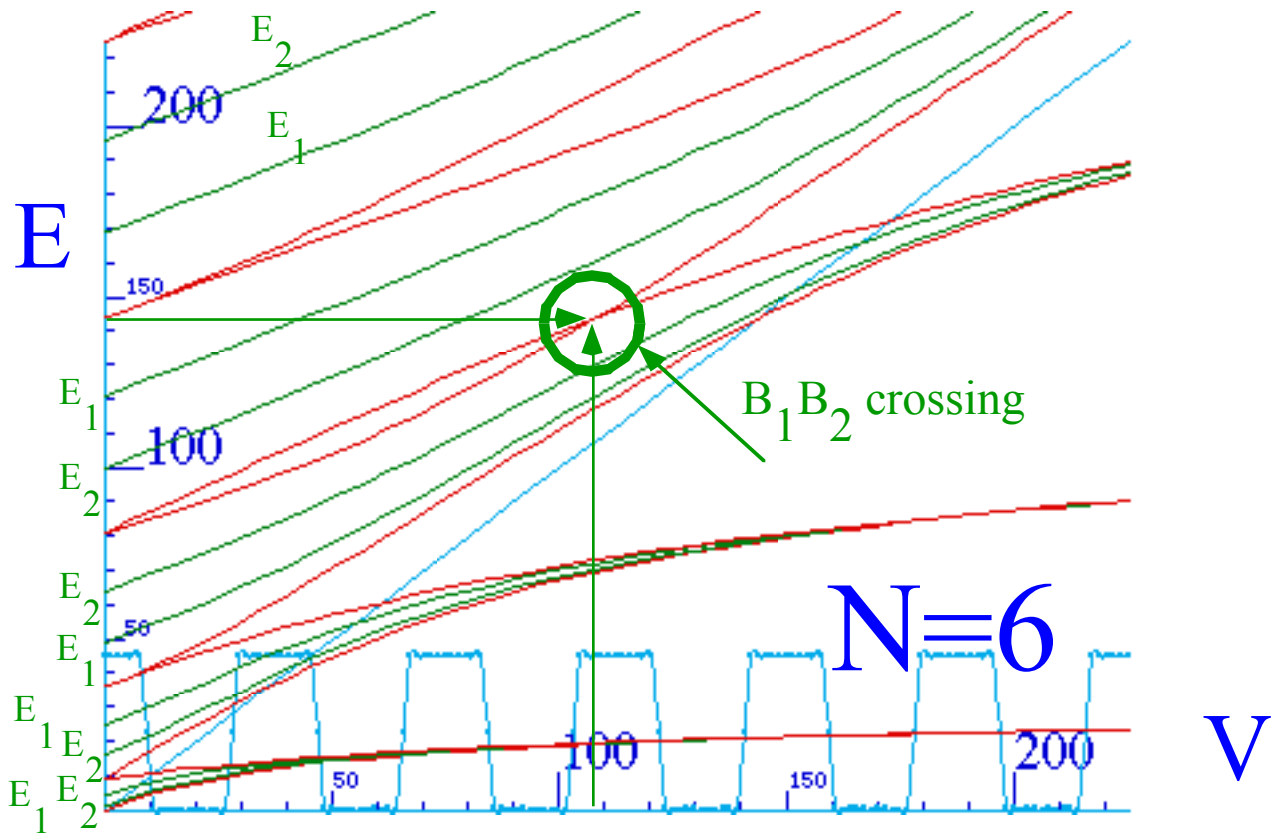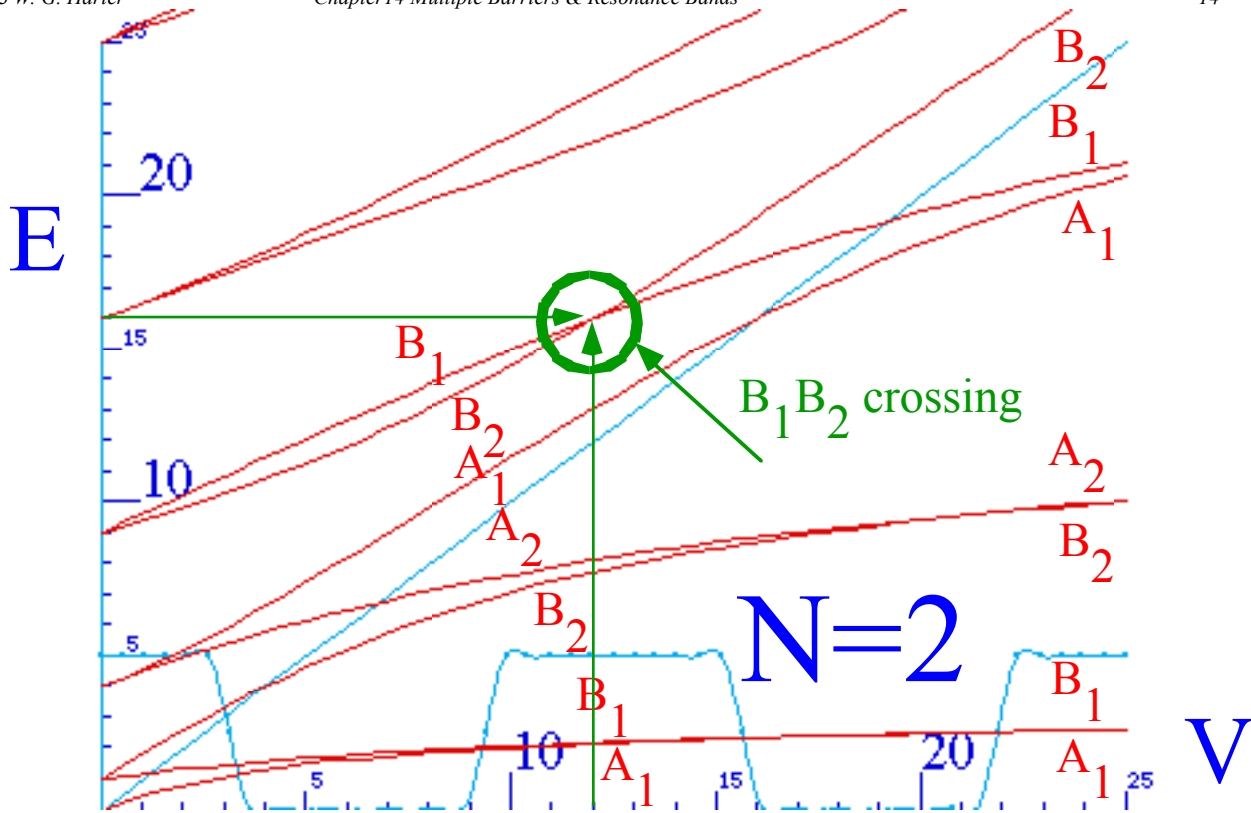
Fig. 14.2.13 (B_1, B_2) crossing for:(N=2) at V=12 and E=16, and (N=6) at V=144 and E=108.

The lower half of Fig. 14.2.13 contains a plot of the same B_1-B_2 level crossing as it appears in the spectrum of a hexagonal $N=6$ Bohr-Bloch lattice of equal square wells. Here, as was done for Fig. 14.2.8, we compare the $N=6$ spectra with that of lesser N which are factors of $N=6$ such as $N = 3, 2,$ and 1.

Note that the B_1-B_2 waves shown for $N=2$ in Fig. 14.2.12 are the same for $N=6$ or any even-N-well ring. The only difference is that the B_1-B_2 waves extend over three times as many lattice-wells since the $N=6$ ring is three times as big as the $N=2$ ring. That is what makes this kind of symmetry analysis powerful; smaller problems are copied into larger ones. Structure of $N=6$ reappears in $N=12, 18, 24,...$

What does change, as we double or triple an N-well, is the number of levels per band, which is <u>always</u> N, and the energy scale or Bohr unit, which according to (14.2.15c) shrinks according to inverse N^2. Both graphs in Fig. 14.2.13 use Bohr energy units exclusively. Each positive energy value that is a perfect square $E_\upsilon = \upsilon^2$ corresponds to a doublet level at the starting point of zero potential $V=0$.

Band splittings occur only for levels for which υ is a multiple of $N/2$, that is, at the beginning of Brillouin zone band boundaries. For $N=6$ these occur for $\upsilon = 3, 6, 9,$ ...and so forth, whereas for $N=2$ they occur at <u>every</u> $\upsilon = 1, 2, 3,$ ... (except for $\upsilon= 0$) and give rise to a sequence (A_1, B_1)-*(gap)*-(B_2, A_2)-*(gap)*. For $N=2$ there are only two levels in each band and they *are* the band boundaries.

Then as N is tripled from $N=2$ to $N=6$ there must appear three times as many energy levels <u>in</u>side each band. The four new levels appear as moving-wave doublets E_1 and E_2, which lie <u>in</u>side the band boundaries and cannot cross. That the E-doublets remain band-bound is a consequence of the Kronig-Penney (KP) construction shown in Fig. 14.2.8. Moving-wave levels must fall <u>in</u>side the ±1 bounds of the KP functions which define the A-or-B band boundaries. For $N=6$, (A_1, E_1, E_2, B_1)-*(gap)*-(B_2, E_2, E_1, A_2)-*(gap)* is the ususal ordering but A or B pairs may switch places and criss-cross in the "smile" regions.

If N is tripled from $N=2$ to $N=6$ then so are the quantum numbers labeling a particular structure. For $N=2$, the first band splitting happens at $\upsilon=1$. For $N=6$, it happens at $\upsilon=3$. The Bohr-unit energy values for a particular criss-crossing or Bohr level splitting involve squares of integer quantum numbers. So the energy for that level crossing is higher by a factor of three-<u>squared</u> ($3^2=9$). Consequently, all the energy values in the $N=6$ part of Fig. 14.2.13 are nine times the corresponding ones in the $N=2$ version. The B_1-B_2 splitting that happens at $V=12$ and $E=16$ for $N=2$, is scaled up to $V=108$ and $E=144$ for $N=6$.

It is interesting to see what happens for odd-N ring lattices, particularly, $N=1$ and $N=3$. As shown in Fig. 14.2.8, the trigonal $N=3$ spectrum is just the hexagonal $N=6$ structure with "half-a-triangle" consisting of the three levels in the E_2 doublet and B_1 or B_2 singlets removed. (Odd-N spectra cannot have B-type band boundaries. Why?) So the B_1-B_2 crossing and levels leading to it are missing from the $N=3$ or any other odd-N problem. But, there are still plenty of A_1-A_2 crossings!

(6) Bragg reflection...and non-reflection

The exact closing of two band boundaries is unusual and has consequences for current transmission properties. The usual situation of separated band boundaries precludes eigenstates with energy in the gap between bands. However, a non-stationary combination state of, say, a B_1B_2 pair of states, could have any in-between value of energy, and it would beat at a frequency equal to the band-gap energy difference.

The resulting beating is called elementary *Bragg-reflection*. An example is seen in the Fig. 14.2.14 below in which a B_1B_2 combination wave beats or gallops between a left-moving and a right-moving wave while pausing briefly as a standing wave between each gallop. When B_1B_2 levels become degenerate, as in Fig. 14.2.12, the beating stops and each possible wave combination becomes stationary in current and magnitude.
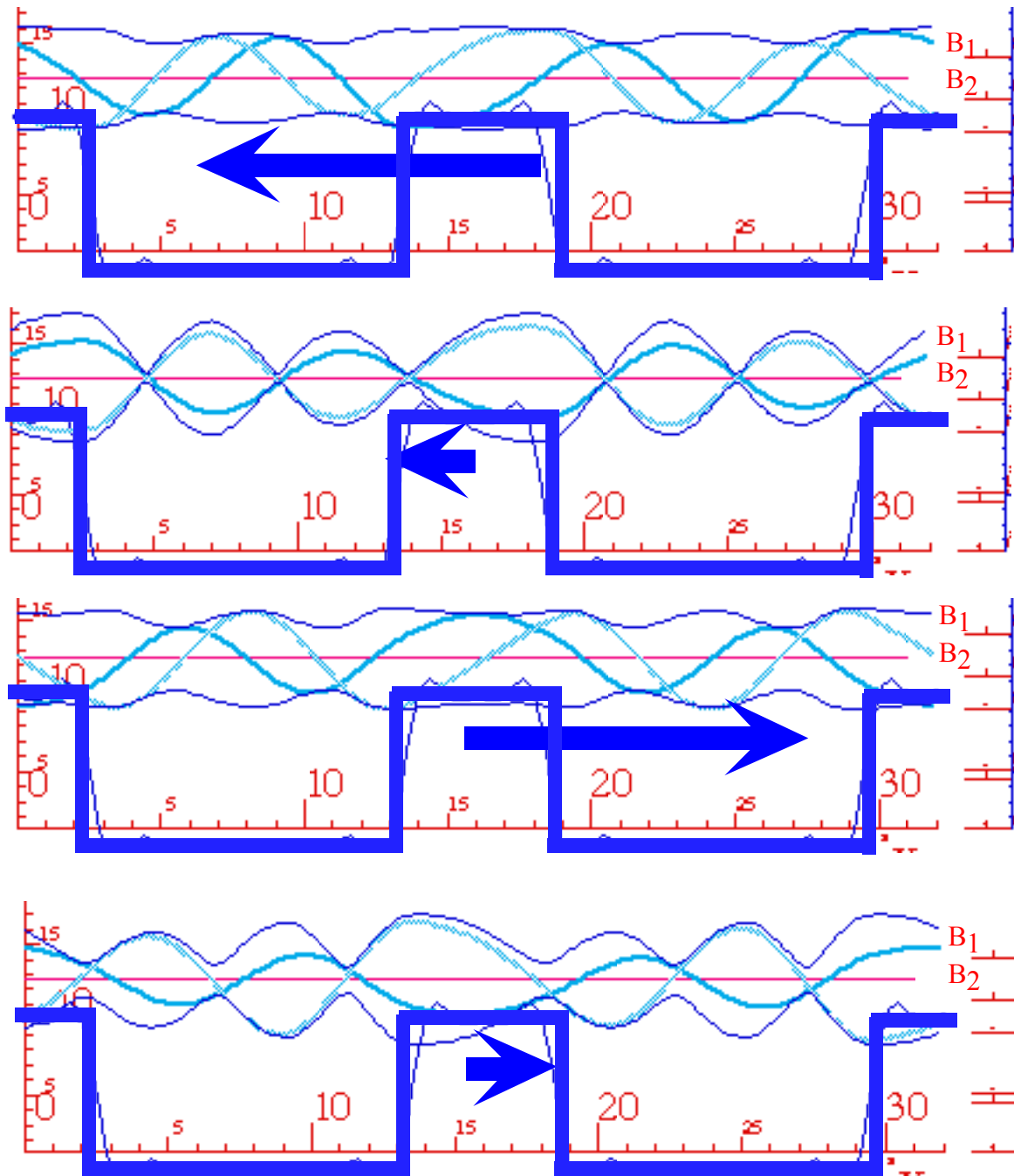
Fig. 14.2.14 Time dependent waves in between a (non-degenerate) B_1B_2 gap. (Elementary Bragg reflection.)

Problems for Chapter 14.

(a)

W=1.5 nm

V=0.8415 eV

x= -0.75 nm   x=0.75 nm

(b)

W=1.5 nm

L=0.5 nm

V=0.8415 eV

x= -1.25 nm   *x=1.25 nm*
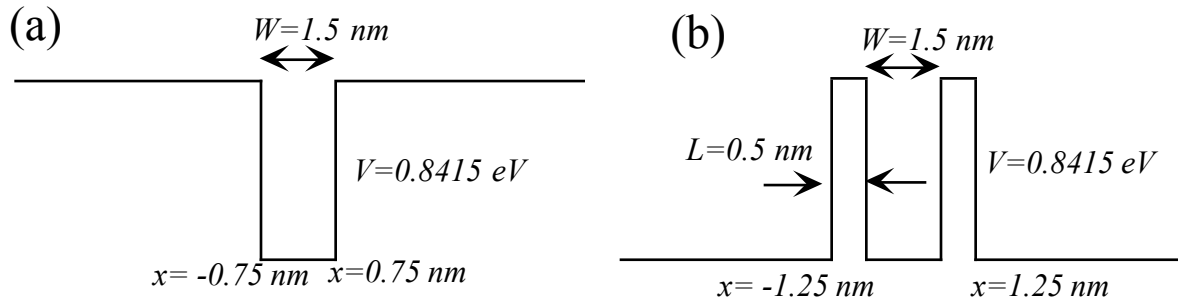
Fig. 1.1

Leapfrogging phases

14.1.1. The eigenchannel phase-shifts for the resonances above the ∞'ly thick walled well (Figure 1.1a above) undergo fairly strong variation for grazing resonances. Pick an energy E = .85eV above the barrier and plot the μ-values as you vary the well bottom V 0.8eV either way. What values of $\mu_\pm$ indicate resonance? (Use sine-line solution to tell when resonance occurs.)

Twin Towers vs. Well

14.1.2. Consider two barriers of height V = -0.8415 eV and width L = 0.5nm separated by a width W = 1.5nm. (See Fig. 1.1b)
(a) Find or plot peaks of transmission function belonging to all resonance states below the barriers and first two resonance states above the barriers. Compare with results of Problem 14.1.1. involving the square well in Fig. 1(a).
(b) Calculate and plot both S-matrix eigenchannel waves for the highest two resonances below the barrier tops and the lowest resonance above them.
(c) Compare symmetry and other properties of "resonant" eigenchannel waves vs. "non-resonant" eigenchannel waves with energies in between the resonant transmission peaks.
(c) Pick one resonant case and one non-resonant case and for each combine the eigenchannel states so they make a left-source-channel wave. Plot your results.

Lorentz Fits

14.1.3. Consider the well of depth *V = -1eV* and width *L = 2.0* in units of distance of 1.23 nm.
(a) Use the sine-line method to characterize the bound states and first two resonance states.
(b) Derive and plot the transmission and inverse transmission functions for the well with walls reduced from ∞ to a thickness of 0.5.
(d) Discuss how the "bound" state eigenvalues and resonance peaks of this well change when the surrounding walls are reduced from ∞ to a thickness of 0.5. Compare and discuss.
(c) Try fitting Lorentzian functions to the lowest resonance peaks. Are there some good fits? ..bad fits?

Quality:a most important product

14.1.4. In classical resonance theory the *Quality Factor* $Q=\upsilon_0/2\Gamma$ is a key figure of merit as is the related *angular quality* $q=\omega_0/2\Gamma=Q/2\pi$. What do these numbers tell about a resonance?
(First, check and discuss (or correct) the statements after (14.1.8) about resonance amplification being a sum of C_{11} or C_{12} components of barrier matrix (13.3.34a).)
(a) Calculate the number of oscillations or "heart beats" of resonance packet in the time it takes to decay by (14.1.13) by 95% (to 5%) of its amplitude. Relate this to *q*.
(b) Find the relative probabilty loss $\Delta P/P$ per cycle (or per radian) and relate to *Q* (or *q*). Give estimates for the E=1.5, 6.1, and 13.4 resonances in Fig. 14.1.6.
(c) Compare results of (b) to Lorentzian theory of Fig. 14.1.9.
Extra credit. (Could be a topic for a paper.)
(d) Does the exact S-matrix for this problem (and others) really have a pole around where we claim it does? (And, does it really matter?)

Delta humps vs. stumps

14.2.1. The effect of a Dirac-delta function potential V(x) = δ(x-a) may be derived directly using the analysis of Sec. 13.3 or as a limit of very narrow and tall "stump" potential.

(a) Derive the C-matrix and S-matrix for a Dirac-delta function potential $V(x) = A\,\delta(x-a)$.
(b) Compare your result to that of a "stump" in the appropriate limit. (Recall Prob. 13.2.1 *Stump*)
(c) Discuss the S-matrix eigenfunctions for $V(x) = \boxtimes(x-a)$ and $k=1$, first for $a=0$, and then for general values of a such as $a=\pi/2$. Sketch the wavefunctions.
(d) A line of N equally spaced delta humps should yield band-like or cluster spectra. Derive equations analogous to KP Eq. (14.2.5b) and solve for lowest couple of bands for $N=5$.

Minor Swindle

14.2.2. Consider a line of N identical wells of depth $V = 15$ (in theorist's units with $m/\hbar^2=1$) and length $L = 1.5$ separated by a barrier of width $W=0.5$. Relating the tunneling parameter $S(0)$ between $N=2$ and $N=3$ involved a minor swindle involving a factor of 2 or 1/2. (See right after Eq. (14.1.21).) Discuss this where appropriate.
(a) Use the coupled pendulum model to approximately predict the form of the generic multiplet structure for the cases $N=2$, $N=3$ (in text), $N=4$, and $N=5$ in terms of H and S parameters. Sketch the wavefunctions for each case of the members of the (0) and (1) resonance, that is, the two lowest resonances.
(b) Use the KP equations to obtain a better and more informative approximation to the (0) resonance multiplet band of the four cases in part (a). Compare the splitting of all four.
(c) Use a numerical evaluation or plot of the exact C-matrix calculation such as *BandIt* for the $N=3$ case to obtain exact (0) resonance peaks. Compare to the results of part (b). What additional information does the C-matrix method give over and above the KP method?

Missing Zeros

14.2.3. In Fig. 14.1.21 the lowest $(1)_3$ resonance seems to have 3 nodes in the potential region while the uppermost $(1)_1$ resonance has 5 nodes. However, the middle $(1)_2$ resonance seems to have only 2 nodes and to disobey Schrodinger's theorem that more nodes means more energy.
(a) Is the above counting correct? Discuss and sketch the waves.
(b) Sketch a complete set of S-matrix eigenchannel waves for the (1) resonance triplet.

Open and closed

14.2.4. Consider a familiar square PE with a barrier-well of height $V = 15$ UserUnits, width $W = 1.5$nm and barrier thickness of $L = 0.5$nm. Now, we derive and use its KP function to analyze its band structures and resonances. First, plot its KP function and bands for $0-1eV$.
(a) Locate the resonances of infinite-line super-lattice with 4-wells and 5-barriers.
(b) Locate the eigenvalues of closed-loop super-lattice with 10-wells and 10-barriers.
Use "professional" notation $A_1, A_2, B_1, B_2, E_1, E_2$, etc. where appropriate to label levels.

Sluggish Asymptotes

14.2.5. The quasi-degenerate multiplets in the lower right hand side of Fig. 14.2.11 appear to approach the even square asymptotes rather sluggishly. Prove that they do in fact approach them and give a simple approximate formula for their behavior as a function of barrier height V and well parameters W and L.
(a) Do this first for the case of the Fig. 14.2.11 (W=1=L) and test the formulas.
(b) Do the general formula and test it with Fig. 14.2.7.

Criss-cross

14.2.6. Consider the location of band "smiles" and crossing points shown in Fig. 14.2.11.
(a) Give a formula for the location of crossing points and a table for the ones in Fig. 14.2.11.
(b) Tell which symmetries (A_1, B_1 , B_2, A_2) are involved and track or label their paths to the right side.
(c) Do the general formula and test it with Fig. 14.2.7.
x. (Open ended problem) Suppose that well-to-well phase shift is different for left-moving waves than for right-moving ones and was described by a retardation deficit angle σ introduced in Ch. 2 equation (2.8.15).

Review Topics & Formulas for Unit 5

Kronig-Penney band conditions.

$$
\left.
\begin{aligned}
(\textit{for } E > V): \quad \cos kW \; \cos \ell L - \frac{2E - V}{2\sqrt{E(E - V)}} \sin kW \; \sin \ell L \\
(\textit{for } E < V): \quad \cos kW \cosh \kappa L + \frac{V - 2E}{2\sqrt{E(V - E)}} \sin kW \sinh \kappa L
\end{aligned}
\right\} = \cos \phi \qquad (14.2.5b)
$$

where rational units are used for energy.

$$
\phi = m\frac{2\pi}{N}, \qquad k = \sqrt{2E}, \qquad \ell = \sqrt{2(E - V)}, \qquad \kappa = \sqrt{2(V - E)}. \qquad (14.2.5c)
$$
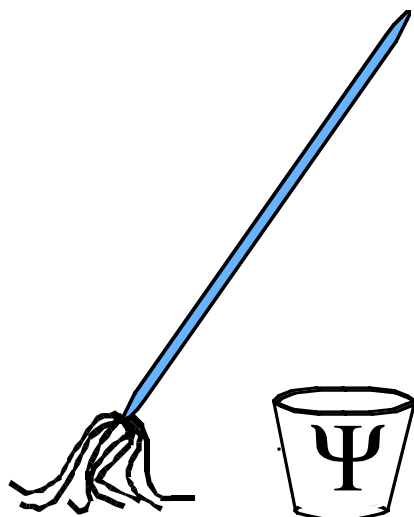
QM
for
AMOP

Chapter 15

Periodic Point Symmetry

D_n Projection Algebra

W. G. Harter

Symmetry labels A_1, B_1, A_2, … E_1, etc. of resonance bands in Chapter 14 belong to D_N or C_{Nv} symmetry groups that are non-Abelian (non-commutative) and require a projection algebra beyond that of C_N symmetry in Chapter 8. The D_N or C_{Nv} contain commutative C_N subgroups, but there are also reflection operators or 180° rotations that, like Hamilton-Pauli reflections, do not commute. Non-commutative algebras use maximal sets of commuting operators (MSCO) to do their spectral decomposition. Also, they have mutually commuting dual sets of global (or "lab-relative") and local (or "body-relative") operators. The payoff of the added complexity is an even more powerful analytic tool than Abelian symmetry analysis, and it will be used a lot in later Chapters. This is a tough chapter but well worth the effort!

CHAPTER 15. PERIODIC POINT SYMMETRY: D$_N$ PROJECTION ALGEBRA 1

Chapter 15. Periodic Point Symmetry: D_n Projection Algebra

15.1 D_n symmetry: Understanding A_1, A_2, B_1, B_2, and E_m labels

Before proceeding, it might help to give a better technical explanation of the symmetry labels A_1, A_2, B_1, B_2, and E_m which are being used. They belong to a famous class of symmetry groups called *D_n or dihedral polygonal symmetries*. Examples of symmetry analysis of *N*-barrier band structure for *N=2,3,...,6* are introduced below. While we're at it, the algebra of general symmetry analysis will be given. Quantum theory is enhanced immeasurably and deeply by such group algebra.

(a) D_2 symmetry

D_2 might be called "double-two" since it is made by combining two cyclic C_2 groups like the $C^A{}_2$ and $C^B{}_2$ that were described at length in Sections 10.2. Indeed, D_2 is closely related to Hamilton's original quaternion group algebra defined by (10.4.6) and (10.5.13). (It's also related to a famous "Star Wars" character R_2D_2, but that's another story.)

D_2 is just the rotational symmetry of the *N=2* potential object shown in Fig. 15.1.1 next to a D_2 group multiplication table. Clearly, this object can be rotated by *180°* around its main *z*-axis without altering the workings of waves ringing inside it. This $C^z{}_2$-symmetry operator $\mathbf{R}_z$ is in a subgroup of D_2 making the top-left quadrant of the table. However and though our Earth-based mind-set may indicate otherwise, there are other symmetry operations including a *180°* rotation $\mathbf{R}_y$ about the y-axis through the center of the potential wells. You must forget gravity for a moment and admit that a D_2 ring, with a pair of *W*-wells and *L*-barriers, works the same upside down as right side up.(Turning an electrostatically charged ring over doesn't "dump" its particle out.) It is the $\mathbf{R}_y$ and $\mathbf{R}_z$-operations that define the labels A_1, A_2, B_1, and B_2 , but a third *180°* x-rotation through the center of the potential barriers, namely,

$$\mathbf{R}_x = \mathbf{R}_z \, \mathbf{R}_y = \mathbf{R}_y \, \mathbf{R}_z \qquad\qquad (15.1.1)$$

completes the D_2 group multiplication table. D_2 is the σ-algebra (10.4.6) without *(i)* factors. D_2 was introduced in (8.3.5) as a symmetry of a rectangular *q*-dot system in Fig. 8.3.2.
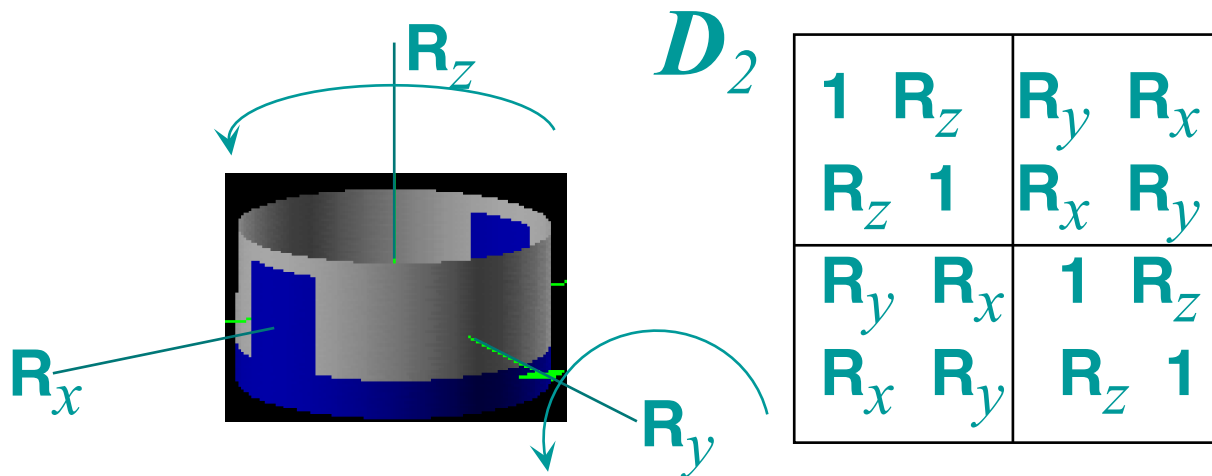
Fig. 15.1.1 D_2 symmetry operations and group multiplication table generated by $C^z{}_2$ and $C^y{}_2$.

   One notation for D_2 uses the *Cartesian or "cross" ($\times$) product* to write D_2 as follows.

$$D_2 = C^z{}_2 \times C^y{}_2 \tag{15.1.2}$$

Cross ($\times$) means that every element of D_2 is a <u>unique</u> product (like (15.1.1)) of one element of $C^z{}_2$ with one element of $C^y{}_2$. This means the product is the same in either order and factors must commute, like (15.1.1). 3-D rotations usually do not commute. Orthogonal $180°$ rotations are an exception.

   The "cross" or outer ($\times$) product implies that spectral decomposition of the group is a simple outer product of the eigenvalues of the factor groups. Starting with two C_2 factors having eigenvalue or "character" tables we quickly build an eigenvalue or character table for the $D_2 = C^z{}_2 \times C^y{}_2$ product.

C_2^z	1	R_z
A	1	1
B	1	−1

$\times$

C_2^y	1	R_y
(1)	1	1
(2)	1	−1

$=$

$C_2^z \times C_2^y$	$1 \cdot 1$	$R_z \cdot 1$	$1 \cdot R_y$	$R_z \cdot R_y$
$A \cdot (1)$	$1 \cdot 1$	$1 \cdot 1$	$1 \cdot 1$	$1 \cdot 1$
$B \cdot (1)$	$1 \cdot 1$	$-1 \cdot 1$	$1 \cdot 1$	$-1 \cdot 1$
$A \cdot (2)$	$1 \cdot 1$	$1 \cdot 1$	$1 \cdot (-1)$	$1 \cdot (-1)$
$B \cdot (2)$	$1 \cdot 1$	$-1 \cdot 1$	$1 \cdot (-1)$	$-1 \cdot (-1)$

$$\tag{15.1.3}$$

$=$

D_2	1	R_z	R_y	R_x
A_1	1	1	1	1
B_1	1	-1	1	-1
A_2	1	1	−1	−1
B_2	1	-1	−1	1

$$\tag{15.1.4}$$

   In the R_z-column of the D_2 table you see that A_1 and A_2 states get +1 while the B_1 and B_2 states get -1. The R_x-column of the D_2 table says that A_1 and B_1 states get +1 while the A_2 and B_2 states get -1. These are exactly the "rules" quoted earlier after (14.2.13) to explain Fig. 14.2.8. The parity in the R_x-column is a product of parity in the R_z and R_y columns, so a label to indicate x-parity isn't needed.

   The algebraic reasoning behind the product (15.1.3) uses *Axiom-4* completeness and the old "*one-equals-one-times-one*" trick first introduced in Chapter 3, equation (3.1.36). Here we multiply the two "ones" provided by the separate C_2 projectors $\mathbf{P}^{A,B} = (\mathbf{1} \pm \mathbf{R}_z)/2$ and $\mathbf{P}^{1,2} = (\mathbf{1} \pm \mathbf{R}_y)/2$.

$$\mathbf{1} \cdot \mathbf{1} = \left(\mathbf{P}^A + \mathbf{P}^B\right) \cdot \left(\mathbf{P}^1 + \mathbf{P}^2\right) = \mathbf{P}^A \cdot \mathbf{P}^1 + \mathbf{P}^B \cdot \mathbf{P}^1 + \mathbf{P}^A \cdot \mathbf{P}^2 + \mathbf{P}^A \cdot \mathbf{P}^2 \tag{15.1.5a}$$

Each term gives an orthogonal D_2 projector having coefficients of operators as parity values (15.1.3).

$$\mathbf{P}^{A_1} \equiv \mathbf{P}^A \cdot \mathbf{P}^1 = \frac{\left(\mathbf{1}+\mathbf{R}_z\right) \cdot \left(\mathbf{1}+\mathbf{R}_y\right)}{2 \cdot 2} = \frac{1}{4}\left(\mathbf{1}+\mathbf{R}_z+\mathbf{R}_y+\mathbf{R}_x\right)$$

$$\mathbf{P}^{B_1} \equiv \mathbf{P}^B \cdot \mathbf{P}^1 = \frac{\left(\mathbf{1}-\mathbf{R}_z\right) \cdot \left(\mathbf{1}+\mathbf{R}_y\right)}{2 \cdot 2} = \frac{1}{4}\left(\mathbf{1}-\mathbf{R}_z+\mathbf{R}_y-\mathbf{R}_x\right)$$

$$\mathbf{P}^{A_2} \equiv \mathbf{P}^A \cdot \mathbf{P}^2 = \frac{\left(\mathbf{1}+\mathbf{R}_z\right) \cdot \left(\mathbf{1}-\mathbf{R}_y\right)}{2 \cdot 2} = \frac{1}{4}\left(\mathbf{1}+\mathbf{R}_z-\mathbf{R}_y-\mathbf{R}_x\right)$$

$$\mathbf{P}^{B_2} \equiv \mathbf{P}^B \cdot \mathbf{P}^2 = \frac{\left(\mathbf{1}-\mathbf{R}_z\right) \cdot \left(\mathbf{1}-\mathbf{R}_y\right)}{2 \cdot 2} = \frac{1}{4}\left(\mathbf{1}-\mathbf{R}_z-\mathbf{R}_y+\mathbf{R}_x\right)$$

$$\tag{15.1.5b}$$

Actually, (15.1.3) are coefficients of the *projectors* in the inverse (spectral decomposition) relations.

$$\begin{aligned}
\mathbf{1} &= (+1)\mathbf{P}^{A_1} + (+1)\mathbf{P}^{B_1} + (+1)\mathbf{P}^{A_2} + (+1)\mathbf{P}^{B_2} \quad (\textit{completeness}) \\
\mathbf{R}_z &= (+1)\mathbf{P}^{A_1} + (-1)\mathbf{P}^{B_1} + (+1)\mathbf{P}^{A_2} + (-1)\mathbf{P}^{B_2} \\
\mathbf{R}_y &= (+1)\mathbf{P}^{A_1} + (+1)\mathbf{P}^{B_1} + (-1)\mathbf{P}^{A_2} + (-1)\mathbf{P}^{B_2} \\
\mathbf{R}_x &= (+1)\mathbf{P}^{A_1} + (-1)\mathbf{P}^{B_1} + (-1)\mathbf{P}^{A_2} + (+1)\mathbf{P}^{B_2}
\end{aligned}$$

(15.1.5c)

These follow from (assumed) eigen-operator relations

$$\begin{aligned}
\mathbf{R}_z\mathbf{P}^{A_1} &= (+1)\mathbf{P}^{A_1}, \ \mathbf{R}_z\mathbf{P}^{B_1} = (-1)\mathbf{P}^{B_1}, \ \mathbf{R}_z\mathbf{P}^{A_2} = (+1)\mathbf{P}^{A_2}, \ \mathbf{R}_z\mathbf{P}^{B_2} = (-1)\mathbf{P}^{B_2}, \\
\mathbf{R}_y\mathbf{P}^{A_1} &= (+1)\mathbf{P}^{A_1}, \ \mathbf{R}_y\mathbf{P}^{B_1} = (+1)\mathbf{P}^{B_1}, \ \mathbf{R}_y\mathbf{P}^{A_2} = (-1)\mathbf{P}^{A_2}, \ \mathbf{R}_y\mathbf{P}^{B_2} = (-1)\mathbf{P}^{B_2},
\end{aligned}$$

(15.1.5d)

The transformation is real-unitary (orthogonal) so it works either way! The last way of writing the symmetry is equivalent to Dirac notational definitions of the D_2 symmetry rules.

$$\begin{aligned}
\mathbf{R}_z|A_1\rangle &= (+1)|A_1\rangle, \ \mathbf{R}_z|B_1\rangle = (-1)|B_1\rangle, \ \mathbf{R}_z|A_2\rangle = (+1)|A_2\rangle, \ \mathbf{R}_z|B_1\rangle = (-1)|B_1\rangle, \\
\mathbf{R}_y|A_1\rangle &= (+1)|A_1\rangle, \ \mathbf{R}_y|B_1\rangle = (+1)|B_1\rangle, \ \mathbf{R}_y|A_2\rangle = (-1)|A_2\rangle, \ \mathbf{R}_y|A_2\rangle = (-1)|A_2\rangle.
\end{aligned}$$

(15.1.5e)

States and operators are associated as is done in Chapter 8 equations (8.2.5) or (8.2.10). Here, *norm=2*.

$$|A_1\rangle = \mathbf{P}^{A_1}|\mathbf{1}\rangle(\textit{norm}), \ |B_1\rangle = \mathbf{P}^{B_1}|\mathbf{1}\rangle(\textit{norm}), \ |A_2\rangle = \mathbf{P}^{A_2}|\mathbf{1}\rangle(\textit{norm}), \ |B_2\rangle = \mathbf{P}^{B_2}|\mathbf{1}\rangle(\textit{norm}).$$

(15.1.5f)

The symmetry algebra becomes a conceptual aid and a powerful computational tool as described in Sec. 8.2. For example, level crossing such as B_1B_2 in Fig. 14.2.13, is unlikely unless certain matrix elements of the Hamiltonian, such as $\langle B_1|\mathbf{H}|B_2\rangle$, vanish identically. As long as the Hamiltonian $\mathbf{H}$ commutes with symmetry operators (and therefore, symmetry projectors) such vanishing is, indeed, guaranteed.

$$\langle B_1(band_3)|\mathbf{H}|B_2(band_2)\rangle = \langle B_1|\mathbf{P}^{B_1}\mathbf{H}\mathbf{P}^{B_2}|B_2\rangle = \langle B_1|\mathbf{H}\mathbf{P}^{B_1}\mathbf{P}^{B_2}|B_2\rangle \equiv 0$$

This is simply a result of projector orthonormality. ($\mathbf{P}^\alpha\mathbf{P}^\beta = \delta^{\alpha,\beta}\mathbf{P}^\beta$) It permits the levels belonging to different bands and symmetries to cross if their diagonal matrix elements happen to be equal.

Two E_m levels may also have equal (or nearly equal) diagonal matrix elements, particularly for high N and $m=N/2-1$ near a Brillouin zone boundary. In Fig. 14.2.13 two E_2 levels pass on either side of B_1B_2 crossing. Larger-N cases may bring them closer still but they will avoid each other because off-diagonal matrix elements $\langle E_m(band_a)|\mathbf{H}|E_m(band_b)\rangle$ are unlikely to be zero just when the diagonals equate. This is *Wigner's avoided-crossing rule: like-symmetries repel* much like the diverging hyperbolic "diablo" shown in Fig. 10.3.1. Wigner's rule does not preclude crossing of an E_1 and an E_2 since they are different symmetries, but it discourages same-symmetry crossings like A_1A_1, B_1B_1 or E_2E_2..

These symmetry statements are not strict "laws" and can be broken if you really work at it by adjusting parameters in order to arrive at the center of a "diablo" on the one and only one point that contains a degeneracy. Wigner rules are more like "taboos" and, in this sense, not too different from societal taboos which also rule about avoiding degeneracy!

(b) D$_3$ symmetry: Non-commutative algebra

D_3 might be called "double-three" since it is made by combining two cyclic groups C_2 and C_3. However, this combination is not; let us repeat: *NOT* a simple cross product of C_2 and C_3. Some elements of C_2 and C_3 do

not commute (for example, $\mathbf{r}\,\mathbf{i}_2 \neq \mathbf{i}_2\,\mathbf{r}$) and so this D_3 group is an example of a *non-Abelian* or *non-commutative* group. The technology of group algebra takes a pretty big step with non-commutative operations, but it is not difficult to obtain a fair understanding of non-Abelian algebra like D_3 by using elementary projection operators.

1	r^2	r	i_1	i_2	i_3
r	1	r^2	i_3	i_1	i_2
r^2	r	1	i_2	i_3	i_1
i_1	i_3	i_2	1	r	r^2
i_2	i_1	i_3	r^2	1	r
i_3	i_2	i_1	r	r^2	1
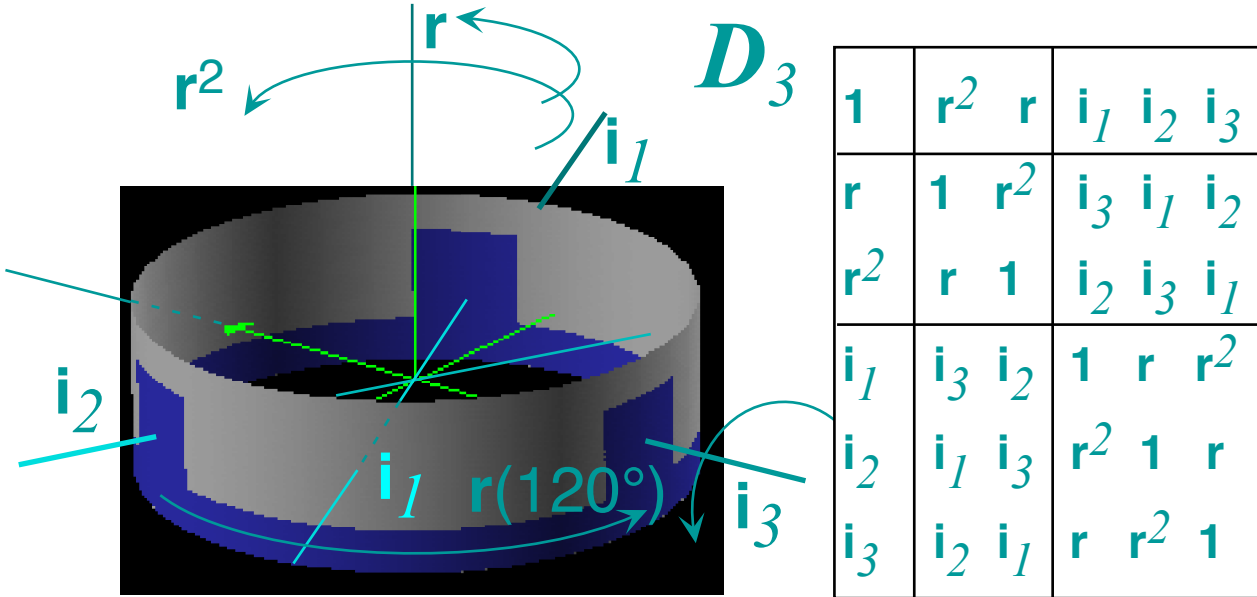
Fig. 15.1.2 D_3 symmetry operations and group multiplication table generated by C^z_3 and C^y_2.

        Non-commutivity of D_3 means we cannot write all six of its operators as the usual spectral decomposition using six commuting idempotents. *Non-Abelian spectral decomposition* takes a more general form which will be described below. One way to understand this general form is to first build a representation of the D_3 operators using the C_3 plane moving-wave bases. We already know the eigenvalues $\varepsilon\pm$ of the $\pm120°$ rotations $\mathbf{r}$ or $\mathbf{r}^2$. These are complex third roots of unity $\varepsilon\pm = e^{\pm2\pi i/3}$ drawn as phasors in the second and third rows of the C_3 table of Fig. 7.3.3 or Fig. 9.4.2. Recall discussion of (9.4.3). A right-moving wave state is labeled $|+1_3\rangle$ while $|-1_3\rangle = |2_3\rangle$ is a left-moving state.

$$D^{E_1}_{\pm1}(\mathbf{r}) = \begin{pmatrix} \langle +1_3|\mathbf{r}|+1_3\rangle & \langle +1_3|\mathbf{r}|-1_3\rangle \\ \langle -1_3|\mathbf{r}|+1_3\rangle & \langle -1_3|\mathbf{r}|-1_3\rangle \end{pmatrix} = \begin{pmatrix} e^{-i2\pi/3} & 0 \\ 0 & e^{+i2\pi/3} \end{pmatrix} = \begin{pmatrix} \varepsilon_- & 0 \\ 0 & \varepsilon_+ \end{pmatrix} = D^{E_1}\!\left(\mathbf{r}^2\right) \qquad (15.1.6)$$

Rotations $\mathbf{r}$ or $\mathbf{r}^2$ are invariant to all rotations around the z-axis. Not so for $180°$ rotations which flip a left-moving wave base $|+1_3\rangle$ into a right-moving base $|-1_3\rangle$ and vice-versa. Let sine and cosine parts have nodes and anti-nodes, respectively, on the x-axis or $\mathbf{i}_3$ axis, that is, let: $\mathbf{i}_3\,|+1_3\rangle = |-1_3\rangle$ and $\mathbf{i}_3\,|-1_3\rangle = |+1_3\rangle$.

$$D^{E_1}_{\pm1}(\mathbf{i}_3) = \begin{pmatrix} \langle +1_3|\mathbf{i}_3|+1_3\rangle & \langle +1_3|\mathbf{i}_3|-1_3\rangle \\ \langle -1_3|\mathbf{i}_3|+1_3\rangle & \langle -1_3|\mathbf{i}_3|-1_3\rangle \end{pmatrix} = \begin{pmatrix} 0 & 1 \\ 1 & 0 \end{pmatrix} \qquad (15.1.7)$$

Then the other $180°$ rotations $\mathbf{i}_1$ and $\mathbf{i}_2$ are represented by $D^E(\mathbf{i}_1)$ and $D^E(\mathbf{i}_2)$ which are matrix products of (15.1.6) and (15.1.7) according to the group table in Fig. 15.1.2.

$$D_{\pm 1}^{E_1}\left(\mathbf{i}_1\right) = D_{\pm 1}^{E_1}\left(\mathbf{i}_3\right) D_{\pm 1}^{E_1}\left(\mathbf{r}\right) = \begin{pmatrix} 0 & 1 \\ 1 & 0 \end{pmatrix} \cdot \begin{pmatrix} \varepsilon_- & 0 \\ 0 & \varepsilon_+ \end{pmatrix} = \begin{pmatrix} 0 & \varepsilon_+ \\ \varepsilon_- & 0 \end{pmatrix}$$

$$D_{\pm 1}^{E_1}\left(\mathbf{i}_2\right) = D_{\pm 1}^{E_1}\left(\mathbf{i}_3\right) D_{\pm 1}^{E_1}\left(\mathbf{r}^2\right) = \begin{pmatrix} 0 & 1 \\ 1 & 0 \end{pmatrix} \cdot \begin{pmatrix} \varepsilon_+ & 0 \\ 0 & \varepsilon_- \end{pmatrix} = \begin{pmatrix} 0 & \varepsilon_- \\ \varepsilon_+ & 0 \end{pmatrix}$$

Collecting these matrices gives what is called an *irreducible representation (irep)* $D_{c_3 d_3}^{E_1}\left(\mathbf{g}\right)$ *of D₃. Irreducible*

means not all the matrices can be diagonalized or reduced at once by a single unitary transformation.

g =	1	r	r²	i₁	i₂	i₃	
$D_{c_3 d_3}^{E_1}\left(\mathbf{g}\right) =$	$\begin{pmatrix} 1 & 0 \\ 0 & 1 \end{pmatrix}$	$\begin{pmatrix} \varepsilon_- & 0 \\ 0 & \varepsilon_+ \end{pmatrix}$	$\begin{pmatrix} \varepsilon_+ & 0 \\ 0 & \varepsilon_- \end{pmatrix}$	$\begin{pmatrix} 0 & \varepsilon_+ \\ \varepsilon_- & 0 \end{pmatrix}$	$\begin{pmatrix} 0 & \varepsilon_- \\ \varepsilon_+ & 0 \end{pmatrix}$	$\begin{pmatrix} 0 & 1 \\ 1 & 0 \end{pmatrix}$	(15.1.8)

For suppose we make a change-of-basis transformation which diagonalizes **i₃**.

$$T \cdot D_{c_3 d_3}^{E_1}\left(\mathbf{i}_3\right) \cdot T^\dagger = \begin{pmatrix} 1/\sqrt{2} & 1/\sqrt{2} \\ i/\sqrt{2} & -i/\sqrt{2} \end{pmatrix} \cdot \begin{pmatrix} 0 & 1 \\ 1 & 0 \end{pmatrix} \begin{pmatrix} 1/\sqrt{2} & -i/\sqrt{2} \\ 1/\sqrt{2} & i/\sqrt{2} \end{pmatrix}$$

$$= \begin{pmatrix} 1 & 0 \\ 0 & -1 \end{pmatrix} \qquad = D_{x_2 y_2}^{E_1}\left(\mathbf{i}_3\right)$$

(15.1.9)

Then that transformation "undiagonalizes" **r** and **r²** to give the resulting *equivalent irep* $D_{x_2 y_2}^{E_1}\left(\mathbf{g}\right)$ of D₃.

g =	1	r	r²	i₁	i₂	i₃
$D_{x_2 y_2}^{E_1}\left(\mathbf{g}\right) =$	$\begin{pmatrix} 1 & 0 \\ 0 & 1 \end{pmatrix}$	$\begin{pmatrix} -1/2 & -\sqrt{3}/2 \\ \sqrt{3}/2 & -1/2 \end{pmatrix}$	$\begin{pmatrix} -1/2 & \sqrt{3}/2 \\ -\sqrt{3}/2 & -1/2 \end{pmatrix}$	$\begin{pmatrix} -1/2 & -\sqrt{3}/2 \\ -\sqrt{3}/2 & 1/2 \end{pmatrix}$	$\begin{pmatrix} -1/2 & \sqrt{3}/2 \\ \sqrt{3}/2 & 1/2 \end{pmatrix}$	$\begin{pmatrix} 1 & 0 \\ 0 & -1 \end{pmatrix}$

(15.1.10)

"Squeezing" one member of a *D*-set has to make another member "unsqueeze" because they cannot all be diagonal or they would fail to satisfy D₃'s non-commuting group table. Transformations $TDT^\dagger$ do not change any group multiplication **gh=k**; if *D(**g**)D(**h**)* = *D(**k**)* holds, then certainly *TD(**g**)T† TD(**h**)T†* = *TD(**k**)T†* holds, too. So, neither *D(g)* set, defined for the whole group, is "compressible" or *reducible*.

The particular $TDT^\dagger$ transformation (15.1.9) is similar to one derived in (10.2.23) between the circular moving wave basis $\{|R\rangle,|L\rangle\}$ and the standing cosine-sine wave or linear polarization basis $\{|x\rangle,|y\rangle\}=\{|c\rangle,|s\rangle\}$. *T* is related to the definition of complex exponentials $e^{\pm i\phi} = cos\,\phi \pm i\,sin\,\phi$, that is: $|\pm I\rangle\sqrt{2} = |c\rangle \pm i\,|s\rangle = |x\rangle \pm i\,|y\rangle$.

$$T = \begin{pmatrix} 1/\sqrt{2} & 1/\sqrt{2} \\ i/\sqrt{2} & -i/\sqrt{2} \end{pmatrix} = \begin{pmatrix} \langle x|+1_3\rangle & \langle x|-1_3\rangle \\ \langle y|+1_3\rangle & \langle y|-1_3\rangle \end{pmatrix} = \begin{pmatrix} \langle x|R\rangle & \langle x|L\rangle \\ \langle y|R\rangle & \langle y|L\rangle \end{pmatrix} = \begin{pmatrix} \langle c|+1\rangle & \langle c|-1\rangle \\ \langle s|+1\rangle & \langle s|-1\rangle \end{pmatrix} \quad (15.1.11)$$

T makes the matrices in (15.1.8) come out real in (15.1.10). This shows a feature of non-Abelian *Dₙ*-groups not present in the commutative *Cₙ*-groups; some *Dₙ*-representations are *multi*-dimensional and *not* uniquely defined; any *U(2)* transformation *T* gives an *equivalent irep* like (15.1.8) or (15.1.10).

Still, a non-commutative group D_3 has commutative *1*-dimensional representations that "cheat" by being *unfaithful*. Consider a one-by-one matrix $D^{A_1}(\mathbf{g})=(1)$ shared by every operator in the group. It is called the *scalar or A_1* representation and is very *un*faithful! It represents each product $\mathbf{gh=k}$ correctly as $D^{A_1}(\mathbf{g})D^{A_1}(\mathbf{h}) = D^{A_1}(\mathbf{k})$ by just doing the same dumb product *(1)(1)=(1)* over and over! Another (not quite so) unfaithful one-by-one representation is called the *pseudo-scalar or A_2* representation. It is listed along with the others in the second line of table (15.1.12) below. We will show how to find all such ireps in an orderly and logical way in the Section 15.2. But for now, let us just study these results. Recall the discussion of S_3 permutations in (3.B.13) of Appendix 3.B. The D_3 rotations are S_3 tricycles *{$\mathbf{r}$=(123), $\mathbf{r}^2$=(132)}* and D_3 flips are S_3 bicycles *{$\mathbf{i}_1$=(23), $\mathbf{i}_2$=(13), $\mathbf{i}_3$= (12)}*. The A_2 representation is permutational parity: (+1) for even permutations and (-1) for the odd ones.

$\mathbf{g} =$	$\mathbf{1}$	$\mathbf{r}$	$\mathbf{r}^2$	$\mathbf{i}_1$	$\mathbf{i}_2$	$\mathbf{i}_3$
$D^{A_1}(\mathbf{g})=$	1	1	1	1	1	1
$D^{A_2}(\mathbf{g})=$	1	1	1	-1	-1	-1
$D^{E_1}_{x_2 y_2}(\mathbf{g})=$	$\begin{pmatrix} 1 & 0 \\ 0 & 1 \end{pmatrix}$	$\begin{pmatrix} -1/2 & -\sqrt{3}/2 \\ \sqrt{3}/2 & -1/2 \end{pmatrix}$	$\begin{pmatrix} -1/2 & \sqrt{3}/2 \\ -\sqrt{3}/2 & -1/2 \end{pmatrix}$	$\begin{pmatrix} -1/2 & -\sqrt{3}/2 \\ -\sqrt{3}/2 & 1/2 \end{pmatrix}$	$\begin{pmatrix} -1/2 & \sqrt{3}/2 \\ \sqrt{3}/2 & 1/2 \end{pmatrix}$	$\begin{pmatrix} 1 & 0 \\ 0 & -1 \end{pmatrix}$

(15.1.12)

(1) D_3 Classes and characters

Group theory books condense *D*-tables like the above into χ-tables of matrix traces or *characters $\chi(\mathbf{g})$ =TraceD(g)* such as the following for D_3. Characters are the same for any equivalent set (15.1.8) or (15.1.10) of 2-by-2 E_1 ireps. This is because *Trace* is invariant to unitary $TDT^\dagger$ transformations.

D_3 *characters* $\mathbf{g} =$	$\mathbf{1}$	$\{\mathbf{r},\mathbf{r}^2\}$	$\{\mathbf{i}_1,\mathbf{i}_2,\mathbf{i}_3\}$
$TraceD^{A_1}(\mathbf{g})= \chi^{A_1}(\mathbf{g})$	1	1	1
$TraceD^{A_2}(\mathbf{g})= \chi^{A_2}(\mathbf{g})$	1	1	-1
$TraceD^{E_1}_{x_2 y_2}(\mathbf{g})= \chi^{E_1}(\mathbf{g})$	2	-1	0

(15.1.13)

Characters are also the same for "look-alike" elements in subsets $\{\mathbf{r}, \mathbf{r}^2\}$ of *120°* rotations or in the subset $\{\mathbf{i}_1, \mathbf{i}_2, \mathbf{i}_3\}$ of *180°* rotations. These subsets are called *classes* of the group D_3, and are collections of operators that are equivalent by <u>internal</u> transformation. For example, examination of Fig. 15.1.2 reveals that the $\mathbf{i}_1$ axis is just a *120°* rotation of the $\mathbf{i}_3$ axis so it must be equivalent through an $\mathbf{r}$ transformation.

$$\mathbf{i}_1 = \mathbf{r}\ \mathbf{i}_3\ \mathbf{r}^{-1} = \mathbf{r}\ \mathbf{i}_3\ \mathbf{r}^2 \qquad\qquad (15.1.14a)$$

(Check by D_3 group table!) Or, $\pm120°$ rotations $\mathbf{r}$ and $\mathbf{r}^2$ must be equivalent by an $\mathbf{i}_3$ transformation

$$\mathbf{r}^2 = \mathbf{i}_3\ \mathbf{r}\ \mathbf{i}_3^{-1} = \mathbf{i}_3\ \mathbf{r}\ \mathbf{i}_3\ , \qquad\qquad (15.1.14b)$$

or by any $\mathbf{i}_m$-operator that flips the *z*-axis. So, $\{\mathbf{r}, \mathbf{r}^2\}$ are in a class by themselves. This concept of class doesn't arise in commutative C_n groups where every operator, like the unit $\mathbf{1}$ here, is a class by itself.

(2) D_3 Regular representation

In Fig. 15.1.2 group table, operators heading column-*n* are inverse to the ones heading row-*n* so it's easy to make *regular representations*. Our first example was for C_6 in equation (8.1.5). A *6-by-6* matrix is made for each operator by replacing its group-table entry by (1) and elsewhere by a (0) or (·). (15.1.15a)

$$R^G(\mathbf{1})= \qquad R^G(\mathbf{r})= \qquad R^G(\mathbf{r}^2)= \qquad R^G(\mathbf{i}_1)= \qquad R^G(\mathbf{i}_2)= \qquad R^G(\mathbf{i}_3)=$$

$$
\begin{array}{c}
\langle 1| \\ \langle \mathbf{r}| \\ \langle \mathbf{r}^2| \\ \langle \mathbf{i}_1| \\ \langle \mathbf{i}_2| \\ \langle \mathbf{i}_3|
\end{array}
\left(\begin{array}{cccccc}
1 & \cdot & \cdot & \cdot & \cdot & \cdot \\
\cdot & 1 & \cdot & \cdot & \cdot & \cdot \\
\cdot & \cdot & 1 & \cdot & \cdot & \cdot \\
\cdot & \cdot & \cdot & 1 & \cdot & \cdot \\
\cdot & \cdot & \cdot & \cdot & 1 & \cdot \\
\cdot & \cdot & \cdot & \cdot & \cdot & 1
\end{array}\right),
\left(\begin{array}{cccccc}
\cdot & \cdot & 1 & \cdot & \cdot & \cdot \\
1 & \cdot & \cdot & \cdot & \cdot & \cdot \\
\cdot & 1 & \cdot & \cdot & \cdot & \cdot \\
\cdot & \cdot & \cdot & \cdot & \cdot & 1 \\
\cdot & \cdot & \cdot & 1 & \cdot & \cdot \\
\cdot & \cdot & \cdot & \cdot & 1 & \cdot
\end{array}\right),
\left(\begin{array}{cccccc}
\cdot & 1 & \cdot & \cdot & \cdot & \cdot \\
\cdot & \cdot & 1 & \cdot & \cdot & \cdot \\
1 & \cdot & \cdot & \cdot & \cdot & \cdot \\
\cdot & \cdot & \cdot & \cdot & 1 & \cdot \\
\cdot & \cdot & \cdot & \cdot & \cdot & 1 \\
\cdot & \cdot & \cdot & 1 & \cdot & \cdot
\end{array}\right),
\left(\begin{array}{cccccc}
\cdot & \cdot & \cdot & 1 & \cdot & \cdot \\
\cdot & \cdot & \cdot & \cdot & \cdot & 1 \\
\cdot & \cdot & \cdot & \cdot & 1 & \cdot \\
1 & \cdot & \cdot & \cdot & \cdot & \cdot \\
\cdot & \cdot & 1 & \cdot & \cdot & \cdot \\
\cdot & 1 & \cdot & \cdot & \cdot & \cdot
\end{array}\right),
\left(\begin{array}{cccccc}
\cdot & \cdot & \cdot & \cdot & 1 & \cdot \\
\cdot & \cdot & \cdot & \cdot & \cdot & 1 \\
\cdot & \cdot & \cdot & 1 & \cdot & \cdot \\
\cdot & \cdot & 1 & \cdot & \cdot & \cdot \\
1 & \cdot & \cdot & \cdot & \cdot & \cdot \\
\cdot & 1 & \cdot & \cdot & \cdot & \cdot
\end{array}\right),
\left(\begin{array}{cccccc}
\cdot & \cdot & \cdot & \cdot & \cdot & 1 \\
\cdot & \cdot & \cdot & 1 & \cdot & \cdot \\
\cdot & \cdot & \cdot & \cdot & 1 & \cdot \\
\cdot & 1 & \cdot & \cdot & \cdot & \cdot \\
\cdot & \cdot & 1 & \cdot & \cdot & \cdot \\
1 & \cdot & \cdot & \cdot & \cdot & \cdot
\end{array}\right)
$$

Regular representations use group-operator-labeled bra-ket bases: $|g\rangle = \mathbf{g}|1\rangle$, and: $\langle h| = \langle 1|\mathbf{h}^\dagger = \langle 1|\mathbf{h}^{-1}$.

$$R^G_{h,f}(\mathbf{g}) = \langle h|\mathbf{g}|f\rangle = \langle 1|\mathbf{h}^\dagger \mathbf{g}\cdot\mathbf{f}|1\rangle = \delta_{h^{-1}gf,1} = \delta_{g,hf^{-1}} = \begin{cases} 1 & \text{if: } \mathbf{g} = \mathbf{h}\cdot\mathbf{f}^{-1} \\ 0 & \text{if: } \mathbf{g} \neq \mathbf{h}\cdot\mathbf{f}^{-1} \end{cases} \qquad (15.1.15b)$$

(3) D₃ Reduction and projectors

The group-based R^G has a lot of empty space filled with zeros and looks like it could be reduced. It cannot be completely diagonalized for reasons already discussed, but it can be reduced or *block-diagonalized* to a combination of the ireps A_1, A_2, and E_1 listed above. To tell which ones we turn to the traces or characters. First, the characters of R^G are as follows. (Again, the logic of this follows, shortly!)

$$
\begin{array}{c|ccc}
\mathbf{g} = & \mathbf{1} & \{\mathbf{r},\mathbf{r}^2\} & \{\mathbf{i}_1,\mathbf{i}_2,\mathbf{i}_3\} \\
\hline
Trace\,R^G(\mathbf{g}) = & 6 & 0 & 0
\end{array}
\qquad (15.1.16)
$$

The following combination of A_1, A_2, and <u>two</u> E_1 characters from (15.1.13) give a needed $\{6, 0, 0\}$ above.

$$
\begin{array}{c|ccc}
\chi^{A_1}(\mathbf{g}) & 1 & 1 & 1 \\
+\chi^{A_2}(\mathbf{g}) & 1 & 1 & -1 \\
+2\chi^{E_1}(\mathbf{g}) & 4 & -2 & 0 \\
\hline
& 6 & 0 & 0
\end{array}
\qquad (15.1.17)
$$

So all six R^G matrices are reducible by some T to *block-diagonal* form with an A_1, A_2, and <u>two</u> E_1 blocks.

$$R^P(\mathbf{g}) = TR^G(\mathbf{g})T^\dagger =
\left(\begin{array}{cc|cc|cc}
D^{A_1}(\mathbf{g}) & \cdot & \cdot & \cdot & \cdot & \cdot \\
\cdot & D^{A_2}(\mathbf{g}) & \cdot & \cdot & \cdot & \cdot \\
\hline
\cdot & \cdot & D^{E_1}_{11}(\mathbf{g}) & D^{E_1}_{12}(\mathbf{g}) & \cdot & \cdot \\
\cdot & \cdot & D^{E_1}_{21}(\mathbf{g}) & D^{E_1}_{22}(\mathbf{g}) & \cdot & \cdot \\
\hline
\cdot & \cdot & \cdot & \cdot & D^{E_1}_{11}(\mathbf{g}) & D^{E_1}_{12}(\mathbf{g}) \\
\cdot & \cdot & \cdot & \cdot & D^{E_1}_{21}(\mathbf{g}) & D^{E_1}_{22}(\mathbf{g})
\end{array}\right)
\qquad (15.1.18)$$

The reduction is done by finding six "placeholder" operators or *generalized projectors* $\mathbf{P}^\mu_{mn}$ having the reduced representations listed below. These matrices are made by simply replacing each of six distinct $D^\mu_{mn}(\mathbf{g})$ components in (15.1.18) by a 1. Each "placeholder" $\mathbf{P}^\mu_{mn}$ is labeled by the $D^\mu_{mn}(\mathbf{g})$ it "re-placed."

$$R^P(P^{A_1})= \quad R^P(P^{A_1})= \quad R^P(P_{11}^{E_1})= \quad R^G(P_{12}^{E_1})= \quad R^G(P_{21}^{E_1})= \quad R^G(P_{22}^{E_1})=$$

$$
\begin{vmatrix}
1 & \cdot & \cdot & \cdot & \cdot & \cdot \\
\cdot & 0 & \cdot & \cdot & \cdot & \cdot \\
\cdot & \cdot & 0 & 0 & \cdot & \cdot \\
\cdot & \cdot & 0 & 0 & \cdot & \cdot \\
\cdot & \cdot & \cdot & \cdot & 0 & 0 \\
\cdot & \cdot & \cdot & \cdot & 0 & 0
\end{vmatrix},\;
\begin{vmatrix}
0 & \cdot & \cdot & \cdot & \cdot & \cdot \\
\cdot & 1 & \cdot & \cdot & \cdot & \cdot \\
\cdot & \cdot & 0 & 0 & \cdot & \cdot \\
\cdot & \cdot & 0 & 0 & \cdot & \cdot \\
\cdot & \cdot & \cdot & \cdot & 0 & 0 \\
\cdot & \cdot & \cdot & \cdot & 0 & 0
\end{vmatrix},\;
\begin{vmatrix}
0 & \cdot & \cdot & \cdot & \cdot & \cdot \\
\cdot & 0 & \cdot & \cdot & \cdot & \cdot \\
\cdot & \cdot & 1 & 0 & \cdot & \cdot \\
\cdot & \cdot & 0 & 0 & \cdot & \cdot \\
\cdot & \cdot & \cdot & \cdot & 1 & 0 \\
\cdot & \cdot & \cdot & \cdot & 0 & 0
\end{vmatrix},\;
\begin{vmatrix}
0 & \cdot & \cdot & \cdot & \cdot & \cdot \\
\cdot & 0 & \cdot & \cdot & \cdot & \cdot \\
\cdot & \cdot & 0 & 1 & \cdot & \cdot \\
\cdot & \cdot & 0 & 0 & \cdot & \cdot \\
\cdot & \cdot & \cdot & \cdot & 0 & 1 \\
\cdot & \cdot & \cdot & \cdot & 0 & 0
\end{vmatrix},\;
\begin{vmatrix}
0 & \cdot & \cdot & \cdot & \cdot & \cdot \\
\cdot & 0 & \cdot & \cdot & \cdot & \cdot \\
\cdot & \cdot & 0 & 0 & \cdot & \cdot \\
\cdot & \cdot & 1 & 0 & \cdot & \cdot \\
\cdot & \cdot & \cdot & \cdot & 0 & 0 \\
\cdot & \cdot & \cdot & \cdot & 1 & 0
\end{vmatrix},\;
\begin{vmatrix}
0 & \cdot & \cdot & \cdot & \cdot & \cdot \\
\cdot & 0 & \cdot & \cdot & \cdot & \cdot \\
\cdot & \cdot & 0 & 0 & \cdot & \cdot \\
\cdot & \cdot & 0 & 1 & \cdot & \cdot \\
\cdot & \cdot & \cdot & \cdot & 0 & 0 \\
\cdot & \cdot & \cdot & \cdot & 0 & 1
\end{vmatrix}
$$

$$(15.1.19a)$$

Multiplication rules for "place-holders" are more elementary than the group itself as can be seen by doing matrix products of the blocks in (15.1.19a). For example, $\mathbf{P}_{12}\mathbf{P}_{22} = \mathbf{P}_{12}$ and $\mathbf{P}_{12}\mathbf{P}_{12} = \mathbf{0}$ follow easily.

$$
\begin{pmatrix} 0 & 1 \\ 0 & 0 \end{pmatrix}\cdot\begin{pmatrix} 0 & 0 \\ 0 & 1 \end{pmatrix}=\begin{pmatrix} 0 & 1 \\ 0 & 0 \end{pmatrix},\quad
\begin{pmatrix} 0 & 1 \\ 0 & 0 \end{pmatrix}\cdot\begin{pmatrix} 0 & 0 \\ 1 & 0 \end{pmatrix}=\begin{pmatrix} 1 & 0 \\ 0 & 0 \end{pmatrix},\quad
\begin{pmatrix} 0 & 1 \\ 0 & 0 \end{pmatrix}\cdot\begin{pmatrix} 0 & 1 \\ 0 & 0 \end{pmatrix}=\begin{pmatrix} 0 & 0 \\ 0 & 0 \end{pmatrix}.
$$
$$(15.1.19b)$$
$$\mathbf{P}_{12}^{E_1}\cdot\mathbf{P}_{22}^{E_1}=\mathbf{P}_{12}^{E_1}\;,\qquad \mathbf{P}_{12}^{E_1}\cdot\mathbf{P}_{21}^{E_1}=\mathbf{P}_{11}^{E_1}(Idempotent),\qquad \mathbf{P}_{12}^{E_1}\cdot\mathbf{P}_{12}^{E_1}=\mathbf{0}\;(Nilpotent)$$

A product $\mathbf{P}_{jk}^{\mu}\mathbf{P}_{mn}^{\nu}$ is zero unless it has equal superscripts ($\mu=\nu$) <u>and</u> the middle subscripts ($k=n$). Then it is just the operator $\mathbf{P}_{jn}^{\mu}$ made out of whatever is left. It's a lot simpler than the original group table!

(4) D_3 Spectral decomposition: The Wigner-Weyl formula

     All six group operators $\mathbf{g}$ expand into six *elementary projection operators* $\mathbf{P}^{\mu}{}_{mn}$ by (15.1.18-19).

$$\mathbf{g}=\sum_{\mu}\sum_{m}\sum_{n}D_{mn}^{\mu}(g)\,\mathbf{P}_{mn}^{\mu}=D^{A_1}(g)\mathbf{P}^{A_1}+D^{A_2}(g)\mathbf{P}^{A_2}+D_{11}^{E_1}(g)\mathbf{P}_{11}^{E_1}+D_{12}^{E_1}(g)\mathbf{P}_{12}^{E_1}$$
$$+D_{21}^{E_1}(g)\mathbf{P}_{21}^{E_1}+D_{22}^{E_1}(g)\mathbf{P}_{22}^{E_1}$$
$$(15.1.20a)$$

This is the form of a *generalized non-commutative spectral decomposition* of an entire <u>non</u>-Abelian group. D_3's decomposition differs from the commutative C_6 in (8.2.4a). D_3 has two *nilpotent* projectors $\mathbf{P}^E{}_{12}$ and $\mathbf{P}^E{}_{12}$ along with four ordinary (*idempotent*) projectors $\mathbf{P}^{A_1}$, $\mathbf{P}^{A_2}$, $\mathbf{P}^E{}_{11}$, and $\mathbf{P}^E{}_{22}$. As we will see, other non-commutative groups and algebras have various numbers of these two kinds of $\mathbf{P}$'s.

     Nilpotent projectors are necessary to expand operators that do not commute. Commutative groups can be reduced to orthogonal idempotents that satisfy simple orthogonality relations given in Ch. 3.

$$\mathbf{P}_i\,\mathbf{P}_j=\delta_{ij}\,\mathbf{P}_i=\mathbf{P}_j\,\mathbf{P}_i\,.\qquad (3.1.15c)_{repeated}$$

(15.1.19) replaces this by a *generalized projector orthonormality relation* for non-commutative projectors.

$$\mathbf{P}_{jk}^{\mu}\mathbf{P}_{mn}^{\nu}=\delta^{\mu\nu}\delta_{km}\mathbf{P}_{jn}^{\mu}\qquad (15.1.20b)$$

For D_3 the following *projector multiplication table* is like a "skeleton" of the group table in Fig. 15.1.2.

	$\mathbf{P}^{A_1}$	$\mathbf{P}^{A_2}$	$\mathbf{P}_{11}^{E_1}$	$\mathbf{P}_{12}^{E_1}$	$\mathbf{P}_{21}^{E_1}$	$\mathbf{P}_{22}^{E_1}$
$\mathbf{P}^{A_1}$	$\mathbf{P}^{A_1}$	.	.	.	.	.
$\mathbf{P}^{A_2}$	.	$\mathbf{P}^{A_2}$	.	.	.	.
$\mathbf{P}_{11}^{E_1}$	.	.	$\mathbf{P}_{11}^{E_1}$	$\mathbf{P}_{12}^{E_1}$	.	.
$\mathbf{P}_{21}^{E_1}$	.	.	$\mathbf{P}_{21}^{E_1}$	$\mathbf{P}_{22}^{E_1}$	.	.
$\mathbf{P}_{12}^{E_1}$	.	.	.	.	$\mathbf{P}_{11}^{E_1}$	$\mathbf{P}_{12}^{E_1}$
$\mathbf{P}_{22}^{E_1}$	.	.	.	.	$\mathbf{P}_{21}^{E_1}$	$\mathbf{P}_{22}^{E_1}$

$$(15.1.20c)$$

To obtain generalized projectors the decomposition (15.1.20a) must be inverted. The result which will be proved below is the famous *Wigner-Weyl projection formula*

$$\mathbf{P}^\mu_{mn} = \frac{\ell^\mu}{{}^o G}\sum_g D^{\mu\,*}_{mn}(g)\,\mathbf{g} \qquad\qquad (15.1.20d)$$

where ${}^o G = 6$ is the order of the group and ℓ^μ is the μ-irep dimension. ($\ell^{A_1} = 1 = \ell^{A_2}$, and $\ell^{E_1} = 2$.) Again, these numbers vary from group to group. For Abelian groups irep dimension is <u>always</u> one ($\ell^\mu = 1$).

(5) Right-and-Left Transformation rules

The spectral decomposition (15.1.20a) is the single most important relation in symmetry analysis of quantum mechanics. Its first use is to define *left and right transformation* of projectors obtained by applying spectrally decomposed $\mathbf{g}$ from (15.1.20a) on the left and right side of a projector $\mathbf{P}^\mu_{mn}$.

$$\mathbf{g}\mathbf{P}^\mu_{mn} = \sum_{\mu'}\sum_{m'}\sum_{n'} D^{\mu'}_{m'n'}(g)\,\mathbf{P}^{\mu'}_{m'n'}\mathbf{P}^\mu_{mn} \qquad\qquad \mathbf{P}^\mu_{mn}\mathbf{g} = \sum_{\mu'}\sum_{m'}\sum_{n'} D^{\mu'}_{m'n'}(g)\,\mathbf{P}^\mu_{mn}\mathbf{P}^{\mu'}_{m'n'}$$

$$= \sum_{\mu'}\sum_{m'}\sum_{n'} D^{\mu'}_{m'n'}(g)\,\delta^{\mu'\mu}\delta_{n'm}\mathbf{P}^\mu_{m'n} \qquad\qquad = \sum_{\mu'}\sum_{m'}\sum_{n'} D^{\mu'}_{m'n'}(g)\,\delta^{\mu'\mu}\delta_{nm'}\mathbf{P}^\mu_{mn'}$$

$$= \sum_{m'} D^\mu_{m'm}(g)\,\mathbf{P}^\mu_{m'n} \qquad\qquad\qquad = \sum_{n'} D^\mu_{nn'}(g)\,\mathbf{P}^\mu_{mn'}$$

$$(15.1.21a) \qquad\qquad\qquad\qquad\qquad\qquad (15.1.21b)$$

The preceding relations become more familiar if expressed using projected bra-kets that are made like the group operator bra-kets for the group regular representation R^G in (15.1.15). Here the projector representation R^P based on $\mathbf{P}$-multiplication table (15.1.20c) has its basis defined similarly. (Note: † only flips indices of elementary ket-bras, that is, $|m\rangle\langle n|^\dagger = |n\rangle\langle m|$. $\mathbf{P}$-operators do the same: $\mathbf{P}_{mn}{}^\dagger = \mathbf{P}_{nm}$.)

$$\left|\mathbf{P}^\mu_{mn}\right\rangle = \mathbf{P}^\mu_{mn}|1\rangle/\sqrt{norm}, \qquad \left\langle\mathbf{P}^\mu_{mn}\right| = \langle 1|\mathbf{P}^{\mu\,\dagger}_{mn}/\sqrt{norm} = \langle 1|\mathbf{P}^\mu_{nm}/\sqrt{norm} \qquad (15.1.22)$$

So the bra-ket $\mathbf{g}$-matrix elements are the ireps $D(g)$ themselves, just where this all started in (15.1.18).

$$\left\langle\mathbf{P}^\mu_{m''n''}\right|\mathbf{g}\left|\mathbf{P}^\mu_{mn}\right\rangle = \langle 1|\mathbf{P}^\mu_{n''m''}\mathbf{g}\mathbf{P}^\mu_{mn}|1\rangle/norm = \sum_{m'} D^\mu_{m'm}(g)\langle 1|\mathbf{P}^\mu_{n''m''}\,\mathbf{P}^\mu_{m'n}|1\rangle/norm$$

$$(15.1.23)$$

$$= D^\mu_{m''m}(g)\langle 1|\mathbf{P}^\mu_{n''n}|1\rangle/norm = D^\mu_{m''m}(g)\delta_{n''n}, \text{ where: } (norm) = \frac{\ell^\mu}{{}^o G}$$

Projection norm is the diagonal element $\langle 1|\mathbf{P}|1\rangle$ if $\mathbf{PP}=\mathbf{P}$ is idempotent and is the coefficient $(\ell^\mu/{}^oG)D(g)$ in (15.1.20d) of unit $\mathbf{g}=1$. Now we derive the $\mathbf{P}$ coefficients $p^\mu_{mn}(g)$ of general $\mathbf{g}$ in the Weyl expansion

$$\mathbf{P}^\mu_{mn} = \sum_g p^\mu_{mn}(g)\,\mathbf{g} \qquad\qquad . \qquad\qquad (15.1.24)$$

This begins by multiplying $\mathbf{P}$ by any operator $\mathbf{f}$ in the group as in (15.1.21a)

$$\mathbf{f}\cdot\mathbf{P}^\mu_{mn} = \sum_g p^\mu_{mn}(g)\,\mathbf{f}\mathbf{g} = \sum_h p^\mu_{mn}(\mathbf{f}^{-1}\mathbf{h})\,\mathbf{h} \text{ , where: } \mathbf{h} = \mathbf{fg}, \text{ or: } \mathbf{g} = \mathbf{f}^{-1}\mathbf{h}, \qquad (15.1.25)$$

Regular representation *TraceR(**h**)* is zero except for *TraceR(**1**)*, which is group-order ${}^o G$ by (15.1.15b).

$$TraceR\left(\mathbf{f}\cdot\mathbf{P}^\mu_{mn}\right) = \sum_h p^\mu_{mn}\left(\mathbf{f}^{-1}\mathbf{h}\right)TraceR\left(\mathbf{h}\right) = p^\mu_{mn}\left(\mathbf{f}^{-1}\mathbf{1}\right)TraceR\left(\mathbf{1}\right) = p^\mu_{mn}\left(\mathbf{f}^{-1}\right){}^o G$$

Using (15.1.20a) and *TraceR($\mathbf{P}^\mu_{nm}$)*$=\delta_{nm}\ell^\mu$ from (15.1.19a), proves the Weyl expansion (15.1.20d).

$$p_{mn}^{\mu}\left(\mathbf{f}\right)=\frac{1}{{}^{o}G}TraceR\left(\mathbf{f}^{-1}\cdot\mathbf{P}_{mn}^{\mu}\right)=\frac{1}{{}^{o}G}\sum_{m'}D_{m'm}^{\mu}\left(\mathbf{f}^{-1}\right)TraceR\left(\mathbf{P}_{m'n}^{\mu}\right)$$

$$=\frac{\ell^{\mu}}{{}^{o}G}D_{nm}^{\mu}\left(\mathbf{f}^{-1}\right)=\frac{\ell^{\mu}}{{}^{o}G}D_{mn}^{\mu*}\left(\mathbf{f}\right)\qquad(QED)$$

(15.1.26)

(5) D-Orthonormality

The ortho-completeness of C_n representations has been noted as being the same as that of Fourier plane waves. That is a special case of a more general result that applies to all ireps of groups and algebras. Indeed, it is a grand re-statement of *Axioms 1-4* in Chapter 2. Replacing a **g**-operator by a **P**-operator in (15.1.20a) is legal since it is valid for all **g** and all linear combinations of **g**'s including the **P**'s.

$$\mathbf{P}_{m'n'}^{\mu'}=\sum_{\mu}\sum_{m}\sum_{n}D_{mn}^{\mu}\left(\mathbf{P}_{m'n'}^{\mu'}\right)\mathbf{P}_{mn}^{\mu}$$

(15.1.27)

This implies that a D_{ab}^{ν} of a $\mathbf{P}_{mn}^{\mu}$ is all zeros except for a single one at $a=m$ and $b=n$ as seen in (15.1.19).

$$D_{mn}^{\mu}\left(\mathbf{P}_{m'n'}^{\mu'}\right)=\delta^{\mu\mu'}\delta_{mm'}\delta_{nn'}$$

(15.1.28)

Inserting the Wigner-Weyl expansion for **P**'s gives.

$$D_{mn}^{\mu}\left(\frac{\ell^{\mu'}}{{}^{o}G}\sum_{\mathbf{g}}D_{m'n'}^{\mu'*}\left(g\right)\mathbf{g}\right)=\delta^{\mu\mu'}\delta_{mm'}\delta_{nn'}$$

(15.1.29)

Using the linearity of the D-functions ($D(g+h) = D(g)+D(h)$) gives the *grand D-orthonormality relation*.

$$\sum_{\mathbf{g}}D_{mn}^{\mu}\left(g\right)D_{m'n'}^{\mu'*}\left(g\right)=\frac{{}^{o}G}{\ell^{\mu'}}\delta^{\mu\mu'}\delta_{mm'}\delta_{nn'}$$

(15.1.30)

There is a completeness relation to go with this, but that will be left as an exercise to derive.

Orthogonality and completeness are two sides of the same coin, and it means that *one* set of ireps is all that is needed to make any representation of this group or algebra, provided the ireps are a complete set. All representations, however huge, must be reducible to a block diagonal combonation of ireps.

For the Abelian symmetries these statements are quite obvious results of Fourier orthogonality and completeness, that is, axioms 1-4 applied to the discrete plane wave eigenfunctions $e^{ik_m x_p}$. At the end of Section 7.2 we noted the multiple mathematical roles which Fourier kernals e^{ikx} play. Add to this the role that Bloch-wave phase plays in (8.2.10) in Chapter 8 and the role the complex conjugates $e^{-ik_m x_p}$ play as irreducible representation (9.4.3) in Chapter 9.

$$D^{k_m*}\left(\mathbf{r}^p\right)=e^{-ik_m x_p}$$

However, group ireps most useful roles may be as *wavefunctions*. This applies particularly to the non-Abelian ireps $D^{\mu*}{}_{mn}$ whose role as wavefunctions is not (yet) quite so famous. But, it will be!

Throughout the rest of this book there are many examples of theoretical insight and computational power provided by ireps in their role as eigensolutions with ready-made completenss, orthonormality, and matrix element formulas. Solutions to differential equations like Schrodinger's may take anywhere from minutes to centuries to basis-organize and compute necessary Hamiltonian or transition matrices in their bases. In contrast, doing this job using ireps $D^{\mu*}{}_{mn}$ is a breeze. The catch, of course, is understanding what the ireps $D^{\mu*}{}_{mn}$ mean and how they are made and applied. That is the purpose of the rest of this Chapter!

15.2 Commuting Observable Sets: Character analysis

The techniques introduced in the preceding section for dealing with non-commuting algebras are quite a bit more complicated than the treatment of commuting groups given earlier. Here we see how the simpler techniques of commuting algebra can be used for the more general quantum symmetry problems. The key is to find the largest number of mutually commuting operators or what is known as a *maximal set of commuting observables (MSOCO)*. Then the simultaneous spectral decomposition of a *MSCO* yields many useful results which provide "shortcut" solutions and diagnostics.

(a) Class algebra and all-commuting operators

While the D_3 group table is non-commutative an algebra based on the class boundaries is always commutative. We're referring here to the following construction based on *class sums c_g*.

$$
\begin{array}{|c|cc|ccc|}
\hline
1 & r^2 & r & i_1 & i_2 & i_3 \\
\hline
r & 1 & r^2 & i_3 & i_1 & i_2 \\
r^2 & r & 1 & i_2 & i_3 & i_1 \\
\hline
i_1 & i_3 & i_2 & 1 & r & r^2 \\
i_2 & i_1 & i_3 & r^2 & 1 & r \\
i_3 & i_2 & i_1 & r & r^2 & 1 \\
\hline
\end{array}
\rightarrow
\begin{array}{|c|c|c|c|}
\hline
 & c_1 = 1 & c_r = r+r^2 & c_i = i_1 + i_2 + i_3 \\
\hline
c_1 & c_1 & c_r & c_i \\
c_r & c_r & 2c_1 + c_r & 2c_i \\
c_i & c_i & 2c_i & 3c_1 + 3c_r \\
\hline
\end{array}
\qquad (15.2.1)
$$

The resulting multiplication table is not that of a group but rather what is loosely called an *algebra*. But, it is a commutative algebra and thus fair game for a complete spectral decomposition into idempotents.

Each class-sum commutes not only with each other but also with every operator in the entire group algebra. In other words the c_g's are *mutually commuting* with respect to themselves and *all-commuting* with respect to the whole group. To show this, do an **h**-**h**$^{-1}$ transformation on a class-sum c_g and observe that it is unaffected (except by reordering its sum which is inconsequential.) For example, doing **r** on c_i gives c_i back.

$$\mathbf{r}\, \mathbf{c}_i\, \mathbf{r}^{-1} = \mathbf{i}_2 + \mathbf{i}_3 + \mathbf{i}_1 = \mathbf{c}_i \quad \text{or:} \quad \mathbf{r}\, \mathbf{c}_i = \mathbf{c}_i\, \mathbf{r} \qquad (15.2.2a)$$

This shows **r** commutes with c_i. But, it is actually stronger than this. The sum over all group operator transformations of any one element **g** is an integral number υ of its class sums c_g, that is,

$$\sum_{\mathbf{h}=1}^{\circ G} \mathbf{hgh}^{-1} = \upsilon_g \mathbf{c}_g \,, \qquad \text{where: } \upsilon_g = \frac{\circ G}{\circ \mathbf{c}_g} = integer \qquad (15.2.2b)$$

The notation $\circ c_g$ is the order of class c_g, that is its population. It must evenly divide the group order $\circ G$.

Now we turn this around to show that an *all-commuting operator* $\mathbb{C} = \Sigma C_g \mathbf{g}$ that is, one that commutes with all **h** in the group, is a combination of class-sums c_g. All-commutation ($\mathbb{C}\, \mathbf{h} = \mathbf{h}\, \mathbb{C}$) implies

$$\mathbb{C} = \sum_{\mathbf{g}=1}^{\circ G} C_g \mathbf{g} = \frac{1}{\circ G} \sum_{\mathbf{h}=1}^{\circ G} \mathbf{h} \left(\sum_{\mathbf{g}=1}^{\circ G} C_g \mathbf{g} \right) \mathbf{h}^{-1} = \sum_{g=1}^{\circ G} C_g \upsilon_g \mathbf{c}_g \,. \qquad (15.2.2c)$$

(b) Characters and all-commuting projectors

The irrep characters are defined as follows according to their trace definition in (15.1.13).

$$\chi^{\mu}\left(\mathbf{g}\right) = Trace\ D^{\mu}\left(\mathbf{g}\right) = \sum_{m=1}^{\ell^{\mu}} D_{mm}^{\mu}\left(\mathbf{g}\right) \tag{15.2.3}$$

Using this definition in the Wigner-Weyl expansion formula (15.1.20d) gives the following operator.

$$\mathbb{P}^{\mu} = \sum_{m=1}^{\ell^{\mu}} \mathbf{P}_{mm}^{\mu} = \frac{\ell^{\mu}}{{}^{o}G}\sum_{\mathbf{g}}\sum_{m=1}^{\ell^{\mu}} D_{mm}^{\mu*}\left(\mathbf{g}\right)\mathbf{g} = \frac{\ell^{\mu}}{{}^{o}G}\sum_{\mathbf{g}}\chi^{\mu*}\left(\mathbf{g}\right)\mathbf{g} \tag{15.2.4}$$

The $\mathbb{P}^{\mu}$ is a combination of class-sums and is called the (μ)-th *all-commuting idempotent* $\mathbb{P}^{\mu}$ or *class projector*.

$$\mathbb{P}^{\mu} = \sum_{classes\,c_{g}} \frac{\ell^{\mu}\chi_{g}^{\mu*}}{{}^{o}G}\,\mathbf{c}_{g}\ ,\ \ where:\ \chi_{g}^{\mu} = \chi^{\mu}\left(\mathbf{g}\right) = \chi^{\mu}\left(\mathbf{hgh}^{-1}\right) \tag{15.2.5a}$$

Class invariance of χ^{μ} is used. The spectral decomposition (15.1.20a) helps to invert this to the following.

$$\mathbf{c}_{g} = \sum_{ireps\,\mu} \frac{{}^{o}c_{g}\chi_{g}^{\mu}}{\ell^{\mu}}\ \mathbb{P}^{\mu} \tag{15.2.5b}$$

To prove the last result one needs the irrep $D_{kq}^{\mu}\left(\mathbf{c}_{g}\right)$ of a class-sum. Such a matrix must be all-commuting, in particular, it must commute with all projectors, a tough requirement since $D_{mn}^{\mu}\left(\mathbf{P}_{qr}\right)$ is all zeros except for a single (1) at row-q and column-r.

$$D^{\mu}\left(\mathbf{c}_{g}\right)D^{\mu}\left(\mathbf{P}_{qr}\right) = \sum_{m=1}^{\ell^{\mu}} D_{km}^{\mu}\left(\mathbf{c}_{g}\right)D_{mn}^{\mu}\left(\mathbf{P}_{qr}\right) = \sum_{\ell=1}^{\ell^{\mu}} D_{k\ell}^{\mu}\left(\mathbf{P}_{qr}\right)D_{\ell n}^{\mu}\left(\mathbf{c}_{g}\right) = D^{\mu}\left(\mathbf{P}_{qr}\right)D^{\mu}\left(\mathbf{c}_{g}\right) \tag{15.2.6}$$

The tough requirement is (15.1.28) and it reduces the all-commuting matrix to a multiple of a unit matrix.

$$\sum_{m=1}^{\ell^{\mu}} D_{km}^{\mu}\left(\mathbf{c}_{g}\right)\delta_{mq}\delta_{nr} = \sum_{\ell=1}^{\ell^{\mu}} \delta_{kq}\delta_{\ell r}D_{\ell n}^{\mu}\left(\mathbf{c}_{g}\right)\ \text{implies:}\ D_{kq}^{\mu}\left(\mathbf{c}_{g}\right) = \delta_{kq}D_{rr}^{\mu}\left(\mathbf{c}_{g}\right)\ \ \left\{k,r = 1...\ell^{m}\right\} \tag{15.2.7a}$$

Trace $D^{\mu}\left(\mathbf{c}_{g}\right)$ is the class order ${}^{o}c_{g}$ times the character χ_{g}^{μ}. That divided by irrep dimension ℓ^{μ} gives

$$D_{kq}^{\mu}\left(\mathbf{c}_{g}\right) = \delta_{kq}\frac{{}^{o}c_{g}\chi_{g}^{\mu}}{\ell^{\mu}}\ . \tag{15.2.7b}$$

Inserting this into the Weyl expansion (15.1.20d) proves (15.2.5b). Unit matrix form is what you get for any irreducible representation of an all-commuting operator $\mathbb{O}$: $D^{\mu}(\mathbb{O})$ must be a multiple of a unit matrix. This is one of *Schur's lemmas*, and is the basis of a well-known old-fashioned approach to group theory.

(c) Computing characters and dimensions

Minimal equations of class-sum operators lead directly to the coefficients of $\mathbb{P}^{\mu}$-$\mathbf{c}_{g}$ relations (15.2.5) and from there to the irep characters χ_{g}^{μ} and dimensions ℓ^{μ}. For example, the class multiplication table (15.2.1) yields the following minimal equations. The roots are eigenvalues (15.2.7) of class sums.

$$\mathbf{c}_{r}^{2} - \mathbf{c}_{r} - 2\,\mathbf{1} = 0 = (\,\mathbf{c}_{r} - 2\,\mathbf{1})(\,\mathbf{c}_{r} + \mathbf{1})\ ,\ \ \ \ \ \ \ \ \ \ \mathbf{c}_{i}^{3} - 9\,\mathbf{c}_{i} = 0 = (\,\mathbf{c}_{i} - 3\,\mathbf{1})(\,\mathbf{c}_{i} + 3\,\mathbf{1})(\,\mathbf{c}_{i} + 0\,\mathbf{1}) \tag{15.2.8}$$

Spectral decomposition follows using the projection formula (3.1.15) from Chapter 3.

$$\mathbb{P}^{\mu} = \frac{\prod\limits_{\varepsilon\neq\mu}\left(\mathbf{c}_{i} - c_{\varepsilon}\mathbf{1}\right)}{\prod\limits_{\varepsilon\neq\mu}\left(c_{\mu} - c_{\varepsilon}\right)} \tag{15.2.9}$$

Three orthogonal projectors arise as examples of (15.2.5a). The $\mathbf{c}_{g}$-coefficient in $\mathbb{P}^{\mu}$ is $\dfrac{\ell^{\mu}\chi_{g}^{\mu*}}{{}^{\circ}G} = \dfrac{\ell^{\mu}\chi_{g}^{\mu*}}{6}$.

$$\mathbb{P}^1 = \frac{(\mathbf{c}_i + 3\mathbf{1})(\mathbf{c}_i - 0\mathbf{1})}{(3+3)(3-0)} = \frac{\mathbf{c}_i^2 + 3\mathbf{c}_i}{18} = \frac{1}{6}\mathbf{c}_1 + \frac{1}{6}\mathbf{c}_r + \frac{1}{6}\mathbf{c}_i = \frac{1}{6}\left(\mathbf{1} + \mathbf{r} + \mathbf{r}^2 + \mathbf{i}_1 + \mathbf{i}_2 + \mathbf{i}_3\right) \quad (15.2.10a)$$

$$\mathbb{P}^2 = \frac{(\mathbf{c}_i - 3\mathbf{1})(\mathbf{c}_i - 0\mathbf{1})}{(-3-3)(-3-0)} = \frac{\mathbf{c}_i^2 - 3\mathbf{c}_i}{18} = \frac{1}{6}\mathbf{c}_1 + \frac{1}{6}\mathbf{c}_r - \frac{1}{6}\mathbf{c}_i = \frac{1}{6}\left(\mathbf{1} + \mathbf{r} + \mathbf{r}^2 - \mathbf{i}_1 - \mathbf{i}_2 - \mathbf{i}_3\right) \quad (15.2.10b)$$

$$\mathbb{P}^3 = \frac{(\mathbf{c}_i + 3\mathbf{1})(\mathbf{c}_i - 3\mathbf{1})}{(0+3)(0-3)} = \frac{\mathbf{c}_i^2 - 9\mathbf{1}}{18} = \frac{2}{3}\mathbf{c}_1 - \frac{1}{3}\mathbf{c}_r \qquad = \frac{1}{3}\left(2\mathbf{1} - \mathbf{r} - \mathbf{r}^2\right) \qquad\qquad (15.2.10c)$$

The inverse relations (15.2.5b) are easily obtained directly from the roots (15.2.8) themselves.

$$\mathbf{c}_1 = \quad \mathbb{P}^1 + \quad \mathbb{P}^2 + \mathbb{P}^3 \qquad\qquad\qquad\qquad (15.2.10d)$$

$$\mathbf{c}_r = 2\,\mathbb{P}^1 + 2\,\mathbb{P}^2 - \mathbb{P}^3 \qquad\qquad\qquad\qquad (15.2.10e)$$

$$\mathbf{c}_i = 3\,\mathbb{P}^1 - 3\,\mathbb{P}^2 \qquad\qquad\qquad\qquad\qquad (15.2.10f)$$

Here the $\mathbb{P}^\mu$ coefficient in $\mathbf{c}_g$ is $\dfrac{{}^o c_g \chi_g^\mu}{\ell^\mu}$. If group order ${}^\circ G$ and class-orders ${}^\circ c_g$ are known then the coefficients can

be identified. The problem is that we still don't know either character $\chi^\mu{}_g$ or dimension ℓ^μ, and they seem intertwined in (15.2.5). However, for the unit class $\mathbf{g}=\mathbf{1}$, the character $\underline{is}$ the dimension so

$$\chi^\mu{}_1 = \ell^\mu = \sqrt{{}^\circ G \frac{\ell^\mu \chi_1^{\mu*}}{{}^\circ G}} = \sqrt{{}^\circ G\left(\mathbf{c}_1\ coefficient\ in\ \mathbf{P}^\mu\right)} = \sqrt{\left(\ell^\mu\right)^2} \qquad (15.2.10g)$$

For D_3 this gives $\ell^1 = \ell^{A_1} = 1$, $\ell^2 = \ell^{A_2} = 1$, $\ell^3 = \ell^{E_1} = 2$. The other characters in (15.1.13) follow from (15.2.10 a-c) or (15.2.10d-f). Since $\ell^{E_1} = 2$ we know $\mathbb{P}^{E_1}$ must "split" in two as in (15.2.11) below.

(d) Maximal sets of commuting operators (MSOCO): Rank

Which are the independent operators in D_3 that can be diagonalized at once? The answer is not unique since many sets of operators vie to be in a distinguished set called a *Maximal Set of Commuting Operators or Observables (MSOCO)*. However, the number of operators is unique and is called the *rank* of the D_3 algebra. The rank of D_3 turns out to be four.

A set diagram of D_3 is shown in Fig. 15.2.1. It shows the class-sum algebra of all-commuting operators at the center of the diagram. Indeed, the all-commuting algebra is called the *Center* of the algebra. Its dimension determines the number of *orthogonal irreducible representations (ireps)* of the algebra. Here that is three corresponding to the ireps A_1, A_2, and E_1 described previously. The three all-commuting projectors $\mathbb{P}^1 = \mathbb{P}^{A_1}$, $\mathbb{P}^2 = \mathbb{P}^{A_2}$, and $\mathbb{P}^3 = \mathbb{P}^{E_1}$ of the center are uniquely defined; no others exist. Clearly they must be part of the *MSOCO*. You might call them "permanent members" of the *MSOCO*. But, there must be another member, too, since the rank of D_3 is four.

The remaining "temporary" member of the rank-4 *MSOCO* is not uniquely chosen; many possible choices exist. One common choice is the operator $\mathbf{i}_3$ picked out in Fig. 15.2.1. By choosing this operator to be diagonal we select a particular way to "split" the $\mathbb{P}^3 = \mathbb{P}^{E_1}$ idempotent and build a particular set of E-ireps given before in table (15.1.10). If instead we choose to diagonalize $\mathbf{r}$, then a different set of ireps given before in table (15.1.8)

will be made. Note that in either case there are only four members of the *MSOCO*. In the second case, r^2 comes with **r** since the class sum $c_r = r + r^2$ is already a permanent member of *MSOCO*.
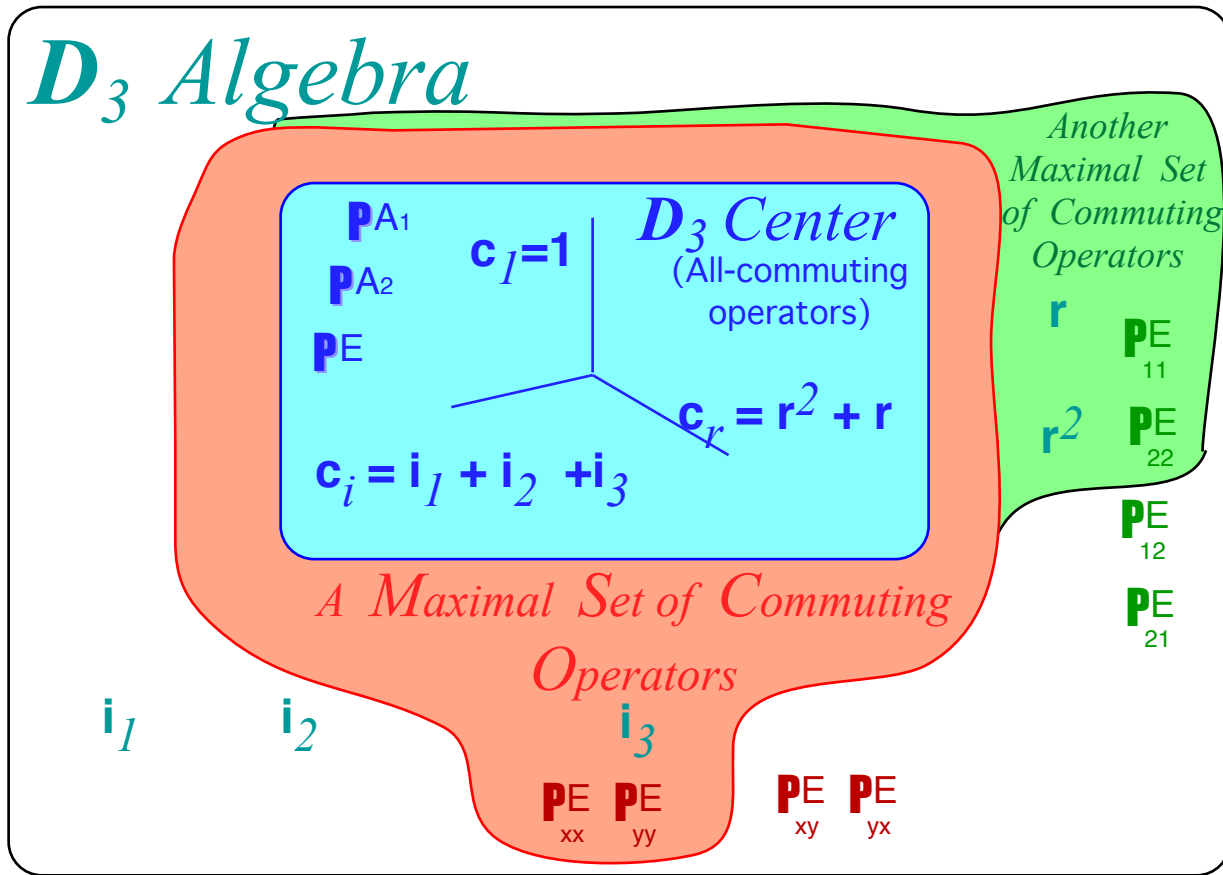
Fig. 15.2.1 D₃ Algebra and sub-algebras

(e) Computing irreducible projectors

The old "*one-equals-one-times-one*" trick is used to split $\mathbb{P}^3 = \mathbb{P}^{E_1}$ in either choice of *MSOCO*. The two idempotents of the i_3 operator are C_2 projectors that sum to **1** in their completeness relation.

$$1 = P^x + P^y = (1 + i_3)/2 + (1 - i_3)/2$$

We multiply this **1** by the **1** resulting from the all-commuting completeness in (15.2.10d).

$$1 = c_1 = \mathbb{P}^{A_1} + \mathbb{P}^{A_2} + \mathbb{P}^{E_1}$$

However, only $\mathbb{P}^3 = \mathbb{P}^{E_1}$ splits into the irreducible projectors $\mathbf{P}^E_{xx}$ and $\mathbf{P}^E_{yy}$ of the irep (15.1.12).

$$\mathbb{P}^{E_1}\ \mathbf{P}^x\ = P^x\,\mathbb{P}^{E_1}\ = (1 + i_3)/2\ (21 - r - r^2)/3 = (21 - r - r^2 - i_1 - i_2 + 2i_3)/6 = \mathbf{P}^E_{xx} \qquad (15.2.11a)$$

$$\mathbb{P}^{E_1}\ \mathbf{P}^y\ = P^y\,\mathbb{P}^{E_1}\ = (1 - i_3)/2\ (21 - r - r^2)/3 = (21 - r - r^2 + i_1 + i_2 - 2i_3)/6 = \mathbf{P}^E_{yy} \qquad (15.2.11b)$$

So, the final irreducible rank-<u>four</u> completeness relation for D_3 is the following <u>four</u> projectors.

$$1 = 1\cdot 1 = (\ \mathbb{P}^{A_1} + \mathbb{P}^{A_2} + \mathbb{P}^{E_1}\ )\ (P^x + P^y) = \mathbb{P}^{A_1} + \mathbb{P}^{A_2} + \mathbf{P}^E_{xx} + \mathbf{P}^E_{yy} \qquad (15.2.12)$$

This **1** is to be "wrapped around" any operator **g** of the D_3 algebra to give the following generalized spectral decomposition of the form shown in (15.1.20a).

$$g = 1\cdot g\cdot 1 = (\ \mathbb{P}^{A_1} + \mathbb{P}^{A_2} + \mathbf{P}^E_{xx} + \mathbf{P}^E_{yy}\ )\cdot g\cdot (\ \mathbb{P}^{A_1} + \mathbb{P}^{A_2} + \mathbf{P}^E_{xx} + \mathbf{P}^E_{yy}\ ) \quad (15.2.13)$$

Because the $\mathbb{P}^{A_1}$ and $\mathbb{P}^{A_2}$ are all-commuting , they leave only two terms.

$$\mathbf{g} = \mathbf{1}\cdot\mathbf{g}\cdot\mathbf{1} = \ \mathbf{g}\cdot\mathbb{P}^{A_1} + \mathbf{g}\cdot\mathbb{P}^{A_2} + \mathbf{P}^E_{xx}\cdot\mathbf{g}\cdot\mathbf{P}^E_{xx} + \mathbf{P}^E_{xx}\cdot\mathbf{g}\cdot\mathbf{P}^E_{yy}$$
$$+ \ \mathbf{P}^E_{yy}\cdot\mathbf{g}\cdot\mathbf{P}^E_{xx} + \mathbf{P}^E_{yy}\cdot\mathbf{g}\cdot\mathbf{P}^E_{yy} \qquad\qquad (15.2.14a)$$

The remaining four terms are the *E*-projectors multiplied by ireps as seen by comparing (15.1.20a).

$$\mathbf{P}^E_{xx}\cdot\mathbf{g}\cdot\mathbf{P}^E_{xx} = D^E_{xx}(\mathbf{g})\ \mathbf{P}^E_{xx}\ , \qquad\qquad \mathbf{P}^E_{xx}\cdot\mathbf{g}\cdot\mathbf{P}^E_{yy} = D^E_{xy}(\mathbf{g})\ \mathbf{P}^E_{xy}\ ,$$
$$\mathbf{P}^E_{yy}\cdot\mathbf{g}\cdot\mathbf{P}^E_{xx} = D^E_{yx}(\mathbf{g})\ \mathbf{P}^E_{yx}\ , \qquad\qquad \mathbf{P}^E_{yy}\cdot\mathbf{g}\cdot\mathbf{P}^E_{yy} = D^E_{yy}(\mathbf{g})\ \mathbf{P}^E_{yy}\ . \qquad (15.2.14b)$$

The preceding completes a set of formulas that can be used to derive *ab-initio* sets of ireps which have desired operators diagonalized. This set favors $\mathbf{i}_3$ and leads to the set of ireps in (15.1.10), but the other *CSOCO* shown in Fig. 15.2.1 favors $\mathbf{r}$ and $\mathbf{r}^2$ and leads to the ireps in (15.1.8).

Let us summarize the first set of six irep projectors which will be used in a band theory model below.

$$\mathbb{P}^{A_1} = \mathbb{P}^{A_1}\ \mathbf{1}\ \mathbb{P}^{A_1} = \qquad\qquad = (\mathbf{1} + \mathbf{r} + \mathbf{r}^2 + \mathbf{i}_1 + \mathbf{i}_2 + \mathbf{i}_3\ )/6 \qquad (15.2.15a)$$

$$\mathbb{P}^{A_2} = \mathbb{P}^{A_2}\ \mathbf{1}\ \mathbb{P}^{A_2} = \qquad\qquad = (\mathbf{1} + \mathbf{r} + \mathbf{r}^2 - \mathbf{i}_1 - \mathbf{i}_2 - \mathbf{i}_3\ )/6 \qquad (15.2.15b)$$

$$\mathbf{P}^E_{xx} = \mathbf{P}^E_{xx}\ \mathbf{1}\ \mathbf{P}^E_{xx} = \qquad\qquad = (2\mathbf{1} - \mathbf{r} - \mathbf{r}^2 - \mathbf{i}_1 - \mathbf{i}_2 + 2\mathbf{i}_3\ )/6 \qquad (15.2.15c)$$

$$\mathbf{P}^E_{yy} = \mathbf{P}^E_{yy}\ \mathbf{1}\ \mathbf{P}^E_{yy} = \qquad\qquad = (2\mathbf{1} - \mathbf{r} - \mathbf{r}^2 + \mathbf{i}_1 + \mathbf{i}_2 - 2\mathbf{i}_3\ )/6 \qquad (15.2.15d)$$

$$\mathbf{P}^E_{xy} = \mathbf{P}^E_{xx}\ \mathbf{i}_2\ \mathbf{P}^E_{yy} = D^E_{xy}(\mathbf{i}_2)\ \mathbf{P}^E_{xy} = \ = (0\mathbf{1} - \mathbf{r} + \mathbf{r}^2 - \mathbf{i}_1 + \mathbf{i}_2 - 0\mathbf{i}_3\ )/4 \qquad (15.2.15e)$$

$$\mathbf{P}^E_{yx} = \mathbf{P}^E_{yy}\ \mathbf{i}_2\ \mathbf{P}^E_{xx} = D^E_{yx}(\mathbf{i}_2)\ \mathbf{P}^E_{yx} = \ = (0\mathbf{1} + \mathbf{r} - \mathbf{r}^2 - \mathbf{i}_1 + \mathbf{i}_2 - 0\mathbf{i}_3\ )/4 \qquad (15.2.15e)$$

Notice that an element $\mathbf{i}_2$ outside of the *CSOCO* must be used to get the two non-zero nilpotent projectors $\mathbf{P}^E_{xy}$ and $\mathbf{P}^E_{yx}$ This is because the idempotents $\mathbf{P}^E_{xx}$ and $\mathbf{P}^E_{yy}$ from (15.2.11a-b) are orthogonal, and a commuting operator would permit the two projectors to annihilate. Then, apart from an overall factor, the result is independent of the choice; any operator like $\mathbf{r}$, $\mathbf{r}^2$, $\mathbf{i}_1$, or $\mathbf{i}_2$ outside of the chosen *CSOCO* can be used.

You will notice that the 2-dimensional *E*-projectors have four values for their double indices *xx, xy, yx,* and *yy*. The meaning of these is quite a deep subject that we will take up, in part, shortly. They come from the splitting (15.2.12) and the "wrap-around" (15.2.13). It should be noted that the scalar $\mathbb{P}^{A_1}$ and pseudo-scalar $\mathbb{P}^{A_2}$ deserve one (and only one) pair of indices, too, which tell which C_2 idempotent, $\mathbf{P}^x$ or $\mathbf{P}^y$ they contain. Their full index notation is as follows. Opposing symmetry partners $\mathbb{P}^{A_1}_{yy}$ and $\mathbb{P}^{A_2}_{xx}$ fail to exist.

$$\mathbb{P}^{A_1} = \mathbb{P}^{A_1}\ \mathbf{P}^x = \mathbb{P}^{A_1}_{xx} \qquad\qquad\qquad\qquad \mathbb{P}^{A_2} = \mathbb{P}^{A_2}\ \mathbf{P}^y = \mathbb{P}^{A_2}_{yy} \qquad (15.2.15f)$$

$$\mathbb{0} = \mathbb{P}^{A_1}\ \mathbf{P}^y \qquad\qquad\qquad\qquad\qquad\qquad \mathbb{0} = \mathbb{P}^{A_2}\ \mathbf{P}^x \qquad (15.2.15g)$$

15.3 Application of irreducible projectors

So far the regular representation and group basis has been an abstract sort of affair with the group operators acting on themselves, a kind of algebraic self-indulgence. However, this facilitates application to a variety of physical models. We consider now another one of these coupled-pendulum models of a quantum system. This one will have (at least) D_3 symmetry but later be one with D_6 symmetry.

Suppose each of three D_3 symmetric wells has a wave that can be described by a two component oscillation or double-pendulum, making six components in all, as shown in Fig. 15.3.1. Each base state $|g\rangle$ has a wave located on one or the other side of a well, and is labeled by a D_3 symmetry operator $\mathbf{g}$ that gives that state by rotating an original "first" state $|I\rangle$ which is chosen to be located just above the x-axis.
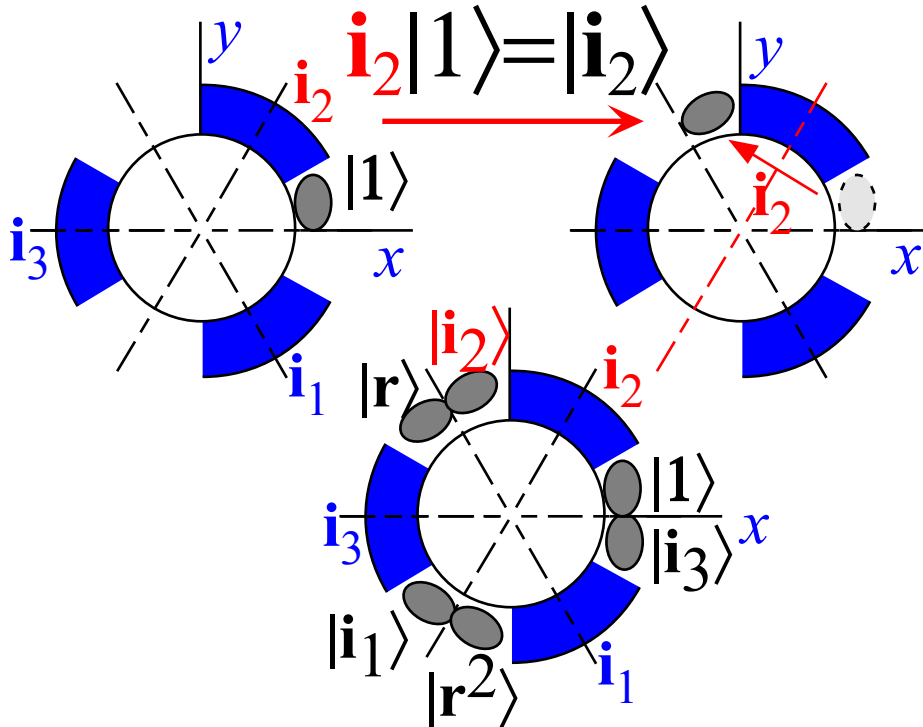
Fig. 15.3.1 Labeling quantum well base states $|g\rangle$ with D_3 operations $|g\rangle = \mathbf{g}\,|1\rangle$.

The six wave base states in Fig. 15.3.1 are defined by

$$|1\rangle = |\mathbf{1}\rangle, \quad |2\rangle = |\mathbf{r}\,\rangle, \quad |3\rangle = |\mathbf{r}^2\rangle, \quad |4\rangle = |\mathbf{i}_1\rangle, \quad |5\rangle = |\mathbf{i}_2\rangle, \quad |6\rangle = |\mathbf{i}_3\rangle,$$
$$= \mathbf{1}|I\rangle, \quad = \mathbf{r}|I\rangle, \quad = \mathbf{r}^2|I\rangle, \quad = \mathbf{i}_1|I\rangle, \quad = \mathbf{i}_2|I\rangle, \quad = \mathbf{i}_3|I\rangle. \qquad (15.3.1)$$

In other words, they are meant to be the embodiment of the regular representation bases (15.1.15b). Besides this ket set, we suppose a bra set, too, that is just the dagger of the ket set.

$$\langle I| = \langle \mathbf{1}|, \quad \langle 2| = \langle \mathbf{r}|, \quad \langle 3| = \langle \mathbf{r}^2|, \quad \langle 4| = \langle \mathbf{i}_1|, \quad \langle 5| = \langle \mathbf{i}_2|, \quad \langle 6| = \langle \mathbf{i}_3|,$$
$$= \langle I|\mathbf{1}, \quad = \langle I|\mathbf{r}^\dagger, \quad = \langle I|\mathbf{r}^{2\dagger}, \quad = \langle I|\mathbf{i}_1^\dagger, \quad = \langle I|\mathbf{i}_2^\dagger, \quad = \langle I|\mathbf{i}_3^\dagger. \quad (15.3.2)$$

Since all regular group representations are real (In fact, they are just 0's with six 1's.) the dagger gives the transpose matrix and it only switches $\mathbf{r}$ and $\mathbf{r}^2$. The other four operators are self-inverse.

$$\mathbf{1}^\dagger = \mathbf{1}, \quad \mathbf{r}^\dagger = \mathbf{r}^2, \quad \mathbf{r}^{2\dagger} = \mathbf{r} \quad \mathbf{i}_1^\dagger = \mathbf{i}_1, \quad \mathbf{i}_2^\dagger = \mathbf{i}_2 \quad \mathbf{i}_3^\dagger = \mathbf{i}_3 \qquad (15.3.3)$$

The unit bras and kets are identical except for their orientation; kets are columns and bras are rows.

$$\langle 1| = \langle 1|\mathbf{1} = \begin{pmatrix} 1 & 0 & 0 & 0 & 0 & 0 \end{pmatrix}$$
$$\langle 2| = \langle 1|\mathbf{r}^2 = \begin{pmatrix} 0 & 1 & 0 & 0 & 0 & 0 \end{pmatrix}$$
$$\langle 3| = \langle 1|\mathbf{r} = \begin{pmatrix} 0 & 0 & 1 & 0 & 0 & 0 \end{pmatrix}$$
$$\langle 4| = \langle 1|\mathbf{i}_1 = \begin{pmatrix} 0 & 0 & 0 & 1 & 0 & 0 \end{pmatrix}$$
$$\langle 5| = \langle 1|\mathbf{i}_2 = \begin{pmatrix} 0 & 0 & 0 & 0 & 1 & 0 \end{pmatrix}$$
$$\langle 6| = \langle 1|\mathbf{i}_3 = \begin{pmatrix} 0 & 0 & 0 & 0 & 0 & 1 \end{pmatrix}$$

$$|1\rangle = \mathbf{1}|1\rangle \quad |2\rangle = \mathbf{r}|1\rangle \quad |3\rangle = \mathbf{r}^2|1\rangle \quad |4\rangle = \mathbf{i}_1|1\rangle \quad |5\rangle = \mathbf{i}_2|1\rangle \quad |6\rangle = \mathbf{i}_3|1\rangle$$

$$= \begin{pmatrix} 1 \\ 0 \\ 0 \\ 0 \\ 0 \\ 0 \end{pmatrix}, \quad = \begin{pmatrix} 0 \\ 1 \\ 0 \\ 0 \\ 0 \\ 0 \end{pmatrix}, \quad = \begin{pmatrix} 0 \\ 0 \\ 1 \\ 0 \\ 0 \\ 0 \end{pmatrix}, \quad = \begin{pmatrix} 0 \\ 0 \\ 0 \\ 1 \\ 0 \\ 0 \end{pmatrix}, \quad = \begin{pmatrix} 0 \\ 0 \\ 0 \\ 0 \\ 1 \\ 0 \end{pmatrix}, \quad = \begin{pmatrix} 0 \\ 0 \\ 0 \\ 0 \\ 0 \\ 1 \end{pmatrix}. \quad (15.3.4)$$

Given this and the irep **P**-operators in (15.2.15) the D_3-symmetry projected states are obtained easily.

$$\left\langle {}^{A_1}\right| = \langle 1|\mathbf{P}^{A_1}\sqrt{6} = \begin{pmatrix} 1 & 1 & 1 & 1 & 1 & 1 \end{pmatrix}/\sqrt{6}$$
$$\left\langle {}^{A_2}\right| = \langle 1|\mathbf{P}^{A_2}\sqrt{6} = \begin{pmatrix} 1 & 1 & 1 & -1 & -1 & -1 \end{pmatrix}/\sqrt{6}$$
$$\left\langle {}^{E}_{xx}\right| = \langle 1|\mathbf{P}^{E}_{xx}\sqrt{3} = \begin{pmatrix} 2 & -1 & -1 & -1 & -1 & 2 \end{pmatrix}/\sqrt{12}$$
$$\left\langle {}^{E}_{yx}\right| = \langle 1|\mathbf{P}^{E}_{xy}\sqrt{3} = \begin{pmatrix} 0 & 1 & -1 & -1 & 1 & 0 \end{pmatrix}/2$$
$$\left\langle {}^{E}_{xy}\right| = \langle 1|\mathbf{P}^{E}_{yx}\sqrt{3} = \begin{pmatrix} 0 & -1 & 1 & -1 & 1 & 0 \end{pmatrix}/2$$
$$\left\langle {}^{E}_{yy}\right| = \langle 1|\mathbf{P}^{E}_{xx}\sqrt{3} = \begin{pmatrix} 2 & -1 & -1 & 1 & 1 & -2 \end{pmatrix}/\sqrt{12}$$

$$\left|{}^{A_1}\right\rangle = \quad \left|{}^{A_1}\right\rangle = \quad \left|{}^{E}_{xx}\right\rangle = \quad \left|{}^{E}_{yx}\right\rangle = \quad \left|{}^{E}_{xy}\right\rangle = \quad \left|{}^{E}_{yy}\right\rangle =$$

$$\mathbf{P}^{A_1}|1\rangle\sqrt{6} \quad \mathbf{P}^{A_2}|1\rangle\sqrt{6} \quad \mathbf{P}^{E}_{xx}|1\rangle\sqrt{3} \quad \mathbf{P}^{E}_{yx}|1\rangle\sqrt{3} \quad \mathbf{P}^{E}_{xy}|1\rangle\sqrt{3} \quad \mathbf{P}^{E}_{yy}|1\rangle\sqrt{3}$$

$$= \begin{pmatrix} 1 \\ 1 \\ 1 \\ 1 \\ 1 \\ 1 \end{pmatrix}\frac{1}{\sqrt{6}}, \; = \begin{pmatrix} 1 \\ 1 \\ 1 \\ -1 \\ -1 \\ -1 \end{pmatrix}\frac{1}{\sqrt{6}}, \; = \begin{pmatrix} 2 \\ -1 \\ -1 \\ -1 \\ -1 \\ 2 \end{pmatrix}\frac{1}{\sqrt{12}}, \; = \begin{pmatrix} 0 \\ 1 \\ -1 \\ -1 \\ 1 \\ 0 \end{pmatrix}\frac{1}{2}, \; = \begin{pmatrix} 0 \\ -1 \\ 1 \\ 1 \\ -1 \\ 0 \end{pmatrix}\frac{1}{2}, \; = \begin{pmatrix} 2 \\ -1 \\ -1 \\ 1 \\ 1 \\ -2 \end{pmatrix}\frac{1}{\sqrt{12}}$$

(15.3.5a)   (15.3.5b)

Each bra or ket is an operation of **P**-operator on the "first" state $|1\rangle$. Note use of conjugation: $\mathbf{P}_{mn}{}^\dagger = \mathbf{P}_{nm}$. A sketch of the resulting wavefunctions is shown in Fig. 15.3.2.

(a) Global and local symmetry

      Let us carefully examine the symmetry properties of these waves. Notice that the two waves projected with the operators $\mathbf{P}^{E}_{xx}$ and $\mathbf{P}^{E}_{xy}$, as well as the scalar $\mathbb{P}^{A_1}_{xx}$ are symmetric to *180°* rotation $\mathbf{i}_3$ around the *x*-axis. We will refer to this as *global C_2-or* $\mathbf{i}_3$ *-symmetry*. Global $\mathbf{i}_3$ -symmetry holds if the *left-hand or global index* is *x*.

      On the other hand, the two waves projected with the operators $\mathbf{P}^{E}_{yx}$ and $\mathbf{P}^{E}_{yy}$, as well as the pseudo-scalar $\mathbb{P}^{A_2}_{yy}$ are anti-symmetric to *180°* rotation $\mathbf{i}_3$ around the *x*-axis. This will be referred to as *global $C_2(\mathbf{i}_3)$-anti-symmetry*. Global $\mathbf{i}_3$ -anti-symmetry means the *left-hand or global index* is *y*.

      Now, notice that the two waves projected with the operators $\mathbf{P}^{E}_{xx}$ and $\mathbf{P}^{E}_{yx}$, as well as the scalar $\mathbb{P}^{A_1}_{xx}$ are symmetric to *180°* rotation around their local $\mathbf{i}_w$-axes $\mathbf{i}_1$, $\mathbf{i}_2$, or $\mathbf{i}_3$, whichever lies in their well. We will call this *local C_2-or* $\mathbf{i}_w$ *-symmetry*. Local $\mathbf{i}_w$ -symmetry means the *right-hand or local index* is *x*.

      Finally, the two waves projected with the operators $\mathbf{P}^{E}_{xy}$ and $\mathbf{P}^{E}_{yy}$, as well as the pseudo-scalar $\mathbb{P}^{A_2}_{yy}$ are anti-symmetric to *180°* rotation around their local $\mathbf{i}_w$-axes $\mathbf{i}_1$, $\mathbf{i}_2$, or $\mathbf{i}_3$ through their wells. We will call this *local C_2-or $\mathbf{i}_w$ anti-symmetry*. Local $\mathbf{i}_w$ anti-symmetry means the *right-hand or local index* is *y*.
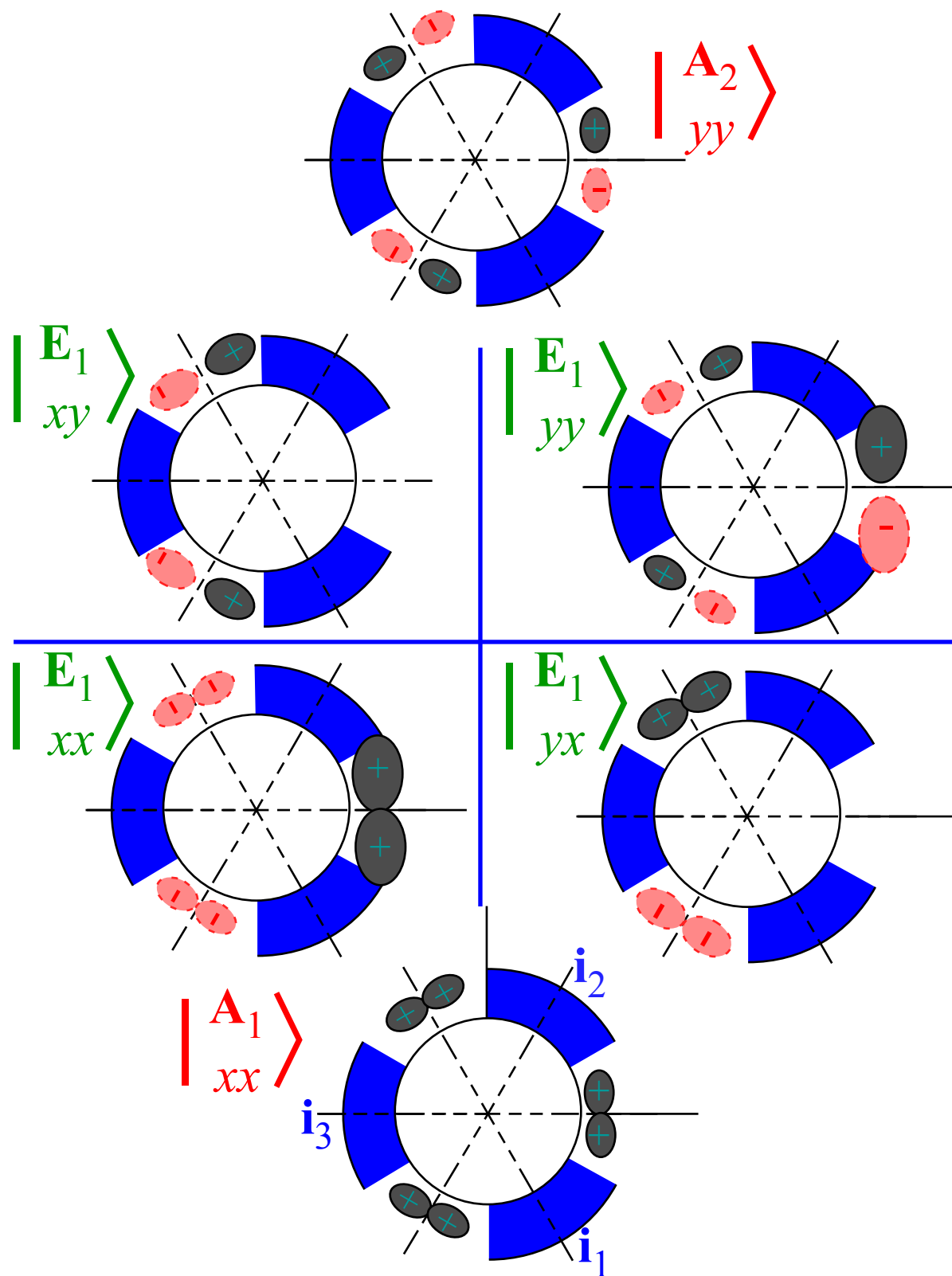
Fig. 15.3.2 Quantum-well states obtained with D₃ symmetry projection
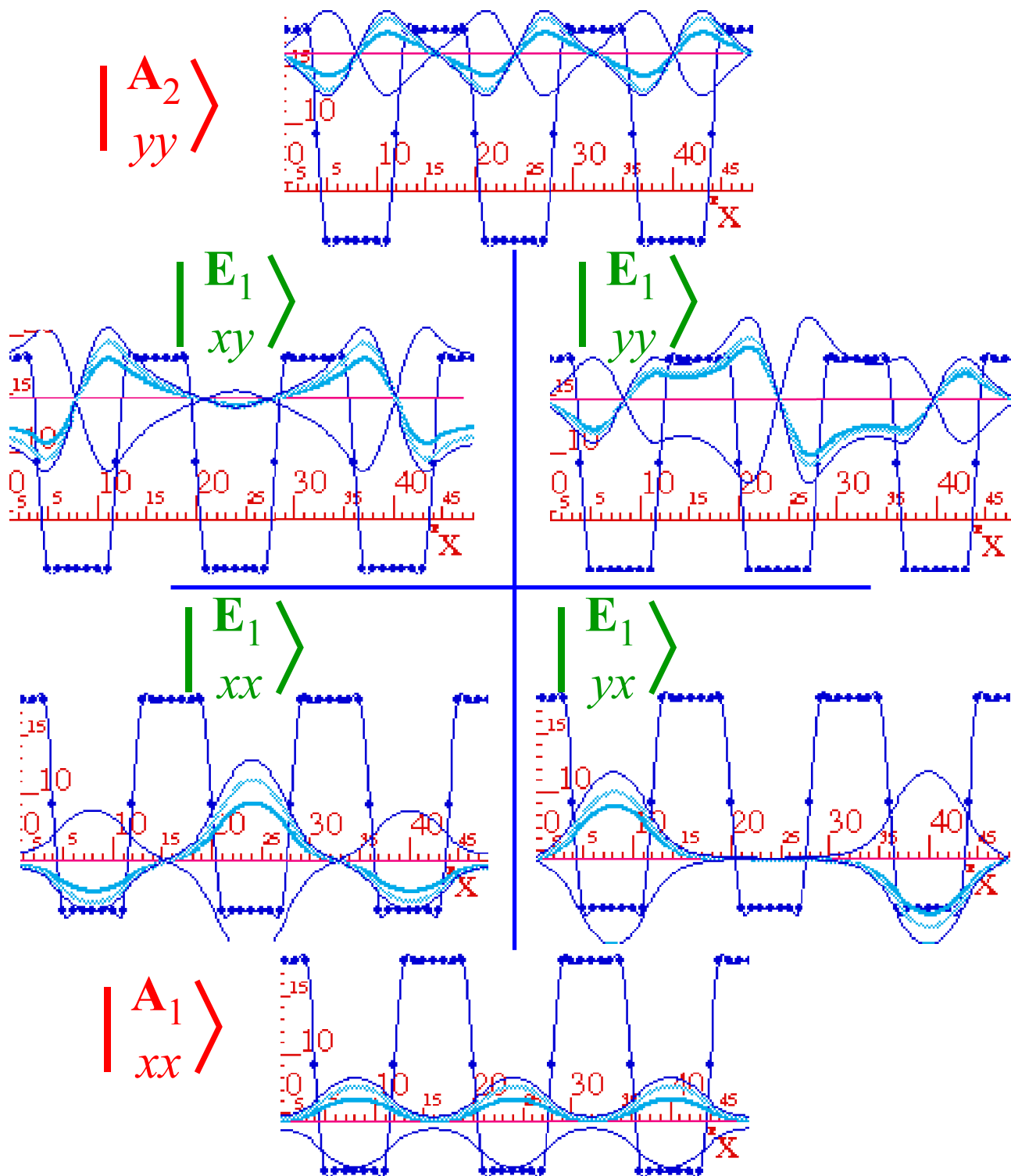
Fig. 15.3.3 *Quantum well states obtained by numerical calculation*

Examples of computer plots of D_3 waves are shown in Fig. 15.3.3 where the defining $\mathbf{i}_3$ symmetry axis lies in the center well. The waves go with the first (A_1, E_1,)-(gap)-(E_1, A_2)-levels in Fig. 14.2.8 (left).

Two of the E_1 levels belong to *degenerate partners of the global D_3 symmetry*. The lowest partners are locally symmetric pair $|E_{1_{xx}}\rangle$ and $|E_{1_{yx}}\rangle$. The next higher level belongs to the locally anti-symmetric pair of states $|E_{1_{xy}}\rangle$ and $|E_{1_{yy}}\rangle$. The Kronig-Penney construction in Fig. 14.2.8 proves this degeneracy, but it is also a general consequence of the global D_3 symmetry as we will prove later on.

The degenerate pairs belong to what are basically x- and y-pairs of vector components. In fact the symmetry label E_1 has "vector" written all over it. Its C_3 ancestors are the 1_3 and $2_3 = -1_3$ moving wave states from which we built sine and cosine standing-waves. To be precise, they are sine and cosine of one-wave-modulo-three-wells (± 1-mod-3). That is like a two-dimensional (x,y)-vector. Indeed, the ireps (15.1.10) are rotation matrices for $120°$ z-rotations and $180°$ transverse rotations of x and y unit vectors.

$$D_{\{xy\}}^{E}(\mathbf{r}) = \begin{pmatrix} \langle x|\mathbf{r}|x\rangle & \langle x|\mathbf{r}|y\rangle \\ \langle y|\mathbf{r}|x\rangle & \langle y|\mathbf{r}|y\rangle \end{pmatrix} = \begin{pmatrix} \cos 120° & -\sin 120° \\ \sin 120° & \cos 120° \end{pmatrix} = \begin{pmatrix} -1/2 & -\sqrt{3}/2 \\ \sqrt{3}/2 & -1/2 \end{pmatrix} \quad (15.3.6)$$

One should be aware of such elementary derivations of irep matrices and visualize consequences. If you now look at the E_1 partners in Fig. 15.3.2 you should see the global-x partner $|E_{1_{xg}}\rangle$ wave trying to "vector" in the x-direction (particularly for the lowest x-partner $|E_{1_{xx}}\rangle$) while the global-y partner $|E_{1_{xg}}\rangle$ is trying to "vector" in the y-direction. If you were to mix either of these with some scalar A_1 wave you would see this immediately as the combination became a *dipole* beating oscillation. The x-global partners would radiate plane-x polarization while the global y-symmetry partners would radiate y-polarization. This is the mechanism of the *dipole transition* phenomena that is responsible for virtually all the light we see. We would be blind as a bat without E_1 or "vector" symmetry components like these!

Symmetry is also connected with wave-node topology. Each of the four levels is associated with a given number of wave nodes. There are *0* nodes for scalar singlet $|A_{1_{xx}}\rangle$, *2* nodes for both degenerate partners $|E_{1_{xx}}\rangle$ and $|E_{1_{yx}}\rangle$, 4 nodes for both degenerate partners $|E_{1_{xy}}\rangle$ and $|E_{1_{yy}}\rangle$, and 6 wave nodes for single $|A_{2_{yy}}\rangle$, the pseudo-scalar singlet state. The nodes are not always easy to see and count particularly if they lie in a region where ψ is near zero as required by $(\mathbf{1}, \mathbf{i}_3)$-symmetry in $|E_{1_{xy}}\rangle$ and $|E_{1_{yx}}\rangle$. Generally, more nodes means more energy.

However, suppose we choose a different temporary member of the *MSOCO* such as the $120°$ $\mathbf{r}$ operator on the right of Fig. 15.2.1. Making $\mathbf{r}$ diagonal gives the ireps (15.1.8) which include the following diagonal matrix. These belong to *C*-type *moving-wave states* of left-and-right-circular polarization.

$$D_{\{1_3 - 1_3\}}^{E}(\mathbf{r}) = \begin{pmatrix} \langle 1_3|\mathbf{r}|1_3\rangle & \langle 1_3|\mathbf{r}|2_3\rangle \\ \langle 2_3|\mathbf{r}|1_3\rangle & \langle 2_3|\mathbf{r}|2_3\rangle \end{pmatrix} = \begin{pmatrix} \cos\dfrac{2\pi}{3} - i\sin\dfrac{2\pi}{3} & 0 \\ 0 & \cos\dfrac{2\pi}{3} + i\sin\dfrac{2\pi}{3} \end{pmatrix} = \begin{pmatrix} e^{-i2\pi/3} & 0 \\ 0 & e^{+i2\pi/3} \end{pmatrix}$$

Such wave states radiate circularly polarized light when set in combination with scalar waves.

Obviously there are many choices for symmetry definition of the E-states, in fact, there is an entire *U(2)* world of possibilities, and most of them are "non-descript" elliptical polarization types. To really be in control of quantum dynamics, it is necessary to be acutely aware of these possibilities. We are now beginning to scratch the tip of a giant iceberg of symmetry related tools. The next section describes a "hidden whopper" of symmetry algebra. Prepare to stretch your mind a bit for this one!

(b) The duality principle: Symmetry operators inside and out

In a story about Archimedes he is supposed to have said, "Give me a place to stand and I'll move the world." This same old idea appears in quantum theory, starting with axioms *1-4*. The basic idea is that all transformations are relative mappings from one basis to another. Simply put: "It takes two to tango!" Indeed, the idea of *transformational duality* may seem so obvious as to be trite. We tire of hearing the old saw, "Everything is relative." In this matter, it is difficult to distinguish the sublime from the trivial.

However, with regard to symmetry operations, the question of duality is anything but trivial. To thoroughly understand symmetry analysis, particularly for non-commuting algebra G, like that of D_3,

$$G = \{1,...,\mathbf{g},...\} = D_3 = \left\{1, \mathbf{r}, \mathbf{r}^2, \mathbf{i}_1, \mathbf{i}_2, \mathbf{i}_3\right\}, \qquad (15.3.7a)$$

it is necessary to introduce a *dual set* or group

$$\bar{G} = \{\bar{1},...,\bar{\mathbf{g}},...\} = \bar{D}_3 = \left\{\bar{1}, \bar{\mathbf{r}}, \bar{\mathbf{r}}^2, \bar{\mathbf{i}}_1, \bar{\mathbf{i}}_2, \bar{\mathbf{i}}_3\right\}, \qquad (15.3.7b)$$

of symmetry operators $\bar{\mathbf{g}}$ which commute with the $\mathbf{g}$ in the original set.

$$\mathbf{g} \cdot \bar{\mathbf{h}} = \bar{\mathbf{h}} \cdot \mathbf{g}, \quad \text{and:} \quad \bar{\mathbf{g}} \cdot \mathbf{h} = \mathbf{h} \cdot \bar{\mathbf{g}}, \text{ for all } \mathbf{g}, \mathbf{h} \text{ in } G \text{ and } \bar{\mathbf{g}}, \bar{\mathbf{h}} \text{ in } \bar{G}. \quad (15.3.7c)$$

But, each satisfy the same (generally non-commutative) multiplication rules as the original set.

$$\mathbf{g} \cdot \mathbf{h} = \mathbf{k} \quad \text{implies:} \quad \bar{\mathbf{g}} \cdot \bar{\mathbf{h}} = \bar{\mathbf{k}} \text{ for all } \mathbf{g}, \mathbf{h}, \mathbf{k} \text{ in } G \text{ and } \bar{\mathbf{g}}, \bar{\mathbf{h}}, \bar{\mathbf{k}} \text{ in } \bar{G}. \qquad (15.3.7d)$$

How do we visualize this dual set? Well, first we recall how to visualize "ordinary" sets of operations.

We might visualize "ordinary" transformation operations like $\mathbf{i}_2$ in Fig. 15.3.1 as belonging to a symmetry axis or reflection plane embedded in a piece of metal or something solid that represents a potential through which some "fluff" called a "wavefunction" is going to wiffle to and fro. A symmetry operation moves "fluff" relative to its axis or plane in a precisely defined way, in the case of $\mathbf{i}_2$, by doing a *180°* rotation as shown in Fig. 15.3.1. The result is a relation between an original state with "fluff" in state $|1\rangle$ and a transformed state with the "fluff" moved relative to the potential wells to state $|\mathbf{i}_2\rangle = \mathbf{i}_2 |1\rangle$.

However, this unfairly distinguishes "fluff" from the "metal" which "contains" the rotation axes and the potential wells. If quantum theory teaches us anything, it is that <u>all</u> matter is "fluff." That potential ring in Fig. 15.3.1 could be part of a massive lab bench or just three protons of an H_3 molecule, but in either case it is still "fluff", too, only the time scale might be different. And, the "real fluff" could as well be a light photon or electron or more massive polymer ring or big molecule in the D_3 potential.

The introduction of the dual symmetry operators levels the playing field for the two kinds of "fluff" . What matters is only the <u>relative</u> position of one kind of fluff relative to the other. It matters not if we use "ordinary" operators like $\mathbf{g} = \mathbf{i}_2$ to move the "real fluff" up to its new potential well, as shown in Fig. 15.3.4(a), or whether a dual operation $\bar{\mathbf{g}} = \bar{\mathbf{i}}_2$ moves the well the opposite way down to enclose the fluff, as shown in Fig. 15.3.4(b). "It's all relative!", or, so says what we will call the *duality principle*

$$\mathbf{g}|1\rangle = |\mathbf{g}\rangle = \bar{\mathbf{g}}^\dagger |1\rangle = \bar{\mathbf{g}}^{-1}|1\rangle \ , \quad \text{or:} \quad \mathbf{g}^{-1}|1\rangle = \mathbf{g}^\dagger |1\rangle = \left|\mathbf{g}^{-1}\right\rangle = \bar{\mathbf{g}}|1\rangle = \bar{\mathbf{g}}|1\rangle. \qquad (15.3.8)$$

The figure part (b) labeled (*after* $\bar{\mathbf{i}}_2$ *and set upright*) has the same <u>relative</u> state as part (a) labeled (*after* $\mathbf{i}_2$)
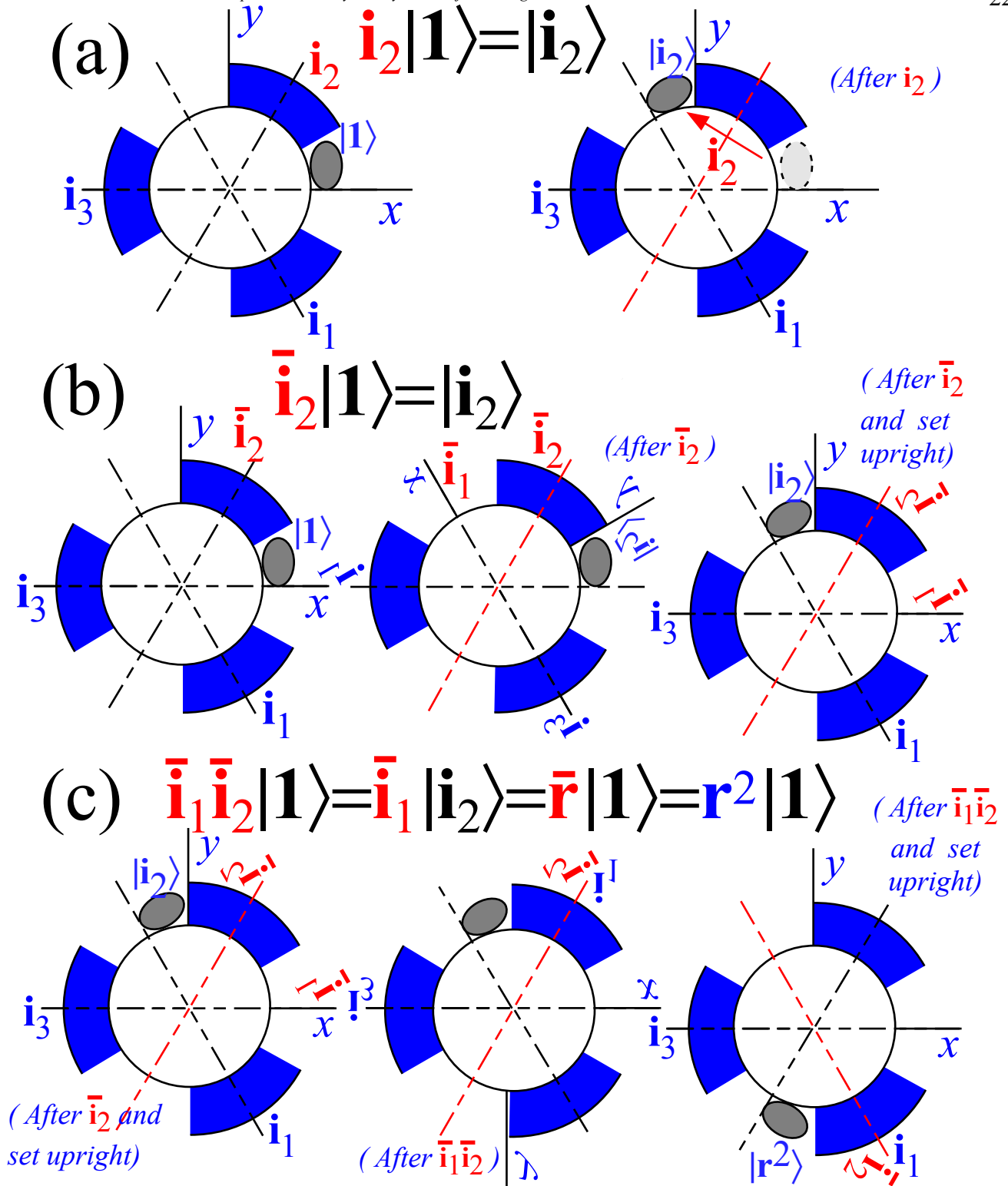
Fig. 15.3.4 Comparison of (a) ordinary symmetry operations and (b-c) dual operations.

The outcome of moving furniture one way along a rug is indistinguishable from dragging the rug the opposite way if we only observe where the furniture makes dents in the rug. Duality-relativity (15.3.8) reminds one of Ernst Mach's famous principle. Interference between waves is what is observed and what gives reference frames including relativity space-time frames in Chapter 4. Waves measure each other.

The duality principle does NOT equate dual operator $\bar{\mathbf{g}}$ with the inverse $\mathbf{g}^{-1} = \mathbf{g}^\dagger$ of an ordinary operator $\mathbf{g}$. This would not give the desired commutation (15.3.7c) between the two sets. It would not even give the same group multiplication as in (15.3.7d). Instead, we require that the two operators $\bar{\mathbf{g}}$ and $\mathbf{g}^\dagger$ (or, else, $\bar{\mathbf{g}}^\dagger$ and $\mathbf{g}$) have the same effect on <u>one</u>, particular "original" state $|I\rangle$. Operators $\mathbf{g}$ and their duals $\bar{\mathbf{g}}$ belong to completely different operator sets (15.3.7a) and (15.3.7b), respectively.

Still, how do you visualize a dual set of $\bar{\mathbf{g}}$ operations? This is often the most difficult part of theory and one that can be subject to personal preference. I prefer to visualize the dual operations as being attached to an equivalent reference frame connected with the "real fluff" that is the body whose wave dynamics is being studied. Now it may seem that something as ephemeral as an electron or photon wave doesn't deserve to have its own reference frame, much less, the ability to flip the whole world over its (insubstantial) shoulders. However, in order to level the playing field as stated earlier, one should not discriminate against any quantum objects for reasons of mass, charge, or any of their intrinsic properties.

This point of view makes the dual operations completely equivalent to the "ordinary" ones. When, starting from state $|I\rangle$, the electron rotates the potential <u>clock</u>wise by $120°$ using $\bar{\mathbf{g}}^\dagger = \bar{\mathbf{r}}^\dagger = \bar{\mathbf{r}}^2$ while the electron "stays put". Nevertheless, the electron winds up in the same well as it would have if, instead, the potential had flipped the electron <u>counter</u> <u>clock</u>wise by $120°$ using $\mathbf{g} = \mathbf{r}$ while the potential frame "stays put" or, by duality (15.3.8),

$$\bar{\mathbf{r}}^2|\mathbf{1}\rangle = \bar{\mathbf{r}}^\dagger|\mathbf{1}\rangle = |\mathbf{r}\rangle = \mathbf{r}|\mathbf{1}\rangle .$$

However, starting from any other state $|\mathbf{t}\rangle = \mathbf{t}|I\rangle$ than $|I\rangle$ the effect of $\bar{\mathbf{r}}^2$ is defined by equivalency since an electron referred to address $|\mathbf{t}\rangle$ has different labels than those labeled by the potential frame.

$$\bar{\mathbf{r}}^2|\mathbf{t}\rangle = \bar{\mathbf{r}}^\dagger|\mathbf{t}\rangle = \bar{\mathbf{r}}^\dagger \cdot \mathbf{t}|\mathbf{1}\rangle = \bar{\mathbf{r}}^\dagger \cdot \bar{\mathbf{t}}^\dagger|\mathbf{1}\rangle = \left(\bar{\mathbf{t}}\cdot\bar{\mathbf{r}}\right)^\dagger|\mathbf{1}\rangle = \mathbf{t}\cdot\mathbf{r}|\mathbf{1}\rangle = \mathbf{t}\cdot\mathbf{r}\cdot\mathbf{t}^{-1}\mathbf{t}|\mathbf{1}\rangle$$
$$= \mathbf{t}\cdot\mathbf{r}\cdot\mathbf{t}^{-1}|\mathbf{t}\rangle$$

The resulting general *duality-relativity principle* is

$$\bar{\mathbf{g}}|\mathbf{t}\rangle = \mathbf{t}\cdot\mathbf{g}^\dagger\cdot\mathbf{t}^{-1}|\mathbf{t}\rangle = \mathbf{t}\cdot\mathbf{g}^\dagger\cdot\mathbf{t}^\dagger|\mathbf{t}\rangle . \qquad\qquad (15.3.9)$$

Again, this does <u>not</u> equate $\bar{\mathbf{g}}$ and $\mathbf{t}\cdot\mathbf{g}^\dagger\cdot\mathbf{t}^{-1}$ except for that one state $|\mathbf{t}\rangle$. However, this suggests we can also visualize the dual operations as moving their axes along with the wave being transformed.

This is shown in Fig. 15.3.4(c) which shows the effect of the product $\bar{\mathbf{i}}_1\cdot\bar{\mathbf{i}}_2$ on $|I\rangle$. The D_3 group table in Fig. 3.6.2 lists the product $\mathbf{i}_1\cdot\mathbf{i}_2 = \mathbf{r}$ or from (15.3.7d) $\bar{\mathbf{i}}_1\cdot\bar{\mathbf{i}}_2 = \bar{\mathbf{r}}$. The first operation of the product $\bar{\mathbf{i}}_1\cdot\bar{\mathbf{i}}_2$ $|I\rangle$ to act is $\bar{\mathbf{i}}_2$ since it's facing ket $|I\rangle$. The effect of $\bar{\mathbf{i}}_2$ is shown in Fig. 15.3.4(b). It rotates both the potential and its operations $\mathbf{i}_1$, $\mathbf{i}_2$, and $\mathbf{i}_3$ around the $\bar{\mathbf{i}}_2$ axis relative to the electron wave and its operations $\bar{\mathbf{i}}_1$, $\bar{\mathbf{i}}_2$, and $\bar{\mathbf{i}}_3$ which "stay put." But, when the whole system (potential+electron) is set back with the PE frame and $\mathbf{i}_a$ in an "upright" position, then it is the $\bar{\mathbf{i}}_1$, $\bar{\mathbf{i}}_2$, $\bar{\mathbf{i}}_3$ that appear rotated *along with the electron* relative to the PE frame.

Now the second operation of the product $\bar{\mathbf{i}}_1\cdot\bar{\mathbf{i}}_2$ $|I\rangle$ to act is $\bar{\mathbf{i}}_1$ since it's facing the ket $\bar{\mathbf{i}}_2|I\rangle$. But, due to the effects of the preceding $\bar{\mathbf{i}}_2$, the dual operation $\bar{\mathbf{i}}_1$ now has its axis along the axis of the regular operation $\mathbf{i}_3$ as

shown Fig. 15.3.4(b). This checks with (15.3.9). Then the effect of $\bar{\mathbf{i}}_1$ is to flip the ordinary operations $\mathbf{i}_1$, $\mathbf{i}_2$,

$\mathbf{i}_3$, and the potential around the current $\bar{\mathbf{i}}_1$ -axis while letting the electron wave and its associated dual operations

$\bar{\mathbf{i}}_1$, $\bar{\mathbf{i}}_2$, and $\bar{\mathbf{i}}_3$ "stay put" as shown in the center of Fig. 15.3.4(c).

However, you can view this, instead, as the rotation around the current $\bar{\mathbf{i}}_1$ -axis of the electron wave <u>and</u> its

associated dual operations $\bar{\mathbf{i}}_1$, $\bar{\mathbf{i}}_2$, and $\bar{\mathbf{i}}_3$ while the ordinary operations $\mathbf{i}_1$, $\mathbf{i}_2$, $\mathbf{i}_3$, and the potential are the ones

that "stay put" as shown by comparing in the extreme right hand sides of Fig. 15.3.4(b) and (c). Since we assume,

"Everything is relative!", either view is valid.

(c) Projector duality: Quantum labels inside and out

The duality principle lends meaning to the two indices $(_{mn})$ of non-commutative projection $\mathbf{P}^{\mu}_{mn}$ operators

and projected states $\mathbf{P}^{\mu}_{mn}|1\rangle = \left|^{\mu}_{mn}\right\rangle$ in Figs. 15.3.2 and 3. To see this, compare the transformation properties of an

operator $\mathbf{g}$ with that of its dual $\bar{\mathbf{g}}$. The ordinary $\mathbf{g}$ transformation properties (15.3.10a) follow from those of left

multiplication (15.1.21a). However, since a dual operator $\bar{\mathbf{g}}$ commutes with every operator in $\mathbf{P}^{\mu}_{mn}$ it slides past

$\mathbf{P}^{\mu}_{mn}$ and, by the duality principle (15.3.8), does *conjugated(†) right* multiplication (15.1.21b) to give (15.3.10b).

$$\mathbf{g}\left|^{\mu}_{mn}\right\rangle = \mathbf{g}\mathbf{P}^{\mu}_{mn}|1\rangle\sqrt{N}$$

$$\bar{\mathbf{g}}\left|^{\mu}_{mn}\right\rangle = \bar{\mathbf{g}}\mathbf{P}^{\mu}_{mn}|1\rangle\sqrt{N} = \mathbf{P}^{\mu}_{mn}\bar{\mathbf{g}}|1\rangle\sqrt{N}$$

$$= \mathbf{P}^{\mu}_{mn}\mathbf{g}^{\dagger}|1\rangle\sqrt{N}$$

$$= \sum_{m'=1}^{\ell^{\mu}} D^{\mu}_{m'm}\left(g\right)\mathbf{P}^{\mu}_{m'n}|1\rangle\sqrt{N}$$

$$= \sum_{n'=1}^{\ell^{\mu}} D^{\mu}_{nn'}\left(g^{\dagger}\right)\mathbf{P}^{\mu}_{mn'}|1\rangle\sqrt{N}$$

$$= \sum_{m'=1}^{\ell^{\mu}} D^{\mu}_{m'm}\left(g\right)\left|^{\mu}_{m'n}\right\rangle \qquad (15.3.10a)$$

$$= \sum_{n'=1}^{\ell^{\mu}} D^{\mu*}_{n'n}\left(g\right)\left|^{\mu}_{mn'}\right\rangle \qquad (15.3.10b)$$

A choice of *MSOCO* that has $D^{E}(\mathbf{i}_3)$ diagonal lets $\mathbf{i}_3$ and its dual $\bar{\mathbf{i}}_3$ label the quantum symmetry states.

The ±*1* eigenvalues of $\mathbf{i}_3$ label the *global parity* of the states $\mathbf{P}^{\mu}_{mn}|1\rangle = \left|^{\mu}_{mn}\right\rangle$ while the ±1 eigenvalues of $\bar{\mathbf{i}}_3$ label the

local parity of the same states as seen below and in Fig. 15.3.2. (Here, $\mu = A_1, A_2,$ or E_1.)

$$\mathbf{i}_3\left|^{\mu}_{mn}\right\rangle = \sum_{m'=1}^{\ell^{\mu}} \delta_{m'm}D^{\mu}_{m'm}\left(\mathbf{i}_3\right)\left|^{\mu}_{m'n}\right\rangle$$

$$= \begin{cases} +\left|^{\mu}_{mn}\right\rangle \text{ for: } m=x \\ -\left|^{\mu}_{mn}\right\rangle \text{ for: } m=y \end{cases} \qquad (15.3.10c)$$

$$\bar{\mathbf{i}}_3\left|^{\mu}_{mn}\right\rangle = \sum_{n'}^{\ell^{\mu}} \delta_{n'n}D^{\mu*}_{n'n}\left(\mathbf{i}_3\right)\left|^{\mu}_{mn'}\right\rangle$$

$$= \begin{cases} +\left|^{\mu}_{mn}\right\rangle \text{ for: } n=x \\ -\left|^{\mu}_{mn}\right\rangle \text{ for: } n=y \end{cases} \qquad (15.3.10d)$$

(15.3.10) show the left hand *(m)*-indices label *global symmetry* of the "potential-relative" operators $\mathbf{g}$ while the

right-hand *(n)*-indices label *local symmetry* seen by "wave-relative" dual operators $\bar{\mathbf{g}}$.

(d) Dual regular representation

The regular representation of a group operator $\mathbf{g}$ is defined by (15.1.15b) and is rewritten here.

$$R^{G}_{h,f}(\mathbf{g}) = \langle h|\mathbf{g}|f\rangle = \langle 1|\mathbf{h}^{\dagger}\mathbf{g}\cdot\mathbf{f}|1\rangle = \delta_{h=gf} = \begin{cases} 1 \text{ if: } \mathbf{h}=\mathbf{g}\cdot\mathbf{f} \\ 0 \text{ if: } \mathbf{h}\neq\mathbf{g}\cdot\mathbf{f} \end{cases} = \delta_{f^{\dagger}=h^{\dagger}g} \qquad (15.3.11a)$$

Commutivity (15.3.7c) and duality principle (15.3.8) gives a regular representation of dual operators $\bar{\mathbf{g}}$.

$$R^G_{h,f}(\bar{\mathbf{g}}) = \langle h|\bar{\mathbf{g}}|f\rangle = \langle 1|\mathbf{h}^\dagger\bar{\mathbf{g}}\cdot\mathbf{f}|1\rangle = \langle 1|\mathbf{h}^\dagger\mathbf{f}\cdot\bar{\mathbf{g}}|1\rangle = \langle 1|\mathbf{h}^\dagger\mathbf{f}\cdot\mathbf{g}^\dagger|1\rangle = \delta_{h^\dagger = gf^\dagger} = \delta_{f = hg} \quad (15.3.11b)$$

This shows that the dual regular representation is just the ordinary one with row-*h* switched with row-*h†* and column-*f* switched with column-*f†*.

$$R^G_{h,f}(\bar{\mathbf{g}}) = \delta_{h^\dagger = gf^\dagger} = R^G_{h^\dagger,f^\dagger}(\mathbf{g}) \quad (15.3.11c)$$

For D_3, only *r* and r^2 rows and columns switch as the other operators are self-inverse: $\mathbf{1}^\dagger = \mathbf{1}$ and $\mathbf{i}_a{}^\dagger = \mathbf{i}_a$. So, regular representation (15.1.15) is easily converted to the following representation of dual operators.

$$R^G(\bar{\mathbf{1}}) = \qquad R^G(\bar{\mathbf{r}}) = \qquad R^G(\bar{\mathbf{r}}^2) = \qquad R^G(\bar{\mathbf{i}}_1) = \qquad R^G(\bar{\mathbf{i}}_2) = \qquad R^G(\bar{\mathbf{i}}_3) =$$

$$(15.3.11d)$$

Compare the original set (15.1.15) repeated below. Both sets satisfy the same group table. Furthermore, <u>every</u> matrix in the dual set (15.3.11d) commutes with <u>each</u> matrix in the "ordinary" set (15.1.15a) as was postulated by the duality commutation requirement (15.3.7c).

$$R^G(\mathbf{1}) = \qquad R^G(\mathbf{r}) = \qquad R^G(\mathbf{r}^2) = \qquad R^G(\mathbf{i}_1) = \qquad R^G(\mathbf{i}_2) = \qquad R^G(\mathbf{i}_3) =$$

$$(15.1.15a)_{repeated}$$

A quick way to see this (short of multiplying every pair twice) is to note that a non-zero matrix element $\langle h|\bar{\mathbf{r}}\cdot\mathbf{i}|f\rangle = \langle h|\bar{\mathbf{r}}|if\rangle$ demands $\mathbf{h} = \mathbf{i}\cdot\mathbf{f}\cdot\mathbf{r}^\dagger$ or $\mathbf{i}\cdot\mathbf{f} = \mathbf{h}\cdot\mathbf{r}$ using (15.3.11b). By the same formula, matrix element $\langle h|\mathbf{i}\cdot\bar{\mathbf{r}}|f\rangle = \langle i^\dagger h|\bar{\mathbf{r}}|f\rangle$ demands $\mathbf{i}^\dagger\cdot\mathbf{h} = \mathbf{f}\cdot\mathbf{r}^\dagger$ or $\mathbf{i}\cdot\mathbf{f} = \mathbf{h}\cdot\mathbf{r}$ which is the same. Contrast this with matrix element $\langle h|\mathbf{r}\cdot\mathbf{i}|f\rangle = \langle h|\mathbf{r}|if\rangle$ which demands $\mathbf{h} = \mathbf{r}\cdot\mathbf{i}\cdot\mathbf{f}$, but this is not the same as the requirement for matrix element $\langle h|\mathbf{i}\cdot\mathbf{r}|f\rangle = \langle h|\mathbf{i}|rf\rangle$ for which $\mathbf{h} = \mathbf{i}\cdot\mathbf{r}\cdot\mathbf{f}$. (It is the same only if **r** and **i** commute.) So, dual operations exist as much as the "ordinary" ones. Matrices (15.1.15) and (15.3.11) satisfy duality postulates (15.3.7) and (15.3.8) no matter how you visualize the operators.

15.4 Hamiltonians Composed and Solved by Dual Operators

The main idea of symmetry operators **g** is that they commute with a Hamiltonian **H**.

$$\mathbf{g}\,\mathbf{H} = \mathbf{H}\,\mathbf{g} \tag{15.4.1}$$

In our first application of this idea, eigenstates of a **T**-matrix (8.2.7) and **H**-matrix (9.3.5) for a C_6-symmetric ring "gizmo" were found using C_6-symmetry projectors. This worked because the matrices **H** or **T**= exp$(-i\mathbf{H}t)$ were combinations of C_6-symmetry operators $\{\mathbf{1},\,\mathbf{r},\,...,\,\mathbf{r}^5\}$. **H** naturally commuted with operators $\{\mathbf{1},\,\mathbf{r},\,...,\,\mathbf{r}^5\}$ in C_6 because **H** was a combination $\mathbf{H} = H\mathbf{1}+S\mathbf{r}+T\mathbf{r}^2...+S\mathbf{*r}^5$ of them and was therefore subject to spectral decomposition (9.3.5d) by C_6-projectors. End of story!

With non-commutative symmetry such as D_3, it is not quite as simple, and indeed, the C_6- story was simplified a bit, too. A D_3 Hamiltonian **H** matrix or a **T**-matrix cannot be built by combining symmetry operators $\{\mathbf{1},\mathbf{r},\,\mathbf{r}^2,\mathbf{i}_1,\mathbf{i}_2,\mathbf{i}_3\}$ from D_3, since some of them (actually <u>most</u> of them) do not commute with one another.

The trick is to build a D_3 Hamiltonian **H** matrix or a **T**-matrix by combining *dual symmetry operators* in $\bar{D}_3 = \left\{ \bar{\mathbf{1}},\bar{\mathbf{r}},\bar{\mathbf{r}}^2,\bar{\mathbf{i}}_1,\bar{\mathbf{i}}_2,\bar{\mathbf{i}}_3 \right\}$ since they <u>all</u> commute with "ordinary" symmetry operators in $D_3 = \{\mathbf{1},\mathbf{r},\mathbf{r}^2,\mathbf{i}_1,\mathbf{i}_2,\mathbf{i}_3\}$. It is only necessary to linearly combine the dual $R(\bar{\mathbf{g}})$ matrices from (15.3.11d) to be guaranteed an **H**-matrix that commutes with all the "ordinary" symmetry operators represented by the $R(\mathbf{g})$ matrices in (15.1.15a). This is done here.

$$\mathbf{H} = H\bar{\mathbf{1}} + R\bar{\mathbf{r}} + R^*\bar{\mathbf{r}}^2 + L\bar{\mathbf{i}}_1 + M\bar{\mathbf{i}}_2 + S\bar{\mathbf{i}}_3 \tag{15.4.2a}$$

$$R^G\left(\mathbf{H}\right) = \begin{array}{c} \langle\mathbf{1}| \\ \langle\mathbf{r}| \\ \langle\mathbf{r}^2| \\ \langle\mathbf{i}_1| \\ \langle\mathbf{i}_2| \\ \langle\mathbf{i}_3| \end{array} \left(\begin{array}{cccccc} H & R & R^* & L & M & S \\ R^* & H & R & M & S & L \\ R & R^* & H & S & L & M \\ L & M & S & H & R & R^* \\ M & S & L & R^* & H & R \\ S & L & M & R & R^* & H \end{array} \right) \tag{15.4.2b}$$

Each of the resulting parameters *H, R, L, M,* and *S* can be visualized as a coupling or tunneling parameter related to the symmetry "path" blazed by the operator it multiplies as sketched in Fig. 15.4.1. These are like the paths for the C_6-symmetric *q-dot* "gizmo" sketched in Fig. 9.2.1.

The new thing here is that now some of the motions characterized by the "paths" do not commute with other motions since they belong to a non-commutative group D_3. D_3 is the smallest non-Abelian group. A vast majority of all the possible groups are *non*-Abelian. (The only exceptions are groups of prime order p which are necessarily Abelian cyclic groups C_p.) So the analysis being discussed here is for the symmetry situation more likely to be encountered. It is also the more interesting one!

$$H = \langle 1|\mathbf{H}|1\rangle = H*$$
$$R = \langle r|\mathbf{H}|1\rangle$$
$$R* = \langle r^2|\mathbf{H}|1\rangle$$
$$L = \langle i_1|\mathbf{H}|1\rangle = L*$$
$$M = \langle i_2|\mathbf{H}|1\rangle = M*$$
$$S = \langle i_3|\mathbf{H}|1\rangle = S*$$
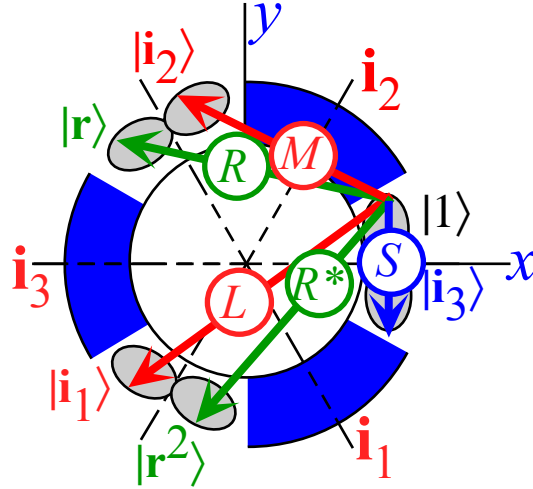
Fig. 15.4.1 Hamiltonian coupling parameters related to D_3 labeled wave coordination states.

The paths blazed by *180°* flips i_1, i_2, and i_3 are labeled by coupling parameters L (for "Long"), M (for "Medium") and S (for "Short"), respectively. The paths blazed by $\pm 120°$ rotations $\mathbf{r}$ and $\mathbf{r}^2$ are labeled R and $R*$. The new idea here is that "path" operations do not always commute.

(a) Reduction of dual operators: Intertwining matrices

With the Hamiltonian expressed in terms of dual operators, its reduction or diagonalization will follow that of the operators from which it is made. The reduction of dual symmetry operators $\overline{\mathbf{g}}$ is similar but not quite the same as that of the ordinary operators $\mathbf{g}$. Both sets have the same group multiplication, and so dual spectral expansions of $\overline{\mathbf{g}}$ into $\overline{\mathbf{P}}_{mn}^\mu$ use the *same* irep coefficients $D^\mu(g)$ as the ordinary operator expansions (15.1.20).

$$\overline{\mathbf{g}} = \sum_\mu \sum_m \sum_n D_{mn}^\mu(g)\,\overline{\mathbf{P}}_{mn}^\mu \quad (15.4.3a) \qquad\qquad \overline{\mathbf{P}}_{mn}^\mu = \frac{\ell^\mu}{{}^oG}\sum_{\mathbf{g}} D_{mn}^{\mu*}(g)\,\overline{\mathbf{g}} \quad (15.4.3b)$$

The duality principle (15.3.8) says dual projectors do the same as ordinary ones with $\left|P_{mn}^\mu\right\rangle \to \left|P_{nm}^{\mu*}\right\rangle$.

$$\overline{\mathbf{P}}_{mn}^\mu\left|1\right\rangle = \frac{\ell^\mu}{{}^oG}\sum_{\mathbf{g}} D_{mn}^{\mu*}(g)\,\overline{\mathbf{g}}\left|1\right\rangle = \frac{\ell^\mu}{{}^oG}\sum_{\mathbf{g}} D_{mn}^{\mu*}(g)\,\mathbf{g}^\dagger\left|1\right\rangle = \frac{\ell^\mu}{{}^oG}\sum_{\mathbf{g}^\dagger} D_{mn}^{\mu*}\left(g^\dagger\right)\mathbf{g}\left|1\right\rangle = \mathbf{P}_{nm}^{\mu*}\left|1\right\rangle \quad (15.4.3c)$$

The regular representation $R^P(\overline{\mathbf{g}})$ in **P**-basis is obtained from $R^P(\mathbf{g})$ just as $R^G(\overline{\mathbf{g}})$ gave $R^P(\mathbf{g})$ in (15.3.11). Roughly speaking, the relation is "star-and-flip", that is, a dagger †. State-$\left|P_{mn}^\mu\right\rangle$ switches with state-$\left|P_{nm}^{\mu*}\right\rangle$. Again, only two bases, $\left|P_{xy}^{E_1}\right\rangle$ and $\left|P_{yx}^{E_1}\right\rangle$, get switched, but, if the ireps were complex they would have to be conjugated (*), too. ($D_{xy}^{E_1} \to D_{xy}^{E_1*}$) Transformation (15.3.10b) demands this.

The result is a duality or pair of *intertwining matrix representations* shown in (15.4.4) below, one set R^P *(g)* for global operators and one set $R^P(\overline{\mathbf{g}})$ for local operators. If $R^P(\mathbf{g})$ is block-diagonalized then $R^P(\overline{\mathbf{g}})$ "block-expands" as in (15.4.4a-b) and vice-versa in (15.4.4c-d).

$R^P(\mathbf{g}) = T R^G(\mathbf{g}) T^\dagger =$

$$
\begin{array}{cccccc}
\left|\mathbf{P}^{A_1}_{xx}\right\rangle & \left|\mathbf{P}^{A_2}_{yy}\right\rangle & \left|\mathbf{P}^{E_1}_{xx}\right\rangle & \left|\mathbf{P}^{E_1}_{yx}\right\rangle & \left|\mathbf{P}^{E_1}_{xy}\right\rangle & \left|\mathbf{P}^{E_1}_{yy}\right\rangle
\end{array}
$$

$$
\begin{pmatrix}
D^{A_1}(\mathbf{g}) & \cdot & \cdot & \cdot & \cdot \\
\cdot & D^{A_2}(\mathbf{g}) & \cdot & \cdot & \cdot \\
\cdot & \cdot & D^{E_1}_{xx}(\mathbf{g}) \ D^{E_1}_{xy}(\mathbf{g}) & \cdot & \cdot \\
\cdot & \cdot & D^{E_1}_{yx}(\mathbf{g}) \ D^{E_1}_{yy}(\mathbf{g}) & \cdot & \cdot \\
\cdot & \cdot & \cdot & \cdot & D^{E_1}_{xx}(\mathbf{g}) \ D^{E_1}_{xy}(\mathbf{g}) \\
 & & & & D^{E_1}_{yx}(\mathbf{g}) \ D^{E_1}_{yy}(\mathbf{g})
\end{pmatrix}
$$

(15.4.4a)

$R^P(\overline{\mathbf{g}}) = T R^G(\overline{\mathbf{g}}) T^\dagger =$

$$
\begin{array}{cccccc}
\left|\mathbf{P}^{A_1}_{xx}\right\rangle & \left|\mathbf{P}^{A_2}_{yy}\right\rangle & \left|\mathbf{P}^{E_1}_{xx}\right\rangle & \left|\mathbf{P}^{E_1}_{yx}\right\rangle & \left|\mathbf{P}^{E_1}_{xy}\right\rangle & \left|\mathbf{P}^{E_1}_{yy}\right\rangle
\end{array}
$$

$$
\begin{pmatrix}
D^{A_1*}(\mathbf{g}) & \cdot & \cdot & \cdot & \cdot \\
\cdot & D^{A_2*}(\mathbf{g}) & \cdot & \cdot & \cdot \\
\cdot & \cdot & D^{E_1*}_{xx}(\mathbf{g}) \quad\cdot & D^{E_1*}_{xy}(\mathbf{g}) \quad\cdot & \\
\cdot & \cdot & \cdot \quad D^{E_1*}_{xx}(\mathbf{g}) & \cdot \quad D^{E_1*}_{xy}(\mathbf{g}) & \\
\cdot & \cdot & D^{E_1*}_{yx}(\mathbf{g}) \quad\cdot & D^{E_1*}_{yy}(\mathbf{g}) \quad\cdot & \\
\cdot & \cdot & \cdot \quad D^{E_1*}_{yx}(\mathbf{g}) & \cdot \quad D^{E_1*}_{yy}(\mathbf{g}) &
\end{pmatrix}
$$

(15.4.4b)

Putting $\left|P^{E_1}_{xy}\right\rangle$ before $\left|P^{E_1}_{yx}\right\rangle$ "quasi-diagonalizes" the dual representation but "expands" the ordinary one.

$\overline{R}^P(\mathbf{g}) = \overline{T} R^G(\mathbf{g}) \overline{T}^\dagger =$

$$
\begin{array}{cccccc}
\left|\mathbf{P}^{A_1}_{xx}\right\rangle & \left|\mathbf{P}^{A_2}_{yy}\right\rangle & \left|\mathbf{P}^{E_1}_{xx}\right\rangle & \left|\mathbf{P}^{E_1}_{xy}\right\rangle & \left|\mathbf{P}^{E_1}_{yx}\right\rangle & \left|\mathbf{P}^{E_1}_{yy}\right\rangle
\end{array}
$$

$$
\begin{pmatrix}
D^{A_1}(\mathbf{g}) & \cdot & \cdot & \cdot & \cdot \\
\cdot & D^{A_2}(\mathbf{g}) & \cdot & \cdot & \cdot \\
\cdot & \cdot & D^{E_1}_{xx}(\mathbf{g}) \quad \cdot & D^{E_1}_{xy}(\mathbf{g}) \quad \cdot & \\
\cdot & \cdot & \cdot \quad D^{E_1}_{xx} & \cdot \quad D^{E_1}_{xy} & \\
\cdot & \cdot & D^{E_1}_{yx}(\mathbf{g}) \quad \cdot & D^{E_1}_{yy}(\mathbf{g}) \quad \cdot & \\
\cdot & \cdot & \cdot \quad D^{E_1}_{yx} & \cdot \quad D^{E_1}_{yy} &
\end{pmatrix}
$$

(15.4.4c)

$\overline{R}^P(\overline{\mathbf{g}}) = \overline{T} R^G(\overline{\mathbf{g}}) \overline{T}^\dagger =$

$$
\begin{array}{cccccc}
\left|\mathbf{P}^{A_1}_{xx}\right\rangle & \left|\mathbf{P}^{A_2}_{yy}\right\rangle & \left|\mathbf{P}^{E_1}_{xx}\right\rangle & \left|\mathbf{P}^{E_1}_{xy}\right\rangle & \left|\mathbf{P}^{E_1}_{yx}\right\rangle & \left|\mathbf{P}^{E_1}_{yy}\right\rangle
\end{array}
$$

$$
\begin{pmatrix}
D^{A_1*}(\mathbf{g}) & \cdot & \cdot & \cdot & \cdot \\
\cdot & D^{A_2*}(\mathbf{g}) & \cdot & \cdot & \cdot \\
\cdot & \cdot & D^{E_1*}_{xx}(\mathbf{g}) \ D^{E_1*}_{xy}(\mathbf{g}) & \cdot & \cdot \\
\cdot & \cdot & D^{E_1*}_{yx}(\mathbf{g}) \ D^{E_1*}_{yy}(\mathbf{g}) & \cdot & \cdot \\
\cdot & \cdot & \cdot & \cdot & D^{E_1*}_{xx}(\mathbf{g}) \ D^{E_1*}_{xy}(\mathbf{g}) \\
\cdot & \cdot & \cdot & \cdot & D^{E_1*}_{yx}(\mathbf{g}) \ D^{E_1*}_{yy}(\mathbf{g})
\end{pmatrix}
$$

(15.4.4d)

Transformations T or $\overline{T}$ reduce the group **g**-based regular representations (15.1.15) and (15.3.11) down to the **P**-based representations. This is simply the change-of-basis between group defined coordination bases $\{..|g\rangle\}$ (15.3.4) and $\left|P^\mu_{mn}\right\rangle$ bases (15.3.5). To be precise, T is the matrix made of the rows in (15.3.5a) and $T^\dagger$ is the matrix made of the columns in (15.3.5b). $\overline{T}$ is just T with the fourth ($P^{E_1}_{xy}$) and fifth ($P^{E_1}_{yx}$) rows switched.

In either basis, any two matrices $R^P(\mathbf{h})$ and $R^P(\overline{\mathbf{g}})$ commute with each other for all **g** and **h**, as do the group-based regular representations $R^G(\mathbf{h})$ and $R^G(\overline{\mathbf{g}})$. Here we verify commutation directly; non-diagonal 2-

by-2 blocks of one R^P must commute with diagonal multiples of the unit matrix in the same matirx blocks of their dual counterparts. It is a remarkable structure. Now we put it to work!

(b) Reduction of a Hamiltonian

From (15.4.4d) comes a reduction of the D_3 Hamiltonian matrix (15.4.2b) to the following form.

$$\bar{R}^P\left(\mathbf{H}\right)=\bar{T}R^G\left(\mathbf{H}\right)\bar{T}^{\dagger}=\begin{array}{c}\left|\mathbf{P}_{xx}^{A_1}\right\rangle\ \left|\mathbf{P}_{yy}^{A_2}\right\rangle\ \left|\mathbf{P}_{xx}^{E_1}\right\rangle\ \ \left|\mathbf{P}_{xy}^{E_1}\right\rangle\ \left|\mathbf{P}_{yx}^{E_1}\right\rangle\ \left|\mathbf{P}_{yy}^{E_1}\right\rangle \\ \left(\begin{array}{cc|cc|cc} H^{A_1} & \cdot & \cdot & \cdot & \cdot & \cdot \\ \cdot & H^{A_2} & \cdot & \cdot & \cdot & \cdot \\ \hline \cdot & \cdot & H_{xx}^{E_1} & H_{xy}^{E_1} & \cdot & \cdot \\ \cdot & \cdot & H_{yx}^{E_1} & H_{yy}^{E_1} & \cdot & \cdot \\ \hline \cdot & \cdot & \cdot & \cdot & H_{xx}^{E_1} & H_{xy}^{E_1} \\ \cdot & \cdot & \cdot & \cdot & H_{yx}^{E_1} & H_{yy}^{E_1} \end{array}\right)\end{array}$$

(15.4.5a)

Eigenvalues H^{A_1}, H^{A_2} or H^{E_1}-elements are derived by writing (15.4.2a) using representation (15.4.4d).

$$H^{A_1}=HD^{A_1*}\left(\mathbf{1}\right)+RD^{A_1*}\left(\mathbf{r}\right)+R^*D^{A_1*}\left(\mathbf{r}^2\right)+LD^{A_1*}\left(\mathbf{i}_1\right)+MD^{A_1*}\left(\mathbf{i}_2\right)+SD^{A_1*}\left(\mathbf{i}_3\right)$$

$$=H+R+R^*+L+M+S$$

$$H^{A_2}=HD^{A_2*}\left(\mathbf{1}\right)+RD^{A_2*}\left(\mathbf{r}\right)+R^*D^{A_2*}\left(\mathbf{r}^2\right)+LD^{A_2*}\left(\mathbf{i}_1\right)+MD^{A_2*}\left(\mathbf{i}_2\right)+SD^{A_2*}\left(\mathbf{i}_3\right)$$

$$=H+R+R^*-L-M-S$$

$$H_{xx}^{E_1}=HD_{xx}^{E_1*}\left(\mathbf{1}\right)+RD_{xx}^{E_1*}\left(\mathbf{r}\right)+R^*D_{xx}^{E_1*}\left(\mathbf{r}^2\right)+LD_{xx}^{E_1*}\left(\mathbf{i}_1\right)+MD_{xx}^{E_1*}\left(\mathbf{i}_2\right)+SD_{xx}^{E_1*}\left(\mathbf{i}_3\right)$$

$$=H-\frac{1}{2}R-\frac{1}{2}R^*-\frac{1}{2}L-\frac{1}{2}M+S$$
(15.4.5b)

$$H_{xy}^{E_1}=HD_{xy}^{E_1*}\left(\mathbf{1}\right)+RD_{xy}^{E_1*}\left(\mathbf{r}\right)+R^*D_{xy}^{E_1*}\left(\mathbf{r}^2\right)+LD_{xy}^{E_1*}\left(\mathbf{i}_1\right)+MD_{xy}^{E_1*}\left(\mathbf{i}_2\right)+SD_{xy}^{E_1*}\left(\mathbf{i}_3\right)$$

$$=0-\frac{\sqrt{3}}{2}R+\frac{\sqrt{3}}{2}R^*-\frac{\sqrt{3}}{2}L+\frac{\sqrt{3}}{2}M+0=H_{yx}^{E_1*}$$

$$H_{yy}^{E_1}=HD_{yy}^{E_1*}\left(\mathbf{1}\right)+RD_{yy}^{E_1*}\left(\mathbf{r}\right)+R^*D_{yy}^{E_1*}\left(\mathbf{r}^2\right)+LD_{yy}^{E_1*}\left(\mathbf{i}_1\right)+MD_{yy}^{E_1*}\left(\mathbf{i}_2\right)+SD_{yy}^{E_1*}\left(\mathbf{i}_3\right)$$

$$=H-\frac{1}{2}R-\frac{1}{2}R^*+\frac{1}{2}L+\frac{1}{2}M-S$$

Evaluation of H-matrix elements requires only the first row $\langle 1|\mathbf{H}|g\rangle$ of the Hamiltonian matrix (15.4.2).

$$H_{ab}^{\mu}=\sum_{g=1}^{°G}\langle 1|\mathbf{H}|g\rangle D_{ab}^{\mu*}\left(g\right)$$

(15.4.5c)

This reduction gives the two singlet eigenvalues.

$$H^{A_1}=H+2\operatorname{Re}R+L+M+S, \quad (15.4.5d) \qquad\qquad H^{A_2}=H+2\operatorname{Re}R-L-M-S \quad (15.4.5e)$$

Then a pair of identical two-by-two matrices may, if $L\neq M$ or $\operatorname{Im}R\neq 0$, still need further diagonalization.

$$\left(\begin{array}{cc} H_{xx}^{E_1} & H_{xy}^{E_1} \\ H_{yx}^{E_1} & H_{yy}^{E_1} \end{array}\right)=\left(\begin{array}{cc} H-\operatorname{Re}R+S-\dfrac{L+M}{2} & -\sqrt{3}\left(\dfrac{L\text{-}M}{2}+i\operatorname{Im}R\right) \\ -\sqrt{3}\left(\dfrac{L\text{-}M}{2}-i\operatorname{Im}R\right) & H-\operatorname{Re}R-S+\dfrac{L+M}{2} \end{array}\right)$$

(15.4.5f)

(1) Non-commutative spectra: Mandatory degeneracy

This is as far as a non-commutative symmetry analysis can go without further information. Just as the regular representation of group cannot be completely diagonalized, so also will a complete *analytic* diagonalization of the general dual operator set be impossible. Unlike the commutative or Abelian C_6 eigenvectors in Ch. 9, the non-commutative E_1 symmetry eigenvectors are not set in stone but depend on internal coupling parameters. This is an important difference between commutative and non-commutative symmetry calculations.

Another more widely known difference is *mandatory degeneracy*. No matter what the (real) values of the parameters H, ReR, ImR, L, M, and S, the two E_1 eigenvalues must remain degenerate because of the two identical 2-by-2 matrices (15.4.5f) in the Hamiltonian matrix (15.4.5a). Even if the R parameter is complex the E_1 levels stick together and remain doublets. For C_6 symmetry, Zeeman splitting happens if tunneling is complex, (Recall discussion of Fig. 9.3.2), but not if D_3 (or D_6) symmetry is present. (Complex L, M, and S would bust D_3 down to C_3 and make a non-conservative $\mathbf{H} \neq \mathbf{H}^\dagger$.) Dual operator analysis proves, *en passant*, the *degeneracy theorem*:

Irreducible G-symmetry representations of dimension ℓ^μ project eigenstates of at least degeneracy ℓ^μ for all Hamiltonian operators with G symmetry.

(2) G*G Super-symmetry

While μ-symmetry eigenstates cannot have less degeneracy than ℓ^μ, it is possible to have greater degeneracy for some parameter values. A "super" degeneracy arises when a Hamiltonian $\mathbf{H}$ commutes with both $\mathbf{g}$ in its symmetry G <u>and</u> all $\bar{\mathbf{g}}$ in its dual symmetry $\bar{G}$, in what is $G \times \bar{G}$ symmetry. Such an all-commuting $\mathbf{H}$ must be a combination of all-commuting projectors $\mathbb{P}^\mu$, and each $\mathbb{P}^\mu$ reduces to ℓ^μ identical multiples of ℓ^μ-by-ℓ^μ unit matrices or an $(\ell^\mu)^2$ degeneracy. This proves a *super-degeneracy theorem*.

Irreducible G-symmetry representations of dimension ℓ^μ project eigenstates of at least degeneracy$(\ell^\mu)^2$ for all Hamiltonian operators with $G \times \bar{G}$ symmetry.

The Hamiltonian (15.4.2) has $D_3 \times \bar{D}_3$ symmetry with equal tunneling parameters ($L=M=S$) and real rotational tunneling ($R^*=R$). Such an $\mathbf{H}$ is a combination of classes $\mathbf{c}_1$, $\mathbf{c}_r$, and $\mathbf{c}_i$ or $\mathbb{P}^{A_1}$, $\mathbb{P}^{A_2}$, and $\mathbb{P}^{E_1}$. Because of this, both E_1 eigenvalues have to join into a single value ($e^{E_1}=H\text{-}R$) with a degeneracy of four.

(c) U(2) Analysis of local symmetry

As may be done for any two-state system, a $U(2)$ analysis of the residual Hamiltonian matrix (15.4.5f) helps to derive and characterize eigensolutions. Here the complex rotational coupling is written: $R=\rho + iI$. The Hamilton-Jordan-Pauli spin vector expansion (10.1.7) is carried out on the H-matrix.

$$\mathbf{H}/\hbar = \frac{1}{2}(A+D)\ \sigma_0\ + 2B\ \mathbf{S}_B\ + 2C\ \mathbf{S}_C + (A-D)\ \mathbf{S}_A$$

$$\mathbf{H}/\hbar = \Omega_0\ \sigma_0\ +\Omega_B\ \mathbf{S}_B +\Omega_C\ \mathbf{S}_C\ +\Omega_A\ \mathbf{S}_A$$

$$\begin{pmatrix} H-\rho+S -\dfrac{L+M}{2} & -\sqrt{3}\left(\dfrac{L\text{-}M}{2}+iI\right) \\[3mm] -\sqrt{3}\left(\dfrac{L\text{-}M}{2}-iI\right) & H-\rho\text{-}S +\dfrac{L+M}{2} \end{pmatrix} = (H-\rho)\mathbf{1}-\sqrt{3}\dfrac{L\text{-}M}{2}\sigma_X + I\sigma_Y + \dfrac{2S-L\text{-}M}{2}\sigma_Z$$

$$= (H-\rho)\ \sigma_0 -\sqrt{3}(L\text{-}M)\mathbf{S}_B +2I\ \mathbf{S}_C+(2S-L\text{-}M)\mathbf{S}_A \tag{15.4.6}$$

If R coupling is real *(I=0)* and intra-well coupling S dominates inter-well amplitudes *(S>>M>L)* then the Hamiltonian crank vector $\Theta=\Omega t$ makes only a small angle ϑ with the A-axis (or Pauli-Z-axis). There can be only a tiny $\sin\vartheta$ component along the B-axis (Pauli-X-axis). With *(I=0)* there can be no circular or C-axis component at all, so azimuth is zero ($\varphi=0$). Combining equations (10.5.20) and (10.5.25) with (15.4.6) above gives Ω.

$$\bar{\Omega} = \begin{pmatrix} \Omega_B & \Omega_C & \Omega_A \end{pmatrix} = |\Omega|\begin{pmatrix} \sin\vartheta & 0 & \cos\vartheta \end{pmatrix} = \begin{pmatrix} \sqrt{3}(M\text{-}L) & 0 & (2S-L-M) \end{pmatrix}$$

$$\text{where: } |\Omega| = \sqrt{\Omega_B^2+\Omega_A^2} = 2\sqrt{S^2 - S(L+M)+M(M\text{-}L)+L^2} \cong 2S \tag{15.4.7}$$

$$\text{and: } \Omega_0 = H-\rho$$

This means that the H-eigenvectors, which have spin vectors aligned or anti aligned to Ω, are the following nearly-spin-up $(+A)$ and nearly-spin-down $(-A)$ states. (Here (10.5.8a) is used with $\beta=\vartheta$ and $\alpha=\varphi=0$.)

$$|\varepsilon(+)\rangle = \begin{pmatrix} \cos\dfrac{\vartheta}{2} \\[2mm] \sin\dfrac{\vartheta}{2} \end{pmatrix} \cong \begin{pmatrix} 1 \\ 0 \end{pmatrix}, \qquad |\varepsilon(-)\rangle = \begin{pmatrix} -\sin\dfrac{\vartheta}{2} \\[2mm] \cos\dfrac{\vartheta}{2} \end{pmatrix} \cong \begin{pmatrix} 0 \\ 1 \end{pmatrix}, \text{ where: } \tan\vartheta = \dfrac{\sqrt{3}(M-L)}{2S-L-M} << 1 \tag{15.4.8a}$$

The corresponding eigenvalues are

$$\varepsilon(+)=\Omega_0 +\frac{|\Omega|}{2} \cong H\text{-}\rho+S\ , \qquad \varepsilon(-)=\Omega_0 -\frac{|\Omega|}{2} \cong H\text{-}\rho\text{-}S. \tag{15.4.8b}$$

So, the eigenstates are nearly equal to the D_3 projected states since H is nearly diagonal.

$$|\varepsilon(+)\rangle = \cos\frac{\vartheta}{2}\left|{}^{E_1}_{mx}\right\rangle + \sin\frac{\vartheta}{2}\left|{}^{E_1}_{my}\right\rangle, \qquad |\varepsilon(-)\rangle = -\sin\frac{\vartheta}{2}\left|{}^{E_1}_{mx}\right\rangle + \cos\frac{\vartheta}{2}\left|{}^{E_1}_{my}\right\rangle$$

$$\cong \left|{}^{E_1}_{mx}\right\rangle \qquad\qquad , \qquad\qquad \cong \left|{}^{E_1}_{my}\right\rangle \text{ (where: } m = x, y) \tag{15.4.8c}$$

Eigenstates will have local symmetry which approximates that of local x and y components, that is, symmetry and anti-symmetry, as seen in Fig. 15.3.3 (sketched in Fig. 15.3.2). Local wave symmetry in each well depends on relative strength of the local or "Short" coupling coefficient S versus distant (and presumably weaker) coupling connections M ("Medium") and L ("Long") in Fig. 15.4.1.

Building a barrier in the middle of the well or reducing the barriers between the wells would change the relative magnitudes of these parameters and alter the local symmetry of eigenstates and energy. Local symmetry labeled by right indices ($n=x,y$) in state $\left| P_{mn}^{E_1} \right\rangle$ will vary as the internal locale changes.

But, global symmetry, the "other side of the coin," is determined by the left indices ($m=x,y$) in state $\left| P_{mn}^{E_1} \right\rangle$. Taking linear combinations of eigenstates with different m-values, $m=x$ or $m=y$, makes a full *U(2)-ABC* range of possibilities from *A*-type standing waves with global x and y symmetry (as in Figs. 15.3.2 and 15.3.3), or else *C*-type moving waves, or *AB*-type standing waves that stand partly in and partly out of the barriers, or even ABC-type galloping waves. The *mandatory global degeneracy* of the *D₃* symmetry demands that this great *U(2)* variety of global wave shapes all have exactly the same energy!

Dual space eigenvector analysis resolves apparent conflicts between global and local symmetry. In particular, the state $\left| P_{xy}^{E_1} \right\rangle$ has symmetric *(x)* global symmetry but anti-symmetric *(y)* local symmetry. The state $\left| P_{yx}^{E_1} \right\rangle$ has the same conflict *vice-versa*. This is a conflict with respect to the well (or barrier) on the *x*-axis because that is the one which has the axis of the global $\mathbf{i}_3$ operator that was chosen to be diagonal and therefore $\mathbf{i}_3$ eigen-values determines global symmetry about the *x*-axis according to (15.3.10c). Having chosen $\mathbf{i}_3$ for this job automatically makes the dual operator $\bar{\mathbf{i}}_3$ the one which determines local symmetry according to (15.3.10d) in all the wells including the one containing both $\mathbf{i}_3$ and $\bar{\mathbf{i}}_3$.

For the "local-conflict states" $\left| P_{xy}^{E_1} \right\rangle$ or $\left| P_{yx}^{E_1} \right\rangle$, the wave in the well (or barrier) on the *x*-axis must be both symmetric and anti-symmetric. The only way this can happen is if the wave in this particular well is identically zero as in the sketches in Fig. 15.3.2. The wave is "forbidden" to occupy the well in conflict. But, the numerically "exact" wavefunctions in Fig. 15.3.3, particularly for the higher energy state $\left| P_{xy}^{E_1} \right\rangle$, show a small amount of wave in the "forbidden" well and in each case it has the "wrong" local symmetry.

The eigenstates (15.4.8) explain what has happened. A small ($\sin\vartheta/2 \ll 1$) component with the "wrong" symmetry will be present in any state that has the slightest connection to the world outside of the well in question. The situation is analogous to the "non-resonant eigenchannels" in Fig. 14.1.13 which always have the opposite symmetry of their resonant partners with the same energy. The non-resonant eigenchannel waves have relatively small amplitudes inside the regions where their resonant partners are enormous, but then the job of the non-resonant state is to maintain a big wave presence outside where the resonant waves are relatively small or, in the "bound-state" limit, practically non-existent.

In the *D₃* wells the "wrong" local symmetry components are needed to keep the wave alive inside the "conflicting" wells and to "grow-up" and contribute to the required global symmetry outside the well. This "wrong-local-symmetry" component becomes dominant as the energy rises or the walls come down and the concept of "locality" loses its meaning since waves are no longer so trapped. When the walls are gone only global symmetry maintains a physical significance. Nothing is left to define relative location. We'll say it again; local or dual symmetry considerations are powerful and anything but trivial!

15.5 D_6 symmetry and Hexagonal Bands

Hexagonal D_6 symmetry is made by combining groups C_2 and D_3. This is one of those rare and welcome cases where such a combination *is* a cross product: D_6 is the product $D_3 \times C_2$ of D_3 and C_2.

$$D_6 = D_3 \times C_2 = \{1, r, r^2, i_1, i_2, i_3 \} \times \{1, R_z\} \qquad (15.5.1a)$$

The $C_2 = \{1, R_z\}$ group has the *180° z-axis rotation* R_z. Both elements of C_2 commute with all elements of $D_3 = \{1, r, r^2, i_1, i_2\ i_3 \}$ because classical orthogonal *180°* rotations commute ($R_z\, i_a = i_a\, R_z$, just like in D_2.) as do co-axial *z*-rotations ($R_z\, r^n = r^n\, R_z$). So derivation of D_6 group and irep properties is reduced to simple multiplication and tabulation. First, we do the $\times$ product and identify operations in Fig. 15.5.1.

$$D_6 = D_3 \times C_2 = \{1, r, r^2, i_1, i_2\ i_3, 1{\cdot}R_z, r{\cdot}R_z, r^2{\cdot}R_z, i_1{\cdot}R_z, i_2{\cdot}R_z, i_3\ {\cdot}R_z\} \qquad (15.5.1b)$$

$$D_6 = D_3 \times C_2 = \{1, h^2, h^4, i_1, i_2\ i_3, h^3, \quad h^5, \quad h, \quad j_1, \quad j_2, \quad j_3 \ \} \qquad (15.5.1c)$$

Recall from the D_2. group in Fig. 3.6.1 that a product of two orthogonal *180°* rotations like $i_3\ {\cdot}R_z$ is another *180°* rotation, in this case j_3, around the axis orthogonal to the other two. Also, the product of $\pm120°$ z-rotations r and r^2 with R_z is another z-rotation by *180°*$\pm120°$, or a *300°* rotation labeled $h^5 = r{\cdot}R_z$ and a *60°* rotation labeled $h = r^2{\cdot}R_z$. The latter is the *hexagonal generator* h of subgroup $C_6 = \{1, h, h^2, h^3, h^4\ h^5\}$ Note: $h^3 = R_z$ and $h^2 = r$.
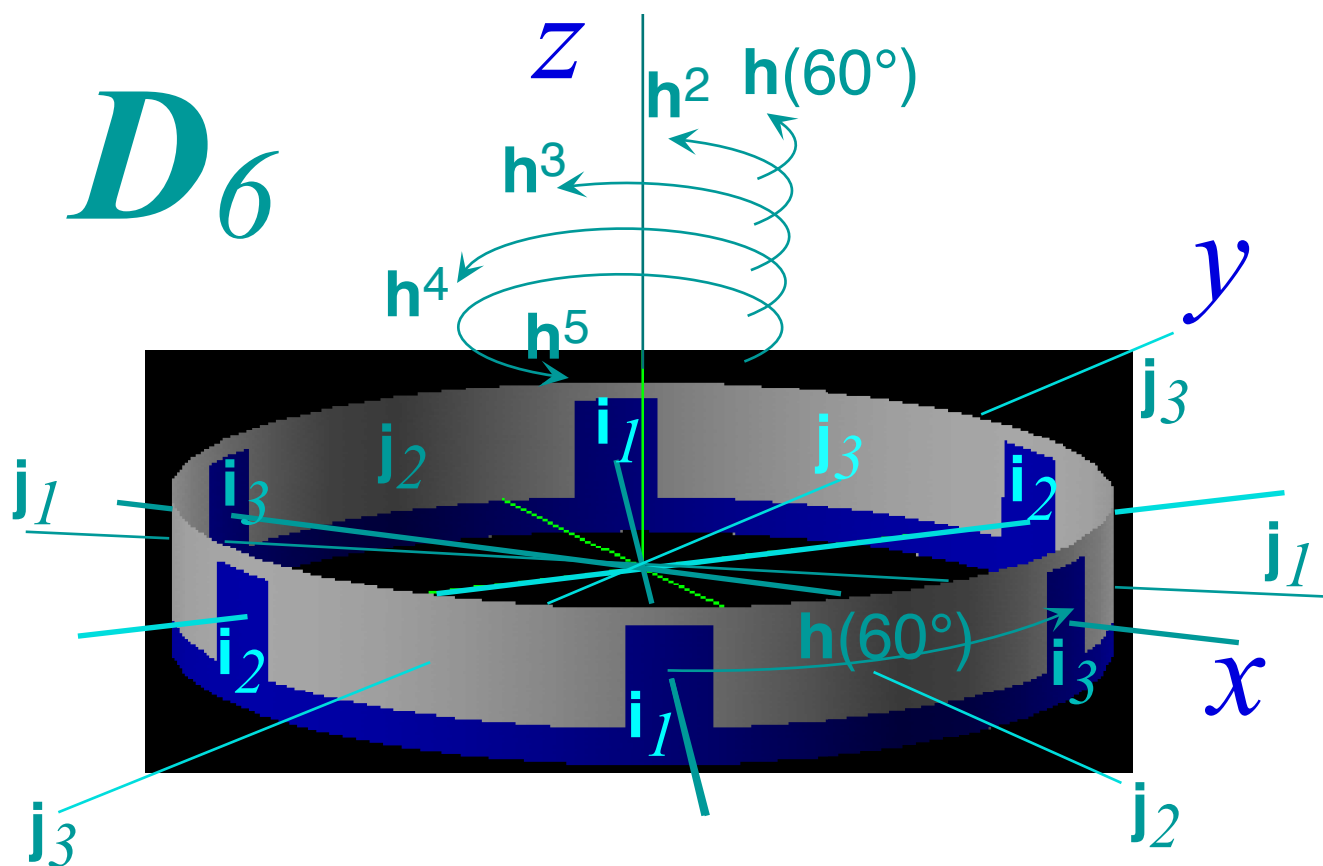
Fig. 15.5.1 D_6 symmetry operations generated by D_3 and C_2.

Fig. 15.5.1 shows that the "old" *180°* flip-over rotations $\{i_1, i_2, i_3 \}$ from D_3 now rotate around barrier centers while the "new" *180°* flip-over rotations $\{j_1, j_2, j_3 \}$ in D_6 rotate around well centers. Again, remember

that these do <u>not</u> flip over the potential plot. The potential is an electrostatic or molecular potential and doesn't care which way is "up." Wells remain wells, and barriers remain barriers under all D_6 operations.

The cross product of the C_2 and D_3 characters (15.1.13) lead to a complete set of $D_6 = D_3 \times C_2$ characters just as we get $C_2 \times C_2 = D_2$ characters from those of two C_2 groups in (15.1.4).

D_3	1	$\{r, r^2\}$	$\{i_1, i_2, i_3\}$
$\chi^{A_1}(g)$	1	1	1
$\chi^{A_2}(g)$	1	1	−1
$\chi^{E_1}(g)$	2	−1	0

$\times$

C_2^z	1	R_z
(A)	1	1
(B)	1	−1

$=$

$D_3 \times C_2^z$	1	$\{r, r^2\}$	$\{i_1, i_2, i_3\}$	$1 \cdot R_z$	$\{r, r^2\} \cdot R_z$	$\{i_1, i_2, i_3\} \cdot R_z$
$A_1 \cdot (A)$	$1 \cdot 1$	$1 \cdot 1$	$1 \cdot 1$	$1 \cdot 1$	$1 \cdot 1$	$1 \cdot 1$
$A_2 \cdot (A)$	$1 \cdot 1$	$1 \cdot 1$	$-1 \cdot 1$	$1 \cdot 1$	$1 \cdot 1$	$-1 \cdot 1$
$E_1 \cdot (A)$	$2 \cdot 1$	$-1 \cdot 1$	$0 \cdot 1$	$2 \cdot 1$	$-1 \cdot 1$	$0 \cdot 1$
$A_1 \cdot (B)$	$1 \cdot 1$	$1 \cdot 1$	$1 \cdot 1$	$1 \cdot (-1)$	$1 \cdot (-1)$	$1 \cdot (-1)$
$A_2 \cdot (B)$	$1 \cdot 1$	$1 \cdot 1$	$-1 \cdot 1$	$1 \cdot (-1)$	$1 \cdot (-1)$	$-1 \cdot (-1)$
$E_1 \cdot (B)$	$2 \cdot 1$	$-1 \cdot 1$	$0 \cdot 1$	$2 \cdot (-1)$	$-1 \cdot (-1)$	$0 \cdot (-1)$

$=$

$D_6 \times C_2^z$	1	$\{h^2, h^4\}$	$\{i_1, i_2, i_3\}$	h^3	$\{h, h^5\}$	$\{j_1, j_2, j_3\}$
A_1	1	1	1	1	1	1
A_2	1	1	−1	1	1	−1
E_2	2	−1	0	2	−1	0
B_2	1	1	1	−1	−1	−1
B_1	1	1	−1	−1	−1	1
E_1	2	−1	0	−2	1	0

(15.5.2)

The Cartesian coordinates are arranged so that the $180°$ i_3 axis lies on the x axis and the j_3 flip-over axis then goes along the y-axis. The three orthogonal $180°$ rotations h^3, j_3, and i_3 make a D_2 *subgroup* of D_6 .

$$D_2(x,y,z) = \{ 1, R_z, R_y, R_x \} = \{ 1, h^3, j_3, i_3 \} \qquad (15.5.3)$$

It is these operation that we prefer to "favor" as "chosen" to have diagonal ireps. Also, it is the first two $180°$ rotations, h^3 and j_3, that are chosen to label "A" or "B-ness" and "1" or "2-ness" of singlet states.

Flip j_3 is chosen since it's on the y-axis and, as shown in Sec. 10.2c, y-or-C-rotations are the only ones that have real rotation matrix representations. (Jordan-Hamilton generator σ_Y is the only pure imaginary σ, so R_Y $(\beta) = e^{-i\sigma_Y\beta/2}$ is the only real rotation R.) Avoidance of complex parity assignments is behind this convention. So A_2 and B_2 go with (-1) j-eigenvalues in (15.5.2), while A_1 and B_1 go with (+1) j-eigenvalues. Meanwhile, A_1 and A_2 go with (+1) h-or h^3-eigenvalues, while, B_1 and B_2 go with (-1) h-or h^3-eigenvalues.

To understand the E_1 and E_2 labeling (which looks out of place in (15.5.2)) or, for that matter, any E_m labeling for a general D_N irep, we need to look closely at the fundamental generator h for z-rotation by angle $2\pi/N$ (For D_6 this angle is $2\pi/6=60°$). All E_m ireps have complex conjugate pairs of eigenvalues that are the m-th multiples of the first of the N-th roots of unity, that is, the m-th C_N character labeled by $\pm m_N = \pm m$-modulo-N in the C_N tables ($N=1, 2,..., 6$) of Fig. 7.3.3. These are the m-th Bohr-Bloch wave function pairs. The first and lowest Bohr doublet has to quantum numbers $m=\pm 1$ of the 2-by-2 irep E_1.

$$D^{E_1}(h) = \begin{pmatrix} \langle +1_6 | h | +1_6 \rangle & \langle +1_6 | h | -1_6 \rangle \\ \langle -1_6 | h | +1_6 \rangle & \langle -1_6 | h | -1_6 \rangle \end{pmatrix} = \begin{pmatrix} e^{-i2\pi/6} & 0 \\ 0 & e^{+i2\pi/6} \end{pmatrix} = \begin{pmatrix} \varepsilon_{-1} & 0 \\ 0 & \varepsilon_{+1} \end{pmatrix} = D^{E}(h^{-1}) \qquad (15.5.4a)$$

For $N=6$ there is one more 2-by-2 irep of D_6 labeled E_2. It belongs to Bohr quantum numbers $m=\pm 2$.

$$D^{E_2}(\mathbf{h}) = \begin{pmatrix} \langle +2_6|\mathbf{h}|+2_6\rangle & \langle +2_6|\mathbf{h}|-2_6\rangle \\ \langle -2_6|\mathbf{h}|+2_6\rangle & \langle -2_6|\mathbf{h}|-2_6\rangle \end{pmatrix} = \begin{pmatrix} e^{-2i2\pi/6} & 0 \\ 0 & e^{+2i2\pi/6} \end{pmatrix} = \begin{pmatrix} \varepsilon_{-2} & 0 \\ 0 & \varepsilon_{+2} \end{pmatrix} = D^{E_2^*}(\mathbf{h}^{-1}) \qquad (15.5.4a)$$

The trace of E_1 and E_2 confirms their character values in the $\{\mathbf{h},\mathbf{h}^5\}$ column of D_6 table (15.5.2).

$$\begin{aligned} Trace\, D^{E_1}(\mathbf{h}) &= e^{i2\pi/6} + e^{-i2\pi/6}, \\ &= 2\cos 2\pi/6 \quad = 1 = \chi^{E_1}(\mathbf{h}). \end{aligned} \qquad (15.5.5a)$$

$$\begin{aligned} Trace\, D^{E_2}(\mathbf{h}) &= e^{i4\pi/6} + e^{-i4\pi/6} \\ &= 2\cos 4\pi/6 = -1 = \chi^{E_2}(\mathbf{h}) \end{aligned} \qquad (15.5.5b)$$

The representation of D_6 rotation $\mathbf{h}$ for Bohr quantum numbers $m=\pm 3$ is just **-1** .

$$\begin{pmatrix} \langle +3_6|\mathbf{h}|+3_6\rangle & \langle +3_6|\mathbf{h}|-3_6\rangle \\ \langle -3_6|\mathbf{h}|+3_6\rangle & \langle -3_6|\mathbf{h}|-3_6\rangle \end{pmatrix} = \begin{pmatrix} e^{-3i2\pi/6} & 0 \\ 0 & e^{+3i2\pi/6} \end{pmatrix} = \begin{pmatrix} -1 & 0 \\ 0 & -1 \end{pmatrix} \qquad (15.5.6)$$

No E_3 label is needed for D_6 because the C_6 waves 3_6 and -3_6 are identical C_6 labels since $\pm 3\ mod\ 6 = \mp 3$. For D_6 the values $m=\pm 3$ correspond to 1st Brillouin band boundary B_1 and B_2-waves. Recall the B_1 and B_2 "band-gap" levels in the $N=6$ side of Fig. 14.2.8. (See below how $\langle 3_6|\mathbf{g}|3_6\rangle$ reduces to B_1 and B_2.)

No higher E_4 or E_5 labels are needed for D_6, either. E_4 is just E_2 and E_5 is just E_1 since $\pm 4\ mod\ 6 = \mp 2$ and $\pm 5\ mod\ 6 = \mp 1$. E_m-labeling stops with m just short of half-way to N, and for even-N, the $m=N/2$ waves are B-type "Back-and-forth" waves. (D_3 has no B's since $N=3$ is odd. See $N=3$ side of Fig. 14.2.8.)

Once again, we pick which $180°$ rotation will directly convert a left-moving wave base $|+m_6\rangle$ into a right-moving base $|-m_6\rangle$ and vice-versa. For D_6 it's convenient to let the sine and cosine parts have a node and anti-node, respectively, on the x-axis or $\mathbf{i}_3$ axis, that is, let: $\mathbf{i}_3\,|+m_6\rangle = |-m_6\rangle$ and $\mathbf{i}_3\,|-m_6\rangle = |+m_6\rangle$.

$$D^{E_m}(\mathbf{i}_3) = \begin{pmatrix} \langle +m_6|\mathbf{i}_3|+m_6\rangle & \langle +m_6|\mathbf{i}_3|-m_6\rangle \\ \langle -m_6|\mathbf{i}_3|+m_6\rangle & \langle -m_6|\mathbf{i}_3|-m_6\rangle \end{pmatrix} = \begin{pmatrix} 0 & 1 \\ 1 & 0 \end{pmatrix}, \quad D^{E_m}(\mathbf{j}_3) = (-1)^m D^{E_m}(\mathbf{i}_3) \qquad (15.5.7)$$

Then other representations of D_6 are found by the D_3 group table in Fig. 15.1.2 and matrix multiplication of (15.5.4) through (15.5.7), or else we use the cross product relation $D_6 = D_3 \times C_2$ and D_3 irreps.

Circularly polarized moving-wave E_m bases $\{|+m_6\rangle, |-m_6\rangle\}$ are related to real cosine-and-sine (linearly polarized) standing wave bases $\{|cm_6\rangle, |sm_6\rangle\}$ by $\sqrt{2}\,|\pm m\rangle = |c\rangle \pm i|s\rangle$ or $e^{\pm im\phi}=\cos m\phi \pm i\sin m\phi$.

$$\begin{aligned} |cm_6\rangle &= (\,|+m_6\rangle + |-m_6\rangle)/\sqrt{2}, & |+m_6\rangle &= (|cm_6\rangle + i|sm_6\rangle)/\sqrt{2} \\ |sm_6\rangle &= (\,|+m_6\rangle - |-m_6\rangle)/i\sqrt{2}, & |-m_6\rangle &= (|cm_6\rangle - i|sm_6\rangle)/\sqrt{2} \end{aligned} \qquad (15.5.8)$$

Then $D^{Em}(\mathbf{h})$ becomes a real rotation matrix while the y-axis $180°$ flip $\mathbf{j}_3$ representation becomes diagonal .

$$D^{E_1}_{c,s}(\mathbf{h}) = \begin{pmatrix} \langle cm_6|\mathbf{h}|cm_6\rangle & \langle cm_6|\mathbf{h}|sm_6\rangle \\ \langle sm_6|\mathbf{h}|cm_6\rangle & \langle sm_6|\mathbf{h}|sm_6\rangle \end{pmatrix} = \begin{pmatrix} \cos m\dfrac{2\pi}{6} & -\sin m\dfrac{2\pi}{6} \\ \sin m\dfrac{2\pi}{6} & \cos m\dfrac{2\pi}{6} \end{pmatrix}, \quad D^{E_1}_{c,s}(\mathbf{j}_3) = \begin{pmatrix} \langle cm_6|\mathbf{j}_3|cm_6\rangle & \langle cm_6|\mathbf{j}_3|sm_6\rangle \\ \langle sm_6|\mathbf{j}_3|cm_6\rangle & \langle sm_6|\mathbf{j}_3|sm_6\rangle \end{pmatrix} = \begin{pmatrix} 1 & 0 \\ 0 & -1 \end{pmatrix}$$

$$(15.5.9a) \qquad\qquad\qquad\qquad\qquad\qquad (15.5.9b)$$

For $m=\pm 3$, the $|\pm m_6\rangle$-bases do not support an irreducible representation. It reduces to B_1 and B_2 ireps.

$$\begin{pmatrix} \langle c3_6|\mathbf{h}|c3_6\rangle & \langle c3_6|\mathbf{h}|s3_6\rangle \\ \langle s3_6|\mathbf{h}|c3_6\rangle & \langle s3_6|\mathbf{h}|s3_6\rangle \end{pmatrix} = \begin{pmatrix} -1 & 0 \\ 0 & -1 \end{pmatrix} = \begin{pmatrix} D^{B_1}(\mathbf{h}) & 0 \\ 0 & D^{B_2} \end{pmatrix}, \quad \begin{pmatrix} \langle c3_6|\mathbf{j}_3|c3_6\rangle & \langle c3_6|\mathbf{j}_3|s3_6\rangle \\ \langle s3_6|\mathbf{j}_3|c3_6\rangle & \langle s3_6|\mathbf{j}_3|s3_6\rangle \end{pmatrix} = \begin{pmatrix} 1 & 0 \\ 0 & -1 \end{pmatrix} = \begin{pmatrix} D^{B_1}(\mathbf{j}_3) & 0 \\ 0 & D^{B_2} \end{pmatrix}$$

$$(15.5.9c) \qquad\qquad\qquad\qquad\qquad\qquad\qquad (15.5.9d)$$

This is a subtle effect demanded by D_6 symmetry: for $|m|=3$, <u>moving</u> wave $\{|+m_6\rangle, |-m_6\rangle\}$ bases are *forbidden* to be eigenstates and *required* to combine into cosine and sine <u>standing</u> wave $\{|cm_6\rangle, |sm_6\rangle\}$ bases which belong to B_1 and B_2 <u>singlets</u> of differing energies. The E_3, E_4, E_5 or higher doublet labels are not used by D_6 symmetry. Since *4 mod 6=-2*, E_4 is just E_2, and *5 mod 6=-1* means E_5 is E_1.

     All D_N symmetries with even-N will place similar requirements on the quantum states with $|m|=N/2$ found at the first Brillouin band boundary. The band sequence for general even-N is as follows

A_1, E_1, E_2, E_3, ..., $E_{N/2-1}$, B_1 (gap) B_2, $E_{N/2-1}$,..., E_3, E_2, E_1, A_2 (gap)...[repeat] (15.5.10a)

The band sequence for odd-N is about the same but without B-boundaries on the odd-numbered gaps.

A_1, E_1, E_2, E_3, ..., $E_{(N-1)/2}$ (gap) $E_{(N-1)/2}$,..., E_3, E_2, E_1, A_2 (gap)...[repeat] (15.5.10b)

This structure is seen in Fig. 14.2.8 and will be encountered again in discussions which follow. The D_6 ireps (15.5.1) are constructed following the cross product structure used in (15.5.2). Note $\mathbf{j}_3$.

| $g =$ | $\mathbf{1}$ | $\mathbf{r}=\mathbf{h}^2$ | $\mathbf{r}^2=\mathbf{h}^4$ | $\mathbf{i}_1$ | $\mathbf{i}_2$ | $\mathbf{i}_3$ | $\mathbf{h}^3$ | $\mathbf{h}^3\mathbf{r}=\mathbf{h}^5$ | $\mathbf{h}^3\mathbf{r}^2=\mathbf{h}^1$ | $\mathbf{h}^3\mathbf{i}_1=\mathbf{j}_1$ | $\mathbf{h}^3\mathbf{i}_2=\mathbf{j}_2$ | $\mathbf{h}^3\mathbf{i}_3=\mathbf{j}_3$ |

$$D^{A_1}(g) = 1, \quad 1, \quad 1, \quad 1, \quad 1, \quad 1, \quad 1, \quad 1, \quad 1, \quad 1, \quad 1, \quad 1$$

$$D^{A_1}(g) = 1, \quad 1, \quad 1, \quad -1, \quad -1, \quad -1, \quad 1, \quad 1, \quad 1, \quad -1, \quad -1, \quad -1$$

$$D^{E_2}(g) = \begin{pmatrix} 1 & 0 \\ 0 & 1 \end{pmatrix}, \begin{pmatrix} \frac{-1}{2} & \frac{-\sqrt{3}}{2} \\ \frac{\sqrt{3}}{2} & \frac{-1}{2} \end{pmatrix} \begin{pmatrix} \frac{-1}{2} & \frac{\sqrt{3}}{2} \\ \frac{-\sqrt{3}}{2} & \frac{-1}{2} \end{pmatrix}, \begin{pmatrix} \frac{-1}{2} & \frac{-\sqrt{3}}{2} \\ \frac{-\sqrt{3}}{2} & \frac{1}{2} \end{pmatrix} \begin{pmatrix} \frac{-1}{2} & \frac{\sqrt{3}}{2} \\ \frac{\sqrt{3}}{2} & \frac{1}{2} \end{pmatrix}, \begin{pmatrix} 1 & 0 \\ 0 & -1 \end{pmatrix} \begin{pmatrix} 1 & 0 \\ 0 & 1 \end{pmatrix}, \begin{pmatrix} \frac{-1}{2} & \frac{-\sqrt{3}}{2} \\ \frac{\sqrt{3}}{2} & \frac{-1}{2} \end{pmatrix} \begin{pmatrix} \frac{-1}{2} & \frac{\sqrt{3}}{2} \\ \frac{-\sqrt{3}}{2} & \frac{-1}{2} \end{pmatrix}, \begin{pmatrix} \frac{-1}{2} & \frac{-\sqrt{3}}{2} \\ \frac{-\sqrt{3}}{2} & \frac{1}{2} \end{pmatrix} \begin{pmatrix} \frac{-1}{2} & \frac{\sqrt{3}}{2} \\ \frac{\sqrt{3}}{2} & \frac{1}{2} \end{pmatrix}, \begin{pmatrix} 1 & 0 \\ 0 & -1 \end{pmatrix}$$

$$D^{B_2}(g) = 1, \quad 1, \quad 1, \quad 1, \quad 1, \quad 1, \quad -1, \quad -1, \quad -1, \quad -1, \quad -1, \quad -1$$

$$D^{B_1}(g) = 1, \quad 1, \quad 1, \quad -1, \quad -1, \quad -1, \quad -1, \quad -1, \quad -1, \quad 1, \quad 1, \quad 1$$

$$D^{E_1}(g) = \begin{pmatrix} 1 & 0 \\ 0 & 1 \end{pmatrix}, \begin{pmatrix} \frac{-1}{2} & \frac{-\sqrt{3}}{2} \\ \frac{\sqrt{3}}{2} & \frac{-1}{2} \end{pmatrix} \begin{pmatrix} \frac{-1}{2} & \frac{\sqrt{3}}{2} \\ \frac{-\sqrt{3}}{2} & \frac{-1}{2} \end{pmatrix}, \begin{pmatrix} \frac{-1}{2} & \frac{-\sqrt{3}}{2} \\ \frac{-\sqrt{3}}{2} & \frac{1}{2} \end{pmatrix} \begin{pmatrix} \frac{-1}{2} & \frac{\sqrt{3}}{2} \\ \frac{\sqrt{3}}{2} & \frac{1}{2} \end{pmatrix}, \begin{pmatrix} 1 & 0 \\ 0 & -1 \end{pmatrix} \begin{pmatrix} -1 & 0 \\ 0 & -1 \end{pmatrix}, \begin{pmatrix} \frac{1}{2} & \frac{\sqrt{3}}{2} \\ \frac{-\sqrt{3}}{2} & \frac{1}{2} \end{pmatrix} \begin{pmatrix} \frac{1}{2} & \frac{-\sqrt{3}}{2} \\ \frac{\sqrt{3}}{2} & \frac{1}{2} \end{pmatrix}, \begin{pmatrix} \frac{1}{2} & \frac{\sqrt{3}}{2} \\ \frac{\sqrt{3}}{2} & \frac{-1}{2} \end{pmatrix} \begin{pmatrix} \frac{1}{2} & \frac{-\sqrt{3}}{2} \\ \frac{-\sqrt{3}}{2} & \frac{-1}{2} \end{pmatrix}, \begin{pmatrix} -1 & 0 \\ 0 & 1 \end{pmatrix}$$

$$(15.5.10)$$

     Examples of D_6 eigenfunctions for a KP potential of height $V=30$ Bohr units is shown in Fig. 15.5.2. The lower band can be compared to the lower half of the D_3 bands shown in Fig. 15.3.3. The E_2 waves of D_6 are similar to the E_1 waves of D_3, and, of course, the A_1 waves are similar, too. Missing from Fig. 15.3.3 are the B_1 waves allowed for D_6 in Fig. 15.5.2.

     The second band shown in Fig. 15.5.2 has quite a different look because it lies above the potential barriers. The lowest wave has nearly flat waveforms in the barrier region because it is barely above them. It resembles a low-KE "grazing" wave such as was shown back in Fig. 13.1.4(a). Greater freedom to move over the barrier causes the local symmetry to become more mixed up as discussed after (15.4.8).

     As local symmetry loses its definition, the Bohr angular momentum quanta $m^{\pm}$ regain theirs. The $(m=6)^-$ A_2 wave is very nearly a pure $m=6$ standing wave. For lower states like 0^+E_1 or 1^-E_1 the Fourier components $m=0$ and $m=1$ aren't the only ones in the waves. Clearly, 0^+A_1 has some 6^+A_1 mixed into it. Each state may be viewed as a Fourier series of Bohr states. We discuss quantum band wave Fourier analysis in the following Chapter 16.
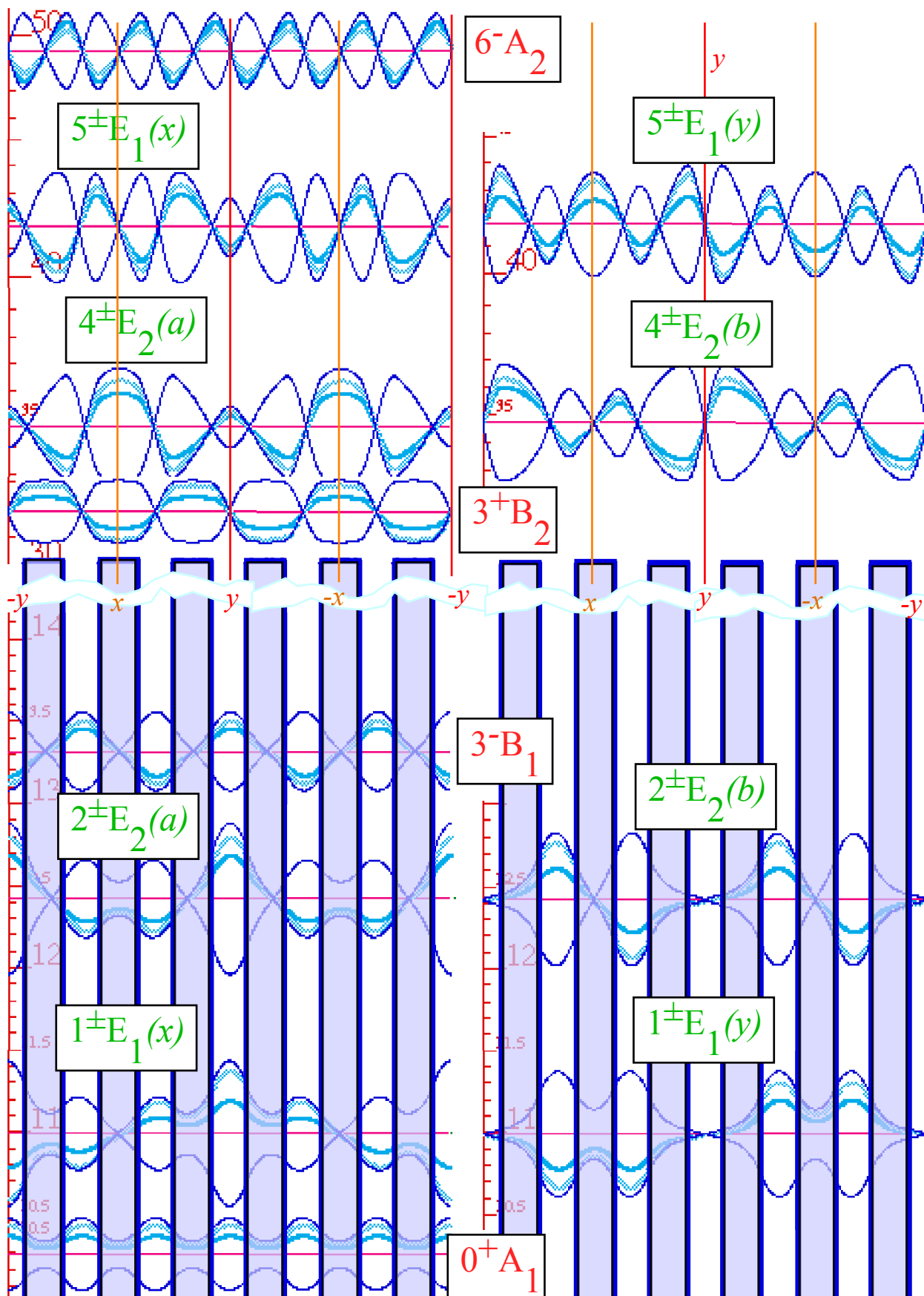
Fig. 15.5.2 Lowest twelve N=6 KronigPenney eigenfunctions. (Top-to-bottom V=30)

Problems for Chapter 15.

A Complete Completeness

15.1.1. The D-orthogonality relation (15.1.30) needs a completeness relation to go with it. Can you derive one? If so, do it, or else explain why not.
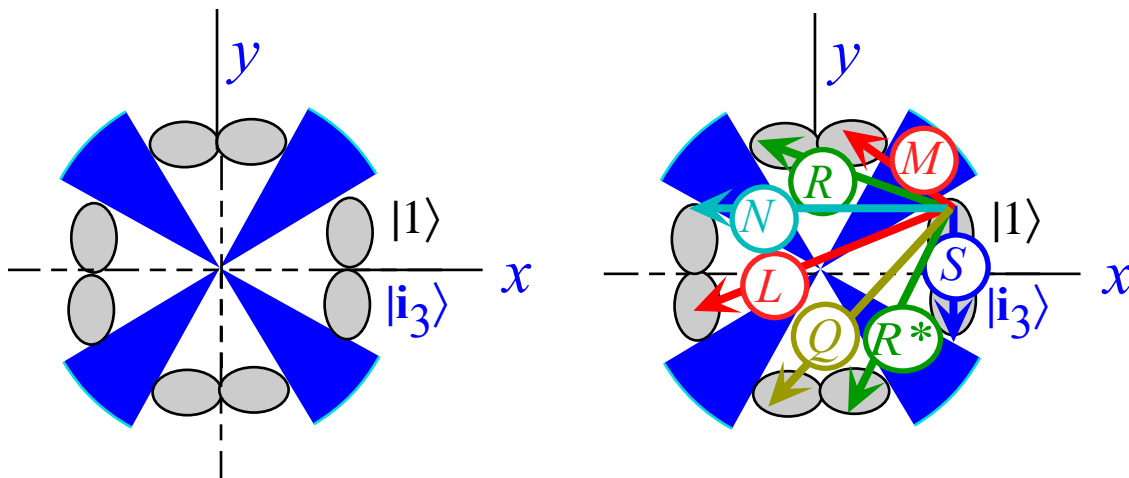
The Square Deal

15.3.1. The analysis of D_3 needs to be extended to the group D_4 of a tetragonal 4-well ring.

(a) Derive an 8-by-8 D_4 group table like Fig. 15.1.2. (Construct an operator/state diagram.) Give a standing wave and moving wave irrep analogous to (15.1.8) and (15.1.10) and check it works for some products.

(b) Derive the D_4 class algebra analogous to (15.2.1) and reduce it so a complete D_4 character table is found. First, how many classes? (It should be more than four.)

(c) Determine the rank of D_4. Write out all the D_4 irrep projectors for the standing wave choice of basis that diagonalizes all elements of the D_2 subgroup from Fig. 15.1.1. Label your D_4 results using the standard labels $A_1, B_1, A_2, ...E_{n-1}$, for D_{2n} groups. (Let A(B) parity be +(-) for $R_z(90°)$, and 1(2) parity be +(-) for $R_x(180°)$.)

(d) Use the irrep projectors to produce a complete set of D_4 band states and sketch them in a way analogous to Fig. 15.3.2 or 3. (You may use actual solutions from previous problems.)

The Square Deal Continued

15.4.1. Apply analysis of the group D_4 of a tetragonal 4-well quantum ring as was done for D_3.

(a) Derive 8-by-8 D_4 dual regular representations like (15.1.15a) and (15.3.11d) for D_3.

(b) Derive the D_4 Hamiltonian analogous to (15.4.2b) based on the Fig. 15.3 above, and reduce to 2-by-2 blocks.

(c) (Extra Credit optional)   Do a U(2) analysis of the residual 2-by-2 Hamiltonian matrix or matrices.

(d) Give eigensolutions if only S and M are non-zero. Consider S>>M and M>>S.

(e) Give eigensolutions if only S and R=R* are non-zero. Consider S>>R and R>>S.

A Super-Degenrate Square Deal

15.4.2. Let the Hamiltonain of the tetragonal 4-well quantum ring have symmetry $D_4 \times \bar{D}_4$.

(a) What form does its Hamiltonian matrix have in the original group basis?

(b) What form do the eigensolutions take? If possible, give answer in closed form.

Standing Hexes

15.5.1. Consider the real standing-wave ireps of D_6 given by (15.5.10).

(a) Use these to construct a 12-dimensional model set of band eigenstates $\left| P_{ab}^{E_m} \right\rangle$ analogous to the D_3 model of (15.3.5).

(b) Construct a sketch of them analogous to Fig. 15.3.2. Tell which could be like electric dipoles and which like electric quadrupoles if mixed with the A_1 ground state. Also, compare them to the numerical plots of Fig. 15.5.2 noting local vs. global symmetry.

Moving Hexes

15.5.2. Consider complex moving-wave ireps of D_6 .

(a) Make a set of complex moving-wave ireps of D_6 using the complex D_3 irep (15.1.8).
Note, in particular the representations of $\mathbf{i}_3$ and $\mathbf{j}_3$. Compare them to a convention stated by (15.5.7). Are they the same or different? Comment.

(b) Use these to construct a 12-dimensional model set of moving band eigenstates $\left| P_{ab}^{E_m} \right\rangle$ analogous to the D_3 model of

(15.3.5).

(c) Using phasor "clocks" or any other diagrammatic ruse, construct a sketch of the $\left| P_{ab}^{E_m} \right\rangle$ states.

Coset sets

15.5.3. Consider left cosets of subgroups of D_6 as described below.

(a). List the left cosets: l-coset 1= C_6, , l-coset 2 = $\mathbf{j}_3$ C_6, where C_6 ={**1**, **h**, $\mathbf{h}^2$, $\mathbf{h}^3$, $\mathbf{h}^4$ $\mathbf{h}^5$}. Let the order of operators listed in coset 1 determine the listing order in coset 2.
(b). List the E_1 and E_2 ireps derived in Exercise 15.5.2 in the order of the cosets in 3(a), one coset above the next. Note any repetition of matrix structure.
(c) List the left cosets: l-coset 1= C_2, , l-coset h = $\mathbf{h}$ $C_{2,}$, l-coset h^2 = $\mathbf{h}^2$ C_2, ... l-coset h^5 = $\mathbf{h}^5$ $C_{2,}$, where C_2 ={**1**, $\mathbf{j}_3$}. Let the order of operators listed in coset 1 determine the listing order in the other cosets.
(d). List the E_1 and E_2 iireps derived in Exercise 15.5.1 in the order of the cosets in 3(c), one coset above the next. Note any repetition of matrix structure.
(d) In either case (a) or (c), are left cosets the same sets as right cosets.
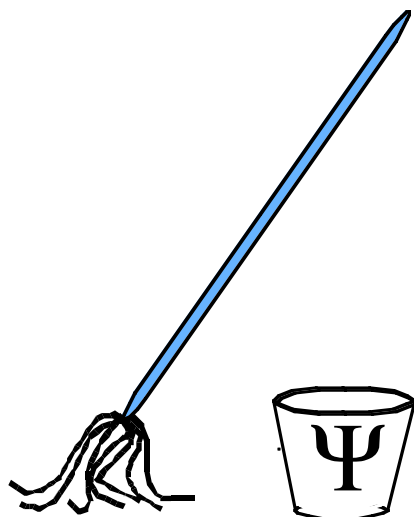
QM
for
Ψ AMOP

Chapter 16

Fourier Analysis of

Periodic Potentials and States

W. G. Harter

Continuously varying periodic potentials *V(x)=V(x+a)* over an unbounded *(-∞<x<∞)* continuum may be treated using continuum Fourier analysis introduced in Chapter 7. Fourier or k-space analysis competes favorably with x-space representations when the potential V(x) varies continuously, while the x-space analysis used in Chapters 12 through 14 is better for potentials with discontinuos steps. If the x-continuum is bounded or periodic *(-π<x<π)* Fourier k-space becomes discrete as discussed in Chapter 7. If the x-space is discrete and bounded *(x_0<x_p< x_{N-1})* then so is Fourier k-space as discussed in Chapters 8 and 9. Here the two cases are exploited to gain computational power and physical insight into x-space-k-space lattice waves.

CHAPTER 16. FOURIER ANALYSIS OF PERIODIC POTENTIALS AND STATES 1

Chapter 16. Fourier Analysis of Periodic Potentials and States

16.1. Fourier Analysis of Mathieu Potential

The *C*-matrix and *S*-matrix analysis of potential barriers and wells is complemented by another theoretical technique based on *Fourier series*. The crossing-*C*-matrix used in Chapters 13 through 14 are best suited for piecewise constant or "square" barriers with long flat wells or barriers that approximate "quantum wells" and superlattices. On the other hand, continuously varying potentials such as

$$V(x) = V_0 \cos \upsilon x \qquad\qquad (16.1.1)$$

are more easily analyzed using Fourier theory. Indeed, the Schrodinger wave equation for the simple cosine potential (16.1.1) is called *Mathieu's equation*.

$$\frac{d^2\psi}{dx^2} + A\big[E - V\cos(2x)\big]\psi = 0 \qquad\qquad (16.1.2)$$

This will be treated first and then compared with other more general potential structures including the Kronig Penney square lattices previously discussed.

(a) Mathieu potential and analogous parametric amplification

The Mathieu equation (16.1.2) is of considerable interest in a wide range of applications. If the independent variable is time t , the (16.1.2) becomes an equation for *nonlinear resonance* or *parametric amplification*. This process has to be understood in a number of classical devices such as the alternating gradient synchrotron. It can be compared to ordinary linear resonance by using a simple string and pendulum model shown in Fig. 16.1.1. Ordinary resonance corresponds to wiggling the pendulum support horizontally as shown in Fig. 16.1.1(a) while parametric resonance corresponds to a vertical wiggle, that is, an oscillating effective gravity field such as one might experience riding an Einstein's elevator (or roller-coaster) furiously pumping up and down. Let us see how to analyze these motions.
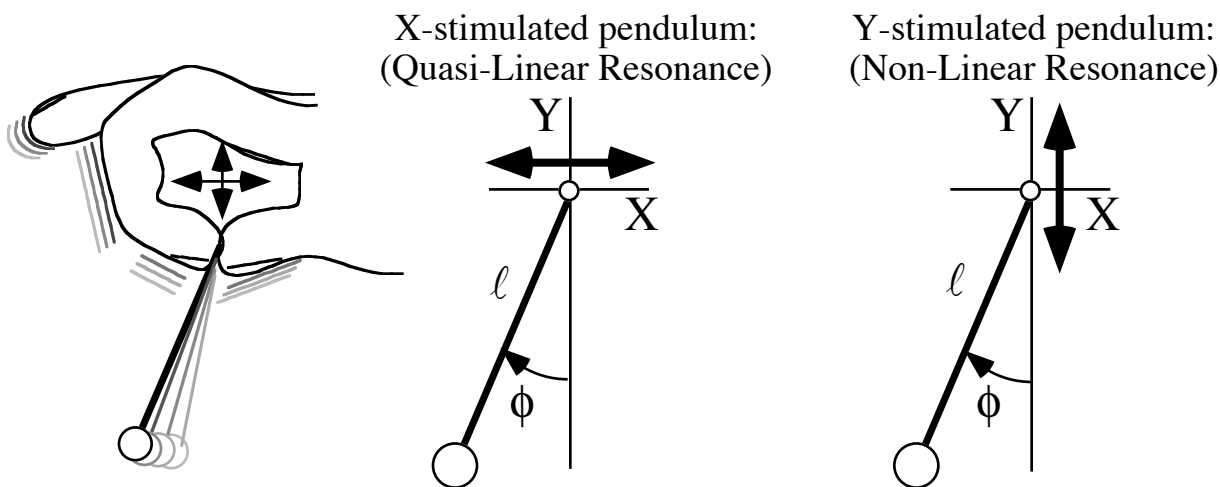
Fig. 16.1.1 Two cases for accelerated pendulum (a) Linear or additive. (b) Nonlinear or multiplicative.

The classical equation for the motion of a pendulum in an effective $\mathbf{g}^{eff}$ field is the following.

$$\frac{d^2\phi}{dt^2} - \frac{g_x^{eff}}{\ell}\cos\phi + \frac{g_y^{eff}}{\ell}\sin\phi = 0 \qquad (16.1.3)$$

For small angles (*cos* $\phi\sim1$ and *sin* $\phi\sim\phi$) this reduces as follows for the two cases indicated in Fig. 16.1.1.

$$\frac{d^2\phi}{dt^2} + \frac{g_y^{eff}}{\ell}\phi = \frac{g_x^{eff}}{\ell} \qquad (16.1.4)$$

First, *x*-stimulation by $g^{eff}{}_x = A_x\omega_x^2 \cos \omega_x t$ acts *additively* to give *linear* resonance in constant *y*-gravity g.

$$\frac{d^2\phi}{dt^2} + \frac{g}{\ell}\phi = -\frac{\omega_x^2 A_x}{\ell}\cos(\omega_x t) \qquad (16.1.5a)$$

Second, *y*-stimulation by $g^{eff}{}_y = A_y\omega_y^2 \cos \omega_y t$ acts *multiplicatively* to give *non-linear* resonance.

$$\frac{d^2\phi}{dt^2} + \left(\frac{g}{\ell} - \frac{\omega_y^2 A_y}{\ell}\cos(\omega_y t)\right)\phi = 0 \qquad (16.1.5b)$$

The latter has the same form as the Schrodinger-Mathieu equation (16.1.2). This shows once again that while quantum theory, by itself, is a linear theory, the imposition of outside forces cause a non-linear parametric or *multiplicative* variation of the equation. Doubling the acceleration A_x in (16.1.5a) simply doubles the response ϕ *(t)* to *2ϕ(t)*, but a doubling of A_y in (16.1.5b) gives a completely different $\phi(t)$. (A solution $\psi(x)$ for a potential *V (x)* such as in Fig. 14.2.7 clearly is not *2ψ(x)* for a potential *2V(x)*.)

(1) Mathieu eigensolutions

We start with the Mathieu equation in either of the following two forms.

$$-\frac{d^2\phi}{dx^2} + V\cos(nx)\phi = E\phi , \qquad \left(\mathbf{D}^2 + \mathbf{V}\right)|\phi\rangle = E|\phi\rangle \qquad (16.1.6)$$

The *(V=0)*-eigen-solutions are the familiar *Bohr orbitals* or, for the pendulum, the familiar phasor waves.

$$\langle x|m\rangle = \phi_m(x) = \frac{e^{\pm i\,mx}}{\sqrt{2\pi}}, \qquad (16.1.7a) \qquad\qquad \langle t|\omega\rangle = \phi_\omega(t) = \frac{e^{\pm i\omega_0 t}}{\sqrt{2\pi}}. \,(16.1.7b)$$

Bohr-ring eigenvalues as given in Bohr units by (7.1.16) are analogous to the pendulum frequency values

$$E = m^2\left(Bohr\ units\ of\ \frac{\pi^2\hbar^2}{2MA^2}\right) \qquad (16.1.7c) \qquad\qquad \omega_0 = \sqrt{\frac{g}{\ell}} \qquad (16.1.7d)$$

The Bohr-ring problem uses *periodic boundary conditions* by restricting *x* between *0* and *L=2A* and demanding the wave repeat every *L*. Doing the same for the pendulum amounts to demanding that the time function repeat perfectly after a time *T* for *two* wiggles. This leads to *quantization conditions* for Bohr orbitals and restricts the allowed pendulum frequency to *harmonics* of a *fundamental frequency 2π/T*.

$$\phi(0) = \phi(L) \Rightarrow e^{ikL} = 1,\ or:\ k = \frac{2\pi m}{L} \quad (16.1.8a) \qquad \phi(0) = \phi(T) \Rightarrow e^{i\omega_0 T} = 1,\ or:\ \omega_0 = \frac{2\pi m}{T} \quad (16.1.8b)$$

If coordinate *x* is taken as polar angle *x=ϕ* , the Bohr orbital angular range limit is 2π. To simplify notation we use this limit *L=2π=T* in both analogies. Then the allowed *(V=0)*-energies and frequencies are

$$E = m^2 \left(\frac{\hbar^2}{2M}\right) = 0,1,4,9,16...\left(\frac{\hbar^2}{2M}\right) \qquad (16.1.9a) \qquad\qquad \omega_0 = m = 0,\pm1,\pm2,\pm3,\pm4,... \quad (16.1.9b)$$

This definition uses lattice spacing $A=\pi$ for the two-well case $(N=2)$ first discussed after Fig. 14.2.8.

     The k-space or Fourier representation of the Schrodinger eigenequation is

$$\Sigma \langle j|\left(\mathbf{D}^2 + \mathbf{V}\right)|k\rangle\langle k|\phi\rangle = E\langle j|\phi\rangle, \qquad (16.1.10a)$$

where energy E and potential V are given in Bohr units as are the k-space kinetic energy matrix elements

$$\langle j|\mathbf{D}^2|k\rangle = k^2 \delta_j^k. \qquad (16.1.10b)$$

Orthonormality relations (7.1.5) to (7.1.10) are used with $L=2\pi$. The potential matrix elements use the same units and wavefunctions (2.7.7).

$$\langle j|\mathbf{V}|k\rangle = \int_0^{2\pi} d\phi \frac{e^{-ij\phi}}{\sqrt{2\pi}} V\cos(N\phi)\frac{e^{ik\phi}}{\sqrt{2\pi}} = \int_0^{2\pi} d\phi \frac{e^{-i(j-k)\phi}}{2\pi} V \frac{e^{-iN\phi} + e^{iN\phi}}{2}$$

$$= \frac{V}{2} \int_0^{2\pi} d\phi \left(\frac{e^{-i(j-k+N)\phi}}{2\pi} + \frac{e^{-i(j-k-N)\phi}}{2\pi}\right) = \frac{V}{2}\left(\delta_j^{k-N} + \delta_j^{k+N}\right)$$

<div align="right">(16.1.10c)</div>

The resulting matrices represent the Mathieu (cosine) potential eigenvalue problem for any number N of wells in a ring. We begin with the case of two wells $(N=2)$ as was done in Sec. 14.2 (b). Indeed, the usual form (16.1.2) of Mathieu's equation has $N=2$. General-N cases (16.1.6) are treated later.

(2) (N=2) Double-well potential and two-wiggle repeat

     Matrices (16.1.10) for a potential $V\cos(2x)$ with $N=2$ wells fall into odd and even cases.

$$\langle j|\left(\mathbf{D}^2 + \mathbf{V}\right)|k\rangle = \quad \text{(for j and k even)} \qquad\qquad \langle j|\left(\mathbf{D}^2 + \mathbf{V}\right)|k\rangle = \quad \text{(for j and k odd)}$$

$$\cdots |{-}6\rangle, |{-}4\rangle, |{-}2\rangle, |0\rangle, |2\rangle, |4\rangle, |6\rangle, \cdots \qquad\qquad \cdots |{-}7\rangle, |{-}5\rangle, |{-}3\rangle, |{-}1\rangle, |1\rangle, |3\rangle, |5\rangle, \cdots \quad (16.1.11a)$$

$$\begin{pmatrix} \ddots & & & & & & \\ & 6^2 & v & & & & \\ & v & 4^2 & v & & & \\ & & v & 2^2 & v & & \\ & & & v & 0 & v & \\ & & & & v & 2^2 & v \\ & & & & & v & 4^2 & v \\ & & & & & & v & 6^2 \\ & & & & & & & & \ddots \end{pmatrix}, \qquad \begin{pmatrix} \ddots & & & & & & \\ & 7^2 & v & & & & \\ & v & 5^2 & v & & & \\ & & v & 3^2 & v & & \\ & & & v & 1^2 & v & \\ & & & & v & 1^2 & v \\ & & & & & v & 3^2 & v \\ & & & & & & v & 5^2 \\ & & & & & & & & \ddots \end{pmatrix}$$

Here the off-diagonal matrix elements are by (16.1.10c).

$$v = \frac{V}{2} \qquad\qquad (16.1.11b)$$

     The matrices go on forever in each direction. However, the lower eigenvalues E_j may be found by truncating them to 2-by-2 , or 3-by-3, ...or the 7-by-7 matrices shown in (16.1.11a) if $v=V/2$ is small compared to the difference $j^2 -(j\pm2)^2$ between the diagonal j^2 values. For example, if $v<<|3^2 - 1^2|$ then the following matrix approximates $E_{1\pm}$ near 1^2, that is, the lowest odd-k eigenvalues.

$$\begin{pmatrix} 1^2 & v \\ v & 1^2 \end{pmatrix} \qquad\qquad (16.1.12a)$$

$$E_{1-} \sim 1^2 - v, \qquad\qquad\qquad E_{1+} \sim 1^2 - v. \qquad\qquad (16.1.12b)$$

The lowest even-k eigenvalues are obtained approximately from the eigenvalues of

$$\frac{1}{2}\begin{pmatrix} 1 & 0 & 1 \\ 0 & \sqrt{2} & 0 \\ 1 & 0 & -1 \end{pmatrix}\begin{pmatrix} 2^2 & v & 0 \\ v & 0 & v \\ 0 & v & 2^2 \end{pmatrix}\begin{pmatrix} 1 & 0 & 1 \\ 0 & \sqrt{2} & 0 \\ 1 & 0 & -1 \end{pmatrix} = \begin{pmatrix} 2^2 & v\sqrt{2} & 0 \\ v\sqrt{2} & 0 & 0 \\ 0 & 0 & 2^2 \end{pmatrix} \qquad (16.1.13a)$$

$$E_0 \sim 0 - 2v^2/2^2 +., \qquad E_{2+} \sim 2^2 + 2v^2/2^2 +.., \qquad E_{2-} \sim 2^2 -.. \qquad (16.1.13b)$$

as long as $v << |4^2 - 2^2|$ allows neglect of the 4^2 rows.

      Approximations to eigenvalues and eigenfunctions are given by direct numerical diagonalization of truncated matrices like the above. One takes as large a matrix (16.1.11) as needed to get a desired accuracy. (You increase $|k|$ by two and see if the resulting changes are less than your tolerance for error.)

      Examples of the $N=2$ eigenvalues for a positively "biased" cosine potential

$$V(x) = V - V\cos 2\phi \quad (0 < \phi < 2\pi)$$

are plotted in Fig. 16.1.2. Each potential $V(x)$ is shifted up by the amplitude V of the potential so that as V varies the bottom $V(0)$ of the potential function remains at zero energy. This permits immediate comparison of the band boundaries of a Mathieu cosine potential with similar band boundaries of a Kronig-Penney square well of the same barrier heights which were plotted in Fig. 14.2.11 and 14.2.13.

      One obvious difference is the absence in the Mathieu levels in Fig. 16.1.2 of band boundary crossing or "smiles" seen in the KP levels in Fig. 14.2.11 or B_1, B_2 crossing seen in 14.2.13. The cosine potential has the simplest band structure of any finite periodic potential. The level order A_1, B_1, B_2, A_2 is not violated. Instead there is an orderly transition between the below-barrier *(E<V)* "(12)-(21) gap-pairs"

     (A_2, A_1)-*(band)*-(B_1, B_2)-*(band)* (A_2, A_1)-*(band)*-(B_1, B_2)-*(gap)*[repeat]   (16.1.14a)

and the above-barrier *(E>V)* "(AB)(BA) band-pairs"

     (A_1, B_1)-*(gap)*-(B_2, A_2)-*(gap)* (A_1, B_1)-*(gap)*-(B_2, A_2)-*(gap)*[repeat]   (16.1.14b)

That is, at *(E=V)*, the sequence -A_1)(B_1, B_2)(A_2 becomes (A_1, B_1)(B_2, A_2) as shown in Fig. 16.1.2.

      The first $m = \pm 1$ (B_1, B_2) splitting at $E = 1$ is shown more clearly in the blow-up of Fig. 16.1.2. For $V < 1$, the energy values closely follow the <u>first</u>-order perturbation approximations (16.1.12b). The $m = \pm 2$ (A_2, A_1) splitting at $E = 2^2 = 4$ is <u>second</u> order in V by (16.1.13b). Higher-m Bohr orbital splittings "stick" even more since they go as V^n with $n > 2$. In contrast, the KP splittings in Fig. 14.2.13 are first order for $m = \pm 1, \pm 3, \pm 5,..$ because a square well **U** has non-zero Fourier components at odd-m values.

$$\langle +m|\mathbf{U}|-m\rangle = U, -U/3, U/5, -U/7, \ldots \text{ for } m = \pm 1, \pm 3, \pm 5, \pm 7,...$$

The "smiles" in Fig. 14.2.11 reflect a "twisting" of the odd-m splitting due to the alternating signs of the first-order splitting which equals the order-m Fourier components. In (16.1.10c), the Mathieu potential $cos(N\phi)$ only splits $m = \pm 1$, but $cos(3N\phi)$ splits $m = \pm 3$, and $cos(5N\phi)$ splits $m = \pm 5$, and so on.
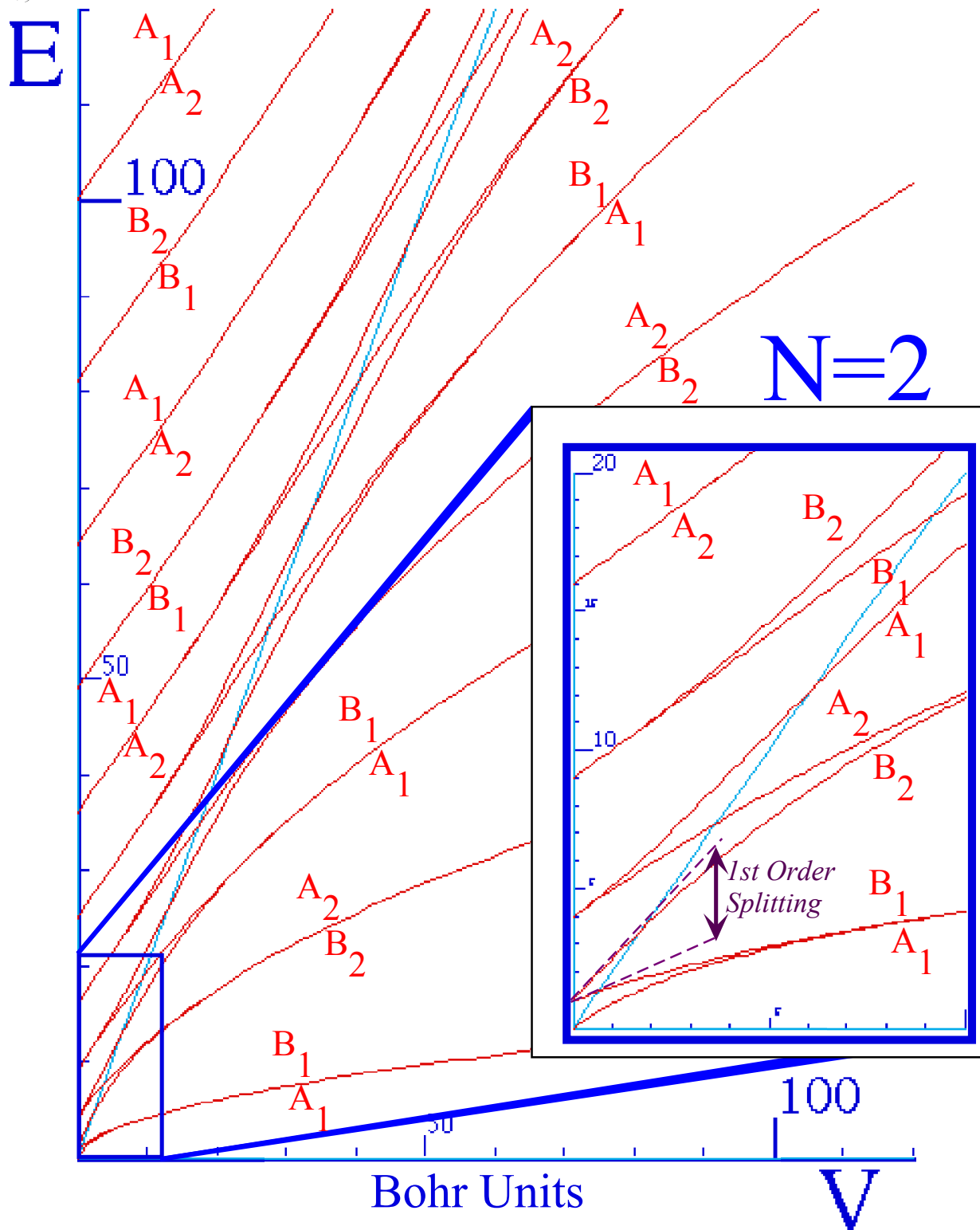
Fig. 16.1.2 Mathieu (cosine) potential band boundary levels and N=2 E-spectrum versus potential depth V.

(b) Pendulum parametric resonance analogy: (N=2) Two-wiggle repeat

A mechanical analogy with pendulum resonance helps visualize Mathieu eigenfunctions. A _y_-stimulated pendulum satisfies a Schrodinger's wave equation (16.1.6) if the independent variables of time _t_ for the pendulum

equation (16.1.5) is spatial coordinate x for a Schrodinger wave. We equate the argument $\omega_y\, t$ of the cosine stimulus to the spatial argument Nx of the Schrodinger cosine potential.

$$\omega_y\, t = Nx, \quad \text{or:}\quad dt = \frac{N}{\omega_y}\, dx, \quad \text{and:}\quad dt^2 = \frac{N^2}{\omega_y^2}\, dx^2. \qquad (16.1.15a)$$

This converts the y-accelerated pendulum equation (16.1.5) to match a Schrodinger equation

$$\frac{d^2\phi}{dx^2} + \frac{N^2}{\omega_y^2}\left(\frac{g}{\ell} - \frac{\omega_y^2 A_y}{\ell}\cos(Nx)\right)\phi = 0 = \frac{d^2\phi}{dx^2} + \left(\frac{N^2}{\omega_y^2}\frac{g}{\ell} - \frac{N^2 A_y}{\ell}\cos(Nx)\right)\phi \qquad (16.1.15b)$$

where pendulum parameters g, ℓ, B, and ω_y match Schrodinger parameters E, V and N as follows.

$$E = \frac{N^2}{\omega_y^2}\frac{g}{\ell}, \qquad (16.1.15c) \qquad\qquad\qquad V = \frac{N^2 A_y}{\ell}. \qquad (16.1.15d)$$

The pendulum y-stimulus frequency ω_y and amplitude A_y are as follows, where we may set $|g|=1=\ell$.

$$\omega_y = N\sqrt{\frac{g}{|E|\ell}} = \frac{N}{\sqrt{|E|}}, \qquad (16.1.15e) \qquad\qquad A_y = \frac{V\ell}{N^2} = \frac{V}{N^2} \qquad (16.1.15f)$$

A *y*-stimulated pendulum analogy for Schrodinger applies at its lowest point *(φ~0)* where *cos φ~1* and *sin φ~φ*. It also applies when the pendulum is "up-side-down", that is, near its highest point *(φ~π)* where *cos φ ~ -1* and *sin φ ~ π−φ* . It's a negative energy *(E<0)* Schrodinger equation if *(g/ℓ<0)*.

$$\frac{d^2\phi}{dt^2} + \left(-\frac{g}{\ell}\frac{N^2}{\omega_y^2} + \frac{\omega_y^2 A_y}{\ell}\cos(\omega_y t)\right)(\phi - \pi) = 0, \quad \text{(where: } \phi \cong \pi) \qquad (16.1.15g)$$

As we will see, it is possible for the oscillating acceleration to stabilize the pendulum up-side-down!

For example, the eigenvalues for *V=0.2* or *v=0.1* and *V=2.0* or *v=1.0* are listed below.

V=0.2 or *v=0.1*   *V=2.0* or *v=1.0*

$E_0 =$	−0.0050		$E_0 =$	−0.4551
$E_{1-} =$	0.8988		$E_{1-} =$	−0.1102
$E_{1+} =$	1.0987		$E_{1+} =$	1.8591
$E_{2-} =$	3.9992		$E_{2-} =$	3.9170
$E_{2+} =$	4.0042		$E_{2+} =$	4.3713
$E_{3-} =$	9.0006		$E_{3-} =$	9.0477
$E_{3+} =$	9.0006		$E_{3+} =$	9.0784

(16.1.16a)   (16.1.16b)

Fig. 16.1.3 is a plot of some *(N=2)* E_m-values versus perturbation amplitude V or wiggle amplitude $4A_y$.

$$A_y = V/N^2 = 2v/N^2 = 2v/4 \qquad (16.1.20a)$$

Plugging each E_m-value into (16.1.15e) with $N=2$ gives a corresponding y-pendulum frequency $\omega_{y(m)}$.

$$\omega_{y(m)} = N/\sqrt{|E|} = 2/\sqrt{|E_m|} \qquad (16.1.20b)$$

(*V= 0.2 or A_y=0.05 and N=2*)

$\omega_{y(0)} = 2 / \sqrt{\lvert-.0050\rvert}$	$= 28.2843$	
$\omega_{y(1^-)} = 2 / \sqrt{.8988}$	$= 2.10959$	
$\omega_{y(1^+)} = 2 / \sqrt{1.0987}$	$= 1.90805$	(16.1.16c)
$\omega_{y(2^-)} = 2 / \sqrt{3.9992}$	$= 1.00010$	
$\omega_{y(2^+)} = 2 / \sqrt{4.0042}$	$= 0.99948$	

(*V= 2.0 or A_y =0.5 and N=2*)

$\omega_{y(0)} = 2 / \sqrt{\lvert-.4551\rvert}$	$= 2.9646$	
$\omega_{y(1^-)} = 2 / \sqrt{\lvert-.1102\rvert}$	$= 6.02475$	
$\omega_{y(1^+)} = 2 / \sqrt{1.8591}$	$= 1.4668$	(16.1.16d)
$\omega_{y(2^-)} = 2 / \sqrt{3.9170}$	$= 1.0105$	
$\omega_{y(2^+)} = 2 / \sqrt{4.3713}$	$= 0.9566$	

A low amplitude oscillation (A_y =0.05 or V=0.2) has only one negative E_m-value. The high amplitude case (A_y =0.5 or V=2.0) has two negative E_m-values. From (16.1.15c,g), negative E corresponds to "up-side-down" motion that is stable for ω_y with $E<0$ inside (A_1,B_1) band of the analogous Schrodinger equation.
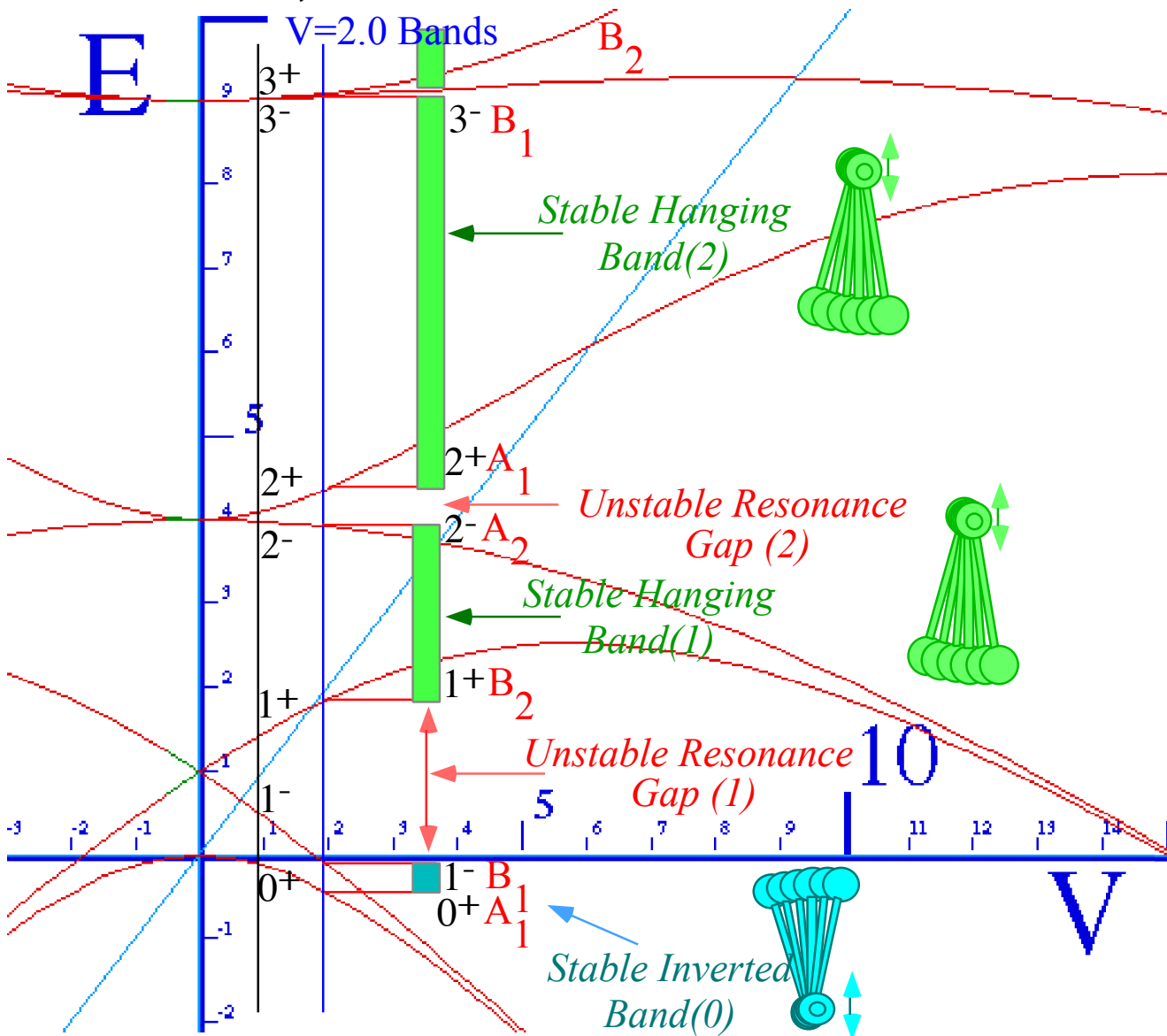
Fig. 16.1.3 E-Values versus perturbation amplitude V . Gray stability regions shown for V=2.0 .

The ±sign of E is irrelevant for observable quantum dynamics. The plot in Fig. 16.1.2 (analogous to Fig. 16.1.3) has all potentials positively biased from $-V\cos(Nx)$ to $V-V\cos(Nx)$ so all E-values come out positive. However, for the classical pendulum analogy the sign of E is all-important and an unbiased symmetrically oscillating acceleration $-A_y\cos(Nx)$ gives two or more negative E-values if A_y is big enough.

The lowest region of stability lies between the $0^+ A_1$ and $1^- B_1$ E-values. For perturbation amplitude V greater than $V=1.8$ these two E-values lie in the negative-E region and both motions correspond to inverted stability. Not until V becomes greater than 15 does another inverted stability region appear as the $1^+ B_2$ and $2^- A_2$ E-values go negative. (See extreme right hand side of Fig. 16.1.3.)

The 0^+A_1 and 1^-B_1 motions (y-stimulus frequency $\omega_{y(0+)}$ =2.9646 and $\omega_{y(1-)}$ =6.02475 from (16.1.16d).) are displayed in Fig. 16.1.4 a-b. As discussed in Sec. 3.6, D_2 symmetry label A stands for "Always-the-same" while B stands for "Back-and-forth". Indices $1(2)$ denote symmetry (anti-symmetry) relative to a V-well where the artificial "g-forces" act most strongly to center the pendulum. For inverted pendula, V-well bottoms occur at the top of the roller-coaster ride where its arm gets pulled up against natural gravity g as car accelerates downward.
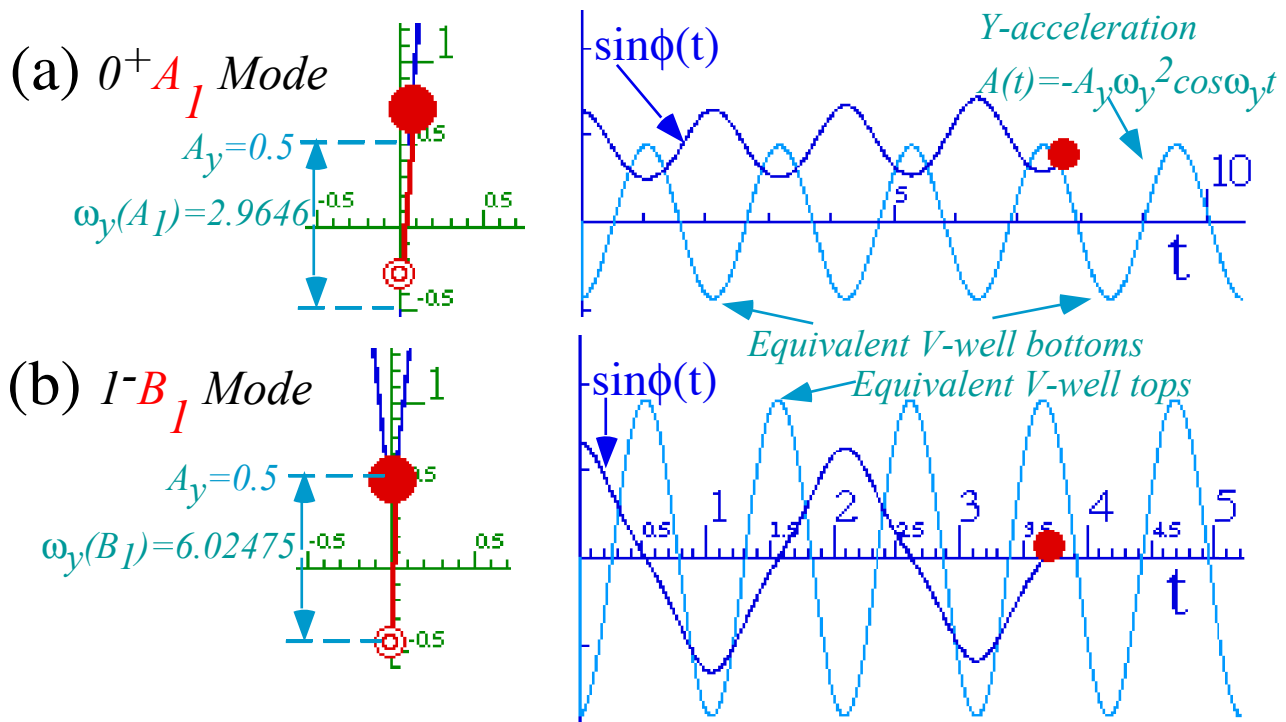
Fig. 16.1.4 Inverted Modes (a) Symmetric (one sided) 0^+A_1 mode, (b) Anti-symmetric $1^- B_1$ mode .

For a normally hanging pendulum the equivalent of a potential V-well happens at the bottom of the roller-coaster ride where the pendulum arm gets pulled down in concert with natural gravity g as car accelerates upward. This is the case for all the stable modes shown in Fig. 16.1.5 below. The 1^+B_2 mode in part (a) is shown at the moment when the pendulum is momentarily floating in "zero-g" as its roller-coaster peaks and centrifugal force cancels natural gravity. To see the analogous quantum potentials this figure must be viewed up-side-down.

(c) $2^{+}A_1$ Mode

$\omega_y(A_1)=0.9566$

$A_y=0.5$

$\sin\phi(t)$

(b) $2^{-}A_2$ Mode

$\omega_y(A_2)=1.01054$

$A_y=0.5$

$\sin\phi(t)$

(a) $1^{+}B_2$ Mode

$\omega_y(B_2)=1.4668$

$A_y=0.5$

$\sin\phi(t)$

Equivalent V-well bottoms

Equivalent V-well tops
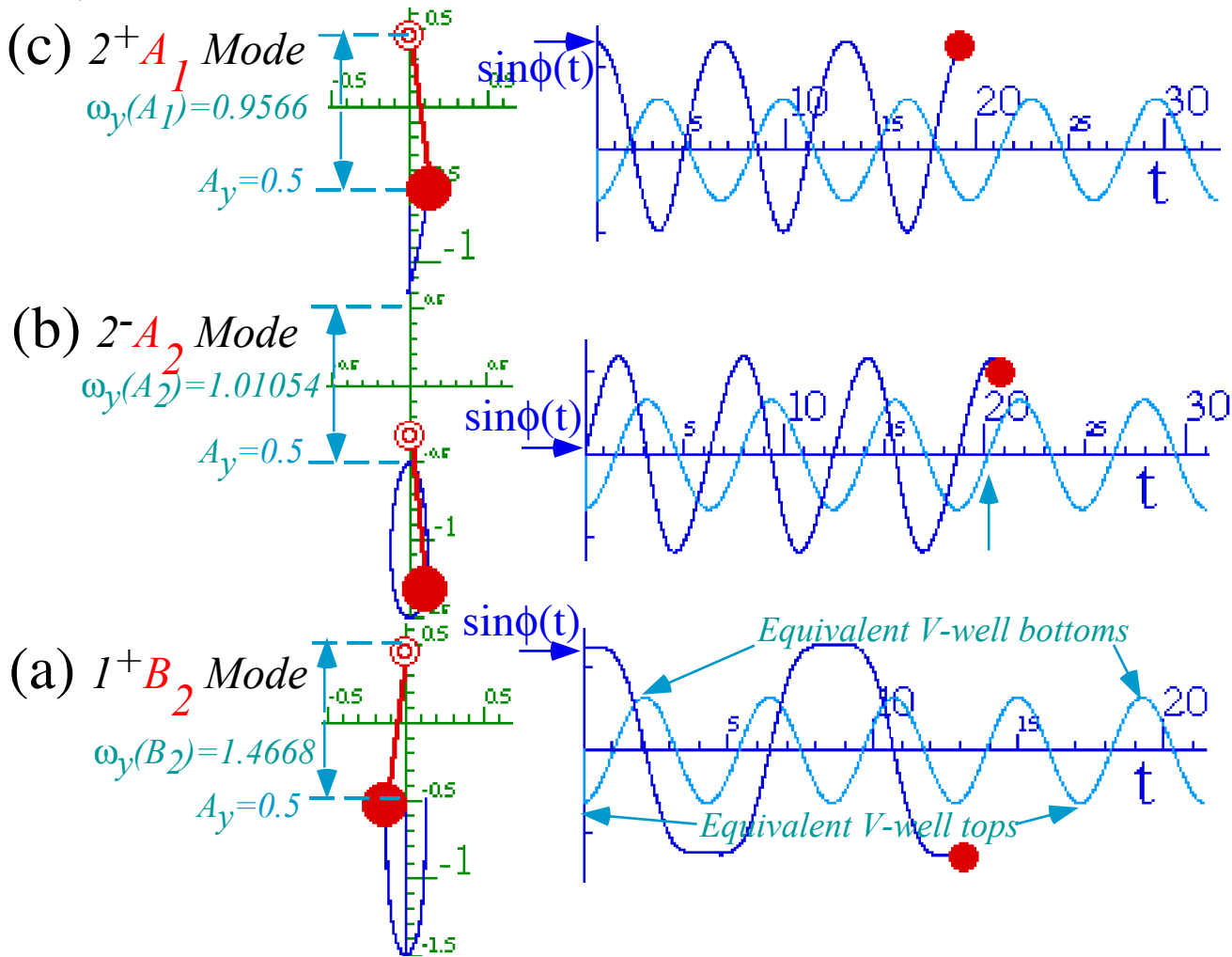
Fig. 16.1.5 Hanging Modes (a) Anti-symmetric $1^{+}B_2$, (b) Anti-symmetric $2^{-}A_2$, (c) Symmetric $2^{+}A_1$.

The first five quantum eigenfunctions of a (+)-biased Mathieu cosine potential $V(x)=2-2cos2x$ are plotted at their energy levels in Fig. 16.1.6. Energy is in Bohr units relative to well-bottom so $V=2.0$ must be subtracted to get unbiased E for the classical pendulum model. The lowest two waves ($0^{+}A_1$ and $1^{-}B_1$) with negative energies -0.4551 and -0.1102 have the same shape as the time trajectories of the inverted pendulum modes in Fig. 16.1.4. The next three eigenfunctions $1^{+}B_2$, $2^{-}A_2$, and $2^{+}A_1$ have the shape of the first three hanging modes in Fig. 16.1.5. Most notable is the "grazing" eigenfunction $1^{+}B_2$ that has flattened crests and corresponds to the classical "zero-g" pendulum mode in Fig. 16.1.5(a).

The quantum waves must have an integral <u>even</u> number of wave nodes or x-axis crossings in the allowed interval $0<x<2\pi$. Waves $0^{+}A_1$ and $1^{-}B_1$ have zero and two, respectively. Waves $1^{+}B_2$, $2^{-}A_2$, and $2^{+}A_1$ have two, four, and four nodes, respectively. A Bohr-orbital $m^{\pm}$ has $2m$ nodes and this is invariant to the size of V.
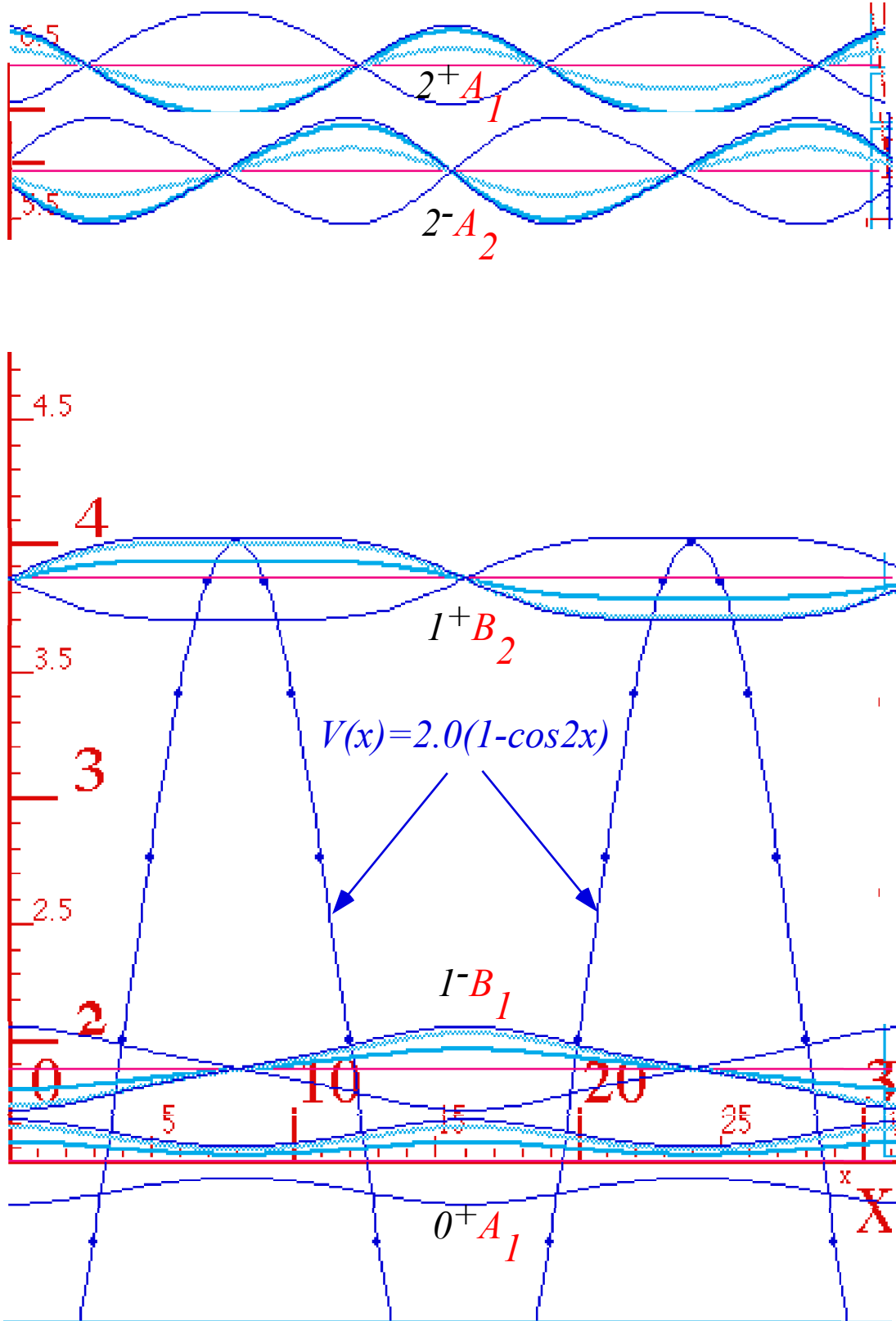
Fig. 16.1.6 (N=2) Mathieu eigenfunctions for V=2.0. 0^+A_1, 1^-B_1, 1^+B_2, 2^-A_2, and 2^+A_1.

However, the classical pendulum model has no such restriction, and this is one reason this analogy is conceptually useful. By varying the frequency of the "roller-coaster" we allow the pendulum trajectory to cross the axes at <u>any</u> number 0.01, 0.97, 2.35, of times in the time it takes for a pair (*N=2*) of up-and-down trips by the

"roller-coaster." So far, our arbitrary demand (16.1.8b) for periodic behavior has restricted the trajectory to the even numbers 0, 2, 2, 4, 4, ... of crossings seen in Fig. 16.1.4 and 16.1.5.

Relaxing periodicity restrictions allows crossing rates between 0 and 2 which, according to (16.1.16b,d), correspond to energies in the stable inverted *Band-(0)* between $E(0^+)= -0.4551$ and $E(1^-)=-0.1102$ ("roller-coaster" frequency between *Band(0)* boundaries $\omega(0^+)= 2.96$ and $\omega(1^-)=6.02$), or else crossing rates between 2 and 4 which correspond to energies in the first stable hanging *Band-(1)* between $E(1^+)=1.8591$ and $E(2^-)=3.9170$ ("roller-coaster" frequency between *Band(1)* boundaries $\omega(1^+)= 1.4668$ and $\omega(2^-)=1.0105$), and so on to higher quantum energies (and <u>lower</u> "roller-coaster" frequencies).

The first unstable region *Gap(1)* in Fig. 16.1.3 is due to having no crossing rates between 2 and 2, (or quantum numbers between 1 and 1) and *Gap(2)* in Fig. 16.1.3 arises because no rates exist between 4 and 4, (or quantum numbers between 2 and 2) and so on. Kronig-Penney theory in Sec. 14.2 is based on exponential blow-up behavior in forbidden gaps. Fig. 16.1.7 shows a pendulum at frequency $\omega_y =1.5$ in *Gap(1)* undergoing <u>non</u>-linear (exponential) resonance. This is called *parametric amplification*.
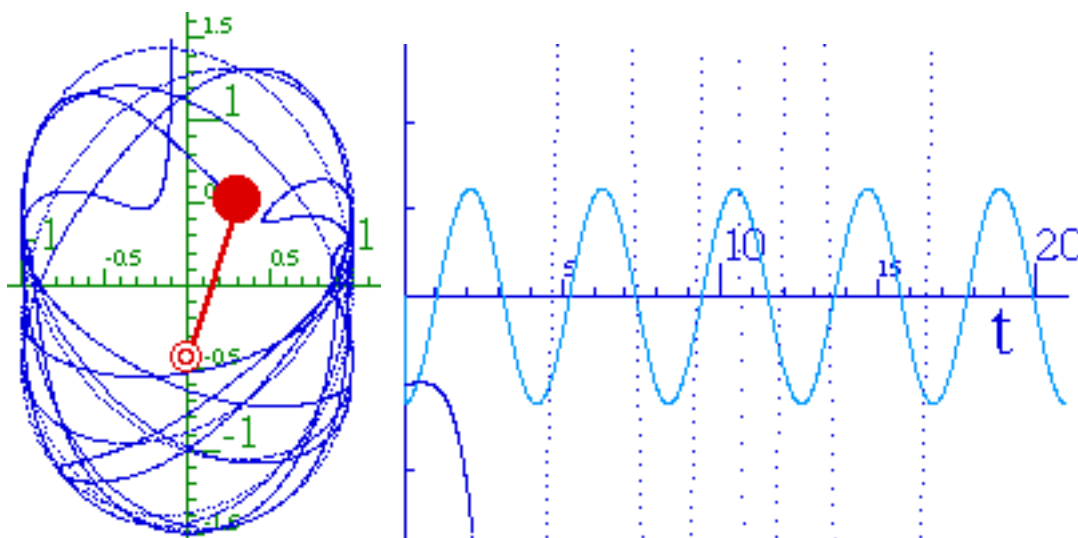
Fig. 16.1.7 Resonant modes for a Gap(1) frequency $\omega_y =1.5$.

Low amplitude oscillation ($A_y=0.05$ or $V=0.2$) is unusual for the classical analog because the lower band boundary is negative ($E(0^+)= -0.0050$) while the upper one is positive ($E(1^-)=+0.8988$) according to (16.1.16) leaving $E=0$ and infinite "roller-coaster" frequency ($\omega_y=\infty$) <u>inside</u> the band! This inverted pendulum is stable on a "roller-coaster" pumping between $\omega_y(0^+)= 28.2843$ and ∞ , and a hanging pendulum is stable if the frequency is between $\omega_y(1^-)= 2.10959$ and ∞. So either pendulum-up or pendulum-down is stable in the frequency range between *28.2843* and ∞. But, such low amplitude can't easily resonate a hanging pendulum. Only *Gap(1)* between $E(1^-)=+0.8988$ and $E(1^+)=1.0987$ ($\omega_y(1^-)= 2.10959$ and $\omega_y(1^+)= 1.90805$) is significant.

(c) (N=3) Triple-well potential and three-wiggle repeat

The periodicity restrictions for the Bohr-Bloch ring potential may be relaxed in discrete steps by increasing the number N of potential wells. Increasing $N=2$ to $N=3$ raises the number of C_N symmetry classes

from two (*Odd* and *Even* or $0_2 = 0 \ mod \ 2$ and $1_2 = 1 \ mod \ 2$) to three ($0_3 = 0 \ mod \ 3$, $1_3 = 1 \ mod \ 3$, and $2_3 = 2 \ mod \ 3 = -1_3$). There are three distinct Hamiltonian matrices in place of the two in (16.1.11a).

$$(16.1.17)$$

$\langle j|(\mathbf{D}+\mathbf{V})|k\rangle=$ (for j and k=0 mod 3) $\langle j|(\mathbf{D}+\mathbf{V})|k\rangle=$ (for j and k=1 mod 3) $\langle j|(\mathbf{D}+\mathbf{V})|k\rangle=$ (for j and k=2 mod 3)

$\cdots \ |-9\rangle, |-6\rangle, |-3\rangle, \ |0\rangle, \ |3\rangle, \ |6\rangle, \ |9\rangle, \cdots$ $\cdots \ |-11\rangle, |-8\rangle, |-5\rangle, \ |-2\rangle, \ |1\rangle, \ |4\rangle, \ |7\rangle, \cdots$ $\cdots \ |-7\rangle, \ |-4\rangle, |-1\rangle, \ |2\rangle, \ |5\rangle, \ |8\rangle, \ |11\rangle, \cdots$

$$\begin{pmatrix} \ddots & & & & & & & \\ & 9^2 & v & & & & & \\ & v & 6^2 & v & & & & \\ & & v & 3^2 & v & & & \\ & & & v & 0 & v & & \\ & & & & v & 3^2 & v & \\ & & & & & v & 6^2 & v \\ & & & & & & v & 9^2 \\ & & & & & & & & \ddots \end{pmatrix} , \begin{pmatrix} \ddots & & & & & & & \\ & 11^2 & v & & & & & \\ & v & 8^2 & v & & & & \\ & & v & 5^2 & v & & & \\ & & & v & 2^2 & v & & \\ & & & & v & 1^2 & v & \\ & & & & & v & 4^2 & v \\ & & & & & & v & 7^2 \\ & & & & & & & & \ddots \end{pmatrix} , \begin{pmatrix} \ddots & & & & & & & \\ & 7^2 & v & & & & & \\ & v & 4^2 & v & & & & \\ & & v & 1^2 & v & & & \\ & & & v & 2^2 & v & & \\ & & & & v & 5^2 & v & \\ & & & & & v & 8^2 & v \\ & & & & & & v & 11^2 \\ & & & & & & & & \ddots \end{pmatrix}$$

This separation due to symmetry happens because the potential equation (16.1.10) cannot couple states $|j\rangle$ and $|k\rangle$ unless k and j differ by ± 3. The first ($0_3 = 0 \ mod \ 3$) matrix is the same as the first ($0_2 = even$) matrix in (16.1.11) multiplied by $3^2/2^2 = 9/4$. Its levels will be the $(0^+A_1)-(2^-A_2)-(2^+A_1)-(4^-A_2)-(4^+A_1)-(6^-A_2)-..$sequence of levels seen in Fig. 16.1.2 and 16.1.3 scaled up by $3^2/2^2 = 9/4$. It is also the $N=1$ spectrum scaled up by $3^2 = 9$.

The second ($1_3 = 1 \ mod \ 3$) matrix and third ($2_3 = 2 \ mod \ 3$) matrix are new and different from the second ($1_2 = odd$) matrix in (16.1.11) so the $(1^-B_1)-(1^+B_2)-(3^-B_1)-(3^+B_2)-..$sequence of levels seen before will not appear here. In its place will be a doubly degenerate set of levels inside the *AB*-bands of Fig. 16.1.2. The degeneracy occurs because the second (1_3) and third (2_3) matrix are identical except for reversed order. In fact this degeneracy is a general consequence of D_3 symmetry. Recall that D_3 symmetry has no *B*-type ireps but its E_1-irep is 2-by-2.

Pendulum modes for $N=3$ repeat with period equal to 3 times the driving "roller-coaster" period $2\pi/\omega_y$. The select values of ω_y which cause this are found from the eigenvalues of the Hamiltonian (16.1.17) using the same equations (16.1.15) with $N=3$. This will be done for $N=6$ below.

(d) (N=6) Hexagonal potential and six-wiggle repeat

The $N=6$ spectrum contains both the $N=2$ and $N=3$ spectrum. The 0_6 and 3_6 matrices are below.

$\langle j|(\mathbf{D}+\mathbf{V})|k\rangle=$ (for j and k=0 mod 6) $\langle j|(\mathbf{D}+\mathbf{V})|k\rangle=$ (for j and k=3 mod 6)

$\cdots \ |-18\rangle, |-12\rangle, |-6\rangle, \ |0\rangle, \ |6\rangle, \ |12\rangle, \ |18\rangle, \cdots$ $\cdots \ |-21\rangle, \ |-15\rangle, |-9\rangle, \ |-3\rangle, \ |3\rangle, \ |9\rangle, \ |15\rangle, \cdots$ $(16.1.18)$

$$\begin{pmatrix} \ddots & & & & & & & \\ & 18^2 & v & & & & & \\ & v & 12^2 & v & & & & \\ & & v & 6^2 & v & & & \\ & & & v & 0 & v & & \\ & & & & v & 6^2 & v & \\ & & & & & v & 12^2 & v \\ & & & & & & v & 18^2 \\ & & & & & & & & \ddots \end{pmatrix} , \begin{pmatrix} \ddots & & & & & & & \\ & 21^2 & v & & & & & \\ & v & 15^2 & v & & & & \\ & & v & 9^2 & v & & & \\ & & & v & 3^2 & v & & \\ & & & & v & 3^2 & v & \\ & & & & & v & 9^2 & v \\ & & & & & & v & 15^2 \\ & & & & & & & & \ddots \end{pmatrix}$$

The first $N=6$ ($0_6=0\ mod\ 6$) matrix is the same as the first $N=2$ ($0_2=even$) matrix in (16.1.11) multiplied by $3^2=9$. The same goes for the second $N=6$ ($3_6=3\ mod\ 6$); it is the second $N=2$ ($1_2=odd$) matrix in (16.1.11) multiplied by 9. So the $N=6$ band boundaries are $N=2$ levels with a scale-up factor of 9. The resulting D_6 levels are labeled like the D_2 levels in Fig. 16.1.2 and (16.1.14). But, the $m^\pm$ values are three times as large.

$$(0^+A_1\ ..(band)..\ 3^-B_1)\ [gap]\ (\ 3^+B_2\ ..(band)..\ 6^-A_2)\ [gap]\ (6^+A_1\ ..(band)..9^-B_1)\ [gap]$$

The levels inside the bands are determined by the eigenvalues of the following 1_6 and 2_6 matrices.

$\langle j|(\mathbf{D}+\mathbf{V})|k\rangle=$ (for j and k=1 mod 6) $\langle j|(\mathbf{D}+\mathbf{V})|k\rangle=$ (for j and k=2 mod 6)

$\cdots\ |-17\rangle,|-11\rangle,|-5\rangle,\ |1\rangle,\ |7\rangle,\ |13\rangle,\ |19\rangle,\cdots$ $\cdots\ |-16\rangle,|-10\rangle,|-4\rangle,\ |2\rangle,\ |8\rangle,\ |14\rangle,\ |20\rangle,\cdots$ (16.1.19a)

$$\begin{pmatrix} \ddots & & & & & & \\ & 17^2 & v & & & & \\ & v & 11^2 & v & & & \\ & & v & 5^2 & v & & \\ & & & v & 1 & v & \\ & & & & v & 7^2 & v \\ & & & & & v & 13^2 & v \\ & & & & & & v & 19^2 \\ & & & & & & & & \ddots \end{pmatrix}, \begin{pmatrix} \ddots & & & & & & \\ & 16^2 & v & & & & \\ & v & 10^2 & v & & & \\ & & v & 4^2 & v & & \\ & & & v & 2^2 & v & \\ & & & & v & 8^2 & v \\ & & & & & v & 14^2 & v \\ & & & & & & v & 20^2 \\ & & & & & & & & \ddots \end{pmatrix}$$

The -1_6 and -2_6 matrices are identical to the 1_6 and 2_6 matrices, respectively, so all eigenvalues are doubly degenerate with $\pm1_6$ belonging to E_1 and $\pm2_6$ belonging to E_2 symmetry ireps of D_6. The E_2 levels arise from the 2_6 matrix which is a copy of the 1_3 matrix in (16.1.17) multiplied by $2^2=4$. So, the D_6 -E_2 levels are scaled copies of the D_3 - E_1 levels. But, the E_2 states, like the B_1 and B_2 are not D_3 symmetry states.

The AB band boundary levels for D_2 in Fig. 16.1.2 and 16.1.3 avoid crossing each other except at $(V=0)$ (no potential). The same applies to their scaled copies for D_6. The E_1 and E_2 levels also avoid each other. The closest approach occurs between the $|2\rangle$ and $|-4\rangle$ states belonging to a pair of E_2 doublets as approximated for low $v=V/2$ by solving the following submatrix of the Hamiltonian matrix (16.1.19).

$$\langle H\rangle = \begin{pmatrix} \ddots & & \\ & 4^2 & v \\ & v & 2^2 \\ & & & \ddots \end{pmatrix},$$

$$E_2' \cong 4^2 + \frac{v^2}{4^2-2^2} = 16 + \frac{V^2}{48}$$

$$E_2 \cong 2^2 - \frac{v^2}{4^2-2^2} = 4 - \frac{V^2}{48}$$

(16.1.19b)

This $|2\rangle$ and $|-4\rangle$ pair of E_2 hyperbolas are closer and sharper than the $|1\rangle$ and $|-5\rangle$ pair of E_1 levels.

$$\langle H\rangle = \begin{pmatrix} \ddots & & \\ & 5^2 & v \\ & v & 1^2 \\ & & & \ddots \end{pmatrix},$$

$$E_1' \cong 5^2 + \frac{v^2}{5^2-1^2} = 25 + \frac{V^2}{96}$$

$$E_1 \cong 1^2 - \frac{v^2}{5^2-1^2} = 1 - \frac{V^2}{96}$$

(16.1.19c)

The beginning of the D_6 spectrum up to $m=9$ is the following cyclic sequence of bands and gaps.

$(0^+A_1,\ 1^\pm E_1,\ 2^\pm E_2,\ 3^-B_1)\ [gap]\ (3^+B_2,\ 4^\pm E_2,,\ 5^\pm E_1,\ 6^-A_2)\ [gap]\ (6^+A_1,\ 7^\pm E_1,\ 8^\pm E_2,\ 9^-B_1)$ (16.1.20)

Examples of the eigenvalues versus strength V of an unbiased potential $Vcos(6x)$ for a D_6 Mathieu potential are shown in Fig. 16.1.8. The avoiding hyperbolas of (16.1.19c) are seen for the $1^\pm$ and $5^\pm$ levels.
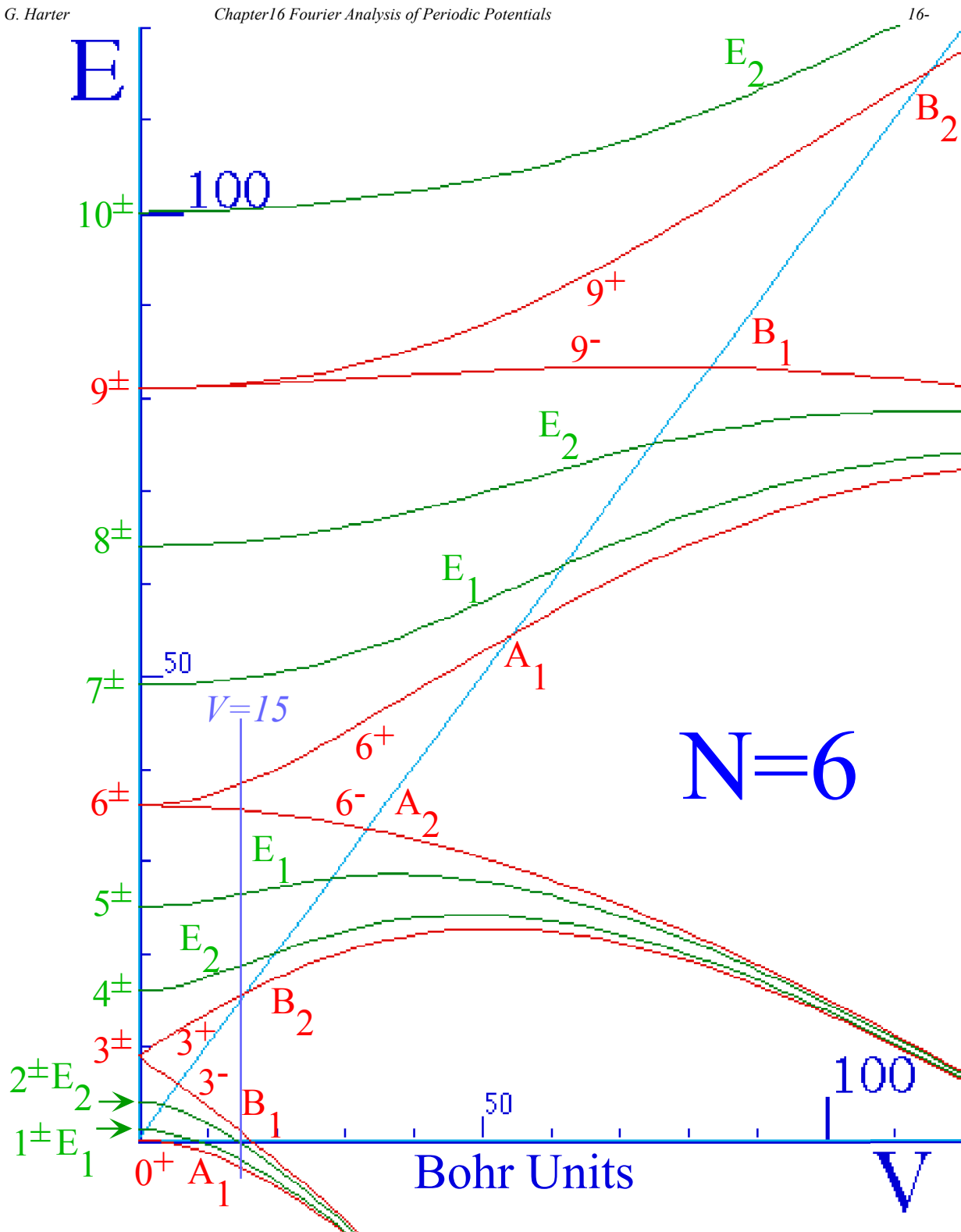
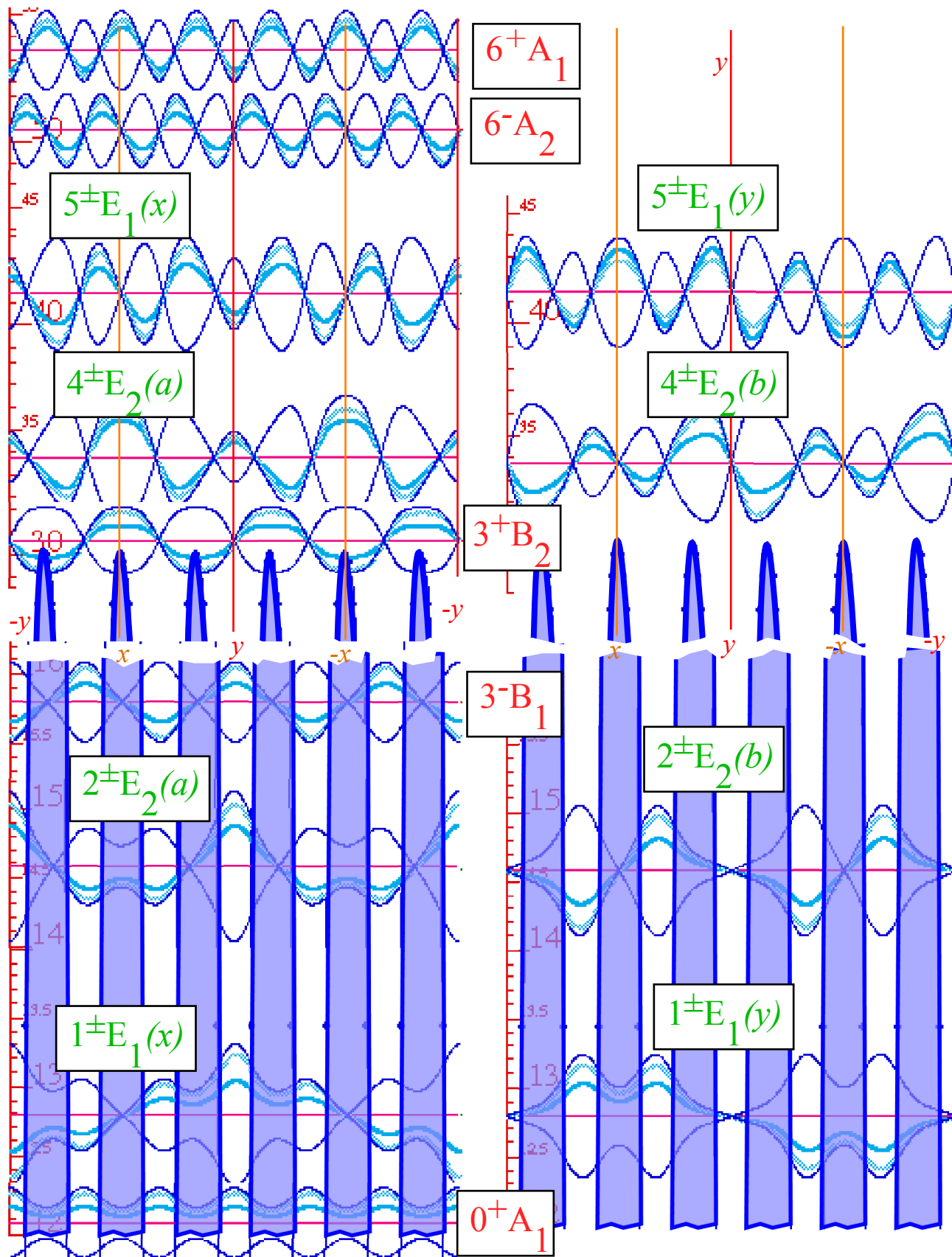*Fig. 16.1.8 N=6 Mathieu (cosine) potential level spectrum versus potential depth V*

Fig. 16.1.9 Lowest twelve N=6 Mathieu eigenfunctions for V=15. (Top-to-bottom =30)

The D_6 Mathieu wavefunctions of a steep cosine potential are shown in Fig. 16.1.9. They belong to first twelve or thirteen energy values along the $V=15$ line in Fig. 16.1.8. We compare them to the square-well wave functions shown in Fig. 3.6.10 for the Kronig-Peney (KP) potential having the same top-to-bottom depth: $V=30$.

The lower band energies for the square-well are a couple of Bohr units lower than those of the cosine-well potential because the latter is narrower at the bottom and "squeezes" the waves up. However, the higher band energies for the square well are slightly higher because the flat tops raise the potential more than the cosine "needles" at the top of the Mathieu potential. The flat tops the square-well make its 3^+B_2 wave in Fig. 3.6.10 much flatter than the corresponding Mathieu 3^+B_2 wave in Fig. 16.1.9. Otherwise, the waves appear remarkably similar even in the higher bands.

For either potential, the 3^-B_1 - 3^+B_2 gap between the bands is much larger than the spread of the lower $(0^+A_1$, $1^\pm E_1$, $2^\pm E_2$, $3^-B_1)$ band but comparable to the spread of the higher $(3^+B_2$, $4^\pm E_2$,, $5^\pm E_1$, $6^-A_2)$ band. The jagged break in either Fig. 16.1.9 or Fig. 15.5.2 indicates a gap and change of energy scale. Tunneling or coupling is much smaller for waves trapped in potential wells, so band splitting there is less.

The energy difference of the first gap between 3^-B_1 and 3^+B_2 is mostly due to potential energy difference between the two waves. Their kinetic energies are the same; they both have three $(m=3)$ wave-node pairs. The lower 3^-B_1 wave is sitting where its anti-nodes are in the low potential wells while its nodes are in the high potential barriers. (It's a "well-sitter.") In contrast, the 3^+B_2 wave is higher because it puts its high probability anti-nodes right on top of the barriers and leaves its zero-probability nodes in the wells. (It's a "barrier-sitter.") This is a simple explanation of the source of the first-order band-gap energy at the 1st Brillouin band boundary.

The second gap energy difference between 6^-A_2 and 6^+A_1 is more complicated, as are the higher gaps such as the next 9^-B_1 - 9^+B_2 gap. Again, the kinetic energies of both 6^- and 6^+ orbitals are the same, but the 6^+A_1 wave is not pure $m=6$. From, Fig. 16.1.9 it is seen that the 6^+A_1 wave has a significant fraction of $m=0$ which makes its amplitude alternate between well and barrier. Previously, we had mentioned that the 0^+A_1 had some $m=6$, in fact, it is just enough to make 0^+A_1 and 6^+A_1 orthogonal.

A resonance-repulsion pushes the 6^+A_1 wave up and pulls the 0^+A_1 wave down. Meanwhile, the 6^-A_2 wave sits near the top of Fig. 16.1.9 without changing much from a pure $m=6$. Symmetry D_6 prohibits a potential coupling between 6^-A_2 and any but another A_2 state. The nearest A_2 is the 12^-A_2 state $(12^2-6^2=108)$ Bohr units above, pretty high for a potential of only 15 Bohr units. In Fig. 16.1.8 you can see the 6^-A_2 level at $V=15$ repelled only a little below its $V=0$ energy. A quantitative analysis of this is given shortly.

The curvature of levels in Fig. 16.1.8 is indicative of changing eigenfunctions or varying mixture of Fourier components, and this gives the complicated second or higher order splittings. To analyze high-m splittings, a more detailed matrix analysis based on D_N symmetry is necessary as shown next.

16.2 General D_N-symmetric periodic potentials

Mathieu D_N potentials have only a single cosine $A \cos N \phi$. Now Mathieu analysis is generalized to potentials which have multi-cosine Fourier series in Hamiltonians of the following form.

$$\mathbf{H} = \mathbf{D} + V = \mathbf{D} + A_1 \cos N \phi + A_2 \cos 2N \phi + A_3 \cos 3N \phi + \qquad (16.2.1a)$$

A general Hamilton matrix element $\langle m|\mathbf{H}|n\rangle$ in a Bohr orbital basis is computed, as follows, in Bohr units.

$$\langle m|\mathbf{H}|n\rangle = \langle m|\mathbf{D}|n\rangle + \langle m|V|n\rangle$$

$$= m^2 \delta_{m,n} + \sum_{k=1}^{N} \int_0^{2\pi} d\phi\, e^{-im\phi} A_k \cos kN\phi\, e^{-in\phi}$$

$$= m^2 \delta_{m,n} + \sum_{k=1}^{N} \frac{1}{2} A_k \int_0^{2\pi} d\phi \left(e^{-i(n-m+kN)\phi} + e^{-i(n-m-kN)\phi} \right)$$

$$= m^2 \delta_{m,n} + \sum_{k=1}^{N} \left(\frac{1}{2} A_k \delta_{m-n,kN} + \frac{1}{2} A_k \delta_{n-m,kN} \right)$$

$$= m^2 \delta_{m,n} + \begin{cases} A_{(m-n)/N} & \text{if} : m > n \quad \text{and} : k = (m-n)/N \text{ is integer} > 0, \\ A_{(n-m)/N} & \text{if} : n > m \quad \text{and} : k = (n-m)/N \text{ is integer} > 0, \\ 0 & \text{otherwise.} \end{cases}$$

Each component $\langle m|\mathbf{H}|n\rangle$ consists of three terms, only one of which is non-zero at a time.

$$\langle m|\mathbf{H}|n\rangle \quad = m^2 \delta_{m,n} + \frac{1}{2} A_{(m-n)/N} + \frac{1}{2} A_{(n-m)/N}$$

$$\langle -m|\mathbf{H}|n\rangle \quad = m^2 \delta_{m,n} + \frac{1}{2} A_{(-m-n)/N} + \frac{1}{2} A_{(n+m)/N}$$

$$\langle m|\mathbf{H}|-n\rangle \quad = m^2 \delta_{m,n} + \frac{1}{2} A_{(m+n)/N} + \frac{1}{2} A_{(-n-m)/N} \qquad (16.2.1b)$$

$$\langle -m|\mathbf{H}|-n\rangle \quad = m^2 \delta_{m,n} + \frac{1}{2} A_{(-m+n)/N} + \frac{1}{2} A_{(-n+m)/N}$$

$\langle \mathbf{H} \rangle$ has a Fourier cosine coefficient $\upsilon_k = {}^1\!/_2\, A_k$ on k-*th* super diagonal. For $N=2$, $\langle \mathbf{H} \rangle$ is as follows.

$\langle m|(\mathbf{D}+\mathbf{V})|n\rangle =$ (for m and n even) $\langle m|(\mathbf{D}+\mathbf{V})|n\rangle =$ (for m and n odd)

$\cdots\ |-6\rangle,\ |-4\rangle,\ |-2\rangle,\ |0\rangle,\ |2\rangle,\ |4\rangle,\ |6\rangle,\cdots$ $\cdots|-7\rangle,|-5\rangle,|-3\rangle,\ |-1\rangle,\ |1\rangle,\ |3\rangle,\ |5\rangle,\cdots$ (16.2.1c)

$$\begin{pmatrix} \ddots & & & & & & \\ & 6^2 & \upsilon_1 & \upsilon_2 & \upsilon_3 & \upsilon_4 & \upsilon_5 & \upsilon_6 \\ & \upsilon_1 & 4^2 & \upsilon_1 & \upsilon_2 & \upsilon_3 & \upsilon_4 & \upsilon_5 \\ & \upsilon_2 & \upsilon_1 & 2^2 & \upsilon_1 & \upsilon_2 & \upsilon_3 & \upsilon_4 \\ & \upsilon_3 & \upsilon_2 & \upsilon_1 & 0 & \upsilon_1 & \upsilon_2 & \upsilon_3 \\ & \upsilon_4 & \upsilon_3 & \upsilon_2 & \upsilon_1 & 2^2 & \upsilon_1 & \upsilon_2 \\ & \upsilon_5 & \upsilon_4 & \upsilon_3 & \upsilon_2 & \upsilon_1 & 4^2 & \upsilon_1 \\ & \upsilon_6 & \upsilon_5 & \upsilon_4 & \upsilon_3 & \upsilon_2 & \upsilon_1 & 6^2 \\ & & & & & & & \ddots \end{pmatrix}, \quad \begin{pmatrix} \ddots & & & & & & \\ & 7^2 & \upsilon_1 & \upsilon_2 & \upsilon_3 & \upsilon_4 & \upsilon_5 & \upsilon_6 \\ & \upsilon_1 & 5^2 & \upsilon_1 & \upsilon_2 & \upsilon_3 & \upsilon_4 & \upsilon_5 \\ & \upsilon_2 & \upsilon_1 & 3^2 & \upsilon_1 & \upsilon_2 & \upsilon_3 & \upsilon_4 \\ & \upsilon_3 & \upsilon_2 & \upsilon_1 & 1^2 & \upsilon_1 & \upsilon_2 & \upsilon_3 \\ & \upsilon_4 & \upsilon_3 & \upsilon_2 & \upsilon_1 & 1^2 & \upsilon_1 & \upsilon_2 \\ & \upsilon_5 & \upsilon_4 & \upsilon_3 & \upsilon_2 & \upsilon_1 & 3^2 & \upsilon_1 \\ & \upsilon_6 & \upsilon_5 & \upsilon_4 & \upsilon_3 & \upsilon_2 & \upsilon_1 & 5^2 \\ & & & & & & & \ddots \end{pmatrix}$$

The preceding generalizes the matrices in (16.1.11). It is a way to derive band eigenvalues and wavefunctions for any periodic potential whose individual wells are C_2 symmetric. An equilateral square-well Kronig-Penney (KP) potential (with $W=L$) is an example treated in Fig. 14.2.12 and 14.2.13.

$$V_{KP} = (V/\pi)[\ \cos N\phi + 0\ \cos 2N\phi - (1/3)\ \cos 3N\phi + 0\ \cos 4N\phi + (1/5)\ \cos 5N\phi\ ..]$$

An unbiased equilateral KP potential has no even harmonics ($\cos 2N\phi$, $\cos 4N\phi$, $\cos 6N\phi$,..); $A_{k\text{-}even}$ appear only when the well width W differs from barrier length L. The coefficients of the $1,3,5,7..$ harmonics are an odd-*harmonic series* with alternating signs $(1, -1/3, +1/5, -1/7,...)$. The alternating signs cause "twisting" and crossing of band boundaries and the "smiles" in Figs. 14.2.11 and 14.2.13.

　　　If a periodic potential is "lop-sided" such as the "hounds-tooth" potential in Fig. 14.2.10, it will also be necessary to include sine Fourier series terms, or what is equivalent, a fully complex Fourier series as in the analysis of C_N symmetry. This will mean complex off-diagonal matrix components in (16.2.1c). Nevertheless, transverse rotation or reflection symmetry breaking ("lop-sidedness") does not, by itself, split the D_N degeneracies, it merely adjusts the local symmetry combinations such as (15.4.8c) so the waves are locally "lop-sided" to match each potential well and barrier.

　　　To estimate band curvature and symmetry effects, including the size of band "smiles," we separate the Hamiltonian matrices using D_2 symmetry bases. We begin with the "scalar" A_1 symmetry bases.

$$\left|0^+ A_1\right\rangle = \left|0\right\rangle, \quad \text{and:} \quad \left|m^+ A_1\right\rangle = \left(\left|m\right\rangle + \left|-m\right\rangle\right)/\sqrt{2} \quad \text{(for: } m>0\text{)} \qquad (16.2.2a)$$

A_1 are *even-m cosine standing waves*. To not double-count, let m and n be positive integers in the matrix.

$$\left\langle m^+ A_1 \left| \mathbf{H} \right| n^+ A_1 \right\rangle = \left(\left(\left\langle m\right| + \left\langle -m\right|\right) \mathbf{H}\left(\left|n\right\rangle + \left|-n\right\rangle\right)\right)/2 = \frac{\left\langle m\right|\mathbf{H}\left|n\right\rangle + \left\langle -m\right|\mathbf{H}\left|-n\right\rangle}{2} + \frac{\left\langle m\right|\mathbf{H}\left|-n\right\rangle + \left\langle -m\right|\mathbf{H}\left|n\right\rangle}{2}$$

$$= \left\langle m\right|\mathbf{H}\left|n\right\rangle + \left\langle m\right|\mathbf{H}\left|-n\right\rangle = \delta_{m,n}m^2 + \upsilon_{n-m} + \upsilon_{n+m} \quad \text{where: } \upsilon_{n\pm m} = \frac{1}{2}A_{(n\pm m)/N} \qquad (16.2.2b)$$

Furthermore, only upper diagonal $(m<n)$ elements are given; transpose are conjugates ($\left\langle n\right|\mathbf{H}\left|m\right\rangle = \left\langle m\right|\mathbf{H}\left|n\right\rangle^*$).

$\left\|m^+ A_1\right\rangle =$	$\left\|0^+ A_1\right\rangle$	$\left\|2^+ A_1\right\rangle$	$\left\|4^+ A_1\right\rangle$	$\left\|6^+ A_1\right\rangle$	$\left\|8^+ A_1\right\rangle$
$\left\langle 0^+ A_1\right\|$	0	$\sqrt{2}\upsilon_1$	$\sqrt{2}\upsilon_2$	$\sqrt{2}\upsilon_3$	$\sqrt{2}\upsilon_4$
$\left\langle 2^+ A_1\right\|$		$2^2 + \upsilon_2$	$\upsilon_1 + \upsilon_3$	$\upsilon_2 + \upsilon_4$	$\upsilon_3 + \upsilon_5$
$\left\langle 4^+ A_1\right\|$			$4^2 + \upsilon_4$	$\upsilon_1 + \upsilon_5$	$\upsilon_2 + \upsilon_6$
$\left\langle 6^+ A_1\right\|$				$6^2 + \upsilon_6$	$\upsilon_1 + \upsilon_7$
$\left\langle 8^+ A_1\right\|$					$8^2 + \upsilon_8$

$$(16.2.2c)$$

Next are the "pseudo-scalar" A_2 symmetry bases or *even-m sine standing waves*.

$$\left|m^- A_2\right\rangle = \left(\left|m\right\rangle - \left|-m\right\rangle\right)/i\sqrt{2} \qquad (16.2.3a)$$

A_1 and A_2 waves are "**A**lways the same" phase and amplitude in every well, but the A_2 waves have mid-well nodes that make them anti symmetric to $180°$ rotations around the well-center.

$$\left\langle m^- A_2 \left| \mathbf{H} \right| n^- A_2 \right\rangle = \left(\left(\left\langle m\right| - \left\langle -m\right|\right) \mathbf{H}\left(\left|n\right\rangle - \left|-n\right\rangle\right)\right)/2 = \frac{\left\langle m\right|\mathbf{H}\left|n\right\rangle + \left\langle -m\right|\mathbf{H}\left|-n\right\rangle}{2} - \frac{\left\langle m\right|\mathbf{H}\left|-n\right\rangle + \left\langle -m\right|\mathbf{H}\left|n\right\rangle}{2}$$

$$= \left\langle m\right|\mathbf{H}\left|n\right\rangle - \left\langle m\right|\mathbf{H}\left|-n\right\rangle = \delta_{m,n}m^2 + \upsilon_{n-m} - \upsilon_{n+m} \quad \text{where: } \upsilon_{n\pm m} = \frac{1}{2}A_{(n\pm m)/N} \qquad (16.2.3b)$$

The A_2 matrix is quite different from the A_1 matrix. Note absence of the forbidden $|0^- A_2\rangle$ state.

$$
\begin{array}{c|ccccc}
\left|m^- A_2\right\rangle = & \left| \ \right\rangle & \left|2^- A_2\right\rangle & \left|4^- A_2\right\rangle & \left|6^- A_2\right\rangle & \left|8^- A_2\right\rangle \\
\hline
\left\langle \ \right| & 0 & 0 & 0 & 0 & 0 \\
\left\langle 2^- A_2\right| & & 2^2 - \upsilon_2 & \upsilon_1 - \upsilon_3 & \upsilon_2 - \upsilon_4 & \upsilon_3 - \upsilon_5 \\
\left\langle 4^- A_2\right| & & & 4^2 - \upsilon_4 & \upsilon_1 - \upsilon_5 & \upsilon_2 - \upsilon_6 \\
\left\langle 6^- A_2\right| & & & & 6^2 - \upsilon_6 & \upsilon_1 - \upsilon_7 \\
\left\langle 8^- A_2\right| & & & & & 8^2 - \upsilon_8 \\
& & & & & & \ddots
\end{array}
\qquad (16.2.3c)
$$

Odd Brillouin-band-boundary B_1 and B_2 symmetry bases or *odd-m cosine B_1 or sine B_2 standing waves*.

$$\left|m^- B_1\right\rangle = \left(\left|m\right\rangle + \left|-m\right\rangle\right)/i\sqrt{2} \qquad\qquad \left|m^+ B_2\right\rangle = \left(\left|m\right\rangle - \left|-m\right\rangle\right)/i\sqrt{2} \qquad (16.2.4a)$$

B_1 and B_2 waves are "<u>B</u>ack-and-forth" in phase and amplitude in going from well-to-well. The B_2 waves have mid-well nodes that make them anti symmetric to *180°* flips, but B_1 waves are symmetric to flips. The 1st order splitting of *m-th* gap is $2\upsilon_m$, twice the *m-th* Fourier component.

$$
\begin{array}{c|cccc}
\left|m^- B_1\right\rangle = & \left|1^- B_1\right\rangle & \left|3^- B_1\right\rangle & \left|5^- B_1\right\rangle & \left|7^- B_1\right\rangle \\
\hline
\left\langle 1^- B_1\right| & 1^2 + \upsilon_1 & \upsilon_1 + \upsilon_2 & \upsilon_2 + \upsilon_3 & \upsilon_3 + \upsilon_4 \\
\left\langle 3^- B_1\right| & & 3^2 + \upsilon_3 & \upsilon_1 + \upsilon_4 & \upsilon_2 + \upsilon_5 \\
\left\langle 3^- B_1\right| & & & 5^2 + \upsilon_5 & \upsilon_1 + \upsilon_6 \\
\left\langle 3^- B_1\right| & & & & 7^2 + \upsilon_7 \\
& & & & & \ddots
\end{array}
\ (16.2.4a)
\quad
\begin{array}{c|cccc}
\left|m^+ B_1\right\rangle = & \left|1^+ B_2\right\rangle & \left|3^+ B_2\right\rangle & \left|5^+ B_2\right\rangle & \left|7^+ B_2\right\rangle \\
\hline
\left\langle 1^+ B_2\right| & 1^2 - \upsilon_1 & \upsilon_1 - \upsilon_2 & \upsilon_2 - \upsilon_3 & \upsilon_3 - \upsilon_4 \\
\left\langle 3^+ B_2\right| & & 3^2 - \upsilon_3 & \upsilon_1 - \upsilon_4 & \upsilon_2 - \upsilon_5 \\
\left\langle 3^+ B_2\right| & & & 5^2 - \upsilon_5 & \upsilon_1 - \upsilon_6 \\
\left\langle 3^+ B_2\right| & & & & 7^2 - \upsilon_7 \\
& & & & & \ddots
\end{array}
\ (16.2.4b)
$$

　　　If the number *N* of wells that is a multiple *M* of 2 it is only necessary to multiply all *m*-quanta by *M* (including *m*'s in the m^2 diagonal elements) and then obtain the band boundary eigenvalues. For *N=6* the following matrices result for the lowest three bases. The Mathieu case has $\upsilon_k=0$ except for $\upsilon_1=V/2$.

$$
\begin{array}{ccc}
\left|0^+ A_1\right\rangle \ \left|6^+ A_1\right\rangle \ \left|12^+ A_1\right\rangle & \left| \ \right\rangle \ \left|6^- A_2\right\rangle \ \left|12^- A_2\right\rangle & \left|3^- B_1\right\rangle \ \left|9^- B_1\right\rangle \ \left|15^- B_1\right\rangle & \left|3^+ B_2\right\rangle \ \left|9^+ B_2\right\rangle \ \left|15^+ B_2\right\rangle \\[4pt]
\begin{pmatrix}
0 & \sqrt{2}\upsilon_1 & \sqrt{2}\upsilon_2 \\
\sqrt{2}\upsilon_1 & 6^2 & \upsilon_1 + \upsilon_3 \\
\sqrt{2}\upsilon_2 & \upsilon_1 + \upsilon_3 & 12^2
\end{pmatrix}
&
\begin{pmatrix}
0 & 0 & 0 \\
0 & 6^2 & \upsilon_1 - \upsilon_3 \\
0 & \upsilon_1 - \upsilon_3 & 12^2
\end{pmatrix}
&
\begin{pmatrix}
3^2 + \upsilon_1 & \upsilon_1 + \upsilon_2 & \upsilon_2 + \upsilon_3 \\
\upsilon_1 + \upsilon_2 & 9^2 + \upsilon_3 & \upsilon_1 + \upsilon_4 \\
\upsilon_2 + \upsilon_3 & \upsilon_1 + \upsilon_4 & 15^2 + \upsilon_5
\end{pmatrix}
&
\begin{pmatrix}
3^2 - \upsilon_1 & \upsilon_1 - \upsilon_2 & \upsilon_2 - \upsilon_3 \\
\upsilon_1 - \upsilon_2 & 9^2 + \upsilon_3 & \upsilon_1 - \upsilon_4 \\
\upsilon_2 - \upsilon_3 & \upsilon_1 - \upsilon_4 & 15^2 + \upsilon_5
\end{pmatrix}
\end{array}
$$

$$(16.2.4c)$$

$$
\begin{pmatrix}
0 & \sqrt{2}\upsilon_1 & 0 \\
\sqrt{2}\upsilon_1 & 6^2 & \upsilon_1 \\
0 & \upsilon_1 & 12^2
\end{pmatrix},
\quad
\begin{pmatrix}
0 & 0 & 0 \\
0 & 6^2 & \upsilon_1 \\
0 & \upsilon_1 & 12^2
\end{pmatrix},
\quad
\begin{pmatrix}
3^2 + \upsilon_1 & \upsilon_1 & 0 \\
\upsilon_1 & 9^2 & \upsilon_1 \\
0 & \upsilon_1 & 15^2
\end{pmatrix},
\quad
\begin{pmatrix}
3^2 - \upsilon_1 & \upsilon_1 & 0 \\
\upsilon_1 & 9^2 & \upsilon_1 \\
0 & \upsilon_1 & 15^2
\end{pmatrix}
$$

(a) Mathieu potential solution by continued fractions

　　　The last set of matrices are all that is needed to estimate the effects of a Mathieu potential on $6^\pm$ levels mentioned after Fig. 16.1.9. Perturbation to order-2 gives a $6^- A_2$ energy downshift of 0.52 units.

$$E\left(6^- A_2\right) \cong 6^2 + \frac{\langle 6|V|12\rangle\langle 12|V|6\rangle}{6^2 - 12^2}$$

$$\cong 6^2 + \frac{\left(V/2\right)^2}{6^2 - 12^2} = 36 - \frac{7.5^2}{108} = 36 - 0.52 \qquad (16.2.5a)$$

However, the approximate 6^+A_2 energy shift is about five times greater and positive.

$$E\left(6^+ A_1\right) \cong 6^2 + \frac{\langle 6|V|0\rangle\langle 0|V|6\rangle}{6^2 - 0^2} + \frac{\langle 6|V|12\rangle\langle 12|V|6\rangle}{6^2 - 12^2}$$

$$\cong 6^2 + \frac{2\left(V/2\right)^2}{6^2 - 0^2} + \frac{\left(V/2\right)^2}{6^2 - 12^2} = 36 + \frac{2\cdot 7.5^2}{36} - \frac{7.5^2}{108} = 36 + 2.6 \qquad (16.2.5b)$$

This is consistent with the $6^\pm$ levels on the $V=15$ line of Fig. 16.1.8.

Since the Mathieu H-matrix has no elements beyond one step from the diagonal, it is relatively easy to derive perturbation expansions for its low eigenvalues $\varepsilon(1), \varepsilon(2), ..., \varepsilon(m)$ and eigenvector components $\psi_j(m)$. The equations that need to be solved are as follows.

$$\begin{array}{llll}
H_{12}\psi_2 & & = & \left(E - H_{11}\right)\psi_1 \\
H_{21}\psi_1 & H_{23}\psi_3 & = & \left(E - H_{22}\right)\psi_2 \\
H_{32}\psi_2 & H_{34}\psi_4 & = & \left(E - H_{33}\right)\psi_3 \\
... & & = & ...
\end{array} \qquad (16.2.6)$$

For the first eigenvalue $E= \varepsilon(1)$ and its components ψ_j, the following relations are exact but "entangled."

$$\varepsilon(1) = H_{11} + H_{12}\frac{\psi_2}{\psi_1}, \quad \psi_2 = \frac{H_{21}\psi_1}{\varepsilon(1) - H_{22}} + \frac{H_{23}\psi_3}{\varepsilon(1) - H_{22}}, \quad \psi_3 = \frac{H_{32}\psi_2}{\varepsilon(1) - H_{33}} + \frac{H_{32}\psi_4}{\varepsilon(1) - H_{33}}, \quad \cdots (16.2.7)$$

One may approximately disentangle them by recursive substitution of approximations for $\varepsilon(1)$ and ψ_j.

$$\varepsilon(1) = H_{11} + \frac{H_{12}H_{21}}{\varepsilon(1) - H_{22}} + \frac{H_{12}H_{23}}{\varepsilon(1) - H_{22}}\frac{\psi_3}{\psi_1}$$

$$= H_{11} + \frac{H_{12}H_{21}}{\varepsilon(1) - H_{22}} + \frac{H_{12}H_{23}H_{32}}{\left(\varepsilon(1) - H_{22}\right)\left(\varepsilon(1) - H_{33}\right)}\frac{\psi_2}{\psi_1} + ... \left[\psi_{\geq 4}terms\right]$$

$$= H_{11} + \frac{H_{12}H_{21}}{\varepsilon(1) - H_{22}} + \frac{H_{12}H_{23}H_{32}H_{21}}{\left(\varepsilon(1) - H_{22}\right)^2\left(\varepsilon(1) - H_{33}\right)} + \frac{H_{12}H_{23}H_{32}H_{23}}{\left(\varepsilon(1) - H_{22}\right)^2\left(\varepsilon(1) - H_{33}\right)}\frac{\psi_3}{\psi_1} + ...$$

$$= H_{11} + \frac{H_{12}H_{21}}{\varepsilon(1) - H_{22}} + \frac{H_{12}H_{23}H_{32}H_{21}}{\left(\varepsilon(1) - H_{22}\right)^2\left(\varepsilon(1) - H_{33}\right)} + \frac{H_{12}H_{23}H_{32}H_{23}H_{32}H_{21}}{\left(\varepsilon(1) - H_{22}\right)^3\left(\varepsilon(1) - H_{33}\right)^2} + ...\left[\psi_{\geq 3}terms\right]$$

$$(16.2.8)$$

Then the entangling energies $\varepsilon(1)$ in the denominator of each term is replaced by low order approximations beginning with $\varepsilon(1) = H_{11}$ and recursively increasing the order giving *continued fraction expansions*.

$$\varepsilon(1) = H_{11} + \cfrac{H_{12}H_{21}}{H_{11} - H_{22} + \cfrac{H_{12}H_{21}}{H_{11} - H_{22} + \cfrac{H_{12}H_{21}}{H_{11} - H_{22} + ...}} + ..} + \frac{H_{12}H_{23}H_{32}H_{21}}{\left(H_{11} - H_{22} + .\right)^2\left(H_{11} - H_{33} + ..\right)} + ... (16.2.9)$$

An elegant solution to Mathieu matrices of the form (16.2.2-4) first converts the eigenequations

$$H_{n,n-1}\psi_{n-1} + \left(\varepsilon_n - E\right)\psi_n + H_{n,n+1}\psi_{n+1} = 0, \qquad where: \quad \varepsilon_n = H_{nn} \qquad (16.2.10a)$$

to continued fractions which relate the *n-th* component ratio $\psi_n/\psi_{n\pm1}$ to lower and to higher ones.

$$\frac{\psi_n}{\psi_{n+1}} = \frac{H_{n,n+1}}{E-\varepsilon_n - H_{n,n-1}\dfrac{\psi_{n-1}}{\psi_n}}$$

$$= \cfrac{H_{n,n+1}}{E-\varepsilon_n - \cfrac{H_{n,n-1}H_{n-1,n}}{E-\varepsilon_{n-1}-H_{n-1,n-2}\dfrac{\psi_{n-2}}{\psi_{n-1}}}}$$

$$= \cfrac{H_{n,n+1}}{E-\varepsilon_n - \cfrac{H_{n,n-1}H_{n-1,n}}{E-\varepsilon_{n-1}-\cfrac{H_{n-1,n-2}H_{n-2,n-1}}{E-\varepsilon_{n-2}-H_{n-2,n-3}\dfrac{\psi_{n-3}}{\psi_{n-2}}}}}$$

(16.2.10b)

$$\frac{\psi_n}{\psi_{n-1}} = \frac{H_{n,n-1}}{E-\varepsilon_n - H_{n,n+1}\dfrac{\psi_{n+1}}{\psi_n}}$$

$$= \cfrac{H_{n,n-1}}{E-\varepsilon_n - \cfrac{H_{n,n+1}H_{n+1,n}}{E-\varepsilon_{n+1}-H_{n+1,n+2}\dfrac{\psi_{n+2}}{\psi_{n+1}}}}$$

$$= \cfrac{H_{n,n-1}}{E-\varepsilon_n - \cfrac{H_{n,n+1}H_{n+1,n}}{E-\varepsilon_{n+1}-\cfrac{H_{n+1,n+2}H_{n+2,n+1}}{E-\varepsilon_{n+2}-H_{n+2,n+3}\dfrac{\psi_{n+3}}{\psi_{n+2}}}}}$$

(16.2.10c)

For example, the expansion of the 0^+ energy eigenvalue for Hamiltonian (16.2.2c) has $H_{12}=\sqrt{2}v = H_{21}$ and $v = H_{23} = H_{32} = H_{34} = H_{43} =...$ Bohr energies $e_1= 0^2$, $e_2= 2^2$, $e_3= 4^2$, in (16.2.10c) give the following.

$$\frac{\psi_2}{\psi_1} = \frac{E-\varepsilon_1}{H_{21}} = \cfrac{H_{21}}{E-\varepsilon_2 - \cfrac{H_{23}H_{32}}{E-\varepsilon_3 - \cfrac{H_{34}H_{43}}{E-\varepsilon_4 - H_{45}\dfrac{\psi_5}{\psi_4}}}} = \cfrac{\sqrt{2}v}{E-2^2 - \cfrac{v^2}{E-4^2 - \cfrac{v^2}{E-6^2 - v\dfrac{\psi_5}{\psi_4}}}} = \frac{E}{\sqrt{2}v}$$ (16.2.11a)

(16.2.10b) with *n=2* or (16.2.7) gives the first equation. Converging approximations start with $E=e_1=0^2$.

$$E \cong 0 \Rightarrow E \cong \frac{-v^2}{2} \Rightarrow E \cong \cfrac{-2v^2}{\dfrac{v^2}{2}+2^2 - \cfrac{v^2}{\dfrac{v^2}{2}+4^2}} = \frac{-2v^2\left(4^2+\dfrac{v^2}{2}\right)}{64+9v^2+\dfrac{v^4}{4}} \cong \frac{-v^2}{2}\left(1-\frac{v^2}{8}\right)$$ (16.2.11b)

The first one $(-v^2/2)$ agrees with elementary perturbation (16.1.13b). The next one straightens it up a bit.

A first approximation of the 2^+ eigenvalue given by (16.2.10c) with *n=2* blows up since the denominator is zero ($E-e_2 =2^2- 2^2=0$). We first appeal to (16.2.10b) with *n=2* before using (16.2.10c).

$$\frac{\psi_2}{\psi_3} = \cfrac{H_{23}}{E-\varepsilon_2 - \cfrac{H_{21}H_{12}}{E-\varepsilon_1 - 0}}, \quad \text{or:} \quad E = \varepsilon_2 + \frac{H_{21}H_{12}}{E-\varepsilon_1}+H_{23}\frac{\psi_3}{\psi_2}$$ (16.2.12a)

This result is exact. Then (16.2.10c) with *n=3* gives continued fraction approximation formulas.

$$E = \varepsilon_2 + \frac{H_{21}H_{12}}{E-\varepsilon_1}+\cfrac{H_{23}H_{32}}{E-\varepsilon_3 - \cfrac{H_{34}H_{43}}{E-\varepsilon_4 - H_{45}\dfrac{\psi_5}{\psi_4}}} = 2^2 + \frac{2v^2}{E-0^2}+\cfrac{v^2}{E-4^2 - \cfrac{v^2}{E-6^2 -...}}$$ (16.2.12b)

Starting with $E=e_2=2^2$, the following two approximations result.

$$E \cong 2^2 + \frac{v^2}{2} \Rightarrow E \cong 2^2 + \frac{v^2}{2} + \frac{v^2}{2^2 + \frac{v^2}{2} - 4^2} \cong 2^2 + \frac{v^2}{2} - \frac{v^2}{20}\left(1 + \frac{v^2}{40}\right) \quad (16.2.12c)$$

Again, the first one $(2^2+v^2/2)$ agrees with elementary perturbation (16.1.13b). The next one bends it down a bit as $v = V/2$ grows, and so the 2^+ band is seen curving over in Fig. 16.1.3 and 16.1.8. Formula (16.2.12c) gives $E(2^+)$ $=4.413$ for $v=1.0$ which is close to the numerical diagonalization result of 4.371 in (16.1.16b). Convergence is slow and more than two fraction levels or "orders" are needed to get four-figure accuracy. (See exercises.)

Continued fraction expansions need to be used with care, particularly, if the continued fraction or other perturbation analyses are used to give the energy values as polynomials in the potential strength v. For example, the fraction formula (16.2.11b) gives $E(0^+)=-.4505$ for $v=1.0$ which is closer to the numerical result -0.4551 in (16.1.16b) than the polynomial expansion in (16.2.11b) which gives a poorer approximation of $-7/16 = -0.4375$. One is tempted to use polynomials since the curves in Fig. 16.1.8 look to be of polynomial form. However, polynomials are generally poor fits to most quantum solutions.

Instead, quantum eigenvalues tend to be more like circular or hyperbolic functions, that is, sine and exponential. Even in the simplest case of a 2-by-2 matrix, the energy levels follow the hyperbolic conic sections of the "diablo" in Fig. 10.3.1. It takes many orders of polynomials to fit even one full oscillation of a sine curve or a 95%-folding of e^{-x}. The hyperbola in the 2-level avoided crossing of Fig. 3.2.2 is even worse; neither the perturbation expansion nor the "exact" polynomial expansion converge on the answer or with each other. Like two quarreling thieves, they are nothing but trouble!

Continued fraction expansions such as (16.2.11a) and (16.2.12b) are, in principle, capable of converging on exact eigenvalues using (16.2.10b-b) which also converge on eigenfunctions. The application of them, however, is tricky, because the desired energy E is repeated forever in the fractions on the right hand side of the equations for E. We're left with the decison of how many fraction levels to actually compute and what approximate value of E to use at each stage of a converging sequence. Since continued fraction calculation is done from the last (bottom) level up to the first (top) level, the effect of an added level is not simply the next term as in a power series. This complicates both the error estimation and the actual calculation.

If, finally, the value of E obtained equals the value of E used for the (infinite) computation of the fractions, then and only then is the E value correct. In other words, the task is to find the fixed point of a mapping function which can only be evaluated approximately, albeit, to an arbitrarily high degree of accuracy. Any technique that gets closer to a fixed point is fair game.

(b) Coordinate x-space vs Momentum k-space:Reaction vs Proaction

Derivations of Schrodinger equations in Chapter 11 gave a coordinate-x-space version (11.4.5d) for wave function $\langle x|\varepsilon\rangle = \Psi_\varepsilon(x)$ and a wavevector-k-space or momentum representation (11.4.13) for $\langle k|\varepsilon\rangle$.

$$\frac{-\hbar^2}{2M}\frac{\partial^2 \langle x|\varepsilon\rangle}{\partial x^2} + V(x)\langle x|\varepsilon\rangle = E\langle x|\varepsilon\rangle \quad (16.2.13a) \qquad \frac{\hbar^2}{2M}k^2\langle k|\varepsilon\rangle + \int dk'V(k-k')\langle k'|\varepsilon\rangle = E\langle k|\varepsilon\rangle \quad (16.2.13b)$$

The k-space version is less popular due to its integral of the Fourier transform $V_{kk'}$ of potential $V(x)$.

$$V(k-k') = \frac{1}{2\pi}\int dx\, e^{-i(k-k')x}V(x) = \langle k|V|k'\rangle = V_{kk'} \qquad (16.2.14)$$

However, the matrix view of Schrodinger's equations reveals how misleading "popularity" can be. The momentum $|m\rangle$-basis used earlier for Hamiltonians (16.1.11) and (16.2.1) is the k-basis and the off-diagonal terms $\upsilon_{k-k'} = V_{kk'}$ are, in fact, $V(x)$-Fourier transforms (16.2.14). We compare x-*vs.*-k for a typical Schrodinger Hamiltonian $\mathbf{H=KE+PE}=(\hbar^2/2M)\mathbf{k}^2+V(\mathbf{x})$ acting on a general state $|\Psi\rangle$. ($\Rightarrow$ is *not* $=$ equality)

$$H|\Psi\rangle: \begin{pmatrix} \ddots & \ddots & & & \\ \ddots & H_{x_0} & -S & & \\ & -S & H_{x_1} & -S & \\ & & -S & H_{x_2} & -S \\ & & & -S & H_{x_3} & -S \\ & & & & -S & H_{x_4} & \ddots \\ & & & & & \ddots & \ddots \end{pmatrix} \begin{pmatrix} \vdots \\ \langle x_0|\Psi\rangle \\ \langle x_1|\Psi\rangle \\ \langle x_2|\Psi\rangle \\ \langle x_3|\Psi\rangle \\ \langle x_4|\Psi\rangle \\ \vdots \end{pmatrix} \Rightarrow \begin{pmatrix} \ddots & \ddots & & & \\ \ddots & H_{k_0k_0} & V_{k_0k_1} & V_{k_0k_2} & V_{k_0k_3} \\ & V_{k_1k_0} & H_{k_1k_1} & V_{k_1k_2} & V_{k_1k_3} & V_{k_1k_4} \\ & V_{k_2k_0} & V_{k_2k_1} & H_{k_2k_2} & V_{k_2k_3} & V_{k_2k_4} \\ & & V_{k_3k_1} & V_{k_3k_2} & H_{k_3k_3} & V_{k_3k_4} \\ & & & V_{k_4k_2} & V_{k_4k_3} & H_{k_4k_4} & \ddots \\ & & & & & \ddots & \ddots \end{pmatrix} \begin{pmatrix} \vdots \\ \langle k_0|\Psi\rangle \\ \langle k_1|\Psi\rangle \\ \langle k_2|\Psi\rangle \\ \langle k_3|\Psi\rangle \\ \langle k_4|\Psi\rangle \\ \vdots \end{pmatrix}$$

$$\text{(16.2.15a)} \qquad\qquad\qquad\qquad\qquad\qquad\qquad\qquad\qquad \text{(16.2.15b)}$$

In x-basis, kinetic $\mathbf{k}^2$ has *off*-diagonal $(-S)$, but it is diagonal in k-basis where $V(\mathbf{x})$ has *off*-diagonal $V_{kk'}$.

$$-S=(\hbar^2/2M) \qquad \text{(16.2.15c)} \qquad\qquad V_{k_mk_n} = \langle k_m|V(\mathbf{x})|k_n\rangle \qquad \text{(16.2.15d)}$$

x-bases put position $\mathbf{x}$ ("x marks the spot!") *on*-diagonal. k-bases put kinetic operator $\mathbf{k}^2$ *on*-diagonal.

$$H_{x_p}=2S+V(x_p) \qquad \text{(16.2.15e)} \qquad\qquad H_{k_mk_m} = Sk_m^2 + V_0 \qquad \text{(16.2.15f)}$$

If $V(x)$ is a one-cosine (Mathieu) potential then x and k matrices have similar numerical structure.

$$H|\Psi\rangle: \begin{pmatrix} \ddots & \ddots & & & \\ \ddots & H_{x_0} & -S & & \\ & -S & H_{x_1} & -S & \\ & & -S & H_{x_2} & -S \\ & & & -S & H_{x_3} & -S \\ & & & & -S & H_{x_4} & \ddots \\ & & & & & \ddots & \ddots \end{pmatrix} \begin{pmatrix} \vdots \\ \langle x_0|\Psi\rangle \\ \langle x_1|\Psi\rangle \\ \langle x_2|\Psi\rangle \\ \langle x_3|\Psi\rangle \\ \langle x_4|\Psi\rangle \\ \vdots \end{pmatrix} \Rightarrow \begin{pmatrix} \ddots & \ddots & & & \\ \ddots & H_{k_0} & \upsilon_1 & & \\ & \upsilon_1 & H_{k_1} & \upsilon_1 & \\ & & \upsilon_1 & H_{k_2} & \upsilon_1 \\ & & & \upsilon_1 & H_{k_3} & \upsilon_1 \\ & & & & \upsilon_1 & H_{k_4} & \ddots \\ & & & & & \ddots & \ddots \end{pmatrix} \begin{pmatrix} \vdots \\ \langle k_0|\Psi\rangle \\ \langle k_1|\Psi\rangle \\ \langle k_2|\Psi\rangle \\ \langle k_3|\Psi\rangle \\ \langle k_4|\Psi\rangle \\ \vdots \end{pmatrix}$$

$$KE_{x_m,x_n} = \langle x_m|S\mathbf{k}^2|x_n\rangle \qquad \text{(16.2.16a)} \qquad\qquad V_{k_mk_n} = \langle k_m|V(\mathbf{x})|k_n\rangle \qquad \text{(16.2.16b)}$$

Mathieu **PE**, diagonal in x-basis, has off-diagonal k-rows υ_1=-υ_0. Other Fourier υ_k are zero ($0=\upsilon_2=\upsilon_3$..).

$$H_{x_p}=2S-2\upsilon_1(1-\cos x_p) \qquad \text{(16.2.16c)} \qquad\qquad H_{k_m} = 2S(1-\cos k_m)-2\upsilon_1 \qquad \text{(16.2.16d)}$$

If the potential is zero, **H** is diagonal in k-basis and, for low-k, gives a Bohr-ring k^2-dispersion.

$$H|\Psi\rangle:\begin{pmatrix} \ddots & \ddots & & & & \\ \ddots & 2S & -S & & & \\ & -S & 2S & -S & & \\ & & -S & 2S & -S & \\ & & & -S & 2S & -S \\ & & & & -S & 2S & \ddots \\ & & & & & \ddots & \ddots \end{pmatrix}\begin{pmatrix} \vdots \\ \langle x_0|\Psi\rangle \\ \langle x_1|\Psi\rangle \\ \langle x_2|\Psi\rangle \\ \langle x_3|\Psi\rangle \\ \langle x_4|\Psi\rangle \\ \vdots \end{pmatrix} \Rightarrow \begin{pmatrix} \ddots & \ddots & & & & \\ \ddots & Sk_0^2 & & & & \\ & & Sk_1^2 & & & \\ & & & Sk_2^2 & & \\ & & & & Sk_3^2 & \\ & & & & & Sk_4^2 & \ddots \\ & & & & & \ddots & \ddots \end{pmatrix}\begin{pmatrix} \vdots \\ \langle k_0|\Psi\rangle \\ \langle k_1|\Psi\rangle \\ \langle k_2|\Psi\rangle \\ \langle k_3|\Psi\rangle \\ \langle k_4|\Psi\rangle \\ \vdots \end{pmatrix}$$

$$\text{(16.2.17a)} \qquad\qquad\qquad\qquad\qquad\qquad \text{(16.2.17b)}$$

Symmetry (16.2.16) is due to the fact that Fourier transformation matrix $F_{mp}=\langle k_m|x_p\rangle$ is symmetric.

Fig. 9.4.2 and Fig. 9.4.3 defined by (9.4.3a) show that F-dagggg ($\dagger$) is F-complex-conjugate ($*$).($F^\dagger=F^\circ$)

$$F_{mp} = \langle k_m|x_p\rangle = e^{\frac{-imp}{2\pi N}} = F_{pm} = \langle x_p|k_m\rangle^* = F_{mp}^{\dagger *} \qquad (16.2.18)$$

So, a real H is the same F-transformed forwards to $(FHF^\dagger)$ or F-transformed backwards to $(F^\dagger HF)$.

$$(FHF^\dagger)=(FHF^*)=(F^*H^*F)^* =(F^\dagger HF)^* \qquad (16.2.19)$$

The effect of F or F° is to diagonalize a hyper-kinetic x-matrix into an arbitrary dispersion function $\omega(k_m)$ while moving an arbitrary potential function $V(x_p)$ from the x-diagonal to off-diagonal Fourier υ_k-bands.

$$F(\mathbf{KE})F^* = F\begin{pmatrix} \ddots & \ddots & & & & \\ \ddots & H_0 & -S & -T & -U & \\ & -S & H_0 & -S & -T & -U \\ & -T & -S & H_0 & -S & -T \\ & -U & -T & -S & H_0 & -S \\ & & -U & -T & -S & H_0 & \ddots \\ & & & & & \ddots & \ddots \end{pmatrix}F^* = \begin{pmatrix} \ddots & \ddots & & & & \\ \ddots & \omega(k_0) & & & & \\ & & \omega(k_1) & & & \\ & & & \omega(k_2) & & \\ & & & & \omega(k_3) & \\ & & & & & \omega(k_4) & \ddots \\ & & & & & \ddots & \ddots \end{pmatrix} \qquad \text{(16.2.20a-b)}$$

$$F(\mathbf{PE})F^* = F\begin{pmatrix} \ddots & \ddots & & & & \\ \ddots & V(x_0) & & & & \\ & & V(x_1) & & & \\ & & & V(x_2) & & \\ & & & & V(x_3) & \\ & & & & & V(x_4) & \ddots \\ & & & & & \ddots & \ddots \end{pmatrix}F^* = \begin{pmatrix} \ddots & \ddots & & & & \\ \ddots & \upsilon_0 & \upsilon_1 & \upsilon_2 & \upsilon_3 & \\ & \upsilon_1 & \upsilon_0 & \upsilon_1 & \upsilon_2 & \upsilon_3 \\ & \upsilon_2 & \upsilon_1 & \upsilon_0 & \upsilon_1 & \upsilon_2 \\ & \upsilon_3 & \upsilon_2 & \upsilon_1 & \upsilon_0 & \upsilon_1 \\ & & \upsilon_3 & \upsilon_2 & \upsilon_1 & \upsilon_0 & \ddots \\ & & & & & \ddots & \ddots \end{pmatrix} \qquad \text{(16.2.20c-d)}$$

Off-diagonal rows hold Fourier-$\upsilon_1, \upsilon_2,\ldots$ of potential $V(x)$ or $-S,-T,\ldots$ of dispersion function $\omega(k)$.

$$V(x)=\upsilon_0+2\upsilon_1\cos x+2\upsilon_2\cos 2x+2\upsilon_3\cos 3x \quad \text{(16.2.20e)} \qquad \omega(k)= H - 2S\cos k - 2T\cos 2k - 2U\cos 3k \quad \text{(16.2.20f)}$$

This relates banded k-matrices (16.2.1) of **PE** to the analogous hyper-connected x-matrices (11.15.10) of the **KE** operator. A two-state version is a type-AB Hamiltonian $A\sigma_A+ B\sigma_B$ discussed in Section 10.3.

$$T\begin{pmatrix} A & 0 \\ 0 & -A \end{pmatrix}T^* + T\begin{pmatrix} 0 & B \\ B & 0 \end{pmatrix}T^* = \begin{pmatrix} B & 0 \\ 0 & -B \end{pmatrix}+\begin{pmatrix} 0 & A \\ A & 0 \end{pmatrix} \qquad where: \quad T=\begin{pmatrix} 1 & 1 \\ 1 & -1 \end{pmatrix}\frac{1}{\sqrt{2}} \qquad (16.2.21)$$

The T-transform simply switches A and B components. Type-AC matrices $A\sigma_A+ C\sigma_C$ behave similarly.

$$F\begin{pmatrix} A & 0 \\ 0 & -A \end{pmatrix}F^* + F\begin{pmatrix} 0 & -iC \\ iC & 0 \end{pmatrix}F^* = \begin{pmatrix} C & 0 \\ 0 & -C \end{pmatrix} + \begin{pmatrix} 0 & iA \\ -iA & 0 \end{pmatrix} \qquad where: \quad F = \begin{pmatrix} 1 & i \\ i & 1 \end{pmatrix}\frac{1}{\sqrt{2}} \qquad (16.2.21)$$

The symmetric F-transform replaces $-C$ (or A) by A (or C), not unlike (16.2.20) replacing $V(x)$ Fourier coefficients $\upsilon_1, \upsilon_2, \ldots$ by kinetic amplitudes $-S, -T, \ldots$, the Fourier components of dispersion $\omega(k)$.

In each of these examples two non-commuting matrices compete to foster their kind of eigenbasis. **PE** and **KE** cannot be diagonalized by one basis as neither can $A\sigma_A$ and $C\sigma_C$, but there is a compromise basis that diagonalizes the sum $A\sigma_A + C\sigma_C$. An A-type potential function of position tries to pile-up wave at one *location*, while a C-type kinetic energy encourages sharing by moving wave momentum and *current*. It is the quantum version of political right-*versus*-left, reaction-*versus*-proaction, and status-quo-*versus*-change. In between is the world as usual, a messy but interesting compromise.

16.3 Finite Fourier Analysis of Potential Structure

The techniques described in preceding sections are based on two main ideas, symmetry and the approximation of a continuous system by discrete Fourier series. There are also practical considerations. Infinite Fourier series may be required in principle but a practical Fourier series must be finite. So ∞ by ∞ matrices or ∞ continued fractions must be truncated since computers, however grandiose and expensive, are finite. So is is our time to calculate.

This section, is devoted to physical models for which truncation yields exact solutions or good approximations. Such models have several advantages. First, they let us compare approximations based on physical properties of models rather than numerical witchcraft. Second, they provide a range of computer simulation techniques. (*BohrIt* is an example.) Third, and most important, they further elucidate quantum phenomena using classical and quantum analogies.

One analogy is between waves and coupled pendulums described in Sec. 11.5(b). Expanding the classical dispersion function from (11.5.4b) shows a quadratic (k^2) dependence for small wave vector k_m.

$$\omega_m = \sqrt{\omega_{cutoff}^2 + 4s\ \sin^2(\frac{k_m\ a}{2}\ )}$$

$$= \omega_{cutoff} + \frac{4s}{2\omega_{cutoff}} \sin^2(\frac{k_m\ a}{2}\ ) - \frac{16s^2}{6\omega_{cutoff}^3} \sin^4(\frac{k_m\ a}{2}\ ) + \dots \qquad (16.3.1)$$

$$= \omega_{cutoff} + \frac{s}{2\omega_{cutoff}} (k_m\ a)^2 - \frac{s^2}{8\omega_{cutoff}^3} (k_m\ a)^4 + \dots$$

The cutoff frequency $\omega_{cutoff} = \sqrt{(g/\ell)}$ is the free pendulum angular frequency. If the product $k_m a$ ($a = L/N$ is distance between pendulums) is small then a k^2 dependence of Schrodinger wave dispersion is modeled. The model improves with increasing number N of pendulums or smaller coupling constant $s = k_{12}/m$.

Another analogy involves C_N symmetric "quantum dot" structures introduced in Sections 7.3, 8.1, and 9.4 and extended to a D_N symmetric "dot" structure in Sec. 15.3 to describe D_3 Kronig-Penney (KP) wave band structure in Figs. 15.3.3. The simplest non-chiral $(\sigma=\pi)$ quantum-dot wave dispersion function (9.3.5g) also has a quadratic (k^2) dependence for small wave vector k_m.

$$\omega_m = H - 2S\cos(k_m a) = H - 2S + S(k_m\ a)^2 - \frac{S}{12}(k_m\ a)^4 \dots \qquad (16.3.2)$$

(a) Finite and discrete Bohr-Bloch waves

Fig. 16.3.1 plots the dispersion function involving the lowest twenty-four *(m=0, 1, 2, ...,24,..)* eigenvalues of a C_{120} symmetric quantum dot ring or a ring of *120* coupled pendulums. The lowest energy or frequency values $E_m = \omega_m$ are quadratic in k_m. Bohr units are used so that frequency is simply $E_m = m^2$ and is plotted relative to cut-off frequency $H = \omega_{cutoff} = \sqrt{(g/\ell)}$ which is the frequency of the very lowest $m=0$ mode in which all oscillators or pendulums swing together in equal phase and amplitude as one huge rigid "curtain." Then coupling S or s has no effect.
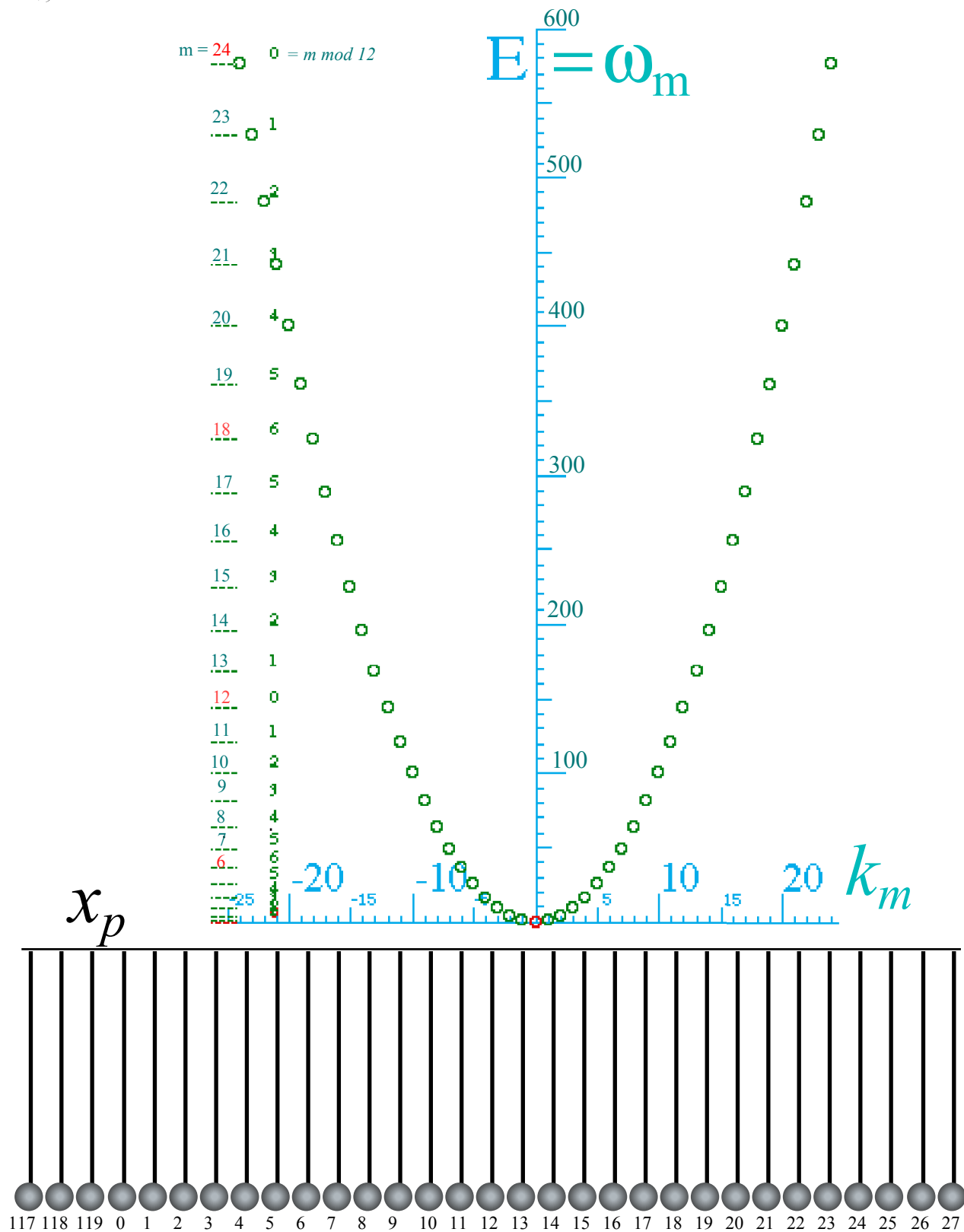
Fig. 16.3.1 Lowest twenty-four eigenvalues for an N=120 homo-cyclic ring of C_{120} coupled oscillators.

For the lowest non-zero k_m modes the frequency rises, at first quadratically with k_m, then (above the figure) according to the exact nearest-neighbor-coupling dispersion function (16.3.2) of Bloch for the quantum-dot model, and the Klein-Gordan dispersion function (16.3.1) for the coupled pendulum model.

(b) Finite and discrete Mathieu waves

In Fig. 16.3.2a the *120* pendulums or dots are divided into identical consecutive sets of ten each with a co-sinusoidal variation in length or local frequency. As described in (11.5.5) and Fig. 11.5.5 this is equivalent to a co-sinusoidal variation in the potential $V(x_p)$ as given by a Mathieu potential.

$$V(x_p) = V - V \cos (N x_p) \qquad\qquad (16.3.3)$$

By dividing a ring of $n=120$ into $N=12$ equivalent sets of $P=10$ we reduce the C_{120} or D_{120} symmetry of the Bohr-Bloch model to C_{12} or D_{12} symmetry, that is, exactly one-tenth the original symmetry. This splits the original band of 120 into 10 bands of 12 states each arranged into seven levels labeled as follows.

A_1 , E_1 , E_2 , E_3 , E_4 , E_5 , B_1 (gap) B_2 , E_5, E_4, E_3 , E_2 , E_1 , A_2 (gap)...[repeat band-pair total of five times]

The lowest levels are effected the most by the sinusoidal variation of the oscillator or pendulum frequency. The total (barrier top to well bottom) height $2V = 100$ of the potential is indicated in Fig. 16.3.2 and shows that only the first pair of bands lie near or below 100 and these are the only dispersion functions that suffer major disruption. A larger potential with $2V = 400$ is shown in Fig. 16.3.2b. Now a pair of bands are caught inside the potential and the lowest of these is practically flat. A flat dispersion function means low or zero group velocity

$$\omega\left(k\right) \cong constant \quad \Rightarrow \quad v_{group} = \frac{d\omega}{dk} \cong 0 \qquad\qquad (16.3.4)$$

The pendulum modes corresponding to the flat-band A_1 , E_1 ..., B_1 would restrict oscillation amplitude to only the longest and slowest pendulums numbered $p = 0, 10, 20,..., 110 = 10\,(\rho-1)$ where $(\rho = 1, 2, ..., 12)$ is the well-number of the "well" that has pendulum number $10\,(\rho-1)$ at the bottom. Next-to-bottom pendulums $p\pm1 = 10\,(\rho-1)\pm1$ and perhaps next-to-next-to-bottom pendulums $p\pm2$, would also swing in phase with the bottom pendulum-p but with reduced amplitude the farther they reside from the bottom. The pendulums far from the bottom are shorter and faster and less able to respond to slowly swinging lower pendulums. The top pendulum motions are exponentially small and analogous to a weak evanescent wave. This keeps in-phase "bottom-wiggling" activity trapped in each well since any coupling between wells must be done through the top pendulums. As a result the mode frequency is practically independent of the relative (wavevector) phase k between different wells. Motion is like that of a string of identical but independently blinking Christmas-tree twinkle-lights.

The next to lowest band B_2 , ..., E_1 , A_2 is not quite as flat. In this band there are next-to-bottom pendulums $p+1, p+2,..$ swinging π-out of phase with pendulums $p-1, p-2,..$ on the other side of the bottom pendulum $p = 10\,(\rho-1)$ of the ρ-*th* well. The bottom pendulum is nearly stationary since it sits near a local symmetry node. Recall that the index $_2$ of B_2 or A_2 labels local well anti-symmetry shared by the whole band. This anti symmetry raises the frequency and slightly increases the coupling due to the top pendulums which are now responding more enthusiastically.
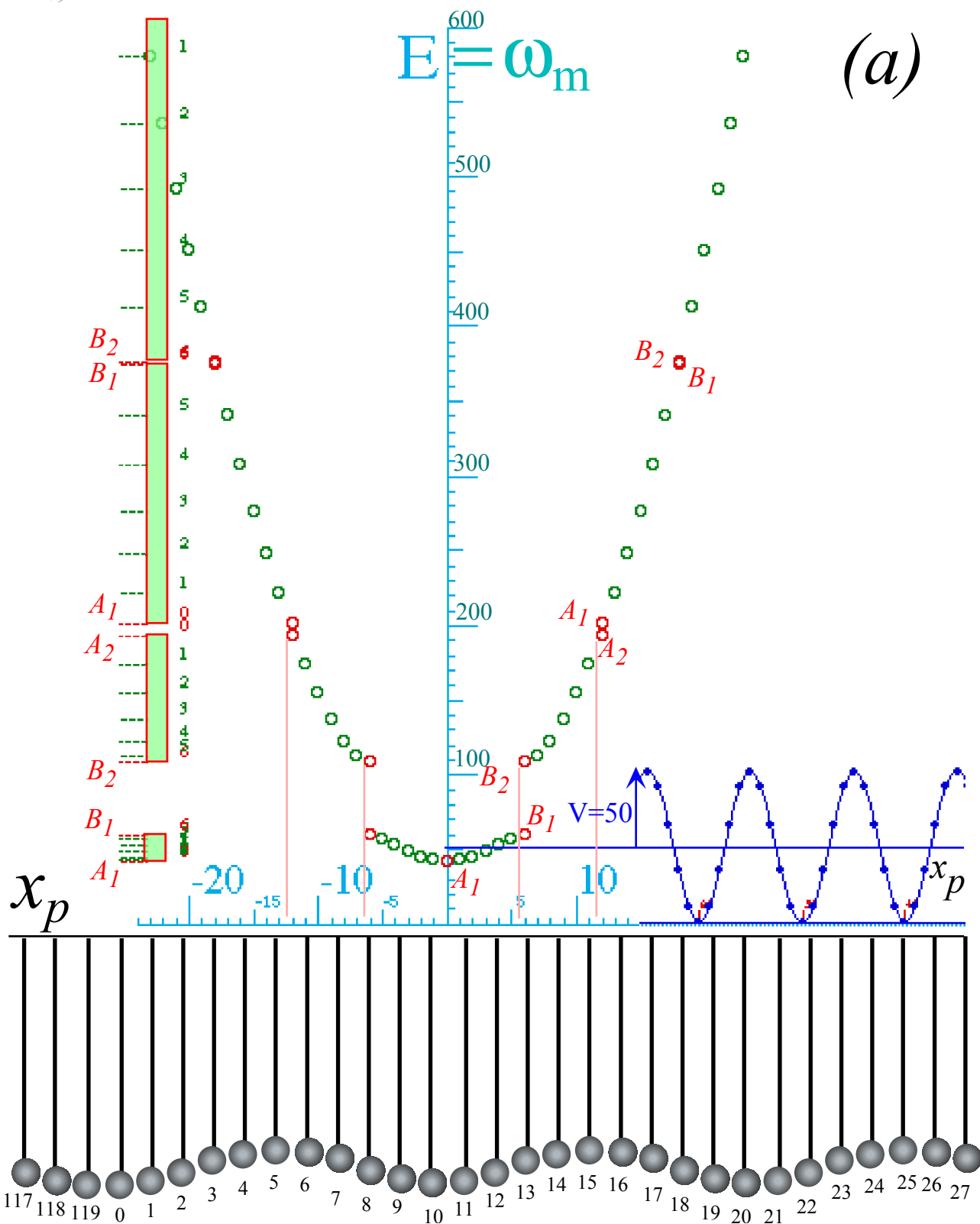
Fig. 16.3.2 Lowest four bands for an N=120 ring of C12 symmetry broken into 12 sets of 10 oscillators.
   (a) V=50 and (b) V = 200.

(b)
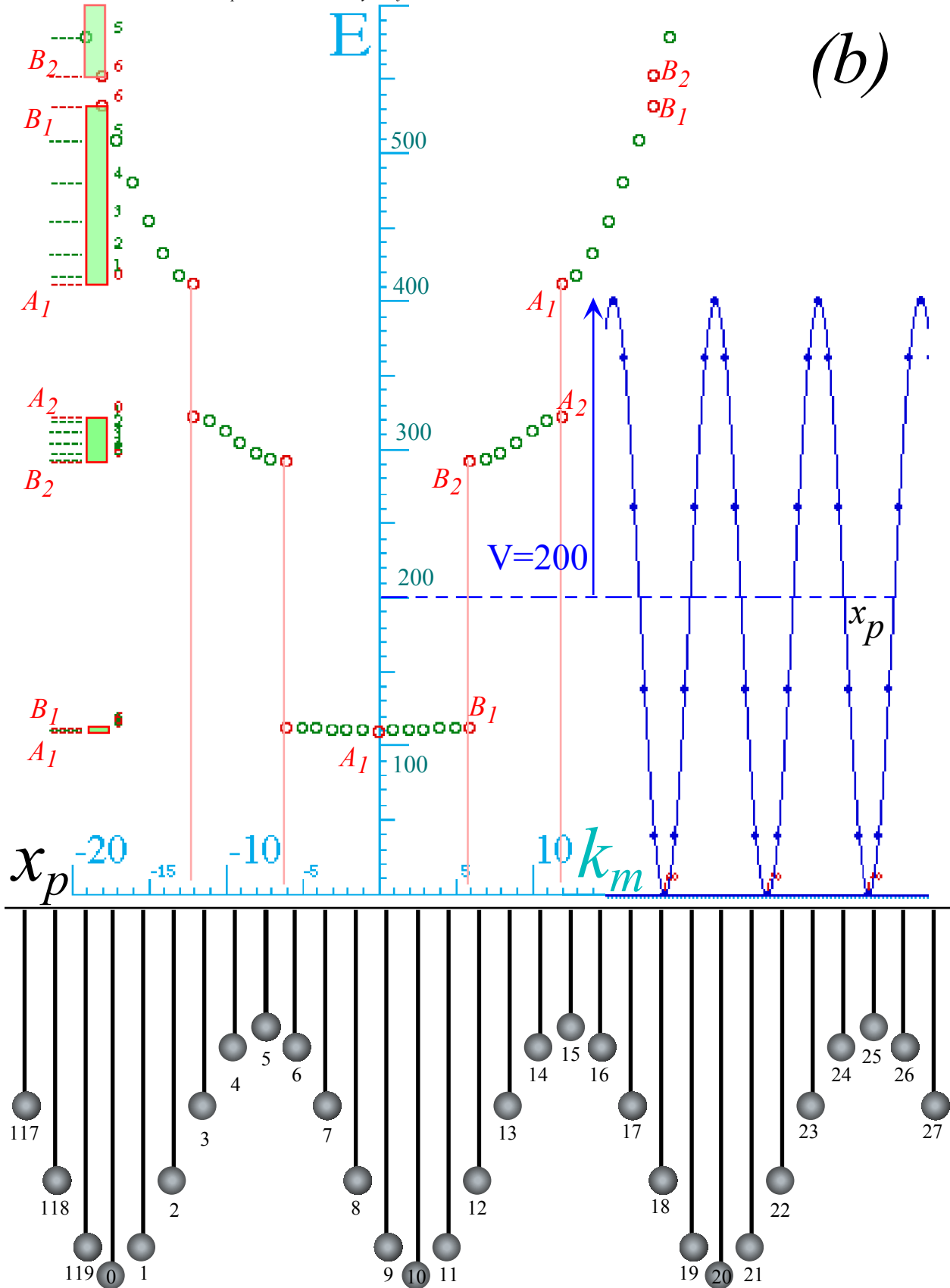
The *H*-matrix is reduced by C_{12} symmetry analysis to exactly 12 matrices of size *10-by-10*. Each matrix belongs to an integer-modulo-12, that is $m = 0_{12},, \pm 1_{12},, \pm 2_{12},, \pm 3_{12},, \pm 4_{12},, \pm 5_{12},,$ and $6_{12},,$ that label the 12 *k*-values in the first (and subsequent) Brillouin zone of C_{12}. First, 0_{12} and 6_{12} matrices:

0_{12} = *O-mod-12 representation:*

	−48	−36	−24	−12	0	12	24	36	48	60
	48^2	v								v
	v	36^2	v							
		v	24^2	v						
			v	12^2	v					
				v	0^2	v				
					v	12^2	v			
						v	24^2	v		
							v	36^2	v	
								v	48^2	v
	v								v	60^2

6_{12} = *6-mod-12 representation:*

	−54	−42	−30	−18	−6	6	18	30	42	54
	54^2	v								
	v	42^2	v							
		v	30^2	v						
			v	18^2	v					
				v	6^2	v				
					v	6^2	v			
						v	18^2	v		
							v	30^2	v	
								v	42^2	v
									v	54^2

(16.3.5a)

(16.3.5b)

Except for energy scale factors of 6^2, these C_{12} Hamiltonians resemble the C_2 or D_2 based matrices of (16.1.11) with a couple of differences. The first difference is that (16.3.5) are *10-by-10* matrices while matrices (16.1.11) are ∞-*by*-∞ . The second difference is the extra v in the corner of the 0_{12} matrix connecting supreme Brillouin zone boundary state of *m=60* to its nearest cohort *m=-48=60-12*.

The Hamiltonian matrices reduce by D_{12} symmetry analysis to matrices of roughly half the size.

0^+_{12} = A_1 *representation:*

	0^+	12^+	24^+	36^+	48^+	60^+
	0	$\sqrt{2}v$				
	$\sqrt{2}v$	12^2	v			
		v	24^2	v		
			v	36^2	v	
				v	48^2	$\sqrt{2}v$
					$\sqrt{2}v$	60^2

(16.3.5c)

6^+_{12} = B_1 *representation:*

	6^+	18^+	30^+	42^+	54^+
	6^2+v	v			
	v	18^2	v		
		v	30^2	v	
			v	42^2	v
				v	54^2

(16.3.5d)

0^-_{12} = A_2 *representation:*

	12^-	24^-	36^-	48^-
	12^2	v		
	v	24^2	v	
		v	36^2	v
			v	48^2

(16.3.5e)

6^-_{12} = B_2 *representation:*

	6^-	18^-	30^-	42^-	54^-
	6^2-v	v			
	v	18^2	v		
		v	30^2	v	
			v	42^2	v
				v	54^2

(16.3.5f)

So, D_{12} symmetry reduces key parts of a formidable *120-by-120* matrix to relatively small 4, 5, and 6 dimensional matrices. This accounts for all the band edges. The reduction occurs because the number of A_1, B_1, A_2, and B_2 -labeled states is, respectively, 6, 5, 4, and 5.

Since there are ten each of the remaining E_1 , E_2 , E_3 , E_4 , E_5 doublet states there is little to be gained by a D_{12} analysis beyond the C_{12} analysis which gives the five *10-by-10* matrices in a form very much like ten-truncated (16.1.19a) matrices. Each E_m is doubly degenerate in the absence of chirality.

(c) Finite and discrete Kronig-Penney waves

In Fig. 16.3.3 the *120* pendulums are adjusted to resemble C_N square well-barriers of a Kronig-Penney potential $V(x_p)$ whose Fourier cosine-series has the following general form.

$$V(x_p) = V_0 + V_1 \cos (P\, x_p) + V_2 \cos (2P\, x_p) + V_3 \cos (3P\, x_p) + ... \qquad (16.3.6)$$

An *(W=L)*-equilateral *(barrier=V)*-KP potential $V(x)$ is a real infinite series of Fourier V_m coefficients.

$$(V_0, V_1, V_2, V_3, V_4, V_5, V_6, V_7, V_8 ..) = (V/2)(1, 4/\pi, 0, -4/3\pi, 0, +4/5\pi, 0, -4/7\pi,\ 0,...) \quad (16.3.7a)$$

$$= (V/2)(\ 1.0, 1.27324, 0, -0.42441, 0, +0.25465, 0, -0.18,\ 0,...) \quad (16.3.7b)$$

If asymmetry is needed, a cosine-sine or complex Fourier series can make arbitrary $V(x)$.

However, a finite system such as Fig. 16.3.3 with just *P=10* pendulums per well has a *finite* Fourier series. Terms beyond $p=P/2=5$ are redundant. A discrete KP arrangement like Fig. 16.3.4 requires just five numbers, but the new V_m are not all quite the same as the first five numbers in (16.3.7b).

$$(V_0, V_1, V_2, V_3, V_4, V_5).= (V/2)(1.0, 1.29442, 0, -0.49442, 0, +0.20000). \qquad (16.3.8)$$

The new V_m coefficients for discrete-x_p are derived from *P*-fold orthonormality and completeness.

$$V_m = \frac{1}{2P} \sum_{p=0}^{P-1} V\left(x_p\right) \cos \frac{2\pi\, mp}{P} \qquad (16.3.9a)$$

The sole non-zero V_m coefficients for *(P=10)*-pendulum equilateral square barriers are as follows.

$$V_1 = \frac{2}{5} + \frac{4}{5} \cos \frac{\pi}{5} + \frac{4}{5} \cos \frac{2\pi}{5} = \frac{4}{5} + \frac{4}{5} \sqrt{\frac{3 - \sqrt{5}}{2}} \qquad (1.6.3.9b)$$

$$V_3 = \frac{2}{5} - \frac{4}{5} \cos \frac{\pi}{5} - \frac{4}{5} \cos \frac{2\pi}{5} = \frac{-4}{5} \sqrt{\frac{3 - \sqrt{5}}{2}} \qquad (1.6.3.9c)$$

$$V_5 = \frac{1}{5} \qquad (1.6.3.9d)$$

Here we note: $\cos \frac{\pi}{5} = \sqrt{\frac{3 + \sqrt{5}}{2}}$ and $\cos \frac{2\pi}{5} = \sqrt{\frac{3 - \sqrt{5}}{2}}$. Also, $V_2 = 0 = V_4$ for the equilateral *W=L* well-barrier.

The V_m coefficients make off-diagonal bands $\upsilon_m = V_m/2$ in the Hamiltonian matrices. The Mathieu matrix of (16.3.5) for *N=12* wells of *P=10* pendulums is generalized below with 0_{12} and 6_{12} matrices given first. As usual, *0* and *N/2* determine *A* and *B*-symmetry band boundaries. For the square-well only $\upsilon_1, \upsilon_3,$ and υ_5 are non-zero. The diagonal origin-placement term $\upsilon_0 = V/2$ is ignored.

0_{12} = O-mod-12 representation (A-levels):

−48	−36	−24	−12	0	12	24	36	48	60
48^2	v_1	v_2	v_3	v_4	v_5	v_4	v_3	v_2	v_1
v_1	36^2	v_1	v_2	v_3	v_4	v_5	v_4	v_3	v_2
v_2	v_1	24^2	v_1	v_2	v_3	v_4	v_5	v_4	v_3
v_3	v_2	v_1	12^2	v_1	v_2	v_3	v_4	v_5	v_4
v_4	v_3	v_2	v_1	0^2	v_1	v_2	v_3	v_4	v_5
v_5	v_4	v_3	v_2	v_1	12^2	v_1	v_2	v_3	v_4
v_4	v_5	v_4	v_3	v_2	v_1	24^2	v_1	v_2	v_3
v_3	v_4	v_5	v_4	v_3	v_2	v_1	36^2	v_1	v_2
v_2	v_3	v_4	v_5	v_4	v_3	v_2	v_1	48^2	v_1
v_1	v_2	v_3	v_4	v_5	v_4	v_3	v_2	v_1	60^2

(16.3.10a)

6_{12} = 6-mod-12 representation (B-levels):

−54	−42	−30	−18	−6	6	18	30	42	54
54^2	v_1	v_2	v_3	v_4	v_5	v_4	v_3	v_2	v_1
v_1	42^2	v_1	v_2	v_3	v_4	v_5	v_4	v_3	v_2
v_2	v_1	30^2	v_1	v_2	v_3	v_4	v_5	v_4	v_3
v_3	v_2	v_1	18^2	v_1	v_2	v_3	v_4	v_5	v_4
v_4	v_3	v_2	v_1	6^2	v_1	v_2	v_3	v_4	v_5
v_5	v_4	v_3	v_2	v_1	6^2	v_1	v_2	v_3	v_4
v_4	v_5	v_4	v_3	v_2	v_1	18^2	v_1	v_2	v_3
v_3	v_4	v_5	v_4	v_3	v_2	v_1	30^2	v_1	v_2
v_2	v_3	v_4	v_5	v_4	v_3	v_2	v_1	42^2	v_1
v_1	v_2	v_3	v_4	v_5	v_4	v_3	v_2	v_1	54^2

(16.3.10b)

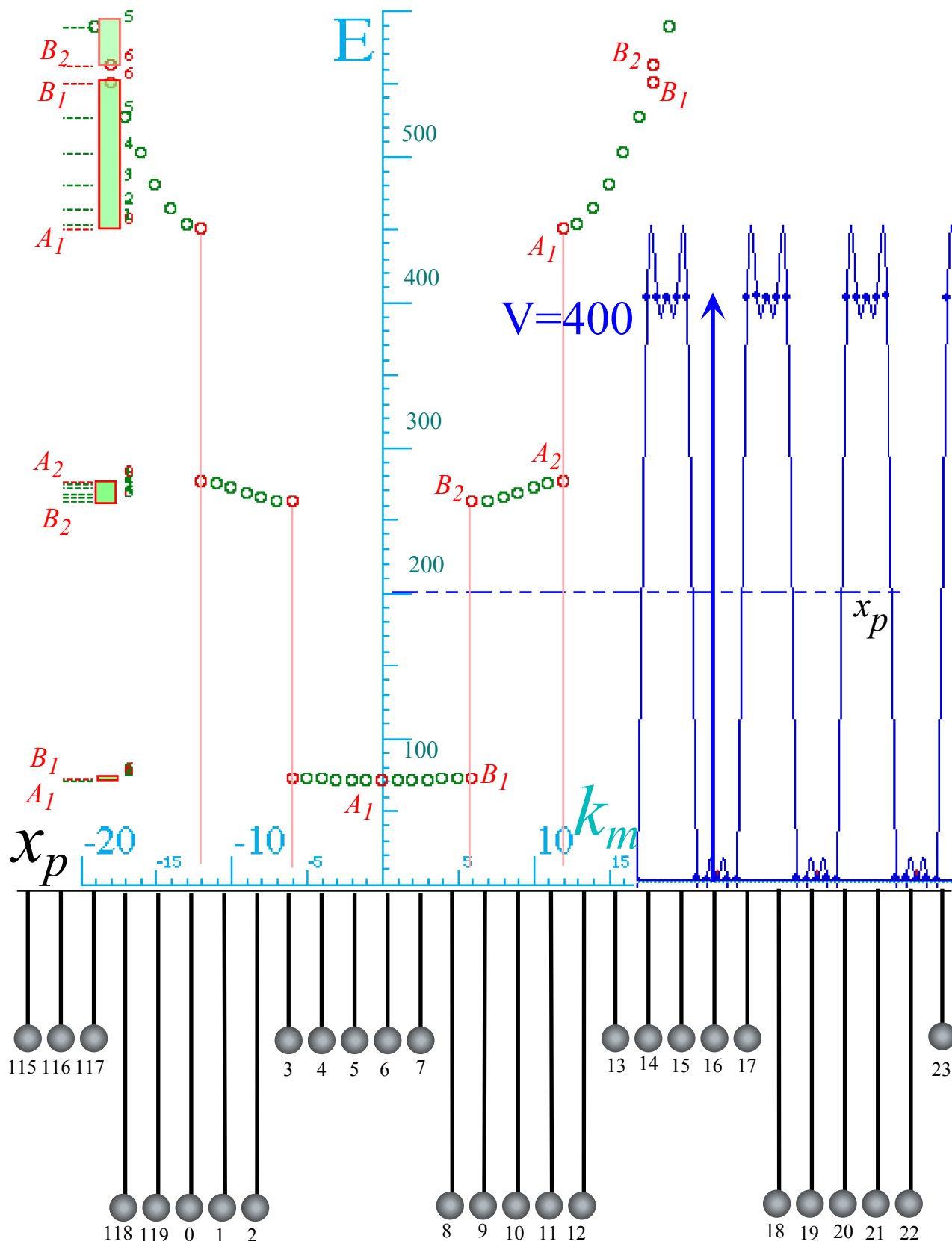*Fig. 16.3.3 Lowest four bands for an N=120 pendulum model for Kronig-Penney potential V = 200.*
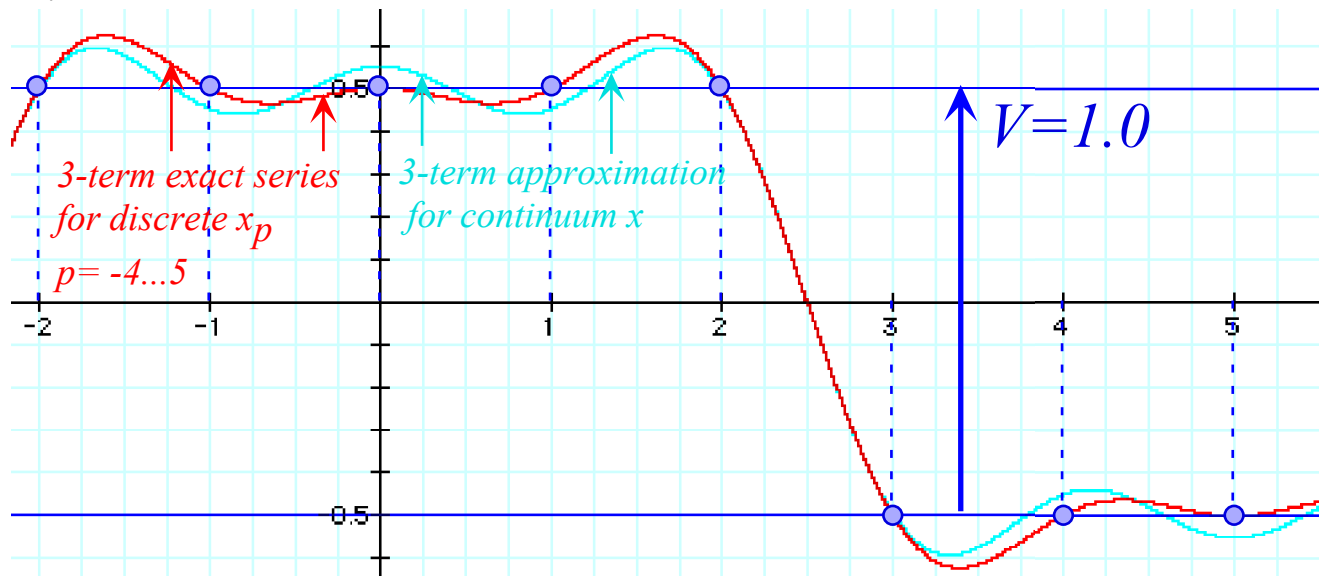
Fig. 16.3.4 Comparison of exact-discrete $V(x_p)$ and approximate continuum $V(x)$ for a square potential .

The difference now is that the H-matrices for P-pendulums and for a given m-value (Momentum quantum m or k_m ranges over N values for N-wells of P-pendulums) are only P-by-P dimensional and there are only (for even number P of pendulums per well) $P/2$ ($=5$ here) coefficients $v_k = v_1 , v_0,...v_{P/2}$. The are repeated in the H-matrices according modular relations such as $v_6 = v_{-4\ mod\ 10} = v_4{}^*$, $v_7 = v_{-3\ mod\ 10} = v_3{}^*$, and so on. The first coefficient $v_1{}^*$ appears in the upper right hand corners of (16.3.10) as in (16.3.5a). Three coefficients fit discrete potential $V(x_p)$ in Fig. 16.3.4 *exactly*. The infinite series only approaches.

Here we are assuming bilateral symmetry so all Fourier coefficients are real $v_k{}^* = v_k$. Then the H-matrix is symmetric and Hermitian. Since all Hamiltonians are Hermitian (self-transpose conjugate $H^\dagger = H$) the presence of complex coefficients presents no essential change in the formalism though it does double the computation. The extreme upper diagonal above $v_{P/2} = v_5$ are filled with conjugate coefficients $v_k{}^*$ in general. The reverse holds for lower diagonal rows. For $m_{12} = m$-mod-12 representations belonging to in-band E_m levels there are E_m matrices with similar off-diagonal v_k -structure.

Band-edge H-matrices are reduced by D_{12} symmetry analysis to generalized versions of (16.3.5).

$0^+{}_{12} = A_1$ representation:

0^+	12^+	24^+	36^+	48^+	60^+
0	$\sqrt{2}v_1$	$\sqrt{2}v_2$	$\sqrt{2}v_3$	$\sqrt{2}v_4$	v_5
	$12^2 + v_2$	$v_1 + v_3$	$v_2 + v_4$	$v_3 + v_5$	$\sqrt{2}v_4$
		$24^2 + v_4$	$v_1 + v_5$	$v_2 + v_4$	$\sqrt{2}v_3$
			$36^2 + v_4$	$v_1 + v_3$	$\sqrt{2}v_2$
				$48^2 + v_2$	$\sqrt{2}v_1$
					60^2

(16.3.10c)

$6^+{}_{12} = B_2$ representation:

6^+	18^+	30^+	42^+	54^+
$6^2 - v_1$	$v_1 - v_2$	$v_2 - v_3$	$v_3 - v_4$	$v_4 - v_5$
	$18^2 - v_3$	$v_1 - v_4$	$v_2 - v_5$	$v_3 - v_4$
		$30^2 - v_5$	$v_1 - v_4$	$v_2 - v_3$
			$42^2 - v_3$	$v_1 - v_2$
				$54^2 - v_1$

(16.3.10d)

$0^-{}_{12} = A_2$ *representation:*

12⁻	24⁻	36⁻	48⁻
$12^2 - v_2$	$v_1 - v_3$	$v_2 - v_4$	$v_3 - v_5$
	$24^2 - v_4$	$v_1 - v_5$	$v_2 - v_4$
		$36^2 - v_4$	$v_1 - v_3$
			$48^2 - v_2$

(16.3.10e)

$6^-{}_{12} = B_1$ *representation:*

6⁻	18⁻	30⁻	42⁻	54⁻
$6^2 + v_1$	$v_1 + v_2$	$v_2 + v_3$	$v_3 + v_4$	$v_4 + v_5$
	$18^2 + v_3$	$v_1 + v_4$	$v_2 + v_5$	$v_3 + v_4$
		$30^2 + v_5$	$v_1 + v_4$	$v_2 + v_3$
			$42^2 + v_3$	$v_1 + v_2$
				$54^2 + v_1$

(16.3.10f)

Note that the v_k parts of the resulting matrices have an anti-diagonal symmetry in the case of real v_k *= v_k . This makes the first-order splittings such as $6^2 \pm v_1$ and $54^2 \pm v_1$ occur equally in the high regions of the spectrum as they do in the low regions. Higher order splittings, however, do not come out the same due to the increased spacing between diagonal m^2-elements for higher m-values.

(d) Acoustical and optical phonon modes

In Sec. 15.3 a D_3 band pair structure was modeled by considering just $P=2$ points in each of $N=3$ wells as shown in Fig. 15.3.2. This is equivalent to a $NP=6$ pendulum model of the quantum waves shown in Fig. 15.3.3. Similarly, the D_6 band pair structure of Fig. 15.5.10 may be modeled by considering a $NP=12$ pendulum model, that is, by considering just $P=2$ points in each of $N=6$ wells. These models are sketched in Fig. 16.3.5. Such very-truncated quantum models are equivalent to elementary classical models of acoustical and optical phonon modes. Diatomic crystals may be modeled by treating heavy and light atoms as long and short pendulums, respectively.
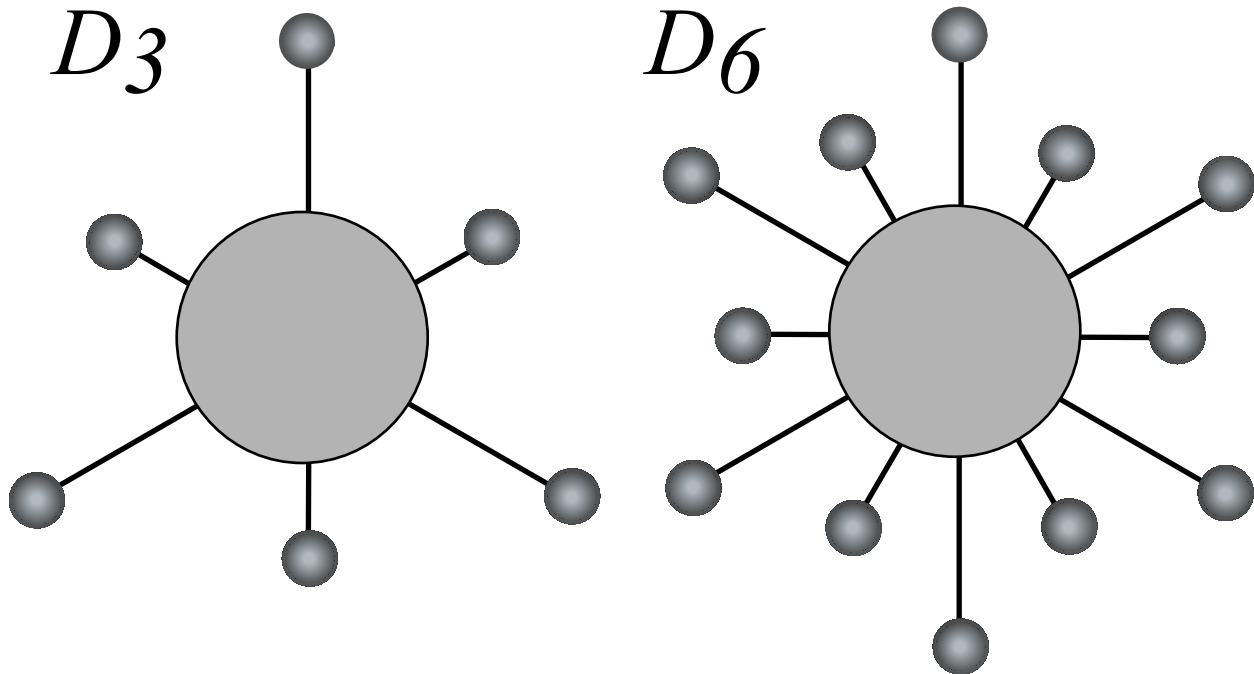

Fig. 16.3.5 Trigonal and hexagonal pendulum models .

A spectrum of a D_8 model is plotted in Fig. 16.3.6 showing the two bands of eight states each.

$$A_1 , E_1 , E_2 , E_3 , B_1 \text{ (gap) } B_2 , E_3 , E_2 , E_1 , A_2$$

The lowest band $(A_1 , E_1 , E_2 , E_3 , B_1)$ is called the *acoustical band* while $(B_2 , E_3 , E_2 , E_1 , A_2)$, the upper band, is called the *optical band*. The acoustical-band-waves swing the long pendulums in phase with their shorter neighbors and are so named because they resemble sound waves. The optical-band-waves swing the long pendulums out of phase with their shorter neighbors and are so named because they can more easily couple with light waves particularly if the two masses are oppositely charged. Also, acoustical waves tend to encourage large amplitudes of the slower pendulums. The A_1 wave in Fig. 16.3.6 has a larger amplitude on the low-frequency pendulum points $p=0,2,4,...,14$ than on the higher frequency pendulum points $p=1,3,5,...,15$. Optical waves, such as B_2 tend to favor the faster pendulums with higher amplitude.
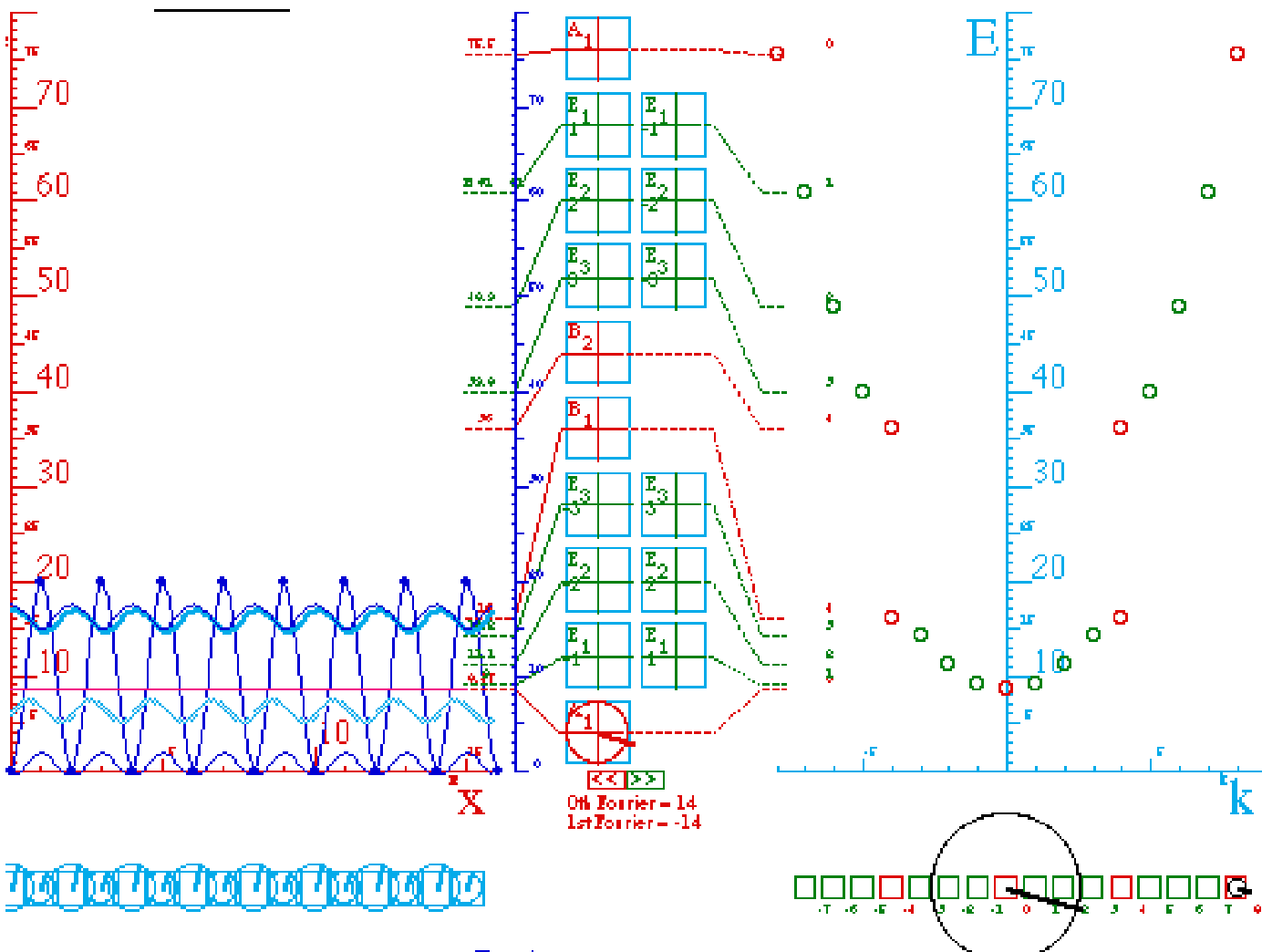

Fig. 16.3.6 Octagonal D_8 pendulum band model in lowest acoustical A_1 wave state .

(e) Dn symmetric quantum dot structures

The preceding analogies between quantum and classical wave structures suggest a more general quantum dot structure of the type introduced in Chapters 8, 9, 14 and 15. So far, the discrete models have been introduced

as approximations to homo-cyclic or periodic potential wells. However, the possibility exists for discrete photonic and electronic devices that are useful in and of themselves.

　　　Imagine a corrals of quantum dots such as are sketched in Fig. 16.3.7. Each dot represents a quantum oscillator which by itself has an assigned frequency or energy that may be higher for smaller dots and lower for larger ones. Between each dot are tunneling paths or links to neighboring ones that may be stronger for nearer neighbors and weaker for more distant ones.

　　　Two examples in Fig. 16.3.7a-b are analogous to the pendulum models in preceding Fig. 16.3.5 but show extra coupling or tunneling paths beyond the near-neighbor S_1 connections of a mechanical device. The third example Fig. 16.3.7c shows a discretely varying near-neighbor tunneling rates $S_1, S_2, S_3, \ldots$ as well as the local dot frequency $V_1, V_2, V_3, \ldots$ in a ring that models a variable potential $V_p = V(x_p)$. Near-neighbor $S_p = S(x_p)$ paths model a variable *effective mass* $M(x) = h^2/2|S(x)|$. Longer paths $T_1, T_2, U_1, \ldots$ sketched in Fig. 16.3.7a-b (also possible in Fig. 16.3.7c) model hyper-kinetics. In fact, there are $N(N-1)/2$ paths in an N-dot system, *15* for *6* dots, *66* for *12* dots, and *276* for *24* dots in Fig. 16.3.7a, b, and c. Symmetry reduces the number of distinct path parameters to *4*, *10*, and *92*, respectively. The number of distinct dot potentials $V(x_p)$ is *2*, *2*, and *8*, repectively, to give *6*, *12*, and *72* free parameters.
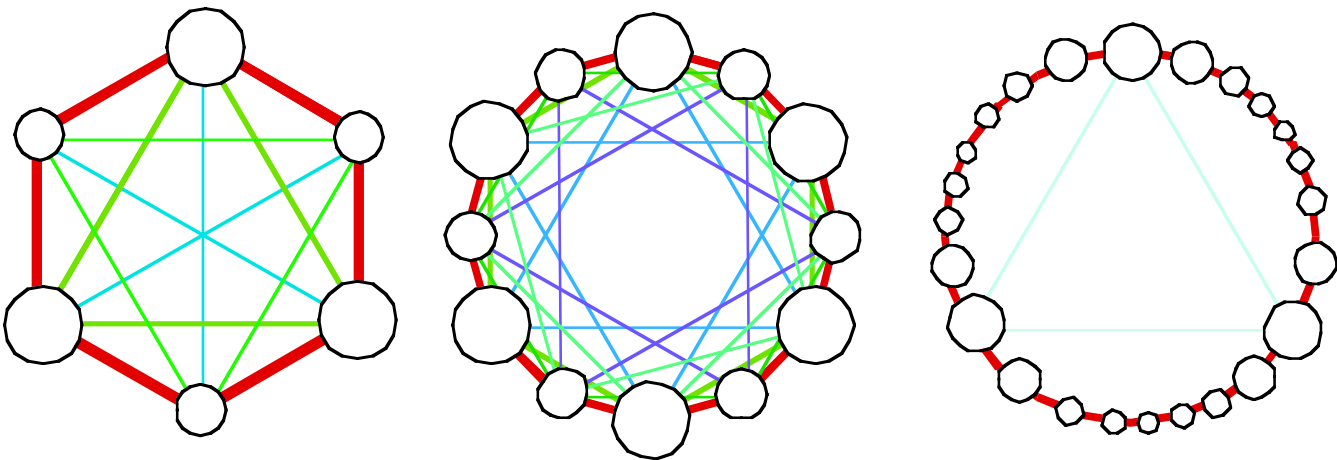

Fig. 16.3.7 Trigonal and hexagonal dot networks. (a-b)Hyperconnected. (c) Simple connection.

　　　There emerges an infinitude of possible "quantum circuits" even for a simple Bohr-ring topology, but even that is dwarfed by the possiblilities for concentric rings or structures in two, three, or higher number of dimensions. A number of independent parameters for a circuit H-matrix serve to vary its eigenfrequncy spectrum and eigenstates subject to the symmetry of the device. Simple circuits in Chapter 9 and Chapter 15 provide examples of the symmetry analysis. The number of physical parameters may be larger since, according to (16.2.20), contibutions to an H-matrix come from its **KE** and **PE** parts.

Problems for Chapter 16.

Continued Fractions

16.1.1. Use the continued fraction approximation technique described in (16.2.10) to (16.2.12).

(a) Give approxiamtion formulas for the 1^- band boundary and determine where it falls below the E=0 line in Fig. 16.1.3 to give inverted stability in the classical pendulum analog.

(b) Apply the technique to 1^+ and 2^- band boundaries. See if it is possible to obtain an accurate approximation for the behavior at higher values V = 10-15 (Bohr units) of the Mathieu cosine potential. Locate the V values where these eigenvalues become negative.

(b) Use the solutions obtained in (b) to determine the E=0 wavefunction for 2^-. Sketch both the 1^+ and 2^- wavefunction for this V. In the classical penulum analogy, what pump frequency range do these two span?

Continued Fractions Continued

16.1.2. Derive an appoximation formula for the levels E_1 and E_2 inside the band boundaries of Fig. 16.1.8.

(a) Apply the formulas to the $1^{\pm}E_1$ and $2^{\pm}E_2$ levels and determine where they cross E=0.

(b) Apply the formulas to the $5^{\pm}E_1$ and $4^{\pm}E_2$ levels and determine where they cross E=0.
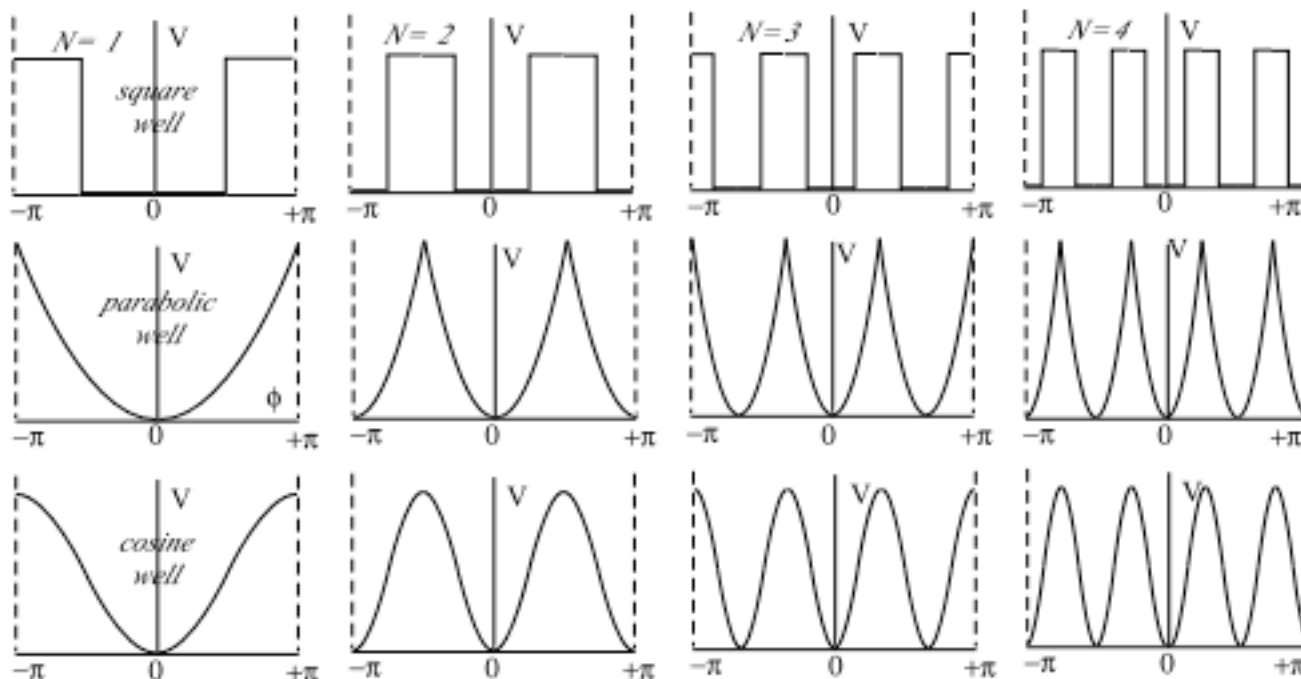
Continued Fractions Terminated

16.1.3. Use the preceding techniques to analyze the two-by-two Hamiltonian (3.2.7) that gave elementary perturbation theory such a problem in Chapter 3.

$$\mathbf{H} = \begin{pmatrix} H_{11} & H_{12} \\ H_{21} & H_{22} \end{pmatrix} = \begin{pmatrix} E_1 & V \\ V & E_2 \end{pmatrix} = \begin{pmatrix} -1 & V \\ V & 1 \end{pmatrix}$$

Show what several iterations of this technique give as approximations and plot them as a function of V for -5<V<5. Are your results any improvement over Fig. 3.2.2?

Bohr(ring) Periodic Potentials

16.3.1 A variety of periodic potentials (See figures below.) can be installed on a Bohr ring. Each may be described by quasi-infinite Hamiltonian matrix of the form also shown below.

	−4	−3	−2	−1	0	1	2	3	4	5	6	7	8	⋯
−5	⋰ ⋱ ⋱ ⋱ ⋱ ⋱ ⋱													
−4	⋱ 4^2	V_1	V_2	V_3	V_4	V_5	⋱	⋱						
−3	⋱ V_1^*	3^2	V_1	V_2	V_3	V_4	V_5	⋱						
−2	⋱ V_2^*	V_1^*	2^2	V_1	V_2	V_3	V_4	V_5						
−1	⋱ V_3^*	V_2^*	V_1^*	1^2	V_1	V_2	V_3	V_4	V_5					
0	⋱ V_4^*	V_3^*	V_2^*	V_1^*	0	V_1	V_2	V_3	V_4	V_5				
1	⋱ V_5^*	V_4^*	V_3^*	V_2^*	V_1^*	1^2	V_1	V_2	V_3	V_4	V_5	⋱	⋱	
2	⋱	V_5^*	V_4^*	V_3^*	V_2^*	V_1^*	2^2	V_1	V_2	V_3	V_4	V_5	⋱	
3	⋱	⋱	V_5^*	V_4^*	V_3^*	V_2^*	V_1^*	3^2	V_1	V_2	V_3	V_4	⋱	
4				V_5^*	V_4^*	V_3^*	V_2^*	V_1^*	4^2	V_1	V_2	V_3	⋱	
5					V_5^*	V_4^*	V_3^*	V_2^*	V_1^*	5^2	V_1	V_2	⋱	
6						V_5^*	V_4^*	V_3^*	V_2^*	V_1^*	6^2	V_1	⋱	
7							V_5^*	V_4^*	V_3^*	V_2^*	V_1^*	7^2	⋱	
8								V_5^*	V_4^*	V_3^*	V_2^*		8^2	
								⋱					V_3^*	

In each case the crest to trough energy is given by $V_{C\text{-to-T}}N^2$ so that the band boundaries are roughly the same height in each diagram. For each of the 12 cases:

   (a) Show or describe the form such a matrix would have. Are complex V_k ever needed?

   (b) Give numbers needed to get the first two bands for $V_{C\text{-to-T}}=5$ in $\varepsilon_{Bohr}(2)$ units (14.2.10)

   (c) Estimate the band energies and label using notation $(0)^{\pm} A_1$, $(m)^{\pm} B_1$, $(n)^{\pm} E_1$,etc.

Summing Discreetly
16.3.2. Consider the comparison between discrete and continuous Fourier potential representations.

   (a) Check the square well decompositions (16.3.7) and (16.3.8) by rederiving them.

   (b) Do similar calculations of the two kinds of Fourier representations if the P=10 pendulums form a quadratic (harmonic oscillator) potential with pendulum 0 mod 10 at the lowest point $V(0) = 0$ and pendulum 5 mod 10 at the highest point $V(5)$ =V.

   (c) Use (b) to estimate the splittings of all the bands in a 120-pendulum model for small positive values of V. Show the resulting ordering of the A_1, B_1, A_2, and B_2 levels. Does this indicate there will be crossing of band-edge levels at some larger V?

Periodic Potential Pile-up
16.3.3 Consider a case where all potential Fourier components υ_m equal the same real constant $\upsilon = \upsilon_1 = \upsilon_2 = \upsilon_3 = \upsilon_4 = \upsilon_5$. The resulting potential $V(x_p)$ "piles-up" into what is called a *Pairing* or *Dirac* potential.

      (a) Derive and plot the resulting potential (as in Fig. 16.3.4) for the P=10 pendulum model.

      (b) Derive and plot the resulting dispersion function.

Dispersion Pile-up
16.3.4 Consider a case where all hyper-kinetic tunneling components $S=S_p=T_p=U_p = \ldots$ equal the same real constant.

      (a) Derive and plot the resulting dispersion function.

Complete Pile-up
16.3.4 Discuss a case where both 16.3.3 and 16.3.4 are in effect.
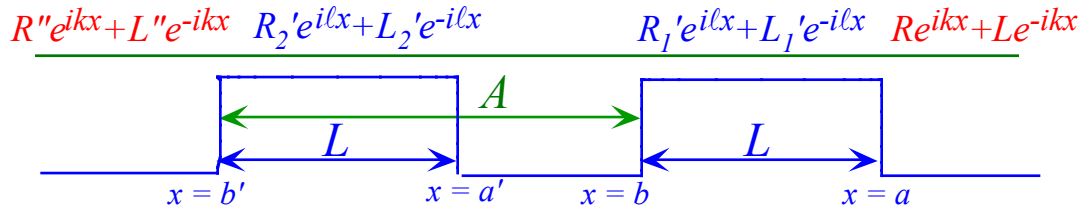
Review Topics & Formulas for Unit 5

$R''e^{ikx} + L''e^{-ikx}$ $R_2'e^{i\ell x} + L_2'e^{-i\ell x}$ $R_1'e^{i\ell x} + L_1'e^{-i\ell x}$ $Re^{ikx} + Le^{-ikx}$

Fig. 14.1.5 C_2-symmetric double barrier .

$$\begin{pmatrix} R'' \\ L'' \end{pmatrix} = \begin{pmatrix} e^{i2kL}\chi^2 + e^{-i2kA}\xi^2 & -i\xi\left(e^{-i2kb}\chi^* + e^{-i2ka'}\chi\right) \\ i\xi\left(e^{i2kb}\chi + e^{i2ka'}\chi^*\right) & e^{-i2kL}\chi^2 + e^{i2kA}\xi^2 \end{pmatrix} \begin{pmatrix} R \\ L \end{pmatrix} \qquad (14.1.6)$$

$\chi = \cosh \kappa L - i \sinh 2\beta \; \sinh \kappa L$, and: $\xi = \cosh 2\beta \; \sinh \kappa L$,   (14.1.7)

$$\cosh 2\beta = \frac{1}{2}\left(\frac{\kappa}{k} + \frac{k}{\kappa}\right) = \frac{\kappa^2 + k^2}{2k\kappa}, \qquad \sinh 2\beta = \frac{1}{2}\left(\frac{\kappa}{k} - \frac{k}{\kappa}\right) = \frac{\kappa^2 - k^2}{2k\kappa} \qquad (14.1.8)$$

Model Lorentz resonance function $\left|\dfrac{1}{C_{11}(\omega)}\right|^2 = \left|\dfrac{c_n}{\omega - \omega_n + i\Gamma_n}\right|^2 = \dfrac{|c_n|^2}{(\omega - \omega_n)^2 + \Gamma_n^2}$ (14.1.10)

resonance frequency ω_n , *resonance decay rate* Γ_n, , *resonance peak strength* $|c_n/\Gamma_n|^2$
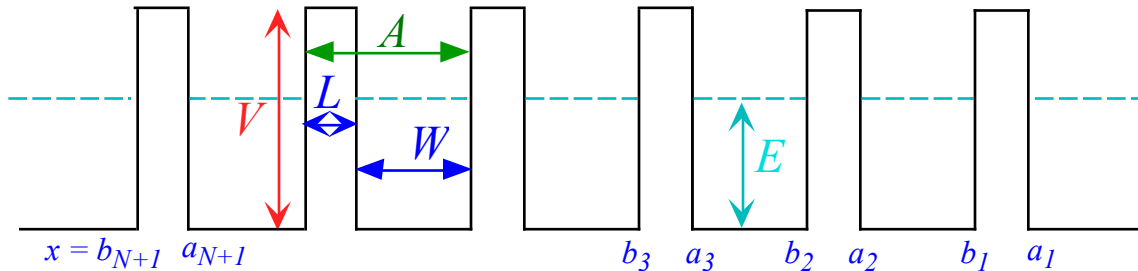Γ_n is the *Lorenztian Half-Width at Half-Maximum (HWHM)*.

Fig. 14.1.18 (N+1)-barrier (N)-well potential

$C^{N+1\,barrier} = C^{[N+1]}\cdots C'\cdot C =$

$$\begin{pmatrix} e^{ikL}\chi^* & -ie^{-ik(a_{N+1}+b_{N+1})}\xi \\ ie^{ik(a_{N+1}+b_{N+1})}\xi & e^{-ikL}\chi \end{pmatrix}\cdots\begin{pmatrix} e^{ikL}\chi^* & -ie^{-ik(a_2+b_2)}\xi \\ ie^{ik(a_2+b_2)}\xi & e^{-ikL}\chi \end{pmatrix}\cdot\begin{pmatrix} e^{ikL}\chi^* & -ie^{-ik(a_1+b_1)}\xi \\ ie^{ik(a_1+b_1)}\xi & e^{-ikL}\chi \end{pmatrix} \quad (14.1.17a)$$

For $(E<V)$ are $k = \sqrt{2E}$, $\kappa = \sqrt{2V-2E}$, and $\sinh 2\beta = (\kappa^2 - k^2)/(2k\kappa)$,

$\chi = \cosh \kappa L - i \sinh 2\beta \; \sinh \kappa L$, and: $\xi = \cosh 2\beta \; \sinh \kappa L$,   (14.1.17a)

For $(E>V)$ they are $\ell = \sqrt{2E-2V}$, and $\cosh 2\alpha = (\ell^2 + k^2)/(2k\ell)$.

$\chi = \cos \ell L + i \cosh 2\alpha \; \sin \ell L$, and: $\xi = \sinh 2\alpha \; \sin \ell L$.   (14.1.17b)

Pendulum model:
$$\mathbf{H}|\varepsilon_k\rangle = \begin{pmatrix} H & -S & 0 \\ -S & H & -S \\ 0 & -S & H \end{pmatrix} \begin{pmatrix} \langle 1|\Psi\rangle \\ \langle 2|\Psi\rangle \\ \langle 3|\Psi\rangle \end{pmatrix} = \varepsilon_k \begin{pmatrix} \langle 1|\Psi\rangle \\ \langle 2|\Psi\rangle \\ \langle 3|\Psi\rangle \end{pmatrix} = \varepsilon_k |\Psi\rangle \qquad (14.1.18)$$

$$\varepsilon_m = H - 2 S \cos(\pi\, m/4) . \qquad (14.1.21b)$$

$$\langle \varepsilon_1| = \begin{pmatrix} 1 & \sqrt{2} & 1 \end{pmatrix}/2 \qquad\qquad \varepsilon_1 = H - \sqrt{2}S$$
$$\langle \varepsilon_2| = \begin{pmatrix} 1 & 0 & -1 \end{pmatrix}/\sqrt{2} \qquad\qquad \varepsilon_2 = H \qquad\qquad (14.1.21c)$$
$$\langle \varepsilon_3| = \begin{pmatrix} 1 & -\sqrt{2} & 1 \end{pmatrix}/2 \qquad\qquad \varepsilon_3 = H + \sqrt{2}S$$

Kronig-Penney band conditions.

$$\left.\begin{aligned} (for\ E>V):\quad & \cos kW\ \cos \ell L - \frac{2E-V}{2\sqrt{E(E-V)}}\sin kW\ \sin \ell L \\[2mm] (for\ E<V):\quad & \cos kW \cosh \kappa L + \frac{V-2E}{2\sqrt{E(V-E)}}\sin kW \sinh \kappa L \end{aligned}\right\} = \cos\phi \qquad (14.2.5b)$$

where rational units are used for energy.

$$\phi = m\frac{2\pi}{N}, \qquad k = \sqrt{2E}, \qquad \ell = \sqrt{2(E-V)}, \qquad \kappa = \sqrt{2(V-E)} . \qquad (14.2.5c)$$

Bohr units
$$\varepsilon_1^{Bohr}(A) = \frac{\hbar^2}{2M}\frac{\pi^2}{A^2} = \frac{\left(1.05\cdot10^{-34}\pi J\cdot s\right)^2}{\left(2\cdot9.109\cdot10^{-31}kg\right)}\frac{10^3\,meV}{1.602\cdot10^{-19}J}\frac{1}{\left(A\cdot10^{-8}m\right)^2} \qquad (14.2.10a)$$

$$= \frac{3.76\,meV}{A^2} \quad (A \text{ in units of } 100\text{Å})$$

Our rational units: $\varepsilon_1^{Bohr}(A) = \dfrac{\pi^2/2}{A^2} = \dfrac{4.93}{A^2} = 1.23$ (for: $A=2$ in 100Å units) $\qquad (14.2.11)$

D_2	1	R_z	R_y	R_x
A_1	1	1	1	1
B_1	1	-1	1	-1
A_2	1	1	−1	−1
B_2	1	-1	−1	1

(15.1.4)

D_3 characters $\mathbf{g} =$	1	$\{\mathbf{r},\mathbf{r}^2\}$	$\{\mathbf{i}_1,\mathbf{i}_2,\mathbf{i}_3\}$
$Trace D^{A_1}(\mathbf{g}) = \chi^{A_1}(\mathbf{g})$	1	1	1
$Trace D^{A_2}(\mathbf{g}) = \chi^{A_2}(\mathbf{g})$	1	1	−1
$Trace D^{E_1}_{x_2 y_2}(\mathbf{g}) = \chi^{E_1}(\mathbf{g})$	2	−1	0

(15.1.13)

$\mathbf{g} =$	1	$\mathbf{r}$	$\mathbf{r}^2$	$\mathbf{i}_1$	$\mathbf{i}_2$	$\mathbf{i}_3$
$D^{E_1}_{c_3 d_3}(\mathbf{g}) =$	$\begin{pmatrix} 1 & 0 \\ 0 & 1 \end{pmatrix}$	$\begin{pmatrix} \varepsilon_- & 0 \\ 0 & \varepsilon_+ \end{pmatrix}$	$\begin{pmatrix} \varepsilon_+ & 0 \\ 0 & \varepsilon_- \end{pmatrix}$	$\begin{pmatrix} 0 & \varepsilon_+ \\ \varepsilon_- & 0 \end{pmatrix}$	$\begin{pmatrix} 0 & \varepsilon_- \\ \varepsilon_+ & 0 \end{pmatrix}$	$\begin{pmatrix} 0 & 1 \\ 1 & 0 \end{pmatrix}$

(15.1.8)

$\mathbf{g} =$	1	$\mathbf{r}$	$\mathbf{r}^2$	$\mathbf{i}_1$	$\mathbf{i}_2$	$\mathbf{i}_3$
$D^{E_1}_{x_2 y_2}(\mathbf{g}) =$	$\begin{pmatrix} 1 & 0 \\ 0 & 1 \end{pmatrix}$	$\begin{pmatrix} -1/2 & -\sqrt{3}/2 \\ \sqrt{3}/2 & -1/2 \end{pmatrix}$	$\begin{pmatrix} -1/2 & \sqrt{3}/2 \\ -\sqrt{3}/2 & -1/2 \end{pmatrix}$	$\begin{pmatrix} -1/2 & -\sqrt{3}/2 \\ -\sqrt{3}/2 & 1/2 \end{pmatrix}$	$\begin{pmatrix} -1/2 & \sqrt{3}/2 \\ \sqrt{3}/2 & 1/2 \end{pmatrix}$	$\begin{pmatrix} 1 & 0 \\ 0 & -1 \end{pmatrix}$

Wigner-Weyl projection formula

$$\mathbf{g} = \sum_\mu \sum_m \sum_n D^\mu_{mn}(g)\,\mathbf{P}^\mu_{mn} = D^{A_1}(g)\mathbf{P}^{A_1} + D^{A_2}(g)\mathbf{P}^{A_2} + D^{E_1}_{11}(g)\mathbf{P}^{E_1}_{11} + D^{E_1}_{12}(g)\mathbf{P}^{E_1}_{12}$$
$$+ D^{E_1}_{21}(g)\mathbf{P}^{E_1}_{21} + D^{E_1}_{22}(g)\mathbf{P}^{E_1}_{22}$$

(15.1.20a)

$$\mathbf{P}^\mu_{mn} = \frac{\ell^\mu}{{}^oG} \sum_\mathbf{g} D^{\mu *}_{mn}(g)\,\mathbf{g} \qquad (15.1.20d) \qquad\qquad \mathbf{P}^\mu_{jk}\mathbf{P}^\nu_{mn} = \delta^{\mu\nu}\delta_{km}\mathbf{P}^\mu_{jn} \qquad (15.1.20b)$$

$$\mathbf{g}\mathbf{P}^\mu_{mn} = \sum_{m'} D^\mu_{m'm}(g)\,\mathbf{P}^\mu_{m'n} \;(15.1.21a) \qquad \mathbf{P}^\mu_{mn}\mathbf{g} = \sum_{n'} D^\mu_{nn'}(g)\,\mathbf{P}^\mu_{mn'} \qquad (15.1.21b)$$

grand D-orthonormality relations.

$$D^\mu_{mn}\left(\mathbf{P}^{\mu'}_{m'n'}\right) = \delta^{\mu\mu'}\delta_{mm'}\delta_{nn'} \;\; \text{or:} \quad \sum_\mathbf{g} D^\mu_{mn}(g)D^{\mu'*}_{m'n'}(g) = \frac{{}^oG}{\ell^{\mu'}}\delta^{\mu\mu'}\delta_{mm'}\delta_{nn'} \quad (15.1.30)$$

$$\mathbb{P}^\mu = \sum_{m=1}^{\ell^\mu} \mathbf{P}^\mu_{mm} = \frac{\ell^\mu}{{}^oG}\sum_\mathbf{g}\sum_{m=1}^{\ell^\mu} D^{\mu *}_{mm}(\mathbf{g})\,\mathbf{g} = \frac{\ell^\mu}{{}^oG}\sum_\mathbf{g} \chi^{\mu *}(\mathbf{g})\,\mathbf{g} \qquad \mathbf{c}_g = \sum_{ireps\,\mu} \frac{{}^o c_g \chi^\mu_g}{\ell^\mu}\,\mathbb{P}^\mu \qquad (15.2.5b)$$

$\mathbb{P}^\mu$ is the (μ)-th *all-commuting idempotent* $\mathbb{P}^\mu$ or *class projector*.

$$\chi^\mu{}_I = \ell^\mu = \sqrt{{}^oG\frac{\ell^\mu \chi^{\mu *}_1}{{}^oG}} = \sqrt{{}^oG\left(\mathbf{c}_1 \text{ coefficient in } \mathbf{P}^\mu\right)} = \sqrt{\left(\ell^\mu\right)^2} \qquad (15.2.10g)$$

Duality principle $\mathbf{g}|\mathbf{1}\rangle = |\mathbf{g}\rangle = \bar{\mathbf{g}}^\dagger|\mathbf{1}\rangle = \bar{\mathbf{g}}^{-1}|\mathbf{1}\rangle$, or: $\mathbf{g}^{-1}|\mathbf{1}\rangle = \mathbf{g}^\dagger|\mathbf{1}\rangle = |\mathbf{g}^{-1}\rangle = \bar{\mathbf{g}}|\mathbf{1}\rangle = \bar{\mathbf{g}}|\mathbf{1}\rangle$.   (15.3.8)

Duality-relativity principle $\bar{\mathbf{g}}|\mathbf{t}\rangle = \mathbf{t}\cdot\mathbf{g}^\dagger\cdot\mathbf{t}^{-1}|\mathbf{t}\rangle = \mathbf{t}\cdot\mathbf{g}^\dagger\cdot\mathbf{t}^\dagger|\mathbf{t}\rangle$.   (15.3.9)

$$\mathbf{g}\left|{}^\mu_{mn}\right\rangle = \sum_{m'=1}^{\ell^\mu} D^\mu_{m'm}(g)\left|{}^\mu_{m'n}\right\rangle \qquad\qquad\qquad \bar{\mathbf{g}}\left|{}^\mu_{mn}\right\rangle = \sum_{n'=1}^{\ell^\mu} D^{\mu *}_{n'n}(g)\left|{}^\mu_{mn'}\right\rangle \qquad (15.3.10)$$

Regular representation of operators **g** and dual operators $\bar{\mathbf{g}}$.

$$R^G_{h,f}(\mathbf{g}) = \langle h|\mathbf{g}|f\rangle = \delta_{h=gf} = \left\{ \begin{array}{l} 1 \ \text{if: } \mathbf{h} = \mathbf{g}\cdot\mathbf{f} \\ 0 \ \text{if: } \mathbf{h} \neq \mathbf{g}\cdot\mathbf{f} \end{array} \right\} = \delta_{f^\dagger = h^\dagger g} \qquad R^G_{h,f}(\bar{\mathbf{g}}) = \langle h|\bar{\mathbf{g}}|f\rangle = \langle 1|\mathbf{h}^\dagger \mathbf{f}\cdot\mathbf{g}^\dagger|1\rangle = \delta_{f=hg} \quad (15.3.11)$$

Symmetry: $\mathbf{g}\,\mathbf{H} = \mathbf{H}\,\mathbf{g}$ of Hamiltonian $\mathbf{H} = H\bar{\mathbf{1}} + R\bar{\mathbf{r}} + R^*\bar{\mathbf{r}}^2 + L\bar{\mathbf{i}}_1 + M\bar{\mathbf{i}}_2 + S\bar{\mathbf{i}}_3$ (15.4.2a)

Solution: $H^\mu_{ab} = \sum\limits_{g=1}^{{}^\circ G} \langle 1|\mathbf{H}|\mathbf{g}\rangle D^{\mu\,*}_{ab}(g)$ (15.4.5c)